NORTHWESTERN UNIVERSITY

Functional Responses Map onto Genetic Subtypes of Dopamine Neurons

A DISSERTATION

SUBMITTED TO THE GRADUATE SCHOOL
IN PARTIAL FULFILLMENT OF THE REQUIREMENTS

for the degree

DOCTOR OF PHILOSOPHY

Northwestern University Interdepartmental Neuroscience Program (NUIN)

By

Maite Azcorra

EVANSTON, ILLINOIS

December 2022

Abstract

Dopamine neurons are characterized by their response to unexpected rewards, but some also fire during movement and in response to aversive stimuli. Dopamine neuron diversity has also been observed based on their genetic expression profiles, suggesting that different functions might map onto such genetic subtypes. However, this has not been tested.

Here, we functionally characterized four previously described genetic subtypes of dopamine neurons in the substantia nigra pars compacta, the Sox6+, Calb1+, Vglut2+, and Aldh1a1+ subtypes, and discover a new subtype, Anxa1+. We first establish that two of these genetic subtypes, Sox6+ and Aldh1a1+, are functionally heterogeneous, which leads us to search for and discover a new sub-population within Sox6+/Aldha1a1+ neurons: the Anxa1+ subtype. We then establish that the Vglut2+, Calb1+ and Anxa1+ subtypes each have a unique set of responses to rewards, aversive stimuli, accelerations and decelerations which are specific to each subtype even when they overlap anatomically. Remarkably, reward responses were not detected in one subtype, Anxa1+, which instead displayed acceleration-correlated signaling. We also show that these signaling patterns are highly-correlated between somas and axons within subtypes, rejecting the possibility that these differences might emerge due to local cholinergic modulation in striatum. Furthermore, we use these same genetic markers to show that different DA subtypes originate from different progenitor pools during development, that they are differentially vulnerable in Parkinson's disease, and provide evidence to help explain why.

Our findings establish a connection between functional and genetic dopamine subtypes and demonstrate that molecular expression patterns can serve as a common framework to dissect dopaminergic functions.

Acknowledgment

First and foremost, I want to thank my PhD advisors, Dr. Daniel Dombeck and Dr. Rajeshwar Awatramani, without whose support and guidance this work could not have been attempted. I especially thank them for their empathy and care during the hard times of the COVID-19 pandemic, which brought the worst of some people but only proved how incredible mentors Dan and Raj are. Together, they have provided me the perfect combination of advice, skills and mentorship that have made my Ph.D. an incredible experience. I am grateful to Dan for believing that someone with little to no experience in survival surgeries, computational analysis and in vivo experiments could be successful in his lab, but especially for always being there for me to discuss anything and everything, however small, and giving the best advice, always with my interest in mind. Thank you for always lifting me in the down times (my favorite quote from Dan is that "in every Ph.D. there's at least one occasion when you think all your data is just noise"), but also for keeping me on track every time a new idea took me on a wild goose chase. I am grateful for Raj always seeing the best in me and being by biggest cheerleader (it really helped in warding off the pervasive impostor syndrome), but also for being perpetually excited to talk about science and new ideas, and for infecting me with this enthusiasm. Thanks also for always treating me as a scientific equal and for including me in big discussions, Raj did so much to introduce me to other professors and spread my work, and I cannot thank him enough for starting me off in the complicated world of networking. I also cannot miss thanking the Northwestern Intercampus shuttle, for making it possible for these two brilliant scientific minds to meet and kickstart this project, but also for allowing this cross-campus collaboration by transporting me and my mice.

I am also grateful to many other professors that helped me throughout my Ph.D., particularly the members of my thesis committee, Genia Kozorovitskiy, Andrew Miri, and Jim Surmeier, for their invaluable advice and feedback. Thank you also to Indira Raman for her heartfelt advice and for organizing the After NUIN Afternoons, an amazing seminar series that showed me all the non-academic options I could have (and ultimately helped me confirm that I do want to stay in academia); and to Marco Galio and Dave McLean for their amazing help with finding the next step in my career. Also thanks to Karl Deisseroth and his lab for sending me their intersectional viruses before publication, without which my project would not have been possible at the time.

I also want to thank all the mentors that guided me in my early career stages, Dr. Jose Antonio Esteban and Dr. Erin Schuman for providing me with my first real research experiences, but especially Dr. Anthony Brown for giving me the chance to work in his lab and the independence to lead my own project. As an undergraduate coming from abroad this opportunity opened so many doors for me, and the skills, scientific and personal, I learnt in his lab have been essential for my success as a graduate student and will be with me for the rest of my career. Also thank you for the wonderful laser pointer that has accompanied me throughout my PhD in every presentation.

Throughout my Ph.D. I have been very lucky to interact with so many postdocs and Ph.D. students that helped me enormously and made my experience here so enriching. I am particularly thankful to Mark Howe and Jean Francois Poulin, who laid the groundwork for my project and taught me everything I needed to be successful. Mike Adoff for training me during my rotation in Dan's lab, he truly made an effort to make sure I got something out of it and was a fantastic teacher. Brad Radvansky for making lab so much fun and for being my Ph.D. guru – his sage teachings will always remain with me, and I will try to pass them on to the next generation; John Issa for being the best sounding board to talk through any idea, and together with Mike for leading the Dombeck

lab basketball team that was so much fun; Jason Climer for all his help with statistics and analysis; Daniel Oh for all his amazing food recommendations; Dom Pinke for his many fun science memes; and all other Dombeck lab members for their great advice and feedback. Special thanks too to the newly assembled *Dopateam*: Shiva Nagappan and Elena He for sharing my interest in dopamine and wanting to discuss papers with me, but also for helping collect the last bit of data to complete this project; Hailey Kim for braving through all the learning and doing some amazing work despite bad luck; and especially Connor Davidson for all his great help with data collection and histology. Thanks also to the Awatramani lab members, especially Mili Pereira Luppi for being my constant comrade-in-arms and for leading to way to get the Sox6 paper finally published (and making the best *Pulpo a la gallega* I've had outside of Spain), and to Zack Gartner for his amazing (and perfectly timely) work to uncover the Anxa1+ subtype, which allowed me to neatly wrap up my Ph.D. work without all the Aldh1a1+ loose ends. Thanks also to Giuliana Caronia-Brown for spearheading the Sox6 project and trusting me to collaborate in it.

I am also very grateful to all the supporting staff at Northwestern University and in NUIN. Alana Lackore and Jena Pitman-Leung, and later and Stephanie Valtierra, Melissa Moore and Asta Stekovic for all their guidance and help to make sure my Ph.D. went smoothly; Northwestern's international office for making sure I don't get deported; the Neurobiology department staff and in particular Anthony Keevan, Franny McNamara, Ginger Gilmore, and Alex Villatoro, for helping me book (so many) conference rooms and navigate purchasing and administrative hurdles; the CCM staff for keeping my mice healthy and happy and for so many cheerful conversations; the shipping dock staff for their wonderful friendliness and the Pancoe Custodians for keeping me company on late-working nights. I want to especially thank all these people for their essential work

during the COVID-19 pandemic, together will all the other essential workers that kept our world running during such hard times.

I also can't forget to thank the funding sources that made this research possible, the La Caixa Fellowship, the Michael J. Fox foundation ASAP program (Aligning Science Across Parkinson's, ASAP-020600), Northwestern University and the NIH (R01MH110556). We cannot take for granted the essential role of organizations like these and all the people in them in advancing science.

Lastly but certainly not least, I want to thank all my friends and family that accompanied and supported me through this whole period of my life, none of this would've been possible without all of you by my side. Thanks to Chelsea Rugel and Seth Thomson (as well as Piper and Tali) for being the best people to Chill with, with capital C – I don't know what would've been of me without you; to my ArtsyFartsy friends Owen Shelton, Torben Noto and Vivek Sagar, for helping bring art back to my life and inspiring me to be original; to Nathan Whitmore more always making me think outside the box; to Miranda Munoz and Sam Minkowicz for helping me keep my love for the Theater and for listening to my frustrations; to Marco Giovannini, Ettore Trainiti, Enrico Deiana, Jiexi Chen, and Madhav Suresh for being the best pandemic bubble gang, you really made my time in Evanston amazing; to my friends in back in Spain, especially Miriam Carrasco Villar, for putting in the effort to maintaining the friendship despite the distance; and to Simone Bianconi, my partner, best friend and newest family, for absolutely everything, but here especially for helping me figure out what I want and what I care about in life. I am also so very grateful for my family, especially my parents and my brother Jaime for always being there for me and their amazing advice, and my grampa for his unwavering cheerfulness and joy for life. Thank you all.

List of Abbreviations

Neurotransmitters

DA	Dopamine
ACh	Acetylcholine

Anatomical locations

FP	Floorplate
SNc	Substantia Nigra Pars Compacta
hSNc	Human SNc
dSNc	Dorsal tier SNc
vSNc	Ventral tier SNc
mSNc	Medial SNc
lSNc	Lateral SNc
SPpl	Substantia Nigra Pars Lateralis
VTA	Ventral Tegmental Area
RRF	Retrorubral Field
CP	Striatum (caudo-putamen)
CPr	Rostral Striatum
CPi	Intermediate Striatum
CPc	Caudal Striatum
TS	Tail of the striatum (caudal-most region)
ACB	Nucleus Accumbens
IPAC	Interstitial nucleus of the Posterior limb of the Anterior Commissure

Genes and proteins

Sox6	SRY-Box Transcription Factor 6
Vglut2	Vesicular Glutamate Transporter 2
Calb1	Calbindin 1
Aldh1a1	Aldehyde Dehydrogenase 1 Family Member A1
Anxa1	Annexin A1

Th	Tyrosine Hydroxylase
DAT	Dopamine Transporter

Fluorescent proteins and other reporters

mCherry	Red fluorescent protein
GFP	Green Fluorescent Protein
EYFP	Enhanced Yellow Fluorescent Protein
GCaMP6f	Green Calcium Indicator version 6-fast
βGal	β-Galactosidase

Other

PD	Parkinson's Disease
MPTP	1-Methyl-4-Phenyl-1,2,3,6-Tetrahydropyridine
SEM	Standard Error of the Mean
GSEA	Gene Set Enrichment Analysis
PRISM	Progenitor Restricted Intersectional Fate Mapping

To my family. *Sin vosotros, nada habría sido posible.*

Table of Contents

List of Tables, Illustrations, Figures, and Graphs

1. Introduction

After the discovery that dopamine (DA) neurons in the substantia nigra pars compacta (SNc) degenerate in Parkinson's Disease (PD)[1], a movement disorder characterized by tremors, slowness, stiffness, and walking and balance problems, attempts were made to understand how these neurons signaled during locomotion[2]. However, while some neurons were found to modulate their firing in response to movements[2], soon they found that many neurons respond to rewards and reward predicting cues in a way consistent with Reward Prediction Error (RPE), by which the amplitude of the response is proportional to the difference between the value of the outcome received and the value expected[3]. The striking similarities between this signaling pattern and the teaching parameter used in computer learning lead to the hypothesis that DA neurons in the brain play a key role in reinforcement learning[3], a theory which has since received endless attention for its important implications.

After the discovery that DA neurons respond to rewards/reward predicting cues, most DA neurons were identified based on these cues, and motor responses were largely ignored. However, DA's role in motor control was still evident through PD patients and had to be factored in. To combine this with the rising model of DA's involvement in reinforcement learning, a new hypothesis proposed that DA acted at different timescales: rapid, phasic changes in DA neurons firing (and thus DA release) signaled RPE, while slow, tonic changes in firing generated a tone of DA that enabled movement control[4]. This theory prevailed for many years, justifying the focus on RPE research, until evidence emerged showing that some DA neurons in the SNc rapidly changed their firing in response to accelerations during movement[5–8]. This showed that phasic changes in DA encode not just RPE but also movement and putting into question the two-timescale hypothesis.

This unifying theory was further challenged by new evidence that DA neurons are not a homogeneous population, with different neurons differently responding to a wide range of stimuli and behaviors. Beyond the previous results, by which some DA neurons increase their firing at accelerations and others decrease it (and others are not modulated by movement)[5–8], DA neurons have been shown to respond differently to rewards, with some neurons not responding to rewards at all[5,6,9,10] and others encoding value rather than RPE[11–13]. Furthermore, they also have been shown to differentially respond to aversive stimuli, with some neurons increasing signaling and others decreasing it[14–16]. On another plane, DA neurons have also been shown to differ on their anatomical[17,18] and electrophysiological properties[16,19,20], their co-release of different neurotransmitters[21,22], their vulnerability in PD[23–26], their inputs[27], and their expression profiles[28], further suggesting that not all DA neurons have the same function.

Despite this, new unifying theories that attempt to assign a common role to all DA neurons continue to appear[29–32]. One reason for this is that reports of functional heterogeneity of DA neurons show inconsistencies in their results. For example, while some recordings from dorsal striatum report no response to reward in these DA axons[5] other studies have found reward responses in similar regions[16,32,33], and while some show DA axons in posterior striatum respond to aversive stimuli[9,14] other instead showed negative responses[34]. Different behavioral paradigms could explain some of these differences (for instance the use of different aversive stimuli[9]), but some remain unexplainable. This consequently leads to the need of ignoring some results in order to have a consistent view of the literature.

Instead, we here explore the idea that DA neurons can be divided into subtypes with their own functions, which would help explain the previous inconsistencies: different subtypes or mixtures of them might have been (unknowingly) studied, resulting in different characteristics measured.

This has been considered by others[29,35], but it is hard to test as it would require each cell to be recorded in a wide range of behavioral paradigms, which is unfeasible especially across studies or animals, or using anatomical approaches to reproducibly segregate neurons, which is complicated by the lack of clear histological boundaries within the striatum or the midbrain, resulting in arbitrary divisions that are hard to replicate. To address this, we here propose the use of genetic markers as access points. DA neurons have been divided into genetic subtypes bases on their expression profiles[28], and some subtypes have been assigned genetic markers that can be used to access them[17], such as Sox6, Aldh1a1, Calb1, and Vglut2. This classification however is not dependent on these marker genes only – subtypes differ in the combined expression of a whole range of genes, among which the marker gene is only one.

The use of genetic subtypes of dopamine neurons can allow science to (i) access the same subset of DA neurons reproducibly across studies, days, animals, and even species; (ii) resolve inconsistencies in the existing literature, by identifying which subtype(s) were studied in each case; (iii) develop new models of DA neuron function that take into account their functional diversity; and (iv) study characteristics of different subtypes that are obscured when all neurons are considered together, like their inputs or development.

Finally, a recent controversy in the DA field comes from a hypothesis proposing that DA release from DA axons is driven by local cholinergic modulation and not somatic firing[13,36,37]. This is supported by the finding that dopamine release in the nucleus Accumbens cannot be explained by firing of VTA neurons[13]. However, DA neuron heterogeneity could again explain these results if different subtypes were studied in each compartment[13,29].

2. Sox6, a first division of dopamine neurons

Most of this chapter was published in Pereira Luppi et al. 2021[38], including additional supplemental information for some sections. This was a collaboration between several authors, particularly Milagros Pereira Luppi, and work conducted by other authors is specified in the figure legends. Printed with permission of Milagros Pereira Luppi and Giuliana Caronia-Brown.

2.1. Introduction

The substantia nigra pars compacta (SNc), a key DA neuron containing cluster, is heterogeneous in its composition. Even before the discovery of dopamine (DA) six decades ago, Hassler demonstrated that in post-mortem Parkinson's disease (PD) brains, neurodegeneration is more prominent in the ventral SNc than in the dorsal SNc, a finding that has been corroborated using immunolabeling techniques for DA neuron markers[24,39–44] and has led to the description of a ventral and dorsal tier of the SNc. Uncovering the molecular, anatomic, and functional differences between these tiers would help explain their susceptibility in PD, yet they remain to be fully elucidated.

Besides distinctions based on selective vulnerability, recent studies suggest physiological and functional heterogeneity of SNc DA neurons. Physiologically, SNc neurons differ by their T type calcium channel-mediated rebound excitability[19], HCN channel current size[16], or burstiness[20]. Functionally, some SNc neurons respond to rewarding stimuli, while others located in the lateral SNc or SN pars lateralis (SNpl) also respond to aversive stimuli[9,15,16]. Axons of SNc neurons projecting to the dorsal striatum display activity time-locked to locomotion, whereas those projecting ventrally appear to be more reward responsive[5]. During movement, some are activated during acceleration, and some are unresponsive[5,6,8]. These studies find major differences across

the medio-lateral axis[16,20], or across the dorso-ventral axis[5,19] of the SNc. To better integrate and extend these findings, a deeper understanding of SNc heterogeneity is key to deciphering the pleiotropic functions of this structure.

To examine SNc heterogeneity at the molecular level, single-cell profiling has been used to group DA neurons based on similar molecular signatures. Recent studies have revealed the presence of several putative DA neuron subtypes[45–50]. For instance, our lab and others have identified a DA neuron population defined by the expression of transcription factor Sox6 and aldehyde dehydrogenase Aldh1a1[47,51], located in the ventral SNc, that was selectively vulnerable in a toxin model of PD. Despite this promising start towards SNc classification, defining the complete catalog of the cellular constituents of the SNc remains a work in progress, in part because of the technical limitations of single-cell transcriptomic analyses, as well as the closely related nature of these neurons[52] Besides, how these molecularly defined subtypes align with dorsal and ventral tiers remains to be fully addressed. Moreover, if there is such a fundamental difference in vulnerability, it opens the possibility it is encoded early in development.

All midbrain DA neurons originate from the Shh+/Foxa2+/Lmx1a+ embryonic floor plate (FP)[53–58], which can be subdivided roughly into a medial Sox6+ and a lateral Sox6-/Wnt1+/Otx2+ progenitor domain[51,59]. Current models disagree on the molecular identity of the medial vs lateral progenitor domain descendants, with some studies suggesting that medially located progenitors represent a key anlage for SNc neurons[51,55] and others suggesting that the lateral progenitor domain is also a prominent source of SNc neurons[56,60]. Additionally, none of these studies have explained the developmental underpinnings of dorsal and ventral tier neurons. Using lineage tracing tools to understand SNc diversity from a developmental perspective could reinforce the robustness of adult single cell-based taxonomic dendrograms[61,62].

This study aims to shed light on dorsal and ventral SNc DA neurons, from a molecular, functional, and developmental perspective. First, we demonstrate that the Sox6+/Aldh1a1+ population exists in the human ventral SNc and is selectively diminished in post-mortem PD brains. Next, we reveal that Sox6 expression defines a population of neurons that are more ventrally located and enriched in molecular pathways that could underpin vulnerability. Furthermore, we uncover a dorsal Sox6- population that includes neurons expressing Calb1 and Slc17a6 (Vglut2), genes associated with resilience to neurodegeneration. We describe distinct projection patterns and functions of Sox6+ and Sox6- neurons, validating this fundamental SNc division. Moreover, we reveal distinct developmental histories between these neuronal cohorts, that demonstrate a dual embryonic origin of the SNc. Altogether, our work facilitates a more granular definition of the cellular landscape of the SNc, beyond current schemes obtained by single-cell profiling studies, and provides insights into the selective vulnerability of ventral tier neurons in PD.

2.2. Anatomical characterization of adult Sox6+ and Sox6- DA neurons in mouse SNc

Sox6+ DA neurons are mainly located in the SNc, with few found in lateral VTA, and project to dorsal striatum[17]. However, it is unknown whether Sox6- DA neurons exist in the SNc, and if so where they are located and project to. To address this question, a new intersectional and subtractional genetic strategy was developed to simultaneously label Sox6+ and Sox6- adult DA neurons. A Sox6-fsf-Cre/Th-Flpo mouse was crossed to the transgenic reporter RC-Frepe (B6;129S6-*Gt(ROSA)26Sor*$^{tm8(CAG-mCherry,-EGFP)Dym}$/J, RRID:IMSR_JAX:029486), which expresses mCherry in Cre+Flpo+ (Th+Sox6-) neurons and GFP in Cre-Flpo+ (Th+Sox6+) neurons (Figure 1A). Because Sox6 is expressed during development in floorplate (FP) progenitors that give rise to midbrain DA neurons, this strategy is designed to label only post-mitotic, adult expression of

Sox6. To achieve this, Cre expression in the Sox6-fsf-Cre mouse line is dependent on Flpo recombination, and because Th expression (which controls Flpo) occurs only post-mitotically, Cre-dependent Frepe recombination can only occur in post-mitotic DA neurons. From here on, we will refer to GFP+ neurons resulting from this genetic strategy as Sox6+ DA neurons, and mCherry+ neurons as Sox6-, as this indicates either insufficient levels or complete lack of Sox6 expression in these neurons.

As expected[17], Sox6+ neurons were found mostly in SNc, with few found in the VTA (Figure 1B-C). However, while most SNc DA neurons were Sox6+, a significant proportion was Sox6- (30.0% ± 3.1%, Figure 1B-C), and particularly the pars lateralis (SNpl) showing that the SNc is genetically diverse and includes at least two distinct subtypes. Interestingly, these two subtypes displayed a biased spatial distribution: Sox6+ neurons were ventrally enriched while mCherry+ neurons were dorsally enriched, although with significant intermingling (Figure 1B). To quantify this, a histogram of the dorso-ventral distribution of Sox6+ and Sox6- DA neurons within the SNc was plotted (Figure 1C-D). To obtain this histogram, the spatial coordinates of SNc Sox6+ and Sox6- DA neurons were plotted and a line of best fit to all SNc cells' coordinates was calculated, identifying the dorso-ventral center of the SNc along its naturally angled axis (Figure 1H). Cell coordinates were then rotated around this axis so that the x coordinate represented the distance along the medio-lateral axis from the medial edge of the SNc (though this was not used for further analysis), while the y coordinate represented the distance from this dorso-ventral midline (Figure 1H'). A histogram was then obtained for the distribution of Sox6+ and Sox6- cells across this dorso-ventral (y) axis (Figure 1H''), then averaged across 4 antero-posterior slices per mouse, and finally averaged across n = 5 mice to obtain Figure 1C. This showed that the ventral tier of the SNc was greatly enriched in Sox6+ neurons, while the dorsal tier was more evenly composed of

Figure 1: Sox6 expression defines a dorsal-ventral division of the murine SNc

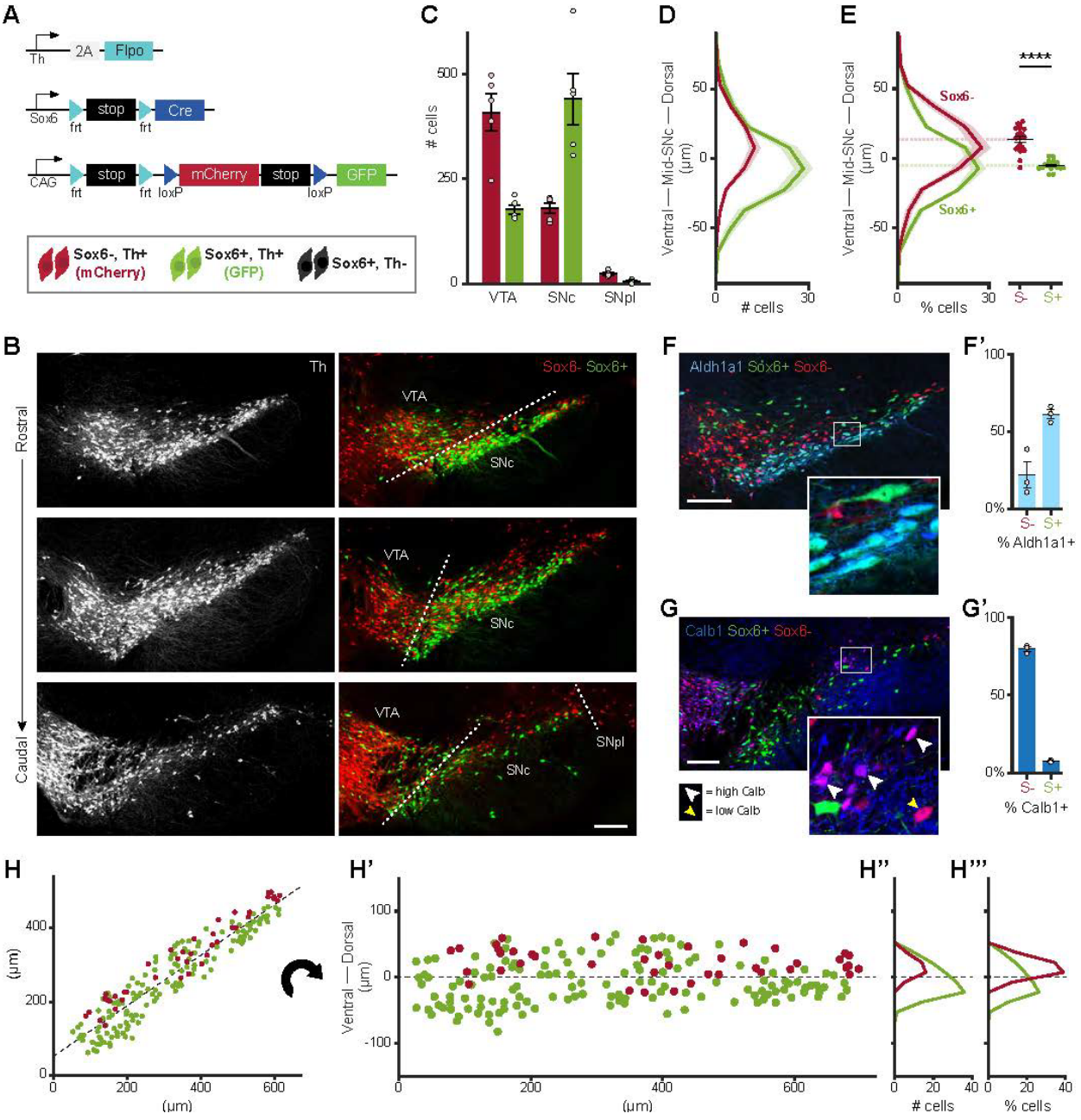

(**A**) Simultaneous intersectional/subtractional genetic labeling strategy.

(**B**) Example of an adult Sox6-FSF-Cre, Th-2A-flpo, RC-Frepe brain.

(**C**) Average number of TH+,mCherry+ (red bars) and TH+,GFP+ (green bars) in the main DA neuron areas. p values: SNc = 0.014, SNpl = 0.004, VTA = 0.008.

(**D**) Histogram of spatial coordinates of TH+,GFP+ or TH+,mCherry+ cells; TH+,mCherry+ neurons are biased dorsally.

(**E**) Left: histogram of spatial coordinates of TH+,GFP+ or TH+,mCherry+ cells normalized to total TH+,GFP+ or TH+,mCherry+ cells. Right: centroid of GFP+ and mCherry+ populations for each section of each mouse included in left panel (4 sections per brain) ($p = 6 \times 10^{-07}$).

(**F**) GFP+ cells co-express ALDH1A1 (SNc).

(**F'**) % of GFP+ (Sox6+) and mCherry+ (Sox6-) neurons co-expressing ALDH1A1 in the SNc. p = 0.02.

(**G**) Most mCherry+ cells express CALBINDIN-D28k (CB) (SNc). CB signal intensity varies from low (yellow arrowhead) to high (white arrowhead).

(**G'**) % of GFP+ (Sox6+) and mCherry+ (Sox6-) neurons co-expressing CB in the SNc. p = 0.0007.

(**H**) Example of methodology used for obtaining dorso-ventral histograms in D-E. Coordinates are obtained for SNc Th+GFP+ (Sox6+) and Th+mCherry+ (Sox6-) cells. A line of best fit is obtained for all cells, which is used to set the center of the SNc. Cell coordinates are then rotated along this line (H'), and a histogram of cells is obtained, perpendicular to the center line (H''). For E, cell counts are then normalized by the total number of Sox6+ or Sox6- cells (H''').

Scale bars: 200 mm. Error bars (C, E, F', G') and shaded areas (D, E) are SEMs. S+: Sox6+,S-: Sox6-.

(A–E) n = 5 mice, (F-G) n = 3 mice.

Experiment and cell counts by Milagros Pereira Luppi, analysis by Maite Azcorra.

Sox6+ and Sox6- neurons. However, because of the uneven numbers of Sox6+ and Sox6- cells in SNc, to analyze whether there was a spatial bias in the distribution of the subtypes themselves we normalized the histograms by the total number of cells of each subtype (Figure 1E, H'''). This showed that Sox6+ cells were biased towards the ventral SNc while Sox6- cells were biased towards the dorsal SNc, with the centers of mass of the two populations significantly different across mice and antero-posterior slices (Figure 1E right, p-value = 6×10^{-07}).

While Sox6 is a key driver of variance in DA neurons, others such as Aldh1a1 and Calb1 are also important markers[28,47]. Thus, we sought to investigate whether and how the Aldh1a1+ and Calb1+ subtypes overlapped with the Sox6+ or Sox6- subtypes. We examined Aldh1a1 or Calb1 expression by immunostaining in Sox6-FSF-Cre/Th-Flpo/RC-Frepe adult brains (same as those used above to determine Sox6+ and Sox6- soma distribution). We found that Aldh1a1+ neurons were mostly a subset of Sox6+ neurons (86.7% ± 6.4% of Aldh1a1+ neurons were GFP+, Figure 1F), though only 61% of Sox6+ cells were Aldh1a1+ (Figure 1F'). This suggests that Sox6+ neurons can be sub-divided into two subtypes, one Aldh1a1+ and one Aldh1a1-; which is in line with previous studies[28,47]. Interestingly, while Sox6+ neurons were already ventrally biased within

SNc, Aldh1a1+ neurons were even more ventrally biased (Figure 1F'). Calb1+ neurons on the contrary were localized dorsally in the SNc, with high and low immunolabeling levels as previously shown[46] (Figure 1G). Furthermore, we found that the majority of SNc Sox6- neurons were Calb1+ (79.3%, Figure 1G'), which was also the case in the VTA (87.2 ± 2.1%) and the SNpl (90.3% ± 6.6%) (data not shown). These findings strongly suggest that Sox6 expression divides the murine SNc into a Sox6+ subtype biased to the ventral SNc (vSNc), which can be further sub-divided two subtypes, Aldh1a1+ (further ventrally biased) and Aldh1a1-; and a Sox6-/Calb1+ subtype biased to the dorsal SNc (dSNc) and SNpl.

Next, we asked whether these two SNc DA subtypes had axonal arbors that projected to different regions within striatum. Our transgenic intersectional/subtractive labeling approach (Figure 1A) labels Sox6+ and Sox6- DA neuron in SNc but also in VTA and RRF, confounding any analysis of axonal projections of SNc neurons. Thus, we instead used a viral intersectional/subtractional strategy (Figure 2A-B, Figure 3A,D) that labeled mainly SNc cells, with few VTA cells labeled (Figure 2D, Figure 3B). Sox6-FSF-Cre/Th-Flpo mice were injected in the SNc (see Methodology) (Figure 2B) with CreOn/FlpOn-EYFP and CreOff/FlpOn-mCherry viruses, simultaneously labeling Sox6+ and Sox6- neurons and their projections.

We found that Sox6+ and Sox6- populations targeted distinct areas of the striatum along the medio-lateral, dorso-ventral, and rostro-caudal axes (Figure 2C, Figure 3C,F). Sox6+ neurons densely innervated the striatum mainly in the medial and ventral areas, including the nucleus accumbens (ACB), and the tail of the striatum (TS) (Figure 2C). In rostral (CPr) and intermediate (CPi) sections, Sox6- axons were denser toward ventral areas (Figure 2E), and in dorsal striatum they

Figure 2: Sox6+ and Sox6- subtypes have distinct and inverted projection patterns

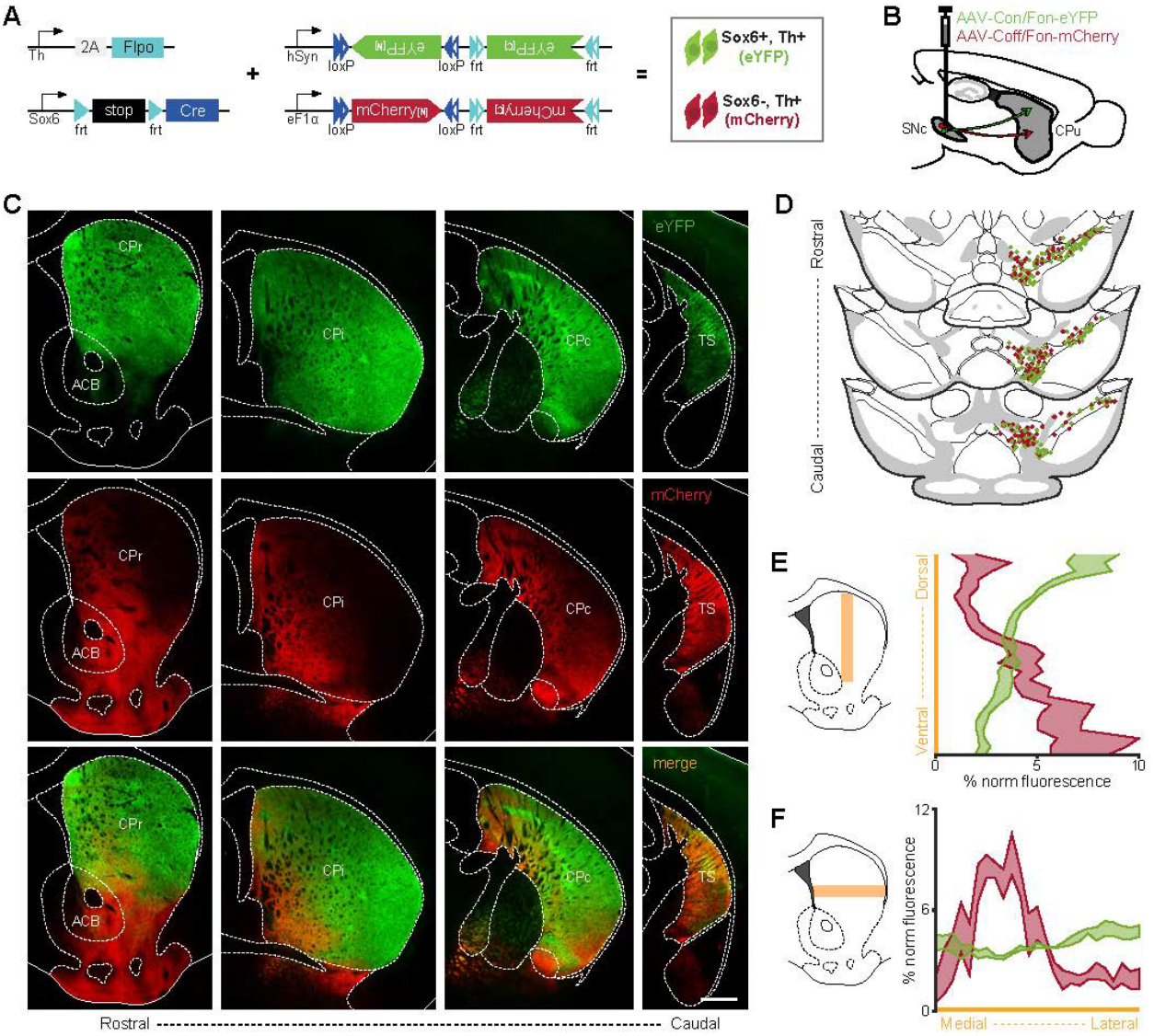

(**A**) Genetic strategy used to simultaneously label Sox6+ and Sox6? neurons and their projections in adult brains.

(**B**) Schematic showing injection location (SNc).

(**C**) Projections across the rostro-caudal axis of the striatum from Th+Sox6+ vSNc neurons (EYFP, top), from Th+Sox6- dSNc neurons (mCherry, center), and merged images (bottom).

(**D**) Representation of labeled cells in the midbrain corresponding to C. Each dot represents 3 labeled cells.

(**E**) Histogram of normalized fluorescence for Sox6+ and Sox6- axons along the dorsoventral axis of the striatum (CPr and CPi). Left, representation of the region of the striatum used for quantification.

(**F**) Histogram of normalized fluorescence for Sox6+ and Sox6- axons along the mediolateral axis of the striatum (CPr and CPi). Left, representation of the region of the striatum used for quantification.

were strongly biased toward the medial striatum (Figure 2F). Conversely, Sox6+ axons densely innervated the dorsal striatum but showed no obvious bias along the medio-lateral axis (Figure 2C, E-F). Sox6+ axons were sparse in the ACB, except in parts of the core and lateral shell (Figure 2C). In more caudal sections (CPc), the dorso-ventral and medio-lateral gradients become less prominent (Figure 2C). mCherry innervation is also particularly prominent in the interstitial nucleus of the posterior limb of the anterior commissure (IPAC) (Figure 2C, Figure 3C,F), in agreement with previous reports[63]. To rule out biases from virus and/or fluorophore distribution, we repeated these experiments with a different set of viruses that label the same populations in reverse colors, with similar results (Figure 3D-F). Furthermore, due to the anatomical proximity of the SNc and VTA it is technically challenging to label all the SNc while avoiding all VTA cells. To confirm that the projection patterns observed were not due to the few VTA cells labeled in Figure 2C-D, we repeated the experiment with a smaller, more lateral viral injection, which spared the VTA but failed to fully label the medial SNc (Figure 3A-C). While the projection patterns were similar as shown in Figure 2C, projections into the ACB core and olfactory tubercle were absent (Figure 3C), probably originating from labelled cells in VTA. Furthermore, in the dorsal striatum Sox6+ axons were sparser in medial regions, possibly due to medial SNc cells not labeled in this strategy (Figure 3A-C), in accordance with previous reports[16].

Overall, the Sox6+ projection pattern to dorsal striatum agrees with our previous work[17], but we additionally show that the Sox6- population of the dSNc/SNpl has markedly distinct projections to the medial, ventral, and tail of the striatum. This roughly matches the projections of Calb1+ neurons[17], consistent with the fact that Sox6- neurons are largely Calb1+ (Figure 1G').

Figure 3: Sox6+ and Sox6- projection patterns are similar when only SNc neurons are labelled, and when an alternative viral strategy is used.

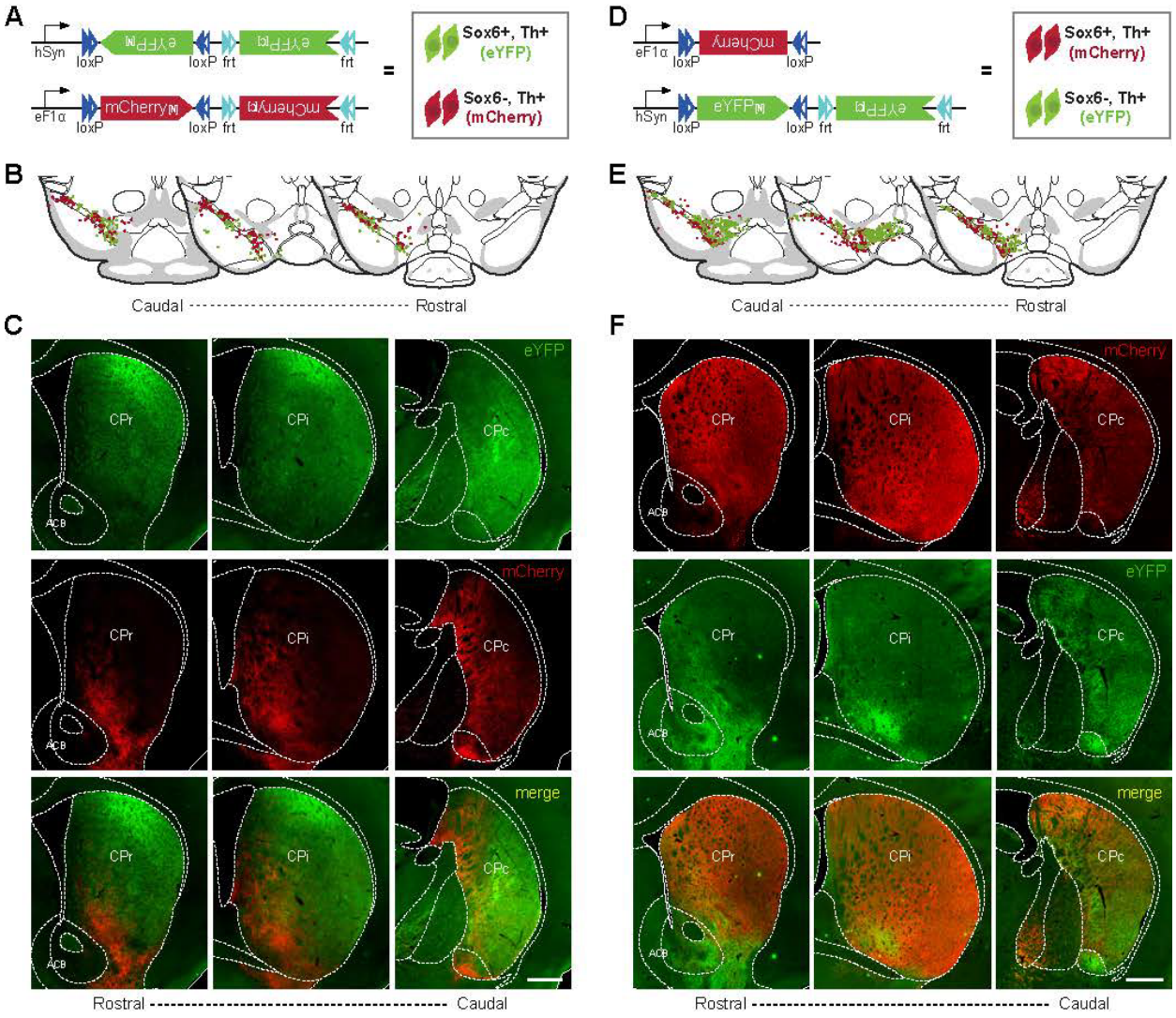

(**A**) Genetic strategy used to simultaneously label Sox6+ and Sox6- neurons and their projections in adult brains, as in Fig 3.

(**B**) Representation of labelled cells in the midbrain for experiment A-C. Each dot represents one cell. Few cells in VTA and less medial SNc cells are labelled, compared to Figure 2D.

(**C**) Projections across the rostro-caudal axis of the striatum from Th+Sox6+ vSNc neurons (eYFP, top), from Th+Sox6- dSNc neurons (mCherry, middle), and merged images (bottom), from cells shown in C. Scale bar 500 μm.

(**D**) Alternative genetic strategy, opposite to Figure 2 and Figure 3A-C, with Sox6+Th+ cells labelled by mCherry and Sox6-Th+ cells labelled by eYFP.

(**E**) Representation of labelled cells in the midbrain for experiment D-F. Each dot represents one cell.

(**F**) Projections across the rostro-caudal axis of the striatum from Th+Sox6+ vSNc neurons (mCherry, top), Th+Sox6- dSNc neurons (eYFP, middle), and merged images (bottom), from cells shown in E. Scale bar 500 μm.

2.3. Sox6+/Aldh1a1+ DA neurons in the human SNc and vulnerability in PD

The existence of this Sox6+/Aldh1a1+ subtype of SNc DA neurons had been previously identified in single-cell profiling analyses of murine SNc[46,47], and was found to be selectively vulnerable to MPTP[47], a model commonly used to mimic several important pathological features of PD in mice. This opened the possibility that a similar subtype exists in the human SNc (hSNc) and that it might be selectively vulnerable in PD. To test this, we performed immunolabeling in control and PD post-mortem brains. In control brains, we observed a defined Aldh1a1+ subset localized ventrally in the hSNc (Figure 4A), the majority of which co-expressed Sox6+ (83.8% ± 3.4%; Figure 3C top). Furthermore, Calb1+ neurons were also present in the hSNc, and were mostly non-overlapping with Aldh1a1+ neurons (Figure 4C bottom). This confirms that subtypes found in mice are similarly found in humans.

To assess their vulnerability, we investigated PD brains and age-matched controls. Th+ neurons were significantly reduced in PD brains, as expected (70.0% ± 4% reduction compared to control brains; Figure 4B,D), but importantly within them Sox6+/Aldh1a1+ DA neurons were more diminished in numbers than other DA neurons (82.1% ± 3.7% vs 50.3% ± 6.8% reduction compared to controls respectively, Figure 4E). On the other hand, Calb1+ DA neurons were less affected than other DA neuron subtypes (13% ± 13.9% vs 69.4% ± 4.4% reduction compared to controls respectively, Figure 4F). Thus, a selectively vulnerable population in the ventral hSNc co-expresses Sox6 and Aldh1a1, while a resilient population expresses Calb1.

However, a more complicated picture emerges when we analyze the vulnerability of cells with different combinations of genes expressed (Figure 4G-H). While Aldh1a1+ neurons were particularly vulnerable in PD, this was the case for both those co-expressing Sox6 and not, while

Figure 4: In the human SNc, Aldh1a1+/Sox6+ neurons are vulnerable in PD while Calb1+ neurons are relatively spared

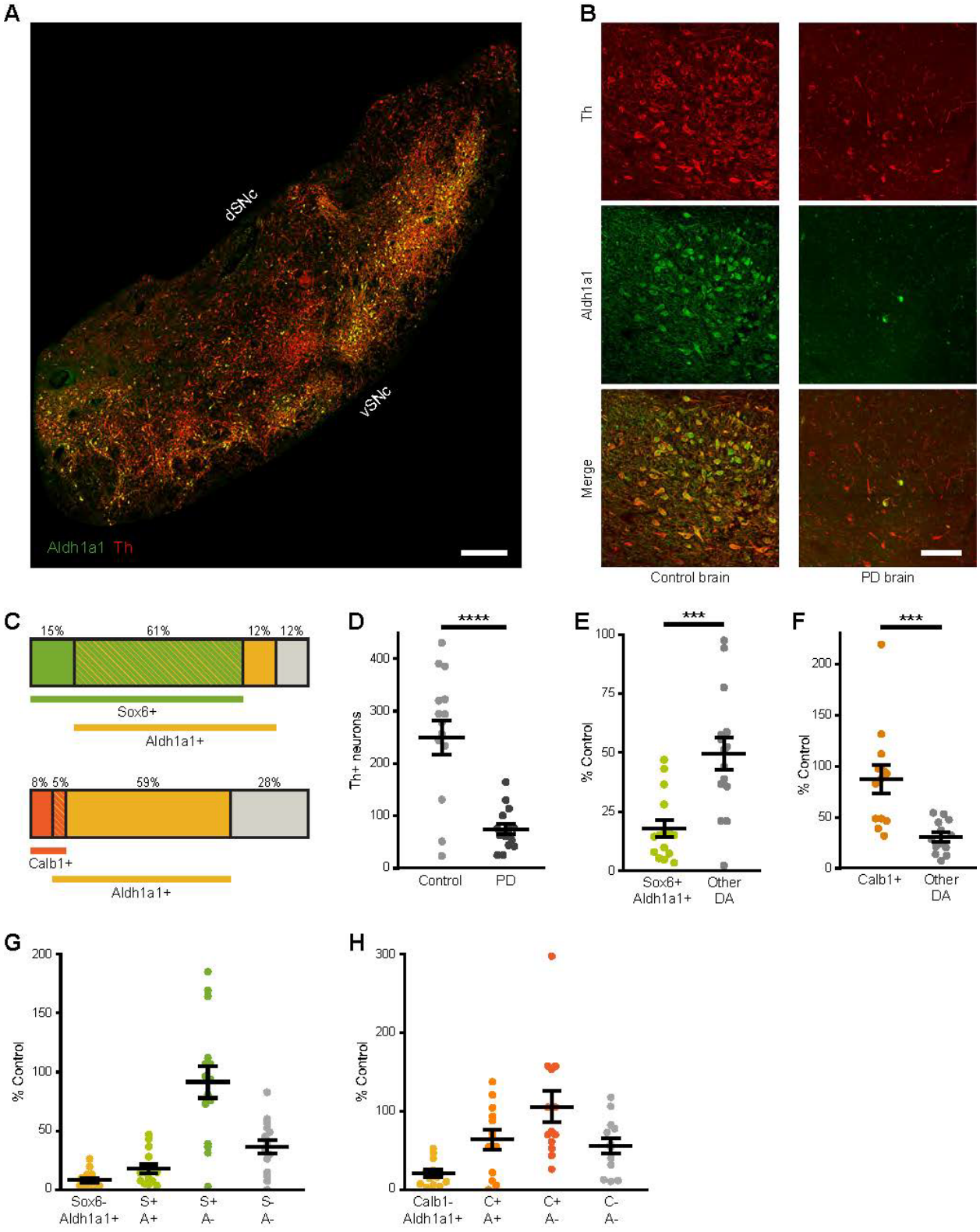

(**A**) Th and Aldh1a1 labeling in SNc of a healthy, control human brain. Scale bar = 1,000 mm.

(**B**) High magnification images of Th and Aldh1a1 labeling in control and PD human brains. Scale bar = 100 mm.

(**C**) Percentage of hSNc Th+ DA neurons expressing different combinations of Sox6 and Aldh1a1 (top) or Calb1 and Aldh1a1 in control brains.

(**D**) Quantification of TH+ neurons in control and PD brains ($p = 1.89 \times 10^{-05}$, n=14 controls, n=15 PD).

(**E**) Sox6+/Aldh1a1+ DA neurons versus other DA neurons in PD hSNc as a percentage of control brains ($p = 3.1 \times 10^{-04}$; controls are set at 100%, n = 14 controls, n = 15 PD).

(**F**) Calb1+ DA neurons versus other DA neurons in PD hSNc as a percentage of control brains ($p = 7.3 \times 10^{-04}$, n = 14 controls, n = 15 PD).

(**G**) Different combinations of Sox6 and Aldh1a1 expressing DA neurons in PD hSNc as a percentage of control brains (same as E).

(**H**) Different combinations of Calb1 and Aldh1a1 expressing DA neurons in PD hSNc as a percentage of control brains (same F).

Error bars are SEMs.

Experiment by Marilyn Dubois and Jean-Francois Poulin, analysis by Maite Azcorra.

Sox6+ neurons not co-expressing Aldh1a1+ were resilient to degeneration (Figure 4G). While it is important to note that Sox6+/Aldh1a1- and Sox6-/Aldh1a1+ neurons are a minority compared to those co-expressing both genes (Figure 4C), this evidence does point towards Aldh1a1 being the determinant marker of vulnerable cells, not Sox6. On the other hand, Calb1+/Aldh1a1+ neurons were not as resilient as Calb1+/Aldh1a1- neurons nor as vulnerable as Calb1-/Aldh1a1+ neurons (Figure 4H) – though in this case co-expressing neurons are the minority (Figure 4C).

2.4. Transcriptomic differences between Sox6+ and Sox6- neurons

Given that Sox6+ and Sox6- neurons exist in humans and mice with similar anatomical distributions, and that Sox6+ neurons (or at least a large Aldh1a1+ subset of them) is selectively vulnerable in PD in humans, we returned to the mouse and sought to determine whether any differences in gene expression between Sox6+ and Sox6- could point to the source of this differential vulnerability.

We performed bulk RNA sequencing in sorted mCherry+ (Sox6-) and GFP+ (Sox6+) cells from the SNc of adult Sox6-FSF-Cre/Th-2A-Flpo/RC-Frepe mice (Figure 1A), which revealed large and significant differential gene expression between these two populations (Figure 5A-B). As expected, Sox6 and Aldh1a1 were preferentially expressed in GFP+ neurons. In addition, genes such as Drd2, Vmat2, Kcnj6, and Kcns3 (which are likely to confer distinct properties in neurons) were significantly enriched in the GFP+ population, whereas others such as the ion transport regulator Fxyd6, neuroglobin (Ngb), and Slc17a6 (Vglut2) were enriched in the mCherry population (Figure 5A). In situ hybridization of Fxyd6, Ngb, and Vglut2 confirmed their expression in mCherry+/Th+ neurons in the dSNc and SNpl, and these markers were also expressed in mCherry+/Th- neurons located above the Th+ SNc. In contrast, somatostatin (Sst) was differentially expressed in the mCherry population but was found only in mCherry+/Th- neurons above the SNc, indicating that some of these cells were included in our transcriptomic analysis. These mCherry+/Th- neurons, like Th+ neurons, have a history of Th expression, and they are FoxA2+ as indicative of a FP origin (data not shown). We postulate that these cells are related to dSNc DA neurons but fail to initiate or maintain robust expression of the DA program and are therefore Th-.

We next asked whether PD risk loci as identified by genome-wide association studies (GWASs)[43] were differentially expressed in the Sox6+ population. Interestingly, we found that six PD loci were enriched in the GFP (Sox6+), but none were enriched in the mCherry (Sox6-) cohort (false discovery rate [FDR] < 0.1; green squares, Figure 5A). Consistent with this, when we performed unbiased pathway enrichment analysis using gene set enrichment analysis (GSEA), a PD-linked gene set was differentially expressed in Sox6+ neurons (4th highest enrichment score [ES], q = 0.04; Figure 5C-D). In total, our GSEA analysis revealed 11 pathways differentially enriched in

Figure 5: Transcriptomic analysis of Sox6+ and Sox6- neurons

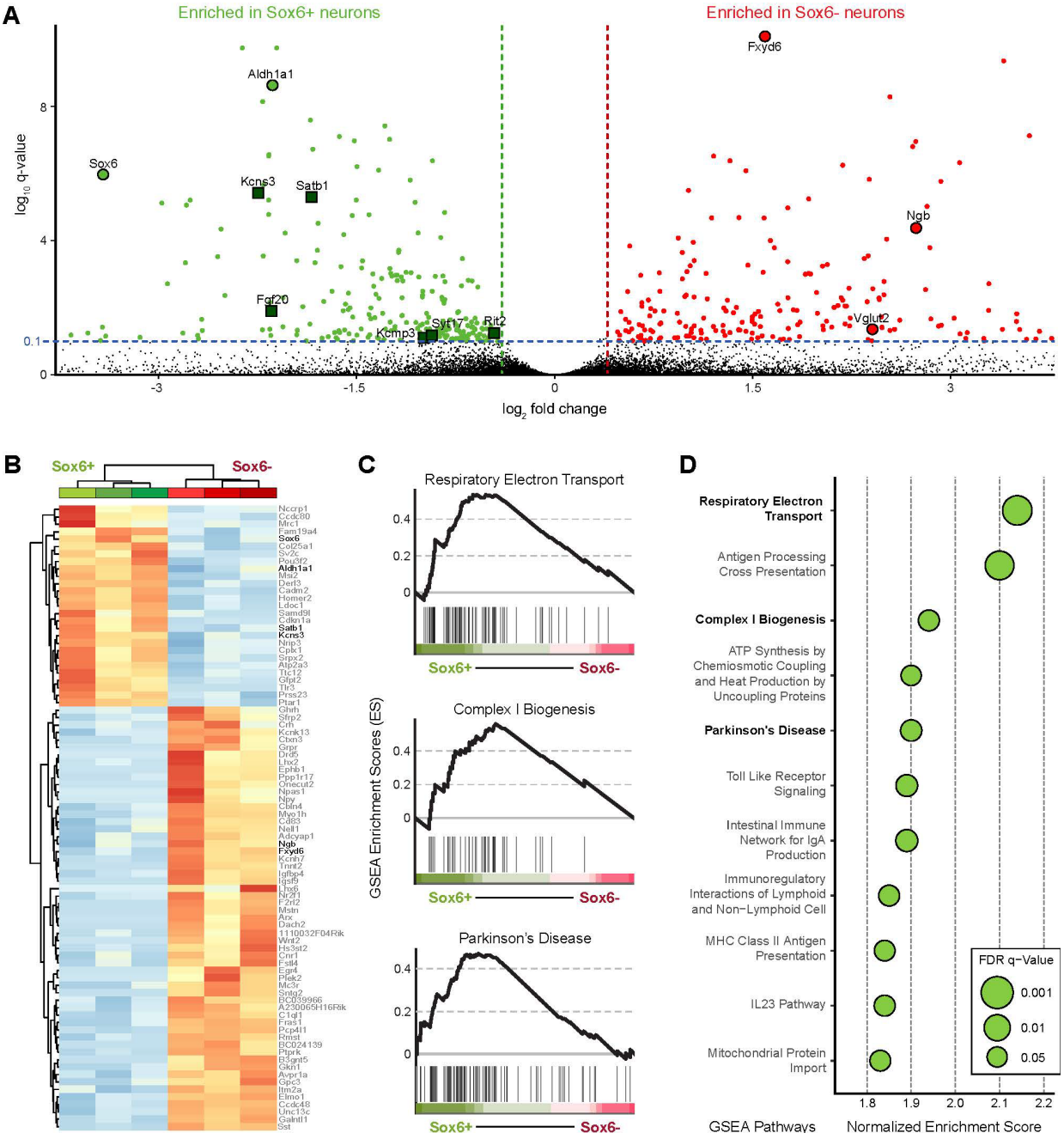

(**A**) Volcano plot showing gene expression differences between GFP+ (Sox6+) and mCherry+ (Sox6-) cells. Green squares are PD risk loci.

(**B**) Unbiased clustering of Sox6+ and Sox6- samples, n = 3 each.

(**C**) Gene set enrichment analysis (GSEA) plots of gene sets enriched in the Sox6+ population associated with mitochondrial function and ATP synthesis (top, center) and PD (bottom). The peak of the curve indicates the enrichment score. $q < 0.05$ in all plots.

(**D**) Dot plot of GSEA enrichment scores in pathways enriched in Sox6+ neurons.

Experiment and analysis by Zack Gaertner and Oscar Andres Moreno Ramos

the Sox6+ population ($q < 0.05$, Figure 5D), some of which appear to be highly relevant to existing theories of PD pathogenesi[64]. For example, three of these pathways were relevant to mitochondrial electron transport and ATP synthesis (electron transport and complex I biogenesis; Figure 5C-D). Several immune-related pathways were also differentially enriched in Sox6+ neurons, including innate immunity and Toll-like receptor (TLR) signaling, which have been of recent interest in PD research[65,66].

Furthermore, our simultaneous intersectional/subtractive strategy to access Sox6+ and Sox6- SNc populations allowed us to better interpret available single-cell sequencing datasets (see Pereira Luppi et al., 2021[38], Figure S4). We plotted differentially expressed genes using the DropViz platform[48] (clusters 4-1 to 4-9 represent DA neurons). Interestingly, Sox6 expression discriminates between clusters 4-3, 4-5, 4-6, 4-7, 4-8, and 4-9 (Sox6+) and 4-1, 4-2, and 4-4 (Sox6-), consistent with our previous findings showing Sox6 expression as a key driver of variance[47]. We thus hypothesized that clusters 4-3, 4-5, 4-6, 4-7, 4-8, and 4-9 represent the GFP population, and accordingly Aldh1a1, Kcns3, Atp2a3, Serpine2, and Satb1 (which were significantly enriched in Sox6+ neurons), were highly expressed in these clusters. Conversely, clusters 4-1, 4-2, and 4-4 expressed a combination of Calb1, Vglut2, and Fxyd6, which we have shown to be enriched in Sox6- neurons (Figure 1G, Figure 5A), suggesting these could represent the mCherry population. Thus, we hypothesize that clusters 4-1, 4-2, and 4-4 represent together the VTA, dSNc, and SNpl, all predominantly Sox6- by our previous analysis (Figure 1C). We attempted to match Sox6- clusters with these midbrain areas and found that Otx2 and Lpl, known ventromedial VTA markers[28], were practically exclusive to cluster 4-1. Calb1 was more widely expressed, in accordance with our results (Figure 1G), although more prominently in the Sox6- clusters, consistent with our previous study[47]. Thus, cluster 4-2, expressing Calb1, Fxyd6, and Vglut2, but

not Otx2 and Lpl, can be associated with dSNc and SNpl, predominantly mCherry+ regions. All in all, Sox6- (mCherry+) cells are similar in that they lack Sox6 but express Calb1, Fxyd6, and/or Vglut2. However, Otx2 and Lpl allow us to distinguish between dSNc/SNpl (4-2; 4-4) and VTA (4-1).

In conclusion, our results provide direct evidence of substantial molecular distinctions between Sox6+ and Sox6- neurons, and that Sox6+ neurons are enriched in known pathways of DA neuron vulnerability. Moreover, the transcriptomic dataset derived from our intersectional/subtractive labeling scheme provides an informative resource, readily combinable with single-cell transcriptomics analyses for a more granular classification of DA neurons such as localizing neurons of the dSNc/SNpl.

2.5. Differential developmental origin of Sox6+ and Sox6- neurons

Besides being a differential marker of adult DA neurons, Sox6 is a key gene in their development, distinguishing between two progenitor domains (a medial Sox6+ and a lateral Sox6-/Wnt1+/Otx2+) within the embryonic floor plate (FP), from which all midbrain DA neurons originate[51]. Thus, we investigated whether differences observed between adult Sox6+ and Sox6- neurons could be encoded early in development. To this end, we designed a multi-pronged series of lineage tracing experiments to capture the full history of Sox6 expression from the progenitor stage.

2.5.1. Cumulative fate map of Sox6

First, we established a cumulative fate map of Sox6, by which any DA neuron that expressed Sox6 at any point (during development or post-mitotically) will be distinguished from DA neurons that never expressed Sox6. This answers the question of whether adult Sox6- DA neurons come from

a Sox6+ progenitor or not but does not tell us anything about the origin of Sox6+ neurons. To confirm that our strategy does indeed label Sox6 progenitors in the midbrain FP, we used Sox6-FSF-Cre/CAG-Flpe/RC-Frepe mice. Unlike the Th-Flpo construct used in previous experiments, CAG-Flpe is expressed during development, allowing labelling of progenitors expressing Sox6 rather than only adult neurons. Indeed, at embryonic day (E)11.5 we observed GFP+ cells located medially in theLmx1a+domain (Figure 6A), consistent with Sox6 embryonic expression[51] and confirming that our strategy appropriately labeled progenitors in the midbrain FP. Thus, we obtained a Sox6-Cre mouse line from our existing Sox6-FSF-Cre line, by permanently deleting the frt-flanked stop cassette with CAG-Flpe. We then crossed this Sox6-Cre to Th-2A-Flpo and

RC-Frepe: in Sox6-FSF-Cre animals (Figure 1), the intersectional reporter RC-Frepe labels only postmitotic cells expressing Sox6, whereas in Sox6-Cre animals Cre recombination in RC-Frepe can occur in both progenitors and post-mitotic neurons, labeling with GFP all the neurons that have expressed Sox6 at any point in their history and with mCherry those DA neurons that have never expressed sufficient levels of Sox6 (Figure 6E). At the end of DA neurogenesis, E14.5 (Figure 6B), these mice showed GFP+ and mCherry+ cells with a distinct distribution as they emanated from the FP into the mantle zone. GFP+ cells were densely located medially, likely migrating radially and then tangentially at the pial surface as previously reported[51,54,67]. mCherry+ cells were prominent laterally, with some GFP+ cells intermingled. Interestingly, we observed a few mCherry+/GFP+ cells, also seen in E16.5 embryos, indicating that some DA neurons activate Sox6 expression postmitotically (Figure 6C).

In the adult midbrain, we observed a prominent ventral SNc Th+/GFP+ population and a less abundant dorsal Th+/mCherry+ population (Sox6+ and Sox6- history, respectively; Figure 6D), with the SNpl predominantly populated by Th+/mCherry+ neurons. We compared the percentage

Figure 6: Sox6 cumulative fate map

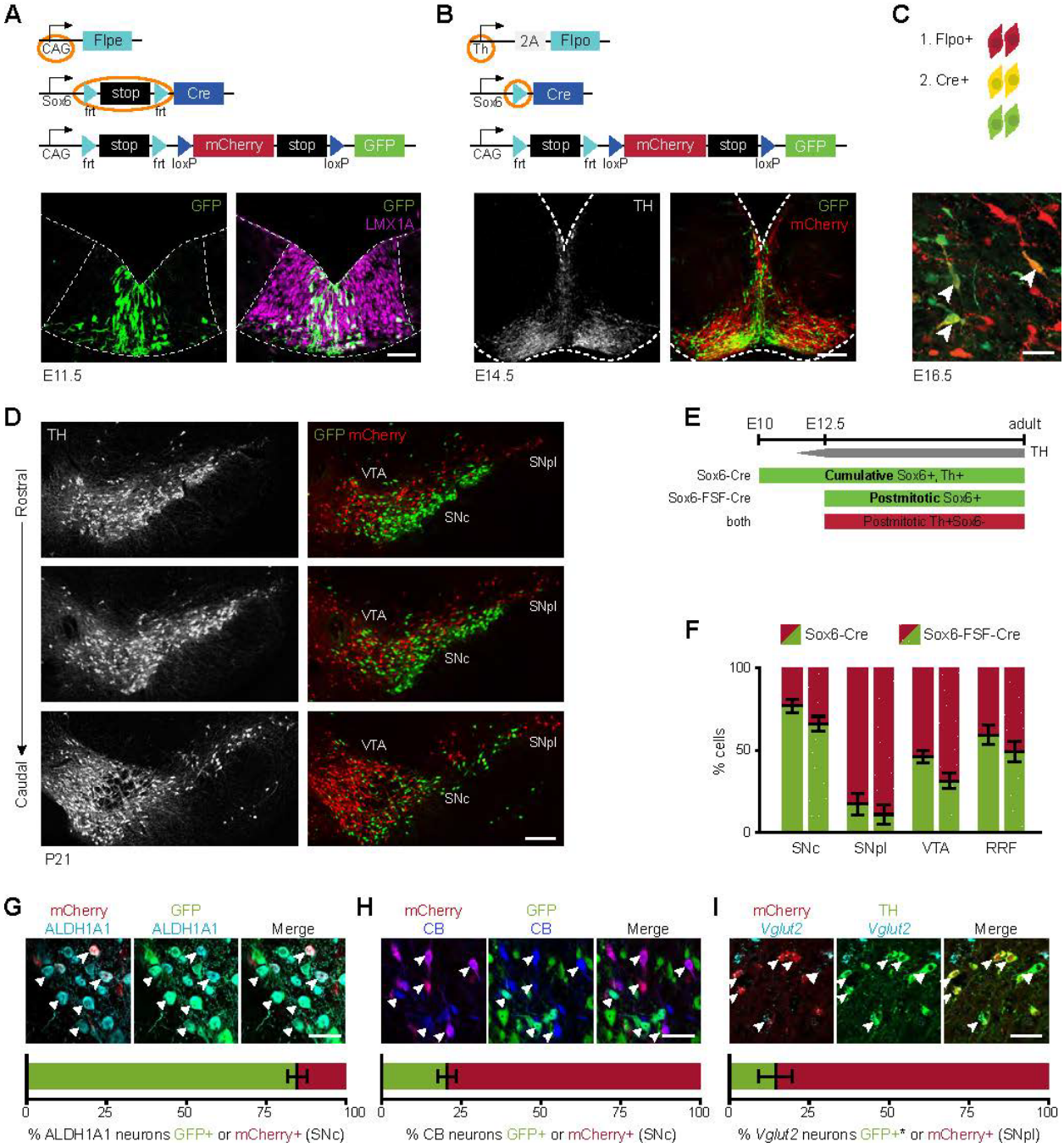

(**A**) Sox6-FSF-Cre, CAG-Flpe, RC-Frepe brain at E11.5 (mCherry not shown).

(**B**) Sox6-Cre, Th-2A-Flpo, RC-Frepe brain at E14.5.

(**C**) Cell-labeling outcome if Flpo expression precedes Cre. 1. Flpo expression induces mCherry expression. 2. Subsequent Cre expression in mCherry+ cells induces expression of GFP. In this scenario, cells express mCherry+ and GFP+ until mCherry is degraded and then the cell expresses only GFP. Bottom: example of mCherry, GFP double-positive cells in E16.5 Sox6-Cre, Th-2A-Flpo, RC-Frepe brains (arrowheads, n=3).

(**D**) Adult Sox6-Cre, Th-2A-Flpo, RC-Frepe brain (n = 9).

(**E**) In Sox6-FSF-Cre, Th-2A-Flpo, RC-Frepe brains, DA neurons expressing Sox6 postmitotically (after the onset of Th expression) are labeled with GFP. In Sox6- Cre, Th-2A-Flpo, RC-Frepe brains, Cre activation no longer depends on Th; thus, TH+ DA neurons expressing Sox6 at any point in their history are labeled with GFP.

(**F**) Comparison of cumulative versus postmitotic labeling. In VTA, there are more GFP+ neurons in the cumulative analysis ($p = 0.06$).

(**G-H**) SNc of Sox6-Cre, Th-2A-Flpo, RC-Frepe brains labeled with Aldh1a1, or Calb1+ (CB+) (GFP, triangles; mCherry arrowheads).

(**I**) In the SNpl, the majority of Vglut2+ neurons are TH+,mCherry+ (arrowheads), while only a few are TH+,mCherry? (triangles). *Typically GFP+, lost during in situ hybridization.

Scale bars: (A) 50 mm; (B) 100 mm; (C) 200 mm. Error bars are SEMs. (A, B, and E–G) n = 3.

Experiment and analysis by Milagros Pereira Luppi.

---

of GFP and mCherry-expressing cells in Sox6-Cre versus Sox6-FSF-Cre animals and found no statistically significant difference in SNc, SNpl, and RRF (Figure 6F), suggesting that adult Sox6+ neurons originate from Sox6+ progenitors, while adult Sox6- neurons originate from Sox6- progenitors. However, while these differences were not statistically significant, there were more GFP+ cells in the Sox6-Cre animals compared to Sox6-FSF-Cre, especially the VTA ($p = 0.06$; Figure 6F), suggesting that some Sox6- neurons might have originated from Sox6+ progenitors and turned it off later during development. In particular, Sox6-FSF-Cre brains showed mCherry+ cells throughout the VTA with some GFP+ cells in the parabrachial region (Figure 6B), whereas in Sox6-Cre brains we also observed GFP+ cells in the paranigral region and the interfascicular nucleus.

Since Sox6 and Otx2 have complementary expression[51], we analyzed Otx2 expression in the cumulative and the post-mitotic analyses (see Pereira Luppi et al., 2021[38], Figure S6). In Sox6-Cre/Th-2A-Flpo/RC-Frepe brains (post-mitotic), the Otx2 signal was low/residual in SNc neurons with no apparent difference between GFP+ and mCherry+ cells. In contrast, in the VTA several neurons co-expressed GFP and Otx2. On the contrary in Sox6-FSF-Cre/Th-2A-Flpo/RC- Frepe

brains (cumulative fate map), most Otx2+ cells in the VTA were mCherry+. These results suggest that Sox6+ progenitors can contribute to Otx2+ neurons in the VTA, indicating some developmental flexibility – though it is possible that the sporadic labeled cells observed in the lateral progenitor domain gave rise to some Otx2+ VTA neurons.

The Otx2 staining also confirmed our transcriptomic analysis, which distinguished VTA from dSNc/SNpl. We found that many mCherry cells in the VTA expressed Otx2 robustly, but mCherry populations in the dSNc/SNpl showed weak/residual Otx2 signal. We observed similar results with Lpl expression, which was robust in ventromedial VTA neurons, but low/residual in dSNc/SNpl populations (not shown). This confirms that the dSNc/SNpl populations were distinct from mCherry+ cells in the VTA. To investigate whether this difference manifests early in development, we examined Otx2 expression in E14.5 embryos. Rostral sections had fewer Otx2+/mCherry+ cells in contrast to caudal sections, where many are observed, suggesting that rostral mCherry+ cohorts contribute to the dSNc and SNpl, while caudal mCherry cohorts contribute to the Otx2+ ventromedial VTA.

Finally, we asked whether the adult Aldh1a1+, Calb1+, and Vglut2+ DA subtypes showed different developmental origins. In the SNc of adult Sox6-Cre/Th-2A-Flpo/RC-Frepe brains, most Aldha1a1+ neurons co-expressed GFP (85% ± 3%, Figure 6G), while in the VTA most Aldh1a1+ neurons co-expressed mCherry (77.4% ± 1.4%, not shown). This data strongly suggests that the SNc Aldh1a1+ subtype has predominantly Sox6+ history while the VTA subtype does not. Calb1+ neurons, on the other hand, appear to lack Sox6 expression in both areas – the majority of Calb1+ neurons were mCherry+ in the SNc (80% ± 3%, Figure 6H) and in the VTA (84.7 ± 5%, not shown), suggesting most Calb1+ neurons must derive from Sox6- progenitors. Finally, we analyzed Vglut2 neurons. We performed in situ hybridization and found that 12% ± 2% of the Th+

SNc neurons expressed Vglut2, consistent with previous reports[68]. As expectedly, Vglut2+/Th+ neurons were mostly mCherry+ in the SNpl (85.6% ± 3%, Figure 6I) and in the VTA (92.2 ± 8%, not shown). In the SNc however, only 48.5% ± 6% of Vglut2+ DA neurons co-expressed mCherry (not shown). These numbers suggest that Vglut2+ neurons, especially in the SNpl and VTA, lack sufficient Sox6 expression to drive recombination throughout their history and thus must predominantly originate from embryonic Sox6- progenitors, a key finding of our work.

In conclusion, our cumulative Sox6 fate mapping experiment shows that the Sox6 dorsoventral division of the SNc must be, at least in part, encoded in the FP progenitors, strongly suggesting a dual developmental origin of the SNc.

2.5.2. Sox6 progenitor fate map of using PRISM

While our cumulative Sox6 analysis showed that Sox6- dSNc neurons (mCherry+ and Calb1+) must predominantly originate from Sox6- progenitors, it does not clarify the origin of Sox6+ vSNc neurons, as this strategy cannot distinguish between cells derived from Sox6+ progenitors or those that acquired Sox6 expression postmitotically. To address this question, we used our PRISM (progenitor restricted intersectional fate mapping) approach to obtain a bona fide Sox6 fate map[69] (for validation details see Pereira Luppi et al., 2021[38], Figure S7). PRISM elements include a Cre driver (in this case, Sox6-Cre) a Nestin-driven Flpo recombinase Nes-LSL-Flpo (NSF), and a Flpo-dependent reporter, RC-LacZ, encoding for β-galactosidase (βGal) (Figure 7A). In this strategy, Flpo expression depends on Nestin (expressed only in progenitors) and simultaneous or earlier Cre expression, and thus the reporter is restricted to progenitors expressing Sox6 and excludes labeling of DA neurons expressing Sox6 postmitotically[70]. First we validated the progenitor specificity of PRISM using Vglut2-Cre, since Vglut2 is expressed in nascent post-mitotic DA neurons[68]. As expected, few to no TH+ cells were labeled with the reporter in adult brains, confirming that

PRISM does not label post-mitotic neurons expressing the Cre driver. Second, we determined the maximum recombination potential of PRISM specifically in DA neurons, using EIIa as Cre driver, since EIIa is active at the one/two-cell stage. We calculated an efficiency of 66.7% ± 2% in the SNc and 71.5% ± 0.01% in the VTA, in line with the overall PRISM efficiency[69]. This efficiency level provides a more complete picture of descendants, compared to genetically induced fate mapping strategies.

To confirm progenitor labeling, we analyzed Sox6-Cre, Nestin-LSL-Flpo, RC-LacZ embryos at E11.5, showing that Sox6+ progenitors (βGal+) were largely localized medially in the embryonic Lmx1a+ domain (Figure 7B). Since not every medial progenitor was labeled, we compared Sox6-Cre, Nestin-LSL-Flpo, Ai65F (Flpo reporter encoding for tdTomato) to Sox6-Cre, Ai9 (Cre reporter encoding for tdTomato) at E12.5, the peak of DA neurogenesis. In brains of both genotypes, tdTomato+ cells were biased toward the medial Lmx1a+ domain. Furthermore, the proportion of tdTomato+,Lmx1A+/Lmx1aA+ cells in the PRISM embryo was 77% of the Sox6-Cre, Ai9 embryo, roughly consistent with the overall PRISM efficiency[69] and the efficiency in DA neurons.

PRISM provides a progenitor-restricted fate map in the adult brain. In adult Sox6 PRISM brains, we observed βGal+ DA neurons in the SNc, as well as the VTA (Figure 7C). We also observed βGal+,TH- cells in the rostral linear nucleus (not shown), characterized by low TH immunoreactivity. In the SNc, 28.7% ± 2.5% of the TH+ neurons originated from Sox6+ progenitors (42.9%, adjusted by PRISM efficiency; Figure 7D). To rule out possible recombination inefficiency due to a rox-flanked destabilized EGFP cassette in the Nestin-LSL-Flpo construct, we deleted the cassette using Dre-deleter mice to reduce the distance between the loxP sites. The adult fate map with a Dre-deleted Nes-LSL-Flpo showed a result similar to that of the undeleted

Figure 7: Sox6 progenitor fate map using PRISM

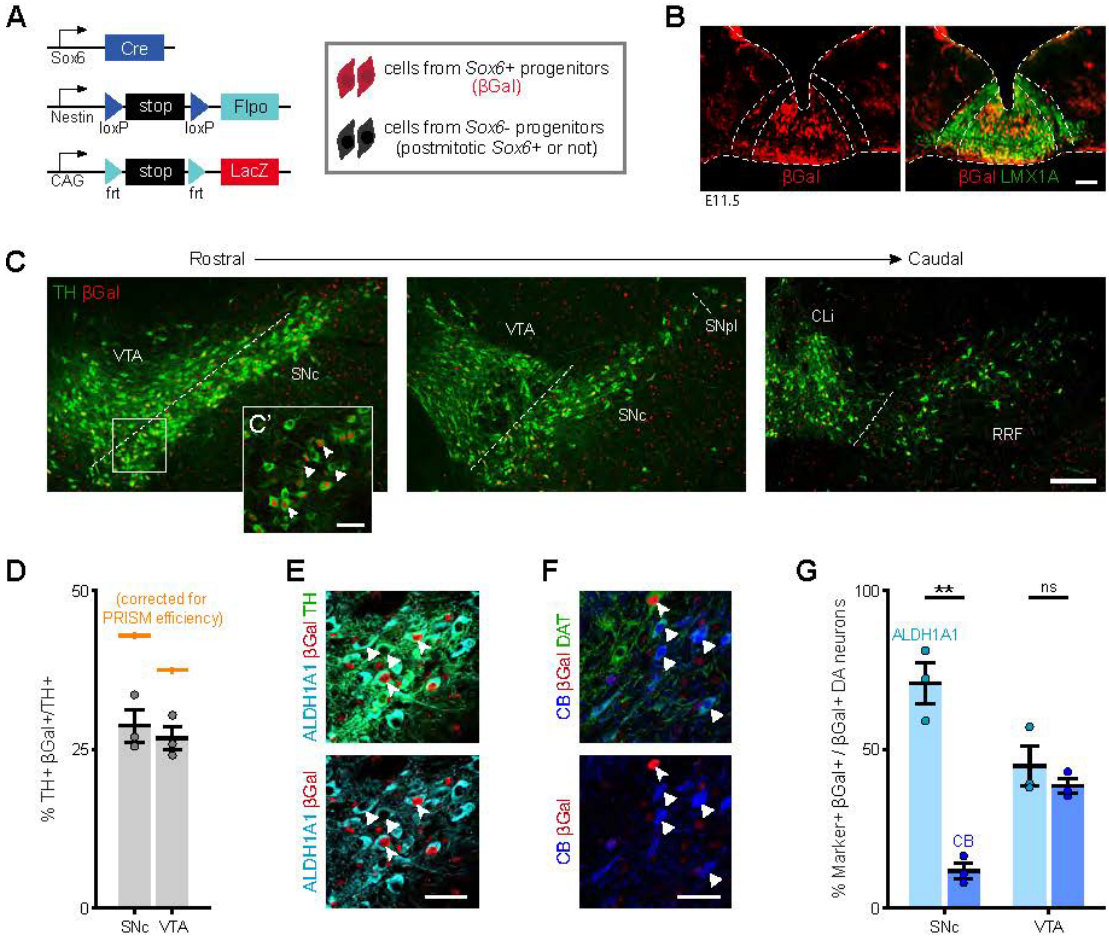

(**A**) Schematic of PRISM alleles.

(**B**) Sox6-Cre, Nestin-LSL-Flpo, RC-LacZ (from here on Sox6 PRISM) at E11.5. βGal+ progenitors (Sox6+) are located medially in the Lmx1a+ floor plate.

(**C**) Sox6 PRISM adult brains show Th+,βGal+ neurons in the SNc and VTA (n = 8).

(**C'**) High magnification of SNc showing Th+,βGal+ cells (arrowheads) and Th+,βGal- cells (triangles).

(**D**) Average Th+,βGal+/Th+ neurons in Sox6 PRISM adult brains, also corrected by PRISM efficiency.

(**E**) High magnification of Sox6 PRISM SNc neurons co-expressing Th, Aldh1a1, and βGal.

(**F**) Sox6 PRISM SNc cells co-expressing dopamine transporter (DAT), Calb1 (CB), and βGal. Most Calb1+,DAT+ cells are βGal- (triangles). For reference, arrowhead shows a βGal+,DAT+,CB- cell.

(**G**) Percentage of βGal+ cells that express Aldh1a1 or Calb1 in the SNc and VTA of Sox6 PRISM adult brains (p values: SNc p = 0.008, VTA p = 0.5).

Scale bars: (C) 200 mm; all other scale bars, 50 mm. Error bars are SEMs. (B and D–G) n = 3.

Experiment and analysis by Milagros Pereira Luppi.

construct. Notwithstanding our several efforts to account for efficiency, we interpret our data cautiously to include the possibility of some amount of temporal delay due to sequential recombination. Therefore, we conclude that at minimum, ~40% of the SNc is derived from Sox6+ progenitors, although this could be an underestimation.

Next, we sought to determine the propensity of Sox6 progenitors to contribute to Sox6, Aldh1a1, and Calb1 populations. In the SNc ~92% of TH+/βGal+ fate-mapped neurons maintained Sox6 expression, whereas in the VTA a substantial proportion of TH+,βGal+ were SOX6- (not shown), further supporting that some VTA neurons originate from Sox6+ progenitors but down-regulate Sox6. Moreover, in Sox6-Cre PRISM brains, we found that 70.7% ± 6% of the βGal+ neurons co-expressed Aldh1a1+ (Figure 7E, G), and 11.6% ± 2.4% of the βgal+ neurons co- expressed Calb1 (Figure 7F, G); these Calb1+ neurons tended to be located more medially in the SNc. We concluded that Sox6+ progenitors have a higher propensity to generate Sox6+ and Aldh1a1+ neurons than Calb1+ neurons. To corroborate our findings, we generated a Sox6-CreER^{T2} knock-in line. Although this approach suffers from substantial mosaicism, among other limitations, it is a well-established technique to temporally restrict the activation of the reporter[71]. In Sox6-CreERT2, Ai9 E11.5 brains, tdTomato+ progenitors localized mainly to the medial domain of the embryonic FP, as expected. We followed the fate of the reporter-labeled cells in P0 brains and observed tdTomato+/Th+ neurons in the SNc, but also in the VTA/interfascicular region. Our results indicate that Sox6+ progenitors contribute to a significant number of SNc neurons, but also to the VTA.

2.6. Functional characterization of Sox6+ and Sox6- neurons

Given the stark differences between SNc Sox6+ and Sox6- dopamine neurons at all levels, we next sought to investigate whether these two subtypes also showed different functional responses. A previous study reported a subset of DA axons in the dorsal striatum with fast signaling associated with locomotion and showing no response to unexpected rewards, while more ventral axons responded to rewards and showed no locomotion-locked signaling[5]. This dorso-ventral bias in functional responses parallels the anatomical distribution of Sox6+ and Sox6- axons in striatum, with Sox6+ projecting to dorsal striatum and Sox6- to more central regions (Figure 2), suggesting these motor-associated dopamine neurons would be included in the Sox6+ population, while the reward responsive population might correspond to the Sox6- population.

To confirm this, we used fiber photometry to record calcium transients from genetically defined axons in behaving mice. We labeled Sox6+ or Sox6- SNc DA neurons with calcium indicator GCaMP6f by injecting Sox6-FSF-Cre/Th-2A-Flpo mice with either an intersectional (AAV-COn/FOn-GCAMP6f) or subtractional (AAV-COff/FOn-GCaMP6f) virus (Figure 8A). Following viral injections, head-fixed mice received unexpected random water rewards while running freely on a cylindrical treadmill[5] (Figure 8B), and at the same time we recorded calcium transients using one-photon fiber photometry. Recordings from Sox6+ axons in dorsal striatum showed calcium transients time locked to acceleration and no detectable response to rewards, as expected[5] (Figure 8C, top), confirming that the Sox6+ population includes motor-associated DA neurons. Recording from Sox6- axons in the striatum proved more challenging (particularly in mid-depth), due to labeling inefficiencies of the available virus, as well as the lower density of Sox6- axons in the striatum. However, in two mice we observed reward-locked calcium transients in ventral striatal axons of Sox6- neurons and, in these same recordings, we did not detect any acceleration-locked

calcium transients (Figure 8C, bottom). Together, this suggests that Sox6+ neurons include those which are locomotion-locked and reward non-responsive, while Sox6- neurons include those with responses to reward but no locomotion.

Figure 8: Functional characterization of Sox6+ and Sox6- DA neurons

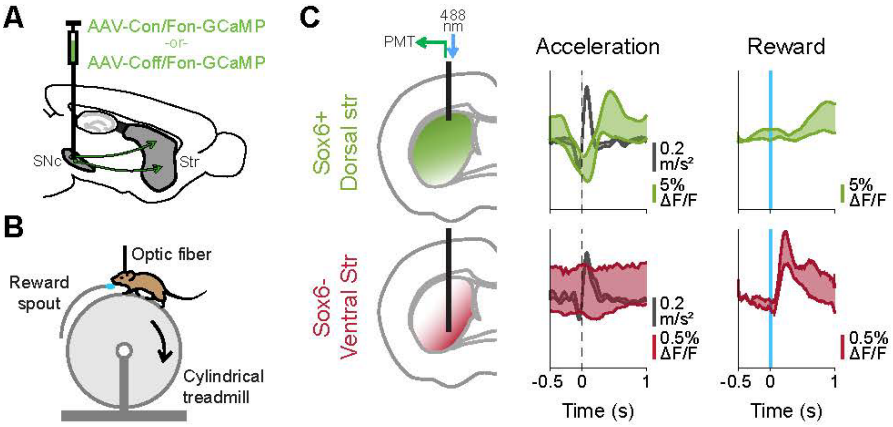

(**A**) Genetic strategy to label either Sox6+ or Sox6- DA neurons with GCaMP6f, a genetically encoded indicator whose changes in fluorescence can be used as a proxy for axonal dopamine release.

(**B**) Schematic of fiber photometry recording setup during behavior.

(**C**) Recordings of Sox6+ (top) and Sox6- (bottom) axons in dorsal and ventral striatum, respectively, the regions of most dense innervation for each population. Left: schematic of recording location for each population. Middle: triggered average at acceleration onsets (acceleration in black, %ΔF/F in red/green) (Sox6+ n = 9, Sox6- n = 2). Right: triggered average at reward delivery, %ΔF/F scale same as in middle (Sox6+ n = 6, Sox6- n = 2). Error bars are SEM.

2.7. Discussion

Despite emerging data on DA neuron heterogeneity, little is known about its developmental basis. Here we demonstrate a dual embryonic origin of the SNc that results in neuronal cohorts with different molecular characteristics, projections, PD pathways, and vulnerability (Figure 9).

The recent identification of putative DA subtypes[28] motivated us to examine whether preferential loss of one of them underpins the anatomically based observations on selective vulnerability in

PD[24,39,41,44]. We show the presence of a ventrally located Sox6+/Aldh1a1+ population in human

Figure 9: Distribution of Sox6+ and Sox6- somas and projections, and developmental origin

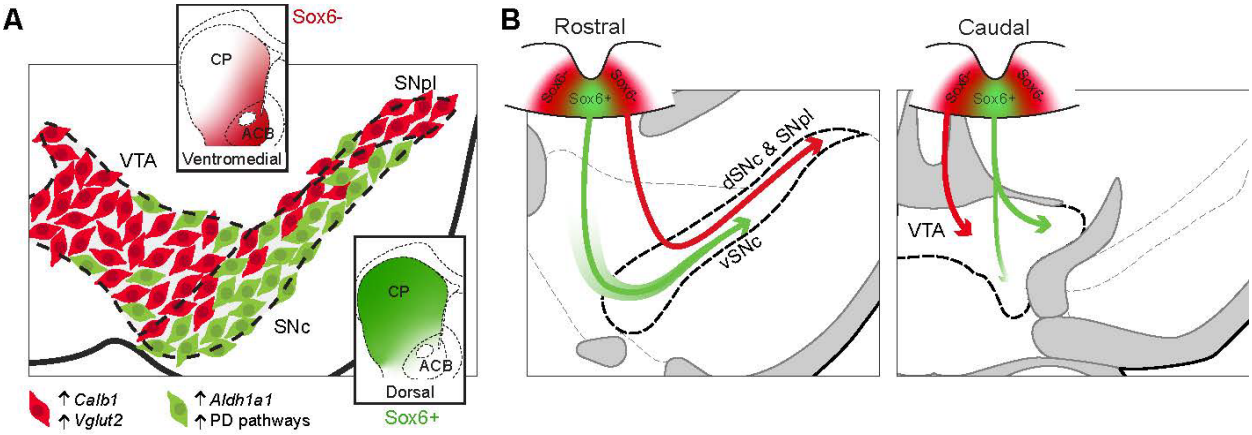

(**A**) In an adult midbrain section Sox6+ DA neurons (green) ventrally biased in the SNc, and in the parabrachial VTA, are enriched in Aldh1a1 as well as in PD pathways and Electron transport pathways. These neurons project to the dorsal striatum. Sox6- DA neurons (red), are enriched in Calb1 and/or Vglut2, and project to the medial, ventral and tail of the striatum.

(**B**) Model depicting main contribution of Sox6 progenitors to the SNc: Sox6+ and Sox6- progenitors, give rise to vSNc and dSNc/SNpl neurons, respectively (left), indicating a dual developmental origin of the SNc. Some neurons in the vSNc can also acquire Sox6 expression postmitotically (green gradient surrounding arrow). Main contribution of Sox6 progenitors to the VTA: In more caudal regions of the embryo, Sox6- progenitors predominantly give rise to ventro-medial VTA neurons (right), and RRF neurons (not shown). On the other hand, Sox6+ progenitors give rise to neurons localized in the parabrachial region, some of which maintain Sox6 expression (solid green arrow) while others localized in the paranigral region, downregulate Sox6 (gradient green arrow). In these more caudal regions, smaller contributions of Sox6+ and Sox6- can be found in the SNc and RRF.

---

control brains, and that these neurons are selectively diminished in post-mortem PD brains; in contrast, Calb1+ cells were resilient. Our findings are consistent with previous reports using Aldh1a1 and Calb1 as markers[24,42], as well as recent studies depicting ventral enrichment of Sox6+ neurons in the human SNc[72]. In mice, we found that Sox6+ neurons displayed large transcriptomic differences from Sox6- neurons that are likely to underpin their different properties (Figure 9A). Sox6+ neurons are enriched in pathways for ATP synthesis and therefore may carry a higher

bioenergetic burden compared to Sox6- neurons[73]. Increased ATP synthesis is likely required to support their continual activity during locomotion, but over time this might lead to oxidative stress in this population. Interestingly, immune-related gene sets are also enriched ventrally, including those for TLR signaling and MHCII pathways, both of which have recently been implicated in PD pathogenesis[65,66]. Our study also showed that dorsal Sox6- cells were enriched for Calb1 and Vglut2 expression. Vglut2 has been recently identified as a marker of resilient DA neurons in toxin models likely conferring resistance by way of Bdnf/TrkB signaling, or by facilitation of cytosolic DA clearance into vesicles[74,75]. Vglut2+ DA neurons have also been observed in primate SNc[76]. Calb1 on the other hand, could confer resiliency based on its calcium buffering properties[73,77]. Overall, our study reveals molecular distinctions between Sox6+ and Sox6- SNc neurons, some of which likely account for their selective vulnerability.

Sox6- dorsal and Sox6+ ventral SNc neurons showed distinctive projection patterns (Figure 9A). Extending our previous work[17], here we show that Sox6+ neurons densely innervate the dorsal striatum; however, with a subtractive strategy, not used in Poulin et al.[17], we reveal that Sox6- axons sparsely innervate the dorsal striatum and instead project more densely to the medial and ventral striatum, including potentially part of the ACB. An inverted projection pattern was also previously reported in rodents and primates[78–80] but it has not been observed consistently across all studies[81,82] and, therefore, has not been depicted in recent models of SNc projections to the striatum[83,84]. The potential overlap of Sox6+ and Sox6- axonal arbors, as shown here and in a recent study[85], together with the diverging criteria used to define the dorsoventral division of the SNc and the partially intermingled nature of these neurons, may all be reasons for those inconsistent findings. Importantly, these anatomical findings can explain the patterns of striatal innervation observed in PD brains[41]; fibers projecting to the medial striatum are likely preserved

because they originate from relatively spared Sox6- neurons in the dSNc, most of which are also Calb1+.

The Sox6- cohort also extends into the SNpl. Using single cell transcriptomic datasets, we were able to identify Sox6- cells, that are Vglut2+ and Calb1+, and we localize these to the SNpl. Consistent with previous genetically and anatomically defined projection maps[9,17,86], we find substantial innervation of the TS. The SNpl to TS projection has recently been shown to have distinctive properties and encode threat prediction[9]. Uchida et al.[87] have postulated that this population may be considered a separate and orthogonal DA axis to the traditional reward encoding axis. Our findings that these SNpl neurons are predominantly part of the developmentally encoded Sox6- cohort, support the notion that these neurons have distinct functional properties.

Towards understanding the basis of SNc neuron diversity, we provide evidence that the SNc has a dual embryonic origin (Figure 9B). From our multi-pronged lineage analysis, we find that the dSNc/SNpl is predominantly derived from Sox6- progenitors. These progenitors are enriched in the lateral FP. More caudally, these lateral FP progenitors give rise to Otx2+ VTA neurons in the ventromedial VTA (Figure 9B), consistent with the model of Panman et al[51]. In contrast, Sox6+ progenitors enriched in the medial FP, give rise to neurons in the SNc, with a greater propensity for Aldh1a1+ compared to Calb1+ fates. However, some of the cells in the vSNc originate from Sox6- progenitors but upregulate Sox6 post-mitotically. This latter conclusion finds support in the following observations: (i) Some transient double-reporter positive cells are observed at embryonic stages in Sox6-Cre, Th-2A-Flpo based experiments (Figure 6C). (ii). Even after accounting for PRISM efficiency, our progenitor restricted fate -map does not label the entire vSNc. Nonetheless, because of potential temporal delay due to sequential recombination in PRISM fate maps, in conjunction with the slightly earlier birth of the SNc[88], it is difficult to exclude the possibility that

a greater fraction of the vSNc was derived from Sox6+ progenitors. Overall, though, we provide evidence that SNc neuron fate is, at least in part, encoded in FP progenitors. Subsequent molecular refinements, coupled with differential migrations, and axon guidance mechanisms, then culminate in the elaborate and diversified midbrain DA system seen in the adult[46,49,54,67,89–91].

Sox6+ progenitors also contribute to DA neurons in the VTA, many of which are located in the parabrachial region, and which continue to maintain Sox6 expression. However, some descendants were also observed in more ventromedial VTA regions, although some of these down-regulate Sox6 during differentiation. The latter finding is supported by the observation that several GFP+ cells of the VTA are Otx2+, and it suggests that all DA progenitors may not be completely fixed in their lineage. This would be in accordance with recent postulates on cell fate determination in the CNS, in which neurons converge on stable states through a process of gradient descent, using "configurational codes" that are somewhat plastic and evolve during development[92]. An alternative explanation could be that some low level Sox6 expressing cells in the lateral progenitor domain, superseded the threshold of recombination and contributed to the VTA fate map.

Understanding DA neuron diversity is a key step towards clarifying the myriad functions of midbrain DA neurons. Leveraging the power of intersectional/subtractive genetic methods and Sox6 as an anchor, we provide a developmental perspective into how this diversity might be generated in the early embryo, and in doing so, we provide clarification to adult taxonomic schemes. Further work will be required to define molecules that might induce Sox6 in the FP, as well as the functional role and direct targets of Sox6, towards the diversification of DA neurons.

2.7.1. Functional responses of Sox6+ and Sox6- neurons

Given the stark differences between SNc Sox6+ and Sox6- dopamine neurons in their anatomical distribution of somas in mice (Figure 1) and humans (Figure 4), their axonal projection patterns to striatum (Figure 2), their vulnerability in human PD patients (Figure 4) and mouse PD models[47], their molecular fingerprints (Figure 5), and their developmental origins (Figure 6, Figure 7), we expected functional differences.

Recent studies have revealed that the activity of some SNc neurons is time-locked to movement initiation and acceleration, thereby rejecting the dogma that slow variations in firing (tens of seconds to minutes) in these same neurons bias animals towards or away from movement[5]. One study measuring DA axon calcium transients in the striatum suggested that axons encoding locomotion and reward signals were distinct – transients time-locked to locomotion was prominent in the dorsal striatum, but reward locked transients were prominent in the ventral[5]. Here, we extend these findings by demonstrating that the Sox6+ subtype includes this population with calcium transients time-locked to acceleration. Together with our data showing selective degeneration of Sox6+/Aldh1a1+ neurons in PD, and the projections of the Sox6+ cohort to the dorsal striatum, this suggests a role for the Sox6+ cohort in motor control. This conclusion is consistent with a recent study showing that ablation of ~80% of Aldh1a1+ neurons (which are a subset of Sox6+ neurons) in the SNc results in motor learning and walking speed deficits (Wu et al., 2019).

However, this study has several limitations. On the one hand, labelling and recording from the Sox6- population was extremely challenging, as axons were only weakly and sparsely labelled with GCaMP, possibly due to inefficiencies in the subtractional virus used. In consequence, in most mice studied we were not able to obtain successful recordings, and in the 2/9 where we did the signal-to-noise ratio was very low. This means that, while these recordings show clear reward

responses (as shown in the triggered averages in Figure 8C), smaller locomotion locked transients might have been obscured by the noise. It is thus complicated to conclude that these neurons do not show locomotion signaling. Furthermore, these successful recordings were only from the most ventral regions within striatum (not the nucleus Accumbens), where Sox6+ axons are absent from. Thus, we were not able to compare the signaling of these two subtypes in a region of striatum where their axons overlap, which would be a conclusive demonstration that functions map onto genetic subtypes, rather than anatomy determining function.

To address these limitations, we later attempted to repeat this experiment in SNc, as here the somas of Sox6+ and Sox6- neurons are intermingled (especially within the spatial resolution of fiber photometry, ~300 μm), and where we hoped GCaMP expression would be stronger in Sox6- neurons. Indeed, we were able to record calcium transients from both Sox6+ and Sox6- neurons in SNc; however, here they did not show strong functional differences (data not shown). This could be due to two possibilities: either local modulation controls DA release from axons in an anatomically restricted way, or Sox6+ and/or Sox6- neurons are not functionally homogeneous groups.

In the next chapter, we will use new genetic markers to access a second level of division of DA neurons which has been previously described[17,28]. On one hand, Sox6+ neurons are divided into Sox6+/Aldh1a1+ and Sox6-/Aldh1a1- neurons, with Aldh1a1+ neurons projecting more dorsal in striatum compared to Sox6+ neurons, which matches the distribution of reward-unresponsive locomotion-locked axons. On the other hand, the expression of Calb1 in SNc DA neurons is mostly non-overlapping with Sox6 expression[47,93], and thus this marker can provide an improved strategy to access the Sox6- population without the inefficient subtractional virus. This Calb1+ subtype can also be subdivided into Vglut2+ and Vglut2+ populations, which we will also characterize.

2.8. Methods

2.8.1. Immunostaining and quantification of human SNc

Tissue samples, clinical and neuropathology data, were supplied by the Parkinson's UK Brain Bank funded by Parkinson's UK, a charity registered in England, in Wales (258197) and Scotland (SC037554). In total, fifteen PD patients between 67-92 years of Braak stages V-VI were evaluated. Cases were age-matched to controls. All post-mortem analyses were approved by the Ethical Research Committee of the Centre Hospitalier Universitaire de Québec (#2016-2564).

We referred to published work[39,94,95] to define human substantia nigra (hSNc) anatomical borders and used Nissl staining to confirm the rostro-caudal level of the sections. Sections were deparaffinized by heated treatment (65°C), treated with citrisolv, (Decon laboratories Inc., #1601) rehydrated in ethanol gradients (70%, 50% and 25% for 2 min) and incubated in cresyl violet solution for 20 min followed by dehydration in ethanol gradients (25%, 50%, 70%, 95%, 100%) and citrisolv. Slides were cover-slipped with DPX mounting medium (Electron Microscopy Sciences #13512) and observed under a Nikon Eclipse E800 bright field microscope.

For immunostaining of hSNc shown in Figure 4A-B, sections were deparaffinized followed by incubation in citrisolv, hydration steps with ethanol gradients (100%, 95%, 70%, and 50%) and quick rinse in PBS - 0.2% Tween. Sections were next incubated in a pre-heated antigen retrieval solution of 10mM citrate buffer (pH6.2) (Sigma-Aldrich, #W302600-1KG-K) for 30 min at 95°C and cooled for 1 hour at RT. Sections were then rinsed in wash buffer (PBS - 0.2% Tween - 5% BSA (BioShop, ALB001.500) - 2.5% Triton X (Sigma-Aldrich, T8787) and incubated in blocking solution (5% BSA, 2.5% Triton X, 10% donkey serum (Sigma-Aldrich, D9663) for 1 hour at RT. Finally, sections were incubated overnight at RT in blocking solution with the following primary

antibodies: rabbit anti-SOX6 (Sigma-Aldrich, #HPA001923, 1:100), sheep anti-TH (Pel-Freez Biologicals, #P60101-0, 1:1000), mouse anti-ALDH1A1 (Sigma, #SAB5300519, 1:200), rabbit anti-CALBINDIN-D-28K (Millipore, #AB1778, 1:500). Subsequently, sections were rinsed three times in wash buffer. Secondary antibodies were diluted in blocking solution and incubated for 2 hours and 30 min at RT with Alexa Fluor 488 donkey anti-rabbit IgG (Life Technologies, #A21206, 1:500), Alexa Fluor 546 donkey anti-sheep IgG (Life Technologies, #A21098, 1:500) and Alexa Fluor 647 donkey anti-mouse IgG (Life Technologies, #A 31571, 1:500). Sections were then washed three times and incubated 7 min at RT in DAPI (Molecular probes by Life Technologies, #D3571), rinsed 3 times, washed for 5 min in ethanol 70% and incubated for 5 min at RT in autofluorescence eliminator reagent (Millipore, #2160) followed by three washes in ethanol 70% for 1 min. Slides were ultimately dried and cover-slipped using fluoromount G (Electron microscopy, #17984-25). To ensure antibodies specificity, positive and negative controls were included. For SOX6 positive control, human tissue was obtained from cases with brain metastases which are known to be immune reactive for SOX6. Negative controls were performed by omitting the primary antibody.

For quantification of subtype survival in PD (Figure 4C-H), images of human SNc (hSNc) were acquired on the slide scanner Zeiss Axio Scan.Z1 with Zen 2.3 lite software. High magnifications were obtained on Zeiss LSM 800 confocal laser microscope with Zen 2.1 software. Images were acquired by z-series and reconstructed in Fiji software. For quantification, the hSNc was first identified and delineated on each slide using Nissl staining. Adjacent slides were used for staining where anatomical delimitations were reproduced. The shape of each region was delineated using Zen 2.3 lite software and both single and double-labeled neurons were counted.

Student's t-tests were used between two means with a Welch correction when the homogeneity of variance could not be confirmed with Bartlett's test. Two-way ANOVA followed by Tukey's post-hoc analyses was used when two categorical data such as "group", "sex" or "levels of analyzed brains" were investigated. No significant statistical differences between sex were identified. Likelihood ratio analysis of contingency tables with Pearson's method was used in the investigation of categorical data such as "sex". P values under 0.05 were considered significant. All statistical analyses were performed using Prism (Graphpad). Data were expressed as mean ± SEM and each point depicted on the graphs represents one sample.

2.8.2. Mice

All animals used in this study were maintained and cared following protocols approved by the Northwestern Animal Care and Use Committee. Cre and Flpo mouse lines were maintained heterozygous by breeding to wild type C57BL6 mice. Reporter lines were maintained homozygous. The Sox6-FSF-Cre and Sox6-FSF-CreERT2 lines were generated at Northwestern University by the Transgenic and Targeted Mutagenesis Laboratory as previously described[17]. To obtain Sox6-FSF-CreERT2, we replaced the Cre cassette with a CreERT2 cassette[17]. We crossed Sox6-FSF-Cre and Sox6-FSF-CreERT2 to CAG-Flpe to obtain Sox6-Cre and Sox6-CreERT2 lines, respectively.

For postmitotic or cumulative analyses respectively (Figure 1, Figure 6), we crossed Sox6-FSF-Cre or Sox6-Cre to Th-2A-Flpo[17], RC-Frepe (JAX 029486) and harvested brains at P56 and P21-P30,. Both males and females were used for all adult brain analyses. As reported in Poulin et. al. 2018[17], Th-2A-Flpo has ~99% recombination efficiency in DA neurons. For projection and functional analyses (Figure 2, Figure 3, Figure 8), Sox6-FSF-Cre mice were crossed to Th-2A-Flpo mice, and offspring were used for viral injections at 3 to 5 months old. To obtain progenitor

labeling at E11.5, Sox6-FSF-Cre animals were crossed to CAG-Flpe, RC-Frepe (Figure 6A). To obtain progenitor labeling at E12.5, Sox6-Cre animals were crossed to Ai9 (JAX 007909). For PRISM analysis (Figure 7), we used our newly generated Nes-LSL-Flpo line[69], Ella-Cre (JAX 003724), Slc17a6-Cre (Vglut2) (JAX 028863), and Sox6-Cre, crossed to RC-FA (RC-LacZ), that was derived by crossing the intersectional reporter RC-Fela[96] (gift from S. Dymecki) with the beta-actin Cre-deleter mouse (JAX 003376). To establish maximum efficiency of PRISM, Nes-LSL-Flpo was first crossed to EIIa-Cre. Offspring with a deletion of the loxP-STOP-loxP cassette (Nes-Flpo) was next crossed to RC-FA. This breeding strategy assured that loxP-STOP-loxP cassette preceding Flpo was excised in the germline. To permanently delete the rox-flanked destabilized eGFP cassette (d4GFP) in Nes-LSL-Flpo, this PRISM line was crossed to a Dre-deleter mice as previously described[69]. Brains of adult males and females were harvested at P21 for all PRISM-related experiments mentioned above. For progenitor-anchored fate maps at E11.5 and E12.5, Nes-LSL-Flpo was crossed to Sox6-Cre with RC-FA and Ai65F (JAX 032864), respectively. For genetically induced fate map experiments, tamoxifen (Sigma Aldrich, prepared in corn oil) was administered by IP injection to pregnant dams of E9.5 Sox6-CreERT2, Ai9 (2mg/40g). For all embryonic time points, the morning of the day when a vaginal plug was detected was designated as E0.5.

2.8.3. Immunofluorescence in mouse tissue

Embryonic brains were harvested and fixed in 1% or 4% PFA-PBS for an amount of time depending upon age, cryoprotected in 30% sucrose-PBS before OCT embedding and sectioning at 16-20 μm on a cryostat. Adult brains were perfused and fixed overnight with 4% PFA-PBS, cryoprotected in 30% sucrose-PBS solution, snap frozen in dry-ice and sectioned at 20-25 μm on a microtome. Sections were rinsed in PBS and blocked in 5% normal donkey serum in PBS 0.3%

Triton X for 30 min at room temperature (overnight at 4°C for staining with goat anti-Aldh1a1), then incubated with primary antibodies diluted in blocking solution overnight at 4°C. Antigen retrieval: Tissue was post-fixed 5 min in 4% PFA-PBS, rinsed in PBS, treated with antigen unmasking Solution (Vector Laboratories) and heated in a microwave for 5-10 minutes depending on the primary antibody, then blocked for 1 hour and incubated overnight at 4°C with primary antibodies diluted in the blocking solution. The following day, sections were rinsed in PBS and incubated with secondary antibodies at room temperature, followed by PBS rinse and mounting. Primary antibodies: rabbit and sheep anti-TH (Pel-Freez, 1:500 and 1:250, respectively), chicken anti-GFP (Abcam, 1:1500), rabbit anti-mCherry (Abcam, 1:1000), rat anti-mCherry (Abcam, 1:1000), mouse anti-CB (Abcam, 1:500), rabbit anti-OTX2 (Proteintech, 1:500), goat anti-ALDH1A1 (Abcam, 1:1000), rabbit anti-Lmx1A (Millipore, 1:1000, antigen retrieval), guinea pig anti-LMX1A (Gift from Dr. Yongchao C. Ma, 1:20,000, antigen retrieval), goat anti-βGal (Biogenesis, 1:1500), rabbit anti-RFP (LSBio, 1:1000, antigen retrieval), rat anti-DAT (Santa Cruz, 1:200). Secondary antibodies: Alexa-488, -555, and -647 (Molecular Probes) or Cy3 and Cy5 (Jackson Immuno Research), diluted 1:250 in blocking solution with DAPI (1mg/mL; Sigma).

2.8.4. In situ hybridization

RNAscope assay was performed on 4% PFA fixed brains (as explained above), using the fluorescent multiplex kit from Advanced Cell Diagnostic according to manual instructions for detection of Slc17a6, (Vglut2) (Mm-Slc17a6-C3; ACD #319171) Sst, (Mm-Sst-C3; ACD #404631) Ngb, (Mm-Ngb-C3; ACD #876171) Fxyd6, (Mm-Fxyd6-C3; ACD #430971). We combined this method with standard immunofluorescence for mCherry and TH as explained above, performing RNAscope first. 16 µm sections were obtained with a cryostat. Slides were cover-slipped with ProLong Gold antifade reagent (Sigma). We determined Vglut2 positivity by

counting the number of puncta surrounding a cell's nucleus. All cells were observed to have basal expression of Vglut2. Any cell that had 10 or more distinct, clustered, puncta were considered Vglut2 positive. All images for this study were obtained on Olympus BX61VS slide scanner, confocal Nikon A1R-spectral microscope, Nikon W1 Dual Cam Spinning Disk Confocal at Northwestern University Center for Advanced Microscopy/Nikon Imaging Center, or Leica TCE SPE DMI4000 B (Dr. Dimitri Krainc, Northwestern University).

2.8.5. Quantitative analysis of mouse samples

We referred to the mouse brain Allen Reference Atlas (by Wiley) and Paxinos G. & Franklin K. B (second edition by Academic Press) to identify brain section levels and establish anatomical boundaries in conjunction with TH expression. Multi-channel images were processed in Fiji to draw boundaries and perform cell counts. All counted cells were DAPI+ and all DA neurons counted were TH+ or DAT+. Specifically, GFP+ and mCherry+ cells counted for Figure 1C-E and Figure 6F were also TH+. Cell counts on adult brains were performed on three brains per genotype and three to six matching sections across the rostro-caudal axis (Allen atlas levels B-2.88 to B-3.52 for SNc, VTA, SNpl and -3.88 for RRF). We quantified 3 sections for all experiments with CB and ALDH1A1 staining, and for PRISM efficiency in adult brains. For Sox6-FSF-Cre, Th-2A-Flpo, RC-Frepe analysis in Figure 1, we quantified 5 brains, 4 sections each. For in situ hybridization of Vglut2 (Figure 6I), we quantified 3 brains, 6 sections each. For quantifications at E12.5, we analyzed 3 sections per brain, 3 brains per genotype.

For genetically induced fate mapping analysis (see Pereira Luppi et al. 2021[38], Fig. S7H-K), we used six animals and at least ten Th+ midbrain sections were counted per brain. All values were expressed as mean ± SEM. Student's t-test was used for statistical comparisons and p values lower than 0.05 were considered significant. Analysis was performed in Matlab.

2.8.6. Characterization of spatial distribution of Sox6+ and Sox6- cells

For the first approach to characterize spatial distribution of reporter-labeled cells, we performed a bisection of the SNc for dorsal-ventral analysis performed in ImageJ. First, a dorsal and a ventral SNc boundary was drawn. The length of each boundary was divided into 10 segments, marked by ticks on the boundary line. Starting from one end, a vertical line was drawn to join the first tick on the dorsal boundary to the first tick on the ventral boundary, the process was repeated for the subsequent 9 ticks. Finally, a bisector line was drawn by crossing each midpoint of the 10 vertical lines. mCherry+TH+ and GFP+TH+ cells were counted on each half. This data were not included in the figures but are in agreement with the second method.

For the second approach, we plotted histograms of cell spatial distribution across the dorso-ventral axis of the SNc (Figure 1D-E, example diagram in Figure 1H-H'''). xy coordinates for mCherry+Th+ and GFP+Th+ cells were obtained with ImageJ cell counter plugin. The angle and the dorso-ventral center of the SNc was obtained using a line of best fit given all SNc cells, and dorso-ventral coordinates were defined perpendicular to this line. Bins for the histograms are 15 μm wide. For Figure 1E (and H''') mCherry and GFP cells were normalized separately by relative probability (sum of each histogram = 100%). The centroids for each population on each section were plotted on Figure 1E right. 4 rostro-caudal sections were analyzed for each n=3 mice, with similar results across all 4 sections. All sections for each mouse were counted together for Figure 1D-E. Shaded area is SEM.

2.8.7. Transcriptome analysis

Sox6-FSF-Cre, Th-2A-Flpo, RC-Frepe adult brains (P56 and older) were used for bulk RNAseq analysis (Figure 5). Anesthetized mice were rapidly decapitated and the SNc was carefully dissected at ~1mm coronal thickness using a brain matrix (Kent Scientific #RBMS-200C) and

further trimmed under an epi-fluorescent microscope, avoiding other dopaminergic populations. Samples were processed with the Papain Dissociation System (Worthington Biochem #LK003150) following the manufacturer's recommendations. However, we substituted the provided EBSS solution with ACSF buffer (200 mM Sucrose, 2.6 mM KCl, 10 mM MgCl2, 0.5 mM CaCl2, 26 mM NaHCO3, 1.27 mM NaH2PO4 and 10 mM Dextrose; equilibrated with 5% CO2/95% O2; pH 7.3). Tissue was dissociated in 20U papain per mL in ACSF, 1mM of L-cysteine, and 0.5mM EDTA. At the end, cells pellets were re-suspended in 400µL of cold ACSF enriched with 1% B27, 1% BSA and DAPI, then FACS sorted. Roughly an equal number of mCherry+ (dorsal SNc) and GFP+ (ventral SNc) cells were collected from 3 independent animals, each sample was processed individually. Total RNA was prepared according to Ambion mirVana miRNA isolation kit (Life technology, AM1561).

Stranded mRNAseq was conducted in the Northwestern University NUSeq Core Facility. Total RNA samples were checked for quality using RINs generated from Agilent Bioanalyzer 2100. RNA quantity was determined with Qubit fluorometer. The Illumina TruSeq Stranded mRNA Library Preparation Kit was used to prepare sequencing libraries of high-quality RNA samples (RIN > 7). The Kit procedure was performed without modifications. This procedure includes mRNA enrichment and fragmentation, cDNA synthesis, 3' end adenylation, Illumina adapter ligation, library PCR amplification and validation. Illumina NextSeq500 NGS Sequencer was used to sequence the libraries with the production of single-end, 75 bp reads. The quality of reads, in FASTQ format, was evaluated using FastQC (v0.11.7). Reads were trimmed to remove Illumina adapters from the 3' ends using cutadapt (v1.14)[97]. Trimmed reads were aligned to the Mus musculus genome (mm10/GRCm38.p6) using STAR (version 020201)[98]. Read counts for each gene were calculated using htseq-count (version 0.6.1p1)[99] in conjunction with a gene annotation

file for mm10 obtained from Ensembl (http://useast.ensembl.org/index.html). Normalization and differential expression were calculated using DESeq2 (version 1.14.1) that employs the Wald test[100]. The cutoff for determining significantly differentially expressed genes was an FDR-adjusted p-value less than 0.05 using the Benjamini-Hochberg method. A pathway analysis was performed using Metascape (http://metascape.org) to identify significant pathways among the significantly differently expressed genes.

For plotting the volcano plot in Figure 5A, after aligning the sequences and calculating the number of reads obtained for each gene, we used DESeq2 (Version 3.10)[100] to estimate fold-change (FC) difference and significance between GFP+ and mCherry+ populations. DESeq was applied to the normalized counts using negative binomial distribution. False discovery rate (FDR<0.1) and -1.4 < FC > 1.4 were used as the parameters to select genes that have a significant expression change.

For plotting of the gene expression heatmap in Figure 5B, we used pheatmap R package (version 1.0.12) to build a heatmap from reads counts. Log2FC threshold was set to 0.65, and alpha to 0.05. Genes were filtered by FDR <0.05 to obtain the heatmap.

To analyze enrichment of gene sets (GSEA, Figure 5C-D) between GFP+ and mCherry+ populations, we used GSEA software v4.0.2, freely available from the Broad Institute[101,102]. First, we converted genes in our mouse RNAseq dataset to human homologues using the Human and Mouse Homologs list available from The Jackson Laboratory website. A total of 15828 genes were subsequently used for GSEA. Next, we compared GFP+ to mCherry+ populations using a curated collection of gene sets, "Canonical Pathways," available from MSigDB[102,103]. All default settings were used for the analysis, except for a minimum gene set size of 25 and use gene set for permutation type (recommended by GSEA for analyzing fewer than seven samples).

2.8.8. Projections in adult brains

The SNc of Sox6-FSF-Cre, Th-2A-Flpo adults (6-8 weeks old, n=3) were injected with AAV5 -hSyn-CreOn/FlpOn-EYFP (UNC AV8357) and AAV8 EF1α-CreOff/FlpOn-mCherry (gift from K. Deisseroth) viruses (Figure 2A-F, Figure 3A-C). For Figure 3D-F, viruses used were AAV5-EF1α-DIO-mCherry (UNC #AV4311B, abbreviated as AAV-CreOn-mCherry) and AAVdj-hSyn-CreOff/FlpOn-eYFP (gift from K. Deisseroth) (n=3). Four weeks later, brains were perfused with 4% PFA-PBS and fixed overnight in 4% PFA-PBS. The following day, after PBS washes, brains were processed to prepare 25μm sections on a freezing microtome. IF for mCherry and GFP (eYFP) was performed on floating sections as described above. Epifluorescence images were acquired on an Olympus Slide Scanner VS120.

For the histograms of Figure 2E-F, sections for CPr and CPi of n=3 mice above were used. A rectangle was drawn for each section in dorso-ventral and medio-lateral direction, as depicted in Figure 2E-F left. These areas were divided into 25 μm bins and the % of total fluorescence for each mCherry and eYFP was calculated in each bin.

2.8.9. One-photon fiber photometry

For calcium fiber photometry, adult mice (6-8 weeks old) of Sox6-FSF-Cre, Th-2A-Flpo genotype were injected within the SNc with either AAV8-EF1α-CreOn/FlpOn-GCaMP6 for AAV8-EF1α-CreOff/FlpOn-GCaMP6f (gifts from K. Deisseroth), respectively (Figure 8). n=9 mice were used for Sox6+ recordings, and n=10 for Sox6-. Mice were head-fixed over a cylindrical treadmill and allowed to run freely. Non-predicted water rewards were delivered through a waterspout, at random intervals. Optic fibers (200 μm diameter, 0.57 NA, Doric MFP_200/230/900-0.57_1.5m_FC-FLT_LAF) were placed into dorsal striatum for Sox6+ recordings (X ±1.8, Y 0.5, Z 1.9 mm) and in the ventral striatum for Sox6- recordings (X ±1.8, Y 0.5, Z 3.9 mm). A 470nm

LED was used for illumination and emitted light was diverged onto the PMT using a 505-sp dichroic and a 540nm/50 filter. Fluorescence was recorded at 4000 Hz and binned at 100 Hz. Mice with no significant transients were excluded (none for Sox6+ and 8 for Sox6-. We confirmed through histology that in most mice few Sox6- axons were labeled, not enough to reach the detection threshold of fiber photometry). %ΔF/F was calculated as in Howe et al. 2016[5]. Triggered averages were calculated for reward delivery and accelerations exceeding 1m/s^2. GCaMP expression and fiber placement were checked by immunofluorescence for GFP performed on floating sections as described above.

Table 1: Key Resources Table 1

REAGENT or RESOURCE	SOURCE	IDENTIFIER
Antibodies		
Chicken Polyclonal anti-GFP	Abcam	Ab13970
Rat Monoclonal anti-mCherry	Thermo Fisher	M11217
Goat Polyclonal anti-βgal	Biogenesis	4600-1409
Mouse monoclonal anti-CALBINDIN-D-28K	Sigma	C9848
Rabbit Polyclonal anti-OTX2	Proteintech	13497-1-AP
Goat Polyclonal anti-Aldh1a1	R&D	AF5869
Rabbit Polyclonal anti-Sox6	Sigma	HPA001923
Guinea pig Polyclonal anti-Lmx1a	Gift from Yongchao C. Ma	N/A
Rabbit Polyclonal anti-Lmx1a	Millipore	AB10533
Rabbit Polyclonal anti-CALBINDIN-D-28K	Millipore	AB1778
Mouse Monoclonal anti-ALDH1A1	Sigma	SAB5300519
Rat Polyclonal anti-DAT	Santa Cruz	sc-32258
Mouse Monoclonal anti-RFP	Abcam	ab125244
Sheep Polyclonal anti-TH	Pel-Freez	P60101-0

Virus strains		
AAV5-hSyn-CreOn/FlpOn-EYFP	UNC	# AV8357
AAV8EF1α-CreOff/FlpOn-mCherry	Gift from Karl Deisseroth	# 2466
AAV5-EF1α-DIO-mCherry	UNC	#AV4311B
AAVdj-hSyn-CreOff/FlpOn-eYFP	gift from K. Deisseroth	#987
AAV8-EF1α-CreOn/FlpOn-GCaMP6f	gift from K. Deisseroth	#2383
AAV8-EF1α-CreOff/FlpOn-GCaMP6f	gift from K. Deisseroth	#2385
Experimental models: Cell lines		
PRX-B6 (C57BL/6N) (mouse ES cells)	The Jackson Laboratory	012448
Experimental models: Mouse strains		
Sox6-FSF-Cre	Poulin et al. 2018[17]	N/A
Sox6-Cre	Pereira Luppi et al. 2021[38]	N/A
Sox6-CreERT2	Pereira Luppi et al. 2021[38]	N/A
Th-2A-Flpo	Poulin et al. 2018[17]	N/A
Mouse: Tg(EIIa-cre)C5379Lmgd	The Jackson Laboratory	003724
Mouse: Slc17a6tm2(cre)Lowl	The Jackson Laboratory	016963
NSF	Poulin et al. 2020	N/A
B6;129S6-Gt(ROSA)26Sortm8(CAG-mCherry,-EGFP)Dym/J	The Jackson Laboratory	029486
RC-Fela	A gift from S. Dymecki (Jensen et al. 2008)	N/A
Mouse: B6.Cg-Gt(ROSA)26Sortm65.2(CAG-tdTomato)Hze/J	The Jackson Laboratory	032864
Mouse: B6;129S6-Gt(ROSA)26Sortm9(CAG-tdTomato)Hze/J	The Jackson Laboratory	007905
Mouse: B6;129-Tg(CAG-dre)1Afst/Mmucd	MMRRC	032246-UCD

Oligonucleotides		
Primers for Cre strains Cre-F: GCAGAACCTGAAGATGTTCGC	Pereira Luppi et al. 2021[38]	N/A
Primers for Cre strain Cre-R: ACACCAGAGACGGAAATCCATC	Pereira Luppi et al. 2021[38]	N/A
Primers for NSF F: CACCAAGACCAAGACCCTGT	Pereira Luppi et al. 2021[38]	N/A
Primers for NSF R: CCTTCAGCAGCTGGTACTCC	Pereira Luppi et al. 2021[38]	N/A
Primers for RC-Fela, RC-Frepe, RC-Ai9, RC-Ai65F -F: TGCAATACCTTTCTGGGAGTTC	Pereira Luppi et al. 2021[38]	N/A
Primers for RC-Fela, RC-Frepe, RC-Ai9, RC-Ai65F -R: AGCGGGAGAAATGGATATGAAG	Pereira Luppi et al. 2021[38]	N/A
Primers for RC-Fela, RC-Frepe, RC-Ai9, RC-Ai65F -R: TACCGTAAGTTATGTAACGCGG	Pereira Luppi et al. 2021[38]	N/A
Primers for Th-2A-Flpo F-TAAGACCCTGCTGATGGTTGG	Pereira Luppi et al. 2021[38]	N/A
Primers for Th-2A-Flpo R-CATAGGGCATTCCTGTGGTTTG	Pereira Luppi et al. 2021[38]	N/A
Primers for Th-2A-Flpo R-GCTTCACTGAGTCTCTGGCATC	Pereira Luppi et al. 2021[38]	N/A
Deposited Data		
RNAseq of GFP and mCherry cells of Sox6-FSF-Cre, Th-2A-Flpo, RC-Frepe SNc	This Paper	GEO: GSE185480
Software and other resources		
VS-ASW-S6	Olympus	https://www.olympus-lifescience.com/en/microscopes/virtual/vs120/
cellSens	Olympus	https://www.olympus-lifescience.com/en/software/cellsens/
Zen 2.3 and 3.3	Zeiss	https://www.zeiss.com/microscopy/us/products/microscope-software/zen.html
Matlab	MathWorks	https://www.mathworks.com/products/matlab.html
RStudio	RStudio	https://www.rstudio.com/

FastQC	Babraham Bioinformatics	http://www.bioinformatics.babraham.ac.uk/projects/fastqc/
STAR	Dobin et al. 2013	https://github.com/alexdobin/STAR
DESeq2	Bioconductor	Bioconductor - DESeq2
cutadapt	cutadapt	Cutadapt removes adapter sequences from high-throughput sequencing reads | Martin | EMBnet.journal
pheatmap	CRAN	CRAN - Package pheatmap (r-project.org)
GSEA	UCSD	https://www.gsea-msigdb.org/gsea/index.jsp
ImageJ	NIH	https://imagej.nih.gov/ij/

3. Genetic subtypes show different responses to locomotion, rewards and air puffs

Most of this chapter will be part of a paper co-authored by Zachary Gaertner, and work conducted by him is specified in the figure legends. Printed with permission of Zachary Gaertner.

3.1. Introduction

For decades, midbrain dopamine neurons in the substantia nigra pars compacta (SNc) and ventral tegmental area (VTA) were defined as a largely homogeneous population responding to unexpected rewards and reward-predicting cues[30,86,104–108]. However, recent studies have revealed a more complicated story, with increasing evidence for functional heterogeneity. In the VTA, dopamine neurons encode other behavioral variables, such as sensory, motor and cognitive, in addition to the classic reward prediction error response[109], and separable aversive-responsive populations have been proposed[110,111]. In the SNc, dopamine neurons can respond to both rewarding and aversive stimuli[9,14–16,112], and increase or decrease firing during movement accelerations[2,5–8,113].While dopamine neurons and their axons in particular regions of the SNc or striatum respond to these other behavioral variables[5,114], reward responses have also been observed in the same regions[16,32,33], leading to the common assumption that most, if not all, dopamine neurons encode reward or reward predicting cues. Therefore, it is currently unclear whether reward, movement and aversion encoding co-occurs in the same neurons or are separately encoded by different groups of dopamine neurons.

Diversity has also been observed in dopamine neurons at the level of gene expression. Previous limitations on the number of molecular markers that could be simultaneously studied resulted in

midbrain dopamine neurons being long considered a largely homogeneous population, but recent advances in single cell-transcriptomics have led to the unbiased classification of several putative subtypes [28,45–49]. This leads to the enticing hypothesis that different functional responses might in fact map onto different subtypes.

Here we address this question with a focus on the SNc. Three different subtypes have been proposed to account for most of the SNc dopamine neurons[28], which we here refer to by marker genes that characterizes each subtype: the Aldh1a1+, Calb1+, and Vglut2+ (which is also enriched in Calb1 expression) subtypes. These subtypes have somas in SNc which, while intermingled, are anatomically biased: Aldh1a1+ somas are biased towards ventral SNc, Calb1+ somas towards dorsal SNc, and Vglut2+ somas towards lateral SNc[17]. Similarly, their axons project to different regions of striatum, though with overlap in some regions: Aldh1a1+ axons project to dorsal and lateral striatum, Calb1+ to dorso-medial and ventro-medial striatum, and Vglut2+ to posterior striatum[17]. If these different subtypes indeed have different functional signaling properties, their anatomical biases might explain previous seemingly conflicting results showing different functional responses of dopamine neurons during the same behaviors[2,5–8,32,33,113–115]: different subtype(s) may have been inadvertently investigated based on the recording location in SNc or striatum.

3.2. Aldh1a1+ is functionally heterogeneous

The functional characterization of Sox6+ DA neurons conducted in the previous chapter (section 2.6) demonstrated that Sox6 is not functionally homogeneous. Instead, the Sox6+ subtype included at least two sub-populations, one with dorsal-striatum projecting axons that did not respond to rewards but instead showed acceleration-locked signaling, and one with axons projecting more

ventral within striatum that did show reward responses. Given that Sox6+ includes an Aldh1a1+ sub-population with precisely dorsal-projecting axons[17], we hypothesized that Aldh1a1+ might be a functionally pure subtype responding only to locomotion.

To functionally characterize the Aldh1a1+ subtype, we used an intersectional genetic strategy to label only Aldh1a1+ neurons with the calcium indicator GCaMP6f[116]. For this, we generated a new Cre line that allows for more comprehensive and robust labelling compared to our previous tamoxifen-dependent line[17] (see Methods). We crossed this new Aldh1a1-Cre line with a Th-Flpo line and injected an intersectional AAV virus (AAV8-CreOn/FlpOn-GCaMP6f[117]) into the SNc to label Aldh1a1+ SNc DA neurons (Figure 10A). We then used fiber photometry to record GCaMP calcium transients from groups of striatal axons of the isolated Aldh1a1+ subtype in head-fixed mice running on a treadmill while periodically receiving unexpected rewards (Figure 10B). To control for any movement artifacts, we also recorded GCaMP fluorescence at its isosbestic wavelength, 405 nm[118]. GCaMP is ideally suited for these experiments because all known mechanisms for triggering axonal dopamine release involve increases in intracellular calcium concentration[119,120], including anterogradely propagating action potentials[121–125] and cholinergic modulation[37,126]. Critically, the detected calcium transients are generated only from the labeled genetic subtype; non-labeled neurons do not contribute. For this reason, GCaMP is preferred over extracellular dopamine sensors (i.e. dLight, GRAB-DA, microdialysis) because axons from different subtypes can densely overlap in many striatal regions[17] and these sensors detect dopamine released from all nearby axons, without subtype specificity.

Unexpectedly, functional recordings revealed clear functional heterogeneity within the Aldh1a1 subtype (Figure 10). In a majority of recordings, Aldh1a1+ axons showed no detectable response to unexpected rewards and calcium transients locked to accelerations (termed a “Type 1”

Figure 10: The Aldh1a1+ subtype is functionally heterogeneous

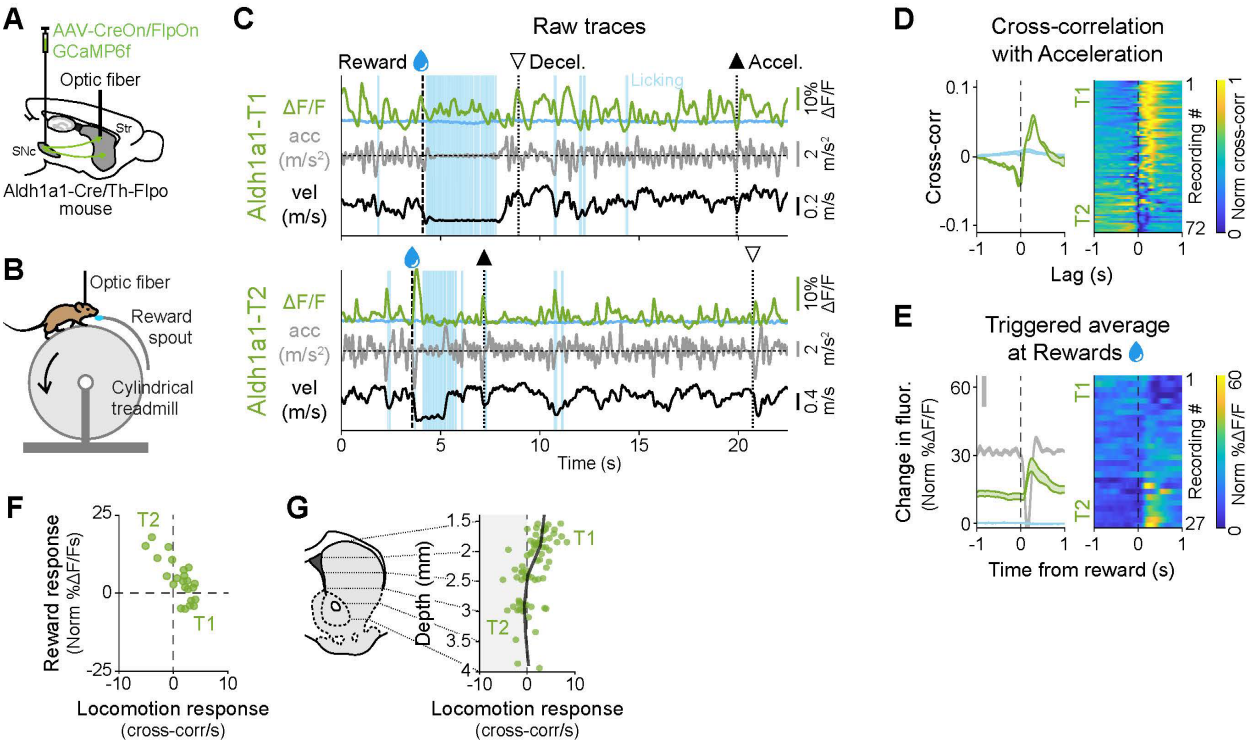

(**A**) Strategy used to label Aldh1a1+ DA neurons and record from their axons in striatum with GCaMP6f, a calcium indicator whose changes in fluorescence can be used as a proxy for axonal dopamine release.

(**B**) Schematic of fiber photometry recording setup during behavior.

(**C**) Two example recordings from Aldh1a1+ axons with different functional signaling patterns, Type 1 (no reward response, acceleration-locked transients) and Type 2 (reward response, deceleration-locked transients), showing fluorescence traces (ΔF/F), velocity, acceleration, licking, and reward delivery times. Isosbestic control shown in blue. Large accelerations = ▲, large decelerations = ▽.

(**D**) Average cross-correlation between ΔF/F traces and acceleration for all recordings from Aldh1a1+ axons. Isosbestic control shown in blue. Shaded regions denote mean ± s.e.m. Heatmap shows cross-correlations for each recording, sorted by the integral of the cross-correlation at positive lags. Mice = 13, n = 72 recordings.

(**E**) ΔF/F triggered averages on reward delivery times for all recordings from Aldh1a1+ axons. Isosbestic control shown in light blue, same scale as ΔF/F average. Acceleration shown in gray in the background (scale bar = 0.2 m/s^2). Shaded regions denote mean ± s.e.m. Heatmap shows triggered average for each recording, sorted by size of reward response. Mice = 7, n = 27 recordings.

(**F**) Relationship between the reward response size and the locomotion response (integral of the cross-correlation at positive lags) for each recording, showing how in Aldh1a1 larger reward responses correspond with deceleration correlation (Type 2), while small or negative reward responses correspond with acceleration correlation (Type 1).

(**G**) Distribution of the locomotion response along the dorso-ventral axis of the striatum for all recordings, showing how in Aldh1a1 dorsal recordings show acceleration correlation (Type 1) while more ventral recordings show deceleration correlation (Type 2). Black line represents moving average (0.5 mm bins).

functional response) (Figure 10C top). However, some recording showed clear reward responses and deceleration-locked transients ("Type 2") (Figure 10C bottom). To further quantify this heterogeneity, we first calculated the cross-correlation between ΔF/F and acceleration (an unbiased measure of the relationship in time between these two traces) (Figure 10D). The average across recordings showed a trough at negative lags and a peak at positive lags, consistent with calcium transients starting around the time of accelerations (acceleration-locked) as seen in Type 1 Aldh1a1+ recordings (Figure 10C top). However, when looking at the cross-correlation for individual recordings (Figure 10D heatmap), 20-30% of recordings showed the opposite response, with a trough at positive lags (blue shading instead of yellow), indicative of deceleration-locked responses as seen in Type 2. Next, we calculated the triggered average at reward delivery times for each recording (Figure 10E) and observed that some recordings showed strong reward responses (Type 2), while others had no detectable response (Type 1). This shows that, just like the Sox6+ subtype, Aldh1a1+ is functionally heterogeneous.

Furthermore, plotting for each recording its reward response (integral of the ΔF/F in the 1s window after reward response minus the baseline, calculated as the integral of the ΔF/F in the 1s window before reward response) vs its locomotion response (integral of the ΔF/F vs acceleration cross-correlation in a 1s window at positive lags), showed that there was a relationship between the two: recordings with the smallest reward responses also showed the strongest acceleration-locked signaling (Type 1), while those with greater reward responses showed stronger deceleration-locked signaling (Type 2) (Figure 10F). This suggests that Aldh1a1+ is composed of two sub-populations with different functional responses whose axons can overlap, in which case the measured response is somewhere in between Type 1 and Type 2 along both the reward and locomotion axis.

Finally, we asked whether, as was the case with Sox6, there was an anatomical bias in the distribution of the different functional responses within Aldh1a1. We plotted the locomotion score vs the depth from the brain surface at which each recording was made (Figure 10G) and, as with Sox6, dorsal striatum recordings show positive locomotion scores (acceleration-locked, Type 1) while more ventral recordings show more negative locomotion scores (deceleration-locked, Type 2). This suggests that within Aldh1a1+ there is one subpopulation of neurons that project even more dorsal in striatum (within the already dorsally biased Aldh1a1+ projection region) that shows acceleration-locked signaling and no response to rewards.

Aldh1a1+ functional responses, its heterogeneity and its dorso-ventral bias will be characterized in further detail in sections 3.4 and 3.5, but this initial characterization was enough to motivate us to reexamine the existing dopamine neuron classification schemes and search for new genetic subtype within the SNc Aldh1a1+ population. Particularly, we were interested in isolating a subtype with Type 1 functional responses, as this remarkable reward-unresponsive population would contradict the notion that all dopamine neurons signal reward.

3.3. Anxa1+, a subtype within Aldh1a1+

Work described in this section was conducted by Zachary Gaertner. Printed with permission.

The current classification of dopamine neurons was derived through single-cell gene expression profiling, primarily via single-cell RNA sequencing (scRNA-seq)[28]. However, such studies are limited by the number of cells analyzed due to technical difficulties in scRNA-seq[127], which could lead to inconclusive identification of closely related clusters. To uncover more granular divisions among dopaminergic subtypes, we first combined the data from four scRNA-seq studies[45,46,48,49] into an unbiased meta-dataset (see Methods). We observed 8 clusters, one of which was defined

by co-expression of Aldh1a1 and Anxa1 (Figure 11A). Plotting the expression of these two genes showed that Anxa1 expression is limited to a subset of Aldh1a1+ neurons (Figure 11B-C). This raised the possibility of at least two molecularly distinct Aldh1a1+ populations. However, while the analysis of this meta-dataset was able to refine our mapping of dopaminergic neuron subtypes, it was still limited by the biases introduced by the individual source datasets and cross-dataset integration methods, and thereby necessitated further validation.

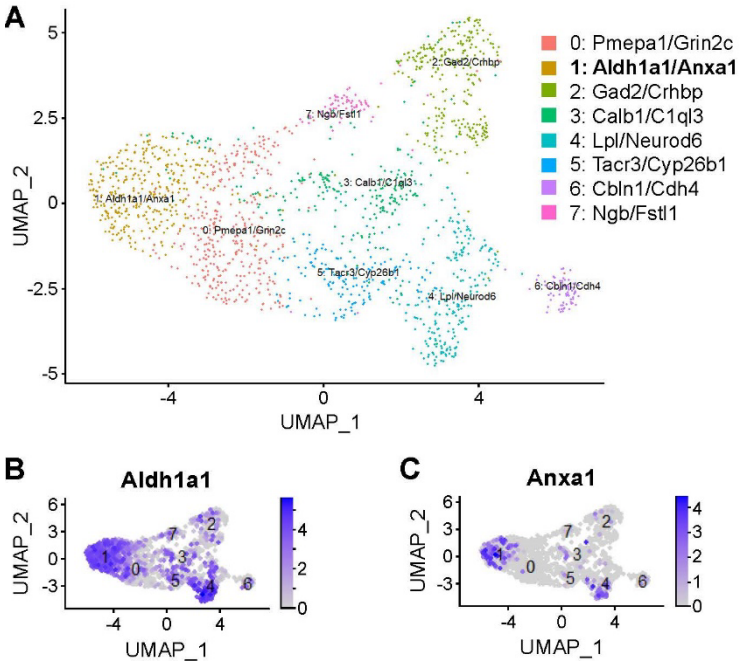

Figure 11: Integration of scRNA-seq datasets reveals a more granular resolution of DA neuron subtypes

(**A**) Resulting clusters from integrating datasets.

(**B-C**) Expression patterns of Aldh1a1 and Anxa1, the top defining markers for cluster 1. Expression of Anxa1 appears to be limited to a subset of Aldh1a1 expressing neurons.

Analysis by Zachary Gaertner.

To overcome the technical limitations of single-cell isolation of dopamine neurons, we utilized single-nucleus gene profiling (snRNA-seq, Figure 12A), a technique that is more efficient in brain regions where the recovery of intact neurons is difficult[128]. Indeed, this strategy allowed us to profile over 12,000 dopaminergic neuron nuclei from five mice, an order of magnitude higher than previous single-cell studies[45–47,49,129]. This approach resulted in the unbiased identification of fifteen clusters, out of which four minor clusters (#12-15 colored in grey in Figure 12B) represent neurons with weak dopaminergic characteristics (see Methods). The remaining clusters show

expression profiles largely in agreement with previous reports from single-cell sequencing studies, but with further subdivision of clusters. Importantly, all clusters were represented in both male and female samples (Figure 26B). Three clusters (#1, #3, #4) were significantly enriched for Sox6 (Wilcoxon Rank Sum test, FDR-adjusted p-values = 4.6×10^{-150}, 9.8×10^{-66}, and 2.8×10^{-276}

Figure 12: snRNA-seq reveals an Anxa1-expressing subtype within Aldh1a1+ DA neurons

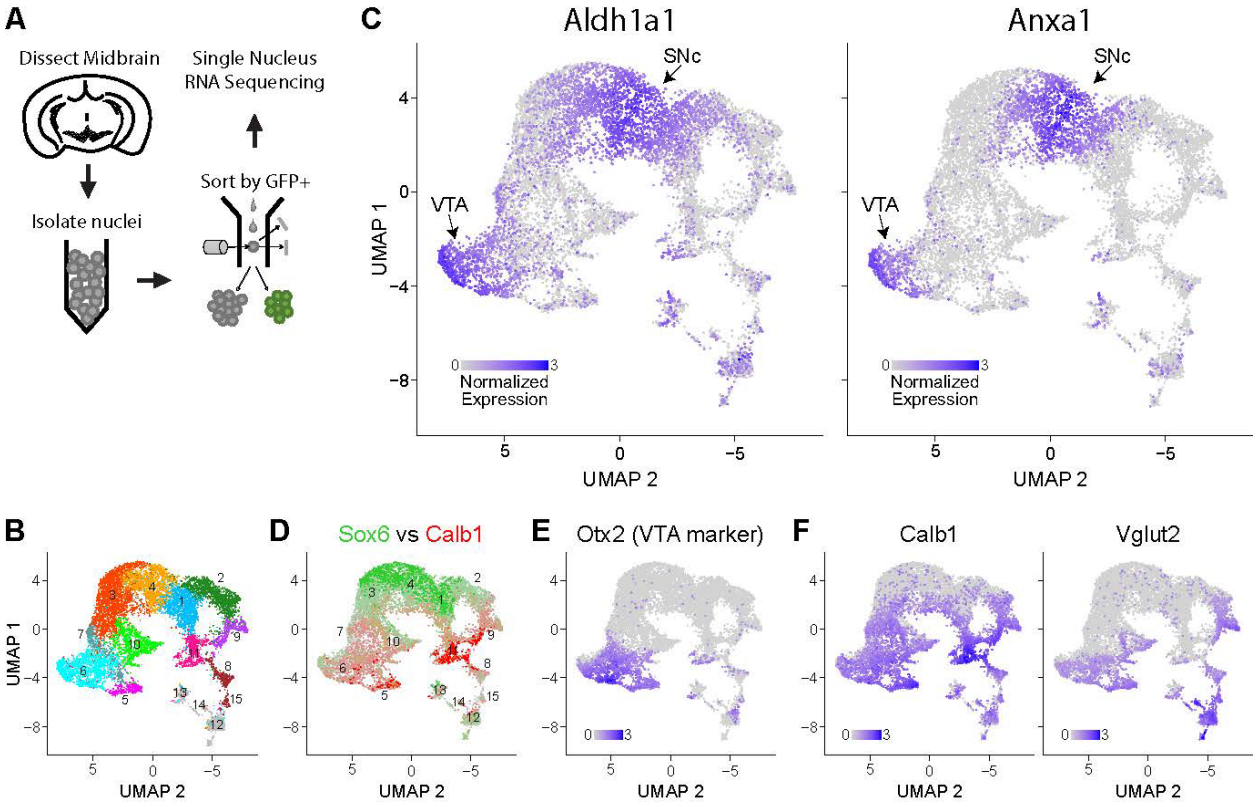

(**A**) Schematic of snRNAseq experimental pipeline.

(**B**) UMAP reduction of resulting clusters. In total, fifteen clusters were found. Notably, four clusters (12, 13, 14 & 15) had weak dopaminergic characteristics.

(**C**) Expression of Aldh1a1 and Anxa1, the latter of which is only expressed within a subset of Aldh1a1-expressing neurons.

(**D**) Overlaid expression patterns of Sox6 (green) and Calb1 (red) recapitulates a previously observed dichotomy among midbrain dopamine neurons.

(**E**) Expression pattern for Otx2 (a classical marker of most VTA neurons), enriched in clusters 5, 6, and 7. This allows us to distinguish between the SNc and VTA Aldh1a1+ subtypes.

(**F**) Expression patterns of the additional markers used for genetic access in experiments later on, Calb1 and Vglut2.

Experiment and analysis by Zachary Gaertner.

respectively); cluster #2 also showed enrichment of Sox6 (p-value = 1.1 $x10^{-04}$), but this result did not survive FDR correction. Four clusters (#5, #6, #9, #11) were significantly enriched for Calb1 (FDR-adjusted p-values = 6.6 $x10^{-30}$, 1.7 $x10^{-04}$, 1.1 $x10^{-22}$, 1.5 $x10^{-71}$, respectively); Cluster 10 also showed Calb1 enrichment (p-value = 6.9 $x10^{-04}$), but this again did not survive FDR correction. Little overlap between Sox6 and Calb1 was observed (Figure 12D), recapitulating a fundamental dichotomy among dopaminergic neurons[47,93]. Furthermore, Vglut2 expression was limited to a subset of Calb1+ cells (Figure 12F), consistent with prior recombinase-based labelling experiments[17]. We observed two likely SNc clusters with high Aldh1a1 expression (#1 & #4, Figure 12C left)–the third Aldh1a1+ cluster (#6) was Sox6- and Otx2+ (Figure 12E) and corresponds to a previously described VTA subtype also expressing Aldh1a1[17]. Cluster #4 was again significantly enriched for Anxa1 expression (FDR-adjusted p-value = 9.4 $x10^{-118}$) (Figure 12C right), corroborating the results from our integrated dataset analysis and establishing Anxa1 as a discrete dopamine neuron subtype marker within Aldh1a1+ neurons.

Following the identification of Anxa1+ as a putative subtype, immunostaining confirmed that SNc neurons expressing Anxa1 are indeed part of the broader Aldh1a1+ population, and in fact have cell bodies located ventrally within the already ventral Aldh1a1+ region (Figure 13A-B). We thus generated a new mouse line, Anxa1-iCre, to genetically access this subtype (see Methods). This allowed us to observe the axonal arbors of Anxa1+ dopamine neurons which, in comparison to Aldh1a1 axon arbors, innervate a more dorsally restricted region of the striatum (Figure 13C). This projection pattern matched the observed anatomical distribution of Aldh1a1+ “Type 1” axons, suggesting these unique functional responses could map onto the Anxa1+ subtype.

Figure 13: Anatomical characterization of Anxa1+ neurons

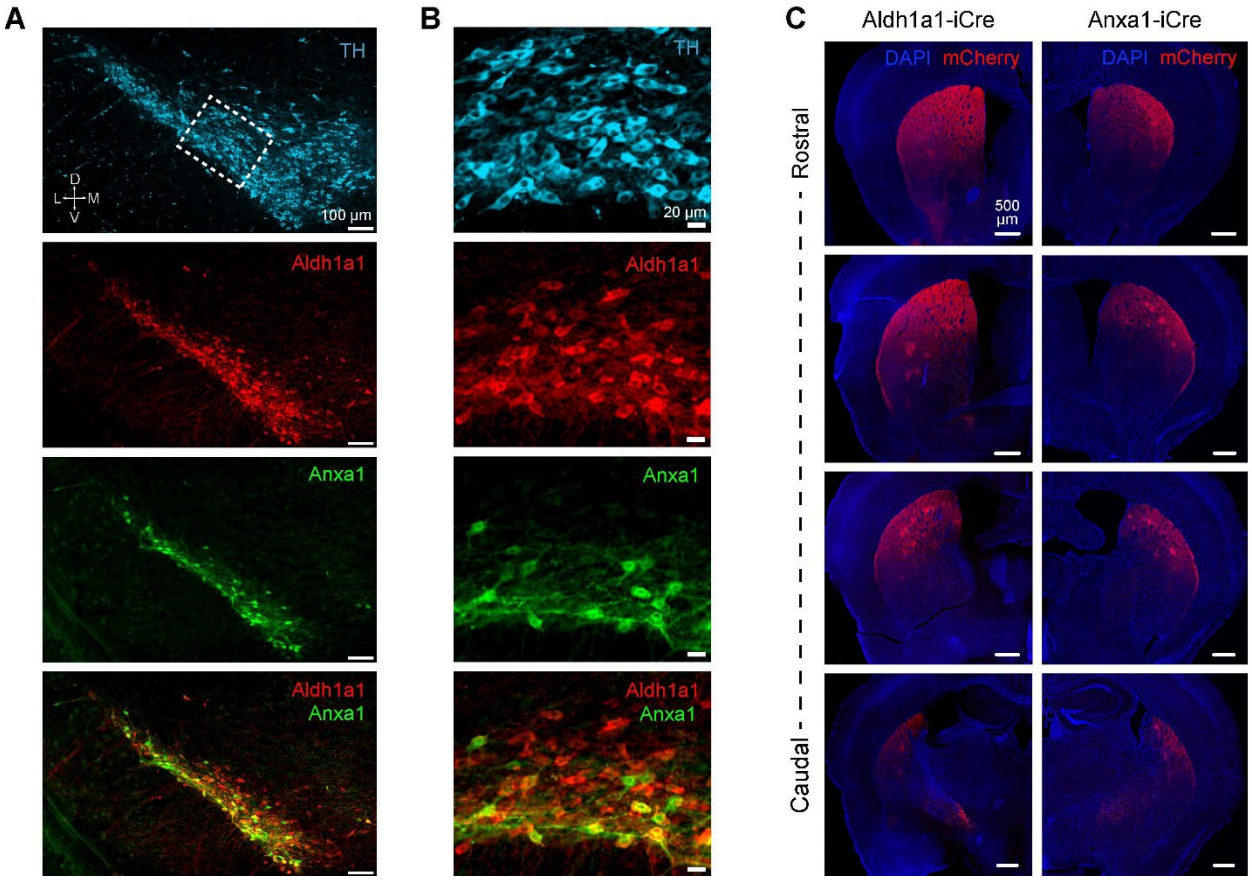

(**A**) Immunofluorescence images of Aldh1a1 and Anxa1 protein expression in SNc. Anxa1 is limited to a ventral subset of Aldh1a1+ neurons.

(**B**) Zoomed-in crops of section shown in panel E. Anxa1 was ventrally biased within SNc neurons.

(**C**) Right: projection patterns of Anxa1+ SNc axons based on viral labeling, which appear highly restricted to dorsolateral striatum and patches. Left: projection patterns of Aldh1a1+ SNc axons utilizing the same virus; projections extend more ventrally relative to Anxa1+.

Experiment by Zachary Gaertner.

3.4. Genetic subtypes show different signaling patterns during locomotion

The rest of this chapter is focused on functionally characterizing different genetic subtypes of DA neurons. We focused on four SNc DA subtypes that make up the majority of the SNc, which will be referred to by the genetic marker gene used to access them: three known DA subtypes[28], Vglut2+, Calb1+ and Aldh1a1+ (though we already know Aldh1a1+ is functionally

heterogeneous), plus Anxa1+. For comparison, we will compare data obtained from each subtype with identical experiments conducted in DAT-Cre mice, where all subtypes are indiscriminately labelled, which is the most common approach when studying dopamine in the literature[5,6,14,16,34].

These subtypes have somas biased to different locations within SNc and axons biased towards different regions of striatum though, critically, there is considerable overlap between subtypes in both SNc and striatum (Figure 14B-D). Furthermore, the Vglut2+ subtype is also Calb1+ (Figure 14A), but we will use anatomical means to separate Calb1+/Vglut2- from Vglut2+. Vglut2+ neurons are found in the lateral SNc (with a few in dorsal SNc) and project to posterior striatum (which includes the tail of the striatum), though a few axons can be found in more anterior dorso-lateral regions of striatum. Calb1+/Vglut2- neurons are found in dorsal SNc (and dorso-medial VTA), as well as in lateral SNc (these being Calb1+/Vglut2+), and project to medial and ventral striatum as well as posterior striatum. Because Vglut2+ neurons do not project to medial and ventral striatum, we can conclude that these axons come from Calb1+/Vglut2- neurons, and thus recording from these areas in Calb1+ mice allows us to separate Calb1+/Vglut2- neurons from Vglut2+ neurons. Aldh1a1+ neurons on the other side are found in ventral SNc and project to dorsal and lateral striatum, while Anxa1+ neurons are found even more ventral in SNc and project more dorso-lateral in striatum (Figure 13, Figure 14).

To functionally characterize the different DA subtypes during locomotion, we used genetic strategies (see Methods for details) to isolate each subtype, then used fiber photometry to record GCaMP calcium transients from populations of striatal axons of isolated dopaminergic subtypes (~300 micron diameter volumes sampled across the striatal project regions) in head-fixed mice running on a treadmill (Figure 15A-B). Since the Vglut2+ subtype is contained within Calb1+, in

Figure 14: DA genetic subtypes display different signaling patterns during locomotion.

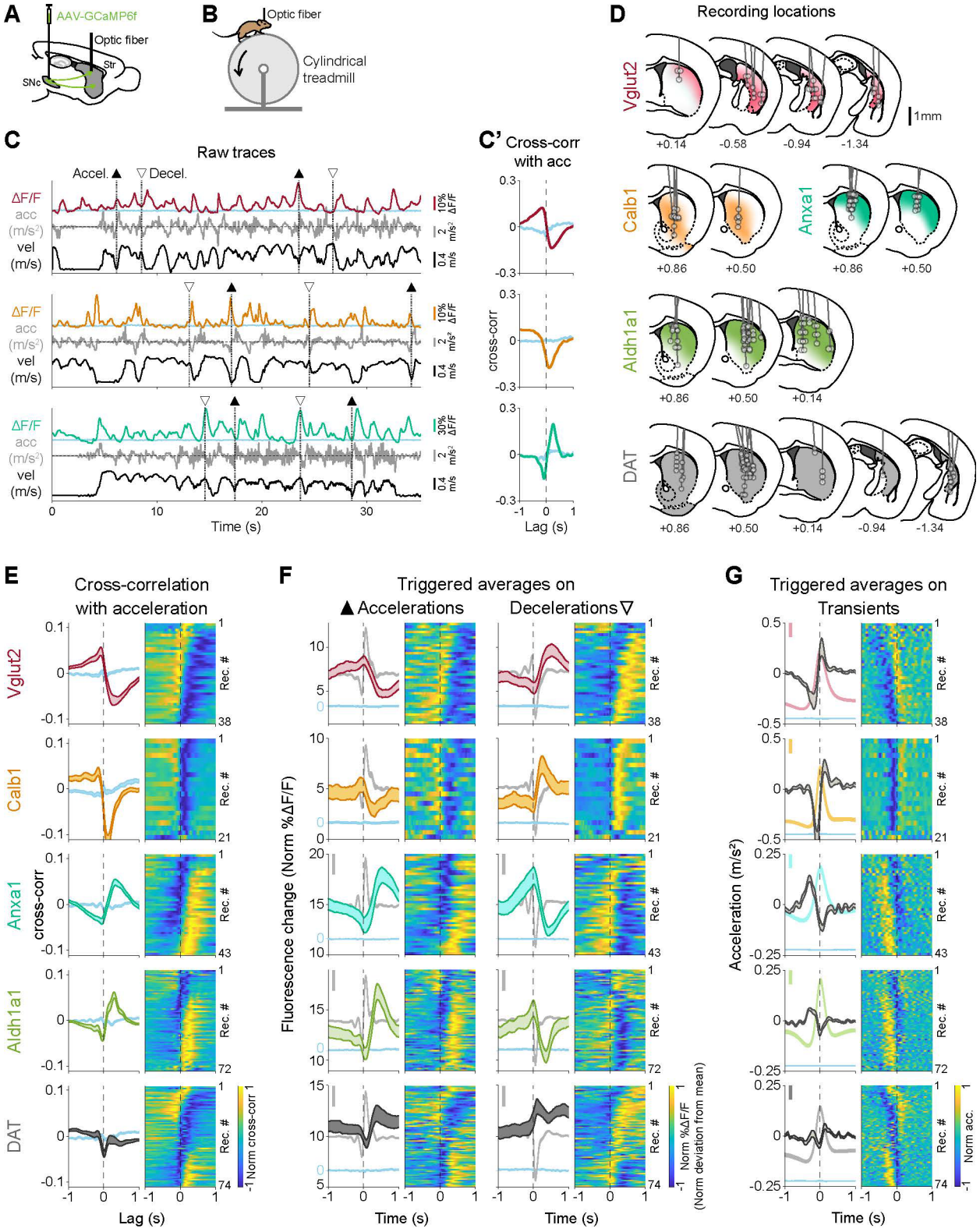

(**A**) Strategy used to label DA subtypes and record from their axons in striatum with GCaMP6f, a calcium indicator whose changes in fluorescence can be used as a proxy for DA release.

(**B**) Schematic of fiber photometry recording setup during locomotion on a cylindrical treadmill.

(**C**) Example recordings from each functionally homogeneous subtype studied, showing fluorescent traces (ΔF/F), mouse acceleration and velocity. Isosbestic control shown in blue. Large accelerations = ▲, large decelerations = ▽.

(**C'**) Cross-correlation between ΔF/F traces and acceleration for traces shown in C. Isosbestic control shown in blue.

(**D**) Recording locations in striatum for recordings shown in E-G. Shaded colors represent projection patterns for each subtype and DAT (subtypes indiscriminately labelled).

(**E**) Average cross-correlation between ΔF/F traces and acceleration for all recordings of each subtype and DAT. Isosbestic control shown in blue. Shaded regions denote mean ± s.e.m. Heatmap shows cross-correlation for each recording, sorted by PC1/PC2 angle (see Figure 16). Vglut2 mice = 11, n = 38 recordings; Calb1 mice = 5, n = 21; Anxa1 mice = 7, n = 43; Aldh1a1 mice = 13, n = 72; DAT mice = 14, n = 74.

(**F**) ΔF/F averages triggered on large accelerations (left, ▲) and large decelerations (right, ▽) for all recordings of each subtype and DAT. Isosbestic control shown in blue, same scale as ΔF/F average but shifted for visibility. Acceleration shown in gray in background (scale bar = 0.2 m/s^2). Shaded regions denote mean ± s.e.m. Heatmap shows triggered average for each recording, sorted as in E.

(**G**) Acceleration averages triggered on ΔF/F transient peaks for all recordings of each subtype and DAT. ΔF/F average and isosbestic control shown in background (bar = 5% Norm ΔF/F). Shaded regions denote mean ± s.e.m. Heatmap shows triggered average for each recording, sorted as in E.

---

our Calb1+ recordings we avoided recording from the posterior striatum where Vglut2+ neurons project, thus our Calb1+ recordings come largely from Calb1+/ Vglut2- neurons.

Remarkably, we observed distinct functional responses in DA neuron subtypes. Calb1+ and Vglut2+ axons preferentially signaled during locomotion decelerations, while Anxa1+ axons preferentially signaled during locomotion accelerations (Figure 15C), similarly to Aldh1a1+ "Type 1". Accordingly, cross-correlations between calcium ΔF/F traces (ΔF/F traces) and acceleration revealed a deep trough at positive time lags for Calb1+ and Vglut2+ axons (indicative of calcium transients following decelerations), but a large peak at positive lags for Anxa1+ axons (transients following accelerations) (Figure 15C'), and this was consistent across a wide range of striatum locations (Figure 15D-E). The opposing signaling patterns of Calb1+ and Vglut2+ vs Anxa1+ was also clear in ΔF/F averages triggered on accelerations or decelerations (Figure 15F)

and acceleration averages triggered on ΔF/F transient peaks (Figure 15G). In contrast, in DAT mice where subtypes were indiscriminately labelled, heterogeneous signaling was observed across striatal recording locations (Figure 15E-G bottom) and to a lesser extent in Aldh1a1+ (Figure 15E-G).

Interestingly, signaling differences were also evident between Vglut2+ and Calb1+ in their timing with respect to decelerations, with Calb1+ transients following decelerations with a shorter lag than Vglut2+ (Figure 16A). To further quantify such differences, we used a dimensionality reduction technique to extract the components that best explain the variance in the cross-correlations. We applied principal component analysis (PCA) to the matrix of all cross-correlation traces from Vglut2+, Calb1+, and Anxa1+ subtypes (only those subtypes that are functionally homogeneous, see Methods), finding that the first two principal components (PC1 and PC2) explained 85% of the variance in the cross-correlations (64% PC1 and 21% PC2). We observed that different combinations of PC1 and PC2 closely approximated the cross-correlation averages of the different subtypes: $PC1^{+} + PC2^{-}$ for Anxa1+, $PC1^{-} + PC2^{-}$ for Calb1+, and $PC1^{-} + PC2^{+}$ for Vglut2+ (Figure 15C). Accordingly, the decomposition of each recording along these principal components revealed distributions that were well separated between the subtypes (Figure 15D). Particularly, subtypes were well differenced by the PC1/PC2 angle, which represents the time-course of the cross-correlations and thus the temporal relationship between ΔF/F and acceleration (mean angles = 141° for Vglut2+, 218° for Calb1+, 244° for Anxa1+; p-values = 5×10^{-07} V-C, 1×10^{-10} V-A, 3×10^{-06} C-A, Wilcoxon rank-sum test with Bonferroni correction). Cross-correlations from DAT recordings decomposed using the same principal components were spread across the same regions of the PC1/PC2 space as individual subtypes, and areas in between (Figure 15D-E, dark grey). Furthermore, decomposing Aldh1a1+ recordings showed that, while most recordings

Figure 15: Quantitative analysis of locomotion signaling differences

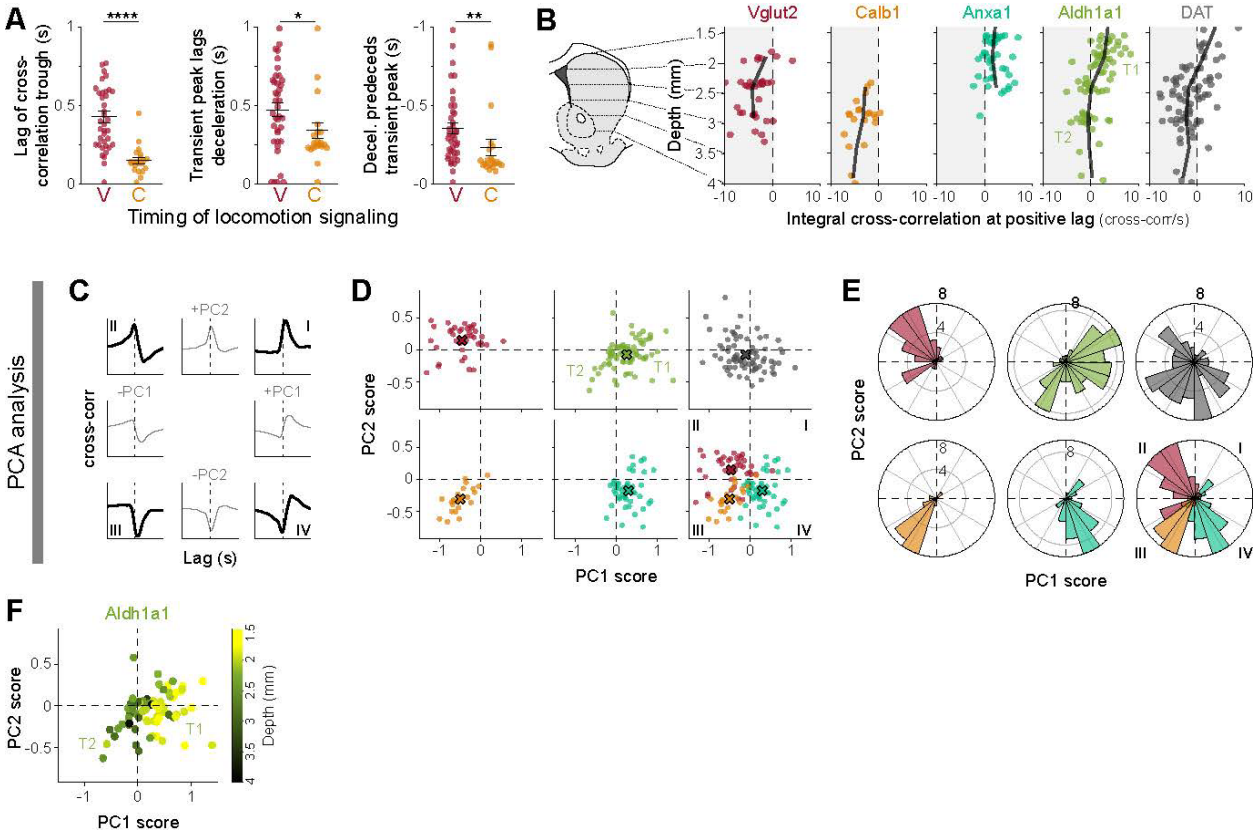

(**A**) Timing analysis showing that in Calb1+ neurons calcium transients follow decelerations with a shorter and less variable lag than in Vglut2+ neurons, by quantifying the lag of the trough in the ΔF/F-acceleration cross-correlations for each recording (mean Vglut2 = 0.43, Calb1 = 0.15; p-value for comparison = 6 x10^{-07} Wilcoxon rank-sum test with Bonferroni correction), the timing of the calcium transient peak in triggered averages on decelerations (means V = 0.35, C = 0.23; p-val = 0.02), and the timing of the deceleration peak in triggered averages on calcium transients (means V = 0.47, C = 0.34, p-val = 0.001).

(**B**) Distribution of locomotion response (integral of the cross-correlation at positive lags) along the dorso-ventral axis of striatum for all subtypes studied and DAT showing that, unlike Aldh1a1+ and DAT, Vglut2+, Calb1+ and Anxa1+ do not show a depth-dependent change in locomotion signaling. Black line represents moving average (0.5 mm bins).

(**C-D**) Principal component analysis conducted on ΔF/F-acceleration cross-correlations for all striatal recordings from Vglut2, Calb1, and Anxa1 subtypes (all functionally homogeneous subtypes).

(**E**) Different combinations of PC1 and PC2 loadings representing the different quadrants shown in F-G. Together PC1 and PC2 account for 85% of variance of all cross correlations (PC1 = 63.7% of variance, PC2 = 21.0%).

(**F**) Principal component scores for each recording of each subtype and DAT along PC1 and PC2. X shows mean for each subtype.

(**G**) Radial histogram showing the PC1/PC2 angle of each recording in K. p-values for comparison between subtypes Vglu2-Calb1 = 5 x10^{-07}, Vglu2-Anxa1 = 1 x10^{-10}, Calb1-Anxa1 = 3 x10^{-06} (Wilcoxon rank-sum test with Bonferroni correction).

(**H**) Same as F but each Aldh1a1+ recording is color-coded by depth within striatum, showing that Aldh1a1+ axons deeper in striatum show similar locomotion signaling to Calb1.

fall within that same region as Anxa1+ recordings, a subset of them fall in the same region as Calb1+ (Figure 15D-E), and color coding them by depth further demonstrates that it is more ventral striatum Aldh1a1+ axons that have Calb1-like signaling (Figure 15D-E).

Overall, these findings demonstrate that during locomotion Calb1+, Vglut2+ and Anxa1+ dopamine neuron subtype axons displayed different average functional signaling patterns; Calb1+ and Vglut2+ axons were largely deceleration correlated with unique timing differences between these subtypes, while Anxa1+ axons were largely acceleration correlated.

3.4.1. Differences between subtypes are not due to behavioral variability

While we found stark differences in locomotion signaling across subtypes, different mouse lines were used for each study, and it some mouse lines can show significant behavioral differences[130,131]. Thus, it could be possible that the observed signaling differences are due to behavioral differences that we cannot capture through our treadmill velocity readout (for example due to differences in gait).

To address this possibility, we can take advantage of the fact that the axons of two subtypes, Vglut2+ and Anxa1+, account for the majority of projections in two anatomically distinct regions, posterior and dorsal striatum respectively. Thus, we labelled all DA subtypes by injecting a Cre dependent GCaMP virus into the SNc of a DAT-Cre mouse and record in dorsal and posterior striatum simultaneously (Figure 17A). This way, we can compare the signaling of Anxa1+ axons vs Vglut2+ axons in the same mouse during the same behavior. As expected, we observed the same signaling pattern in this simultaneous experiment as with isolated subtypes, with dorsal striatal axons showing acceleration-locked signaling that matches Anxa1+ signaling, while posterior striatum axons show deceleration-locked signaling that matches Vglut2+ signaling

(Figure 17B-C). This confirms that the signaling differences that we observed between subtypes (Figure 15) are not due to differences in behavior.

Figure 16: Different signaling during locomotion is not due to behavioral differences

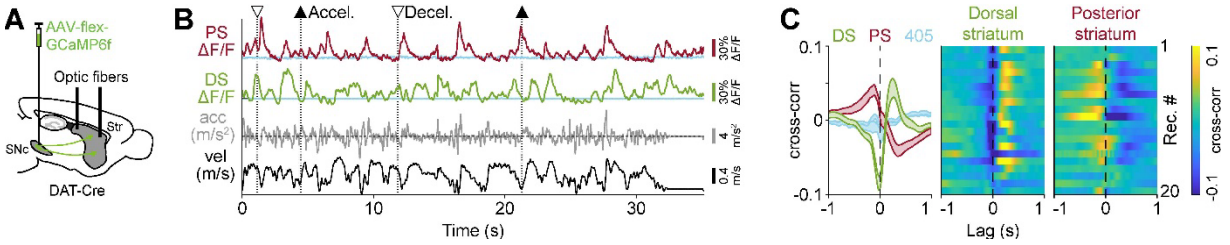

(**A**) Strategy used to label all DA subtypes in DAT-Cre mice with GCaMP, but record only from axons in dorsal striatum (where Anxa1+ axons predominate) and in posterior striatum (where Vglut2+ axons predominate) simultaneously with two optic fibers.

(**B**) Example recording showing fluorescent traces (ΔF/F) from dorsal striatum (DS) and posterior striatum (PS), mouse acceleration and velocity. Isosbestic controls shown in blue. Large accelerations = ▲, large decelerations = ▽.

(**C**) Average cross-correlation between acceleration and ΔF/F traces for simultaneous recordings from DS and PS. Isosbestic controls shown in blue. Shaded regions denote mean ± s.e.m. Heatmaps shows cross-correlation for each recording from DS and PS, randomly sorted. Mice = 7, n = 20 recordings.

3.4.2. Locomotion responses before and after rewards

Most commonly, DA neuron's locomotion signaling has been studied in contexts where rewards were available, either as a positive reinforcement for a particular action studied[2,113] or as an independent stimulus to simultaneously study locomotion and reward-related response[5,7]. Thus, it has been proposed that seemingly locomotion-locked responses could actually reflect reward expectation or motivation[30,132].

To determine whether the locomotion-locked signals observed in different DA subtypes is due to or modified by reward availability, we first recorded from each subtype in the absence of rewards (with mice never having experienced rewards in the experimental context) and then recorded again while the mice were receiving rewards on the treadmill (having been trained with rewards for at

least one session before) (Figure 18A). We observed that, while Anxa1+ neurons showed no change in locomotion signaling between before and after reward delivery, both Calb1+ and Vglut2+ showed greater responses during locomotion, as indicated by a higher average deceleration triggered on transients (Figure 18B, E) and a greater amplitude in the cross-correlation between ΔF/F and acceleration (Figure 18C). This suggest that Anxa1+ has a pure locomotion-locked signaling that is not affected by reward context, while in Calb1+ and Vglut2+ subtypes it is modified by reward availability. Nonetheless, it is important to note that locomotion signaling is still present in the Vglut2 and Calb1+ subtypes ever before rewards were ever present, and thus these responses cannot be purely reward related.

It is important to note however, that reward context somewhat changes the behavior of the animals. For example, mice lick sporadically (possibly to check for reward availability due to its unpredictability), and they often decelerate to lick. And, as we have mentioned before, mouse lines can show significant behavioral differences[130,131], so it is possible that changes in behavior are behind the changes in signaling. As a coarse measure of behavior, we calculated the autocorrelation of the acceleration traces for each recording and did indeed find differences between before and after rewards in Vglut2 and Calb1 mice that were not apparent in Anxa1 mice (Figure 18D), which could explain the signaling differences in the first two subtypes. However, to fully address this question, this experiment should be repeated in a similar way to Figure 17: by labelling all DA neurons and simultaneously recording in posterior striatum (mostly Vglut2+ axons) and dorsal striatum (mostly Anxa1+ axons) before and after rewards. Given that the same mice would be used to simultaneously study two subtypes, behavioral changes will be identical and thus any differences in signaling must be due to neuronal differences.

Figure 17: Locomotion responses of Calb1 and Vglut2 but not Anxa1 subtypes are modulated by reward context

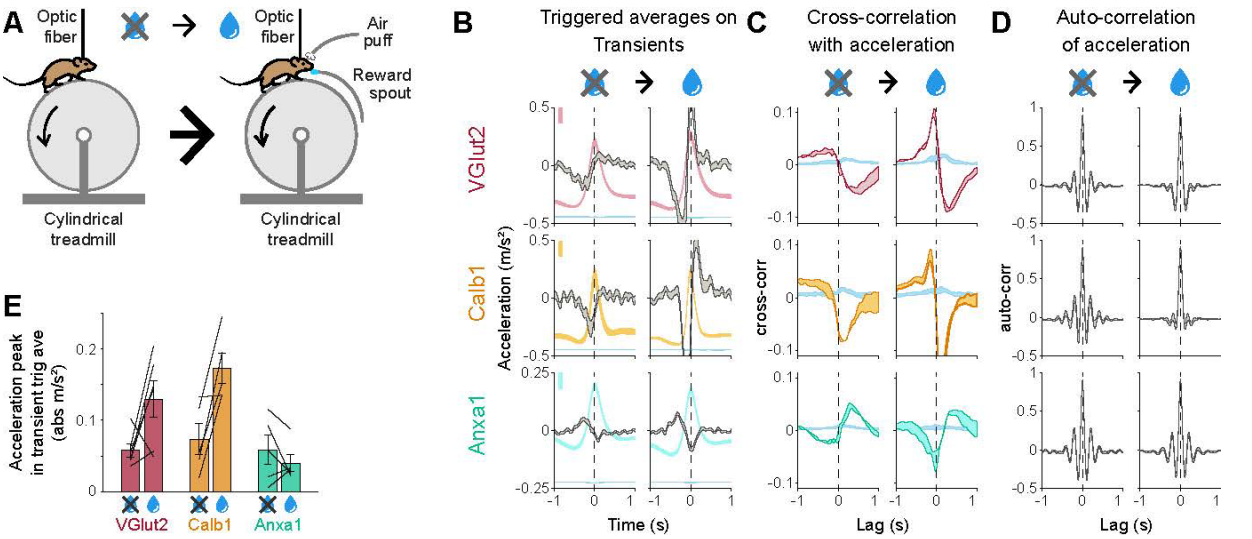

(**A**) Mice first ran on the treadmill with no rewards having ever been received, and later they were exposed to rewards (and air puffs) on the same treadmill.

(**B**) Triggered averages on large transients for all recordings of Vglut2+, Calb1+, and Anxa1+ subtypes before and after rewards were present. ΔF/F average and isosbestic control shown in the background (scale bar = 5% Norm ΔF/F). Shaded regions denote mean ± s.e.m.

(**C**) Average cross-correlation between ΔF/F traces and acceleration for all recordings of each subtype before and after rewards were present. Isosbestic control shown in light blue. Shaded regions denote mean ± s.e.m.

(**D**) Average auto-correlation for acceleration traces for all recordings of each subtype before and after rewards were present. Shaded regions denote mean ± s.e.m.

(**E**) Change in the amplitude of peak acceleration triggered on large transients before and after rewards (as shown in B) averaged per mouse. Black lines represent change in amplitude for individual mice. Error bars denote mean ± s.e.m.

3.5. Subtypes show different responses to rewards and aversive stimuli

We then asked whether DA subtypes respond differently to rewards and aversive stimuli. We randomly delivered unexpected water rewards and aversive air puffs to the whiskers/face to mice already habituated to run on the treadmill (Figure 19A), and again used fiber photometry to record ΔF/F transients from populations of axons at different striatal locations (Figure 19B). We found that both Calb1+ and Vglut2+ axons responded robustly to rewards (Figure 19C-E, G; 0.5s

cumulative response: mean = 7.9 and 13.4 Norm %ΔF/Fs, p-values = 2 $x10^{-04}$ and 2 $x10^{-04}$, respectively, Wilcoxon Signed Rank test with Bonferroni correction) and air puffs (Figure 19C, F-G; 0.5s cumulative response: mean = 15.3 and 6.4, p-values = 1 $x10^{-04}$ and 2 $x10^{-04}$, respectively) consistently across nearly all recording locations. The reward signaling in Calb1+ and Vglut2+ axons could not be explained by their responses to mouse movement during reward delivery, as similar results were obtained for reward delivery during rest (Figure 19J-K). For air puffs however, it was not possible to exclude this possibility since mice invariably moved in response to the aversive stimulus.

In contrast, unexpected reward responses were not detectable from Anxa1+ axons (Figure 19C-E, G; 0.5s cumulative response: mean = -0.4, p-value = 0.3, not significant), even though they were licking to consume the reward similarly to Calb1 and Vglut2 mice (Figure 19D); but they did respond to air puffs with a signaling decrease (Figure 19C, F-G; 0.5s cumulative response: mean = -3.0, p-value = 2 $x10^{-05}$), though again this response could have been due to mouse movement. Similarly, Anxa1+ did not respond to rewards at rest (Figure 19J-K). 3 of 39 Anxa1+ recordings locations displayed a small increase in ΔF/F post-reward (Figure 19J, Anxa1+, bottom rows), however these were likely movement responses since no increases were observed when rewards were delivered at rest (Figure 19J-K). Furthermore, both DAT and Aldh1a1+ showed a mixture of responses, where some recordings showed responses to rewards and air puffs (similarly to Calb1+) while other did not (similarly to Anxa1+), as expected of a mixture of subtypes (Figure 19D-F bottom). Importantly, Aldh1a1+ shows a greater proportion of Anxa1+ like responses, as expected from an enrichment in Anxa1+ neurons in this labelling scheme compared to DAT.

Interestingly, while the Vglut2+ and Calb1+ subtype axons both responded to rewards and air puffs, their responses still differed. Vglut2+ axons displayed larger responses to air puffs than

Figure 18: DA subtypes show different responses to rewards and aversive stimuli.

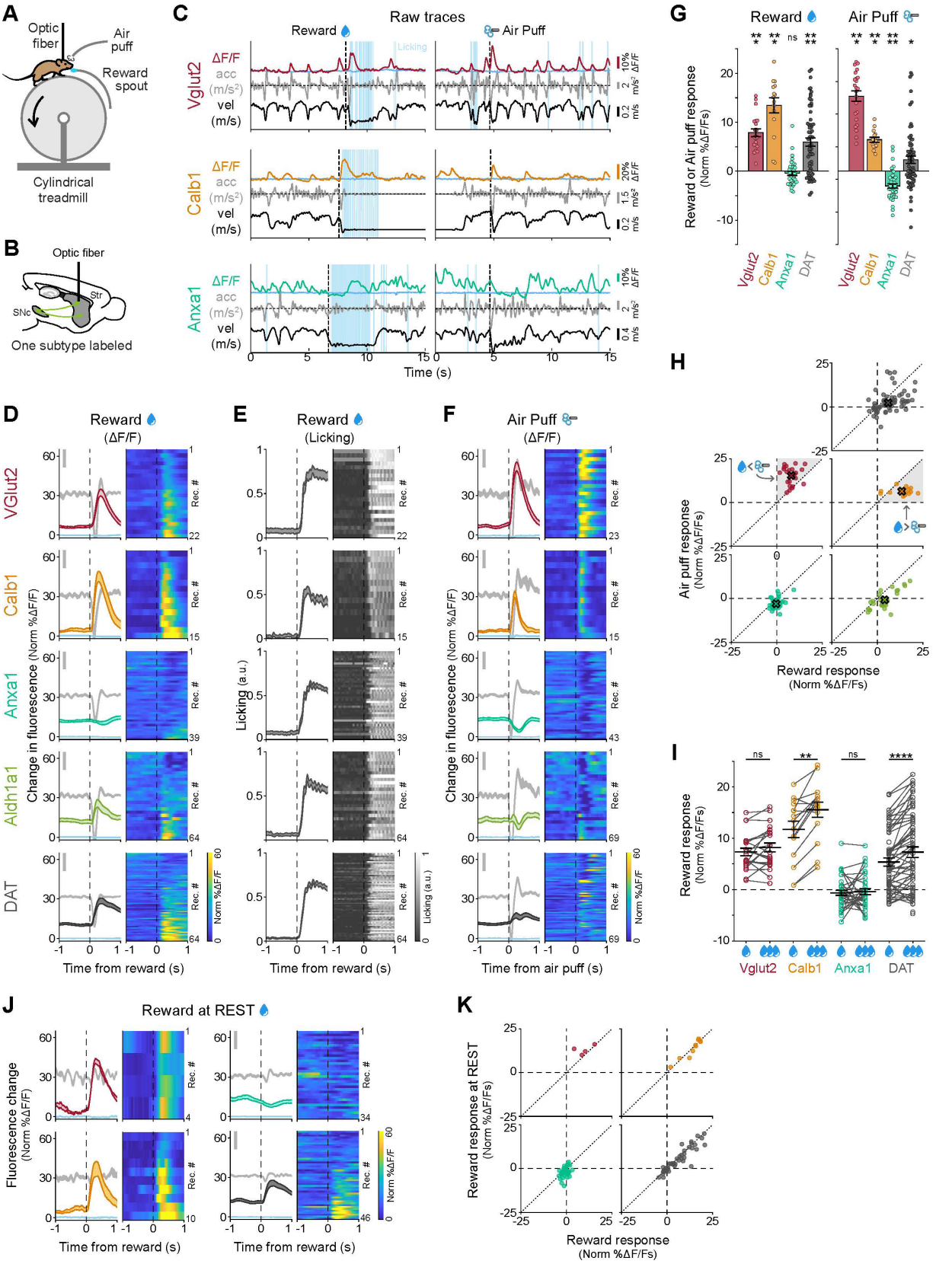

(**A**) Mouse running on treadmill during fiber photometry while receiving unexpected rewards and air puffs.

(**B**) Schematic of fiber photometry recording strategy.

(**C**) Example recordings for each functionally homogeneous subtype studied, showing fluorescence traces (ΔF/F), mouse velocity, acceleration, licking, and reward (left) or air puff (right) delivery times. Isosbestic controls in light blue, same scale as ΔF/F traces. Reward and Air puff examples for each subtype are from the same recording.

(**D**) ΔF/F averages triggered on reward delivery times for all recordings of each subtype and DAT. Isosbestic control in light blue, same scale as ΔF/F average. Acceleration shown in gray in background (scale bar = 0.2 m/s^2). Shaded regions denote mean ± s.e.m. Heatmaps show triggered average for each recording, sorted by size of reward response. Vglut2 mice = 10, n = 22 recordings; Calb1 mice = 7, n = 15; Anxa1 mice = 6, n = 39; Aldh1a1 mice = 7, n = 27; DAT mice = 12, n = 64.

(**E**) Licking average triggered on reward delivery times for all recordings of each subtype and DAT (as D). Shaded regions denote mean ± s.e.m. Heatmap shows triggered average for each recording, sorted as in D.

(**F**) ΔF/F averages triggered on air puff delivery times for all recordings of each subtype and DAT. Isosbestic control in light blue, same scale as ΔF/F average. Acceleration shown in gray in background (scale bar = 0.2 m/s^2). Shaded regions denote mean ± s.e.m. Heatmap shows triggered average for each recording, sorted by reward size as in D,E. Vglut2 mice = 11, n = 23 recordings; Calb1 mice = 7, n = 15; Anxa1 mice = 7, n = 43; Aldh1a1 mice = 7, n = 27; DAT mice = 12, n = 69.

(**G**) Average reward and air puff responses for each subtype except Aldh1a1+ (integral of fluorescence in a 0.5 s window after stimulus minus integral in 0.5 s before stimulus). Error bars denote ± s.e.m. Means and p-values for reward: Vglut2 m = 7.9 Norm ΔF/Fs, p = 2 $x10^{-04}$; Calb1 m = 13.4, p = 2 $x10^{-04}$; Anxa1 m = -0.4, p = 0.3 (not significant); DAT m = 6.0, p = 5 $x10^{-07}$. Means and p-values for air puff: Vglut2 m = 15.3, p = 1 $x10^{-04}$; Calb1 m = 6.4, p = 2 $x10^{-04}$, Anxa1 m = -3.0, p = 2 $x10^{-05}$; DAT m = 2.3, p = 0.02. Wilcoxon signed-rank test with Bonferroni correction.

(**H**) Reward vs air puff responses for all recordings of each subtype and DAT. X shows mean for each subtype. Shaded regions are areas representing greater air puff than reward response (for Vglut2) or greater reward vs air puff response (for Calb1). Aldh1a1+ recordings fall within the Anxa1+ or Calb1+ regions.

(**I**) Comparison of responses to small vs large rewards for each subtype. Error bars denote mean ± s.e.m. Mean difference and p-values: Vglut2 m = 0.9 Norm ΔF/Fs, p = 0.2 (not significant); Calb1 m = 3.8, p = 2 $x10^{-04}$; Anxa1 m = 0.2, p = 1 (not significant); DAT m = 1.9, p = 7 $x10^{-06}$. Paired Wilcoxon Signed Rank test with Bonferroni correction.

(**J**) ΔF/F averages triggered on rewards delivered during rest. Isosbestic control in light blue, same scale as ΔF/F average. Acceleration shown in gray in background (scale bar = 0.2 m/s^2). Shaded regions denote mean ± s.e.m. Heatmaps show triggered average for each recording, sorted by size of reward response. Vglut2 mice = 3, n = 4 recordings; Calb1 mice = 7, n = 10; Anxa1 mice = 6, n = 34; DAT mice = 11, n = 46.

(**K**) Comparison between the response to rewards at rest (J) vs the response to all rewards (D) for each recording of each subtype (except Aldh1a1+) and DAT. Diagonal dotted line represents identity line (same response to rewards at rest vs all).

---

reward while Calb1+ axons displayed larger responses to rewards than air puffs (Figure 19H). Furthermore, Calb1+ axons displayed larger responses to increased reward size–a hallmark of reward prediction error (RPE)[3,133]. This response increase was not detectable from Vglut2+ axons

(Figure 19I). Thus, these results further highlight the functional diversity within these subtypes: Vglut2+ axons displayed a greater response to aversive stimuli than rewards, Calb1+ axons displayed greater response to rewards than aversive stimuli and was robustly sensitive to reward size, while reward responses were not detectable from Anxa1+ axons, which instead displayed a signaling decrease to aversive stimuli.

3.5.1. DA released at rewards and air puffs matches GCaMP signaling

As we have explained (and will discuss in detail in chapter 5.2.2), GCaMP is ideal to study signaling differences between genetically identified subtypes of DA neurons. In the axons, it can be used as a proxy for DA release (all known mechanisms for DA release involve changes in calcium[37,119–126,134]), while avoiding contamination from unlabeled DA subtypes. However, the relationship between DA release and GCaMP signaling hasn't been comprehensively studied, and it thus remains possible that the GCaMP transients we observe are not matched by release of DA.

To test this, we used the DA indicator $GRAB_{DA}$[135] to measure extracellular changes in DA concentration in regions of striatum where axons from different subtypes predominate: dorsal striatum (Anxa1+), posterior striatum (Vglut2+) and mid-ventral striatum (Calb1+, although here there is a greater mixture of subtypes). We injected a $GRAB_{DA}$ AAV virus into these different regions in wild-type mice, and recorded using the same fiber photometry methods as used for GCaMP recordings (Figure 20A).

As expected, we saw no or small reward and air puff responses in dorsal striatum, matching Anxa1+ GCaMP signaling; strong reward and small air puff responses in mid-ventral striatum, matching Calb1+ signaling; and smaller reward and large air puff responses in posterior striatum, matching Vglut2+ signaling (Figure 20B). While we did detect very small reward responses in

dorsal striatum, this is probably due to contamination from DA released from few Calb1+ axons in the area, highlighting the importance of separating DA subtypes to accurately characterize their functional responses. Still, in the same session and mice we recorded from dorsal striatum and then more ventral regions along the same fiber path, and found greater reward and air puff responses in ventral locations (Figure 20C), consistent with an increase in the proportion of Calb1+ axons vs Anxa1+ axons. As for locomotion, previous work has observed acceleration-locked signaling in dorsal striatum using DA sensors[136], matching GCaMP signaling in Anxa1+ neurons. Together, this all shows that indeed DA release matches GCaMP signaling, confirming that GCaMP transients can be used as proxy for DA release and that the signaling differences across subtypes does translate into differences in DA release.

Figure 19: DA release in responses to rewards and air puffs matches GCaMP signaling

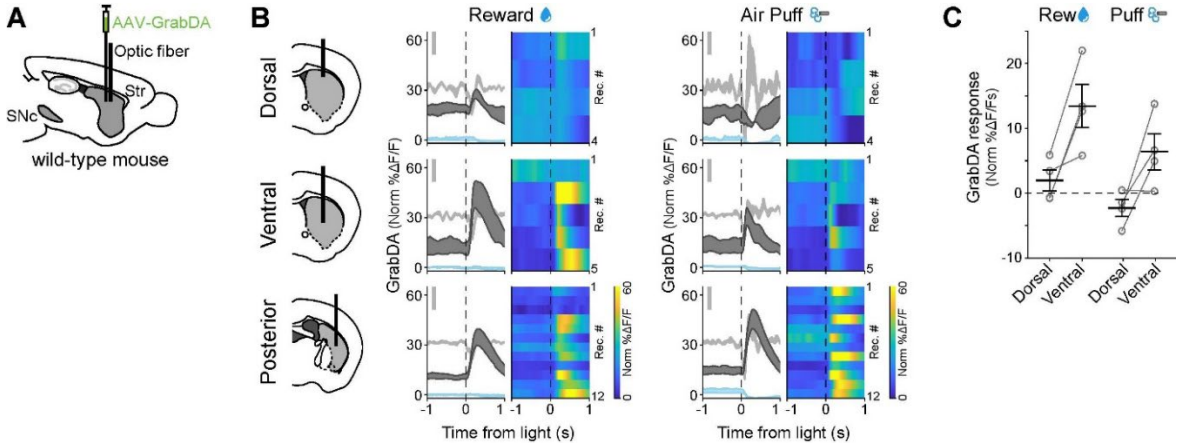

(**A**) Schematic of labelling and fiber photometry recording strategies. Wild-type mice were injected into the striatum with a GrabDA virus. The recording fiber was then placed into the same injection location to record DA transients coming from all DA axons in the area (subtype nonspecific).

(**B**) (Left) Schematic or recording locations in dorsal, vid-ventral, and posterior striatum. (Middle) GrabDA ΔF/F averages triggered on reward delivery times. (Right) GrabDA ΔF/F averages triggered on air puff delivery times. Isosbestic control in light blue, same scale as ΔF/F average. Acceleration shown in gray in background (scale bar = 0.2 m/s^2). Shaded regions denote mean ± s.e.m. Heatmaps show triggered average for each recording, randomly sorted but with Air puff heatmap sorting matching Reward heatmap sorting. Mice: dorsal = 4, ventral = 5, posterior = 5.

(**C**) Comparison of responses to rewards and air puffs in dorsal vs ventral striatum within the same mice (each pair of dots is one mouse), showing how more ventral recordings show stronger responses to rewards and air puffs compared to dorsal striatum. Error bars denote mean ± s.e.m. Mice = 5.

3.5.2. All subtypes respond to neutral light stimuli

While we have shown that different subtypes show different responses to rewarding and aversive stimuli, in our experimental design we also included a putatively neutral stimulus, a blue light flash in front of the mouse (Figure 21A). All subtypes seemed to similarly respond to this stimulus (Figure 21B), though triggered averages show that Vglut2+ neurons seem to show a more sustained response than Calb1+ neurons, and Anxa1+ even more (Figure 21C). This stimulus did cause the mouse to decelerate slightly (as seen by the acceleration traces in the background of Figure 21C), but this is similar across mice and subtypes. When we plotted the response to rewards vs light (Figure 21D), we found no relationship between the two in any subtype.

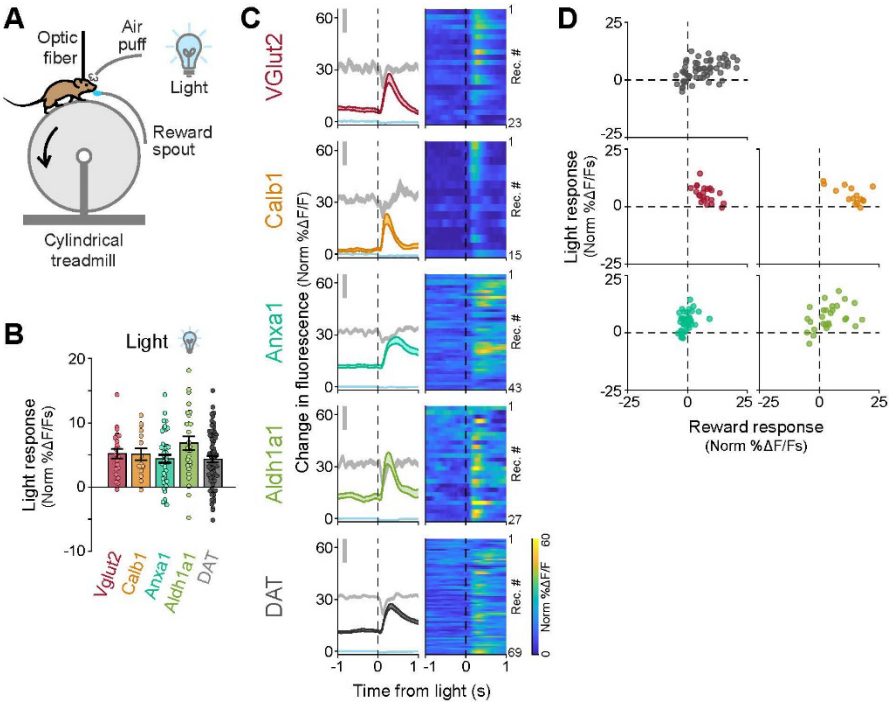

Figure 20: All DA subtypes respond to neutral light stimuli

(**A**) Mouse running on treadmill during fiber photometry while receiving unexpected light stimuli.

(**B**) Average light responses for each subtype (integral of fluorescence in 0.5 s window after stimulus minus integral in 0.5 s before stimulus). Error bars denote ± s.e.m. Means: Vglut2 = 5.2 Norm ΔF/Fs; Calb1 = 5.1; Aldh1a1 = 6.8; Anxa1 = 4.4; DAT = 4.3.

(**C**) ΔF/F averages triggered on light onset time for all recordings of each subtype and DAT. Isosbestic control in light blue, same scale as ΔF/F average. Acceleration shown in gray in background (scale bar = 0.2 m/s^2). Shaded regions denote mean ± s.e.m. Heatmaps show triggered average for each recording, sorted by size of reward response. Vglut2 mice = 11, n = 23 recordings; Calb1 mice = 7, n = 15; Anxa1 mice = 7, n = 43; Aldh1a1 mice = 7, n = 27; DAT mice = 12, n = 69.

(**D**) Reward vs light responses for all recordings of each subtype and DAT.

3.6. Subtype identity determines functional responses beyond anatomy

While the observable differences in functional responses from different subtypes is remarkable, it is possible that these differences were be determined by the anatomical location of recording rather than the genetic characteristics of the subtype. Given that dopaminergic axons projecting to different striatal locations have different functional responses[5,14,16,33,34,114,137,138] and that subtypes have axonal arbors biased to different regions of striatum, it is possible that, rather than subtypes determining function, location determines function and subtypes just help separate location.

To distinguish between these two hypotheses, we compared recordings from two subtypes with overlapping axons (Calb1+ and Anxa1+) made only in the region of overlap (mid depth, mid medio-lateral striatum) (Figure 22A left). In agreement with subtypes determining function and not location, recordings from Anxa1+ in this area showed clear acceleration-locked signaling, no reward responses, and a small decrease in ΔF/F in response to aversive stimuli, while recordings from Calb1+ in this same area showed deceleration-locked signaling and strong responses to rewards and air puffs (Figure 22A).

Another region where different subtypes overlap is their somas in SNc which, while anatomically biased to different regions of SNc, are too close together for the spatial resolution of fiber photometry. Thus, recordings from different subtypes in SNc can also serve to answer whether genetic identity or anatomical location of projection determines the functional characteristics of a neuron. As we will see in Chapter 4 section 4.2, recordings from subtypes in SNc also show functional differences (Figure 30, Figure 31) that match each subtypes' axons (Figure 32), confirming that it is the genetic identity of a neuron that determines it's functional properties.

Figure 21: Subtype identity determines functional properties beyond anatomy

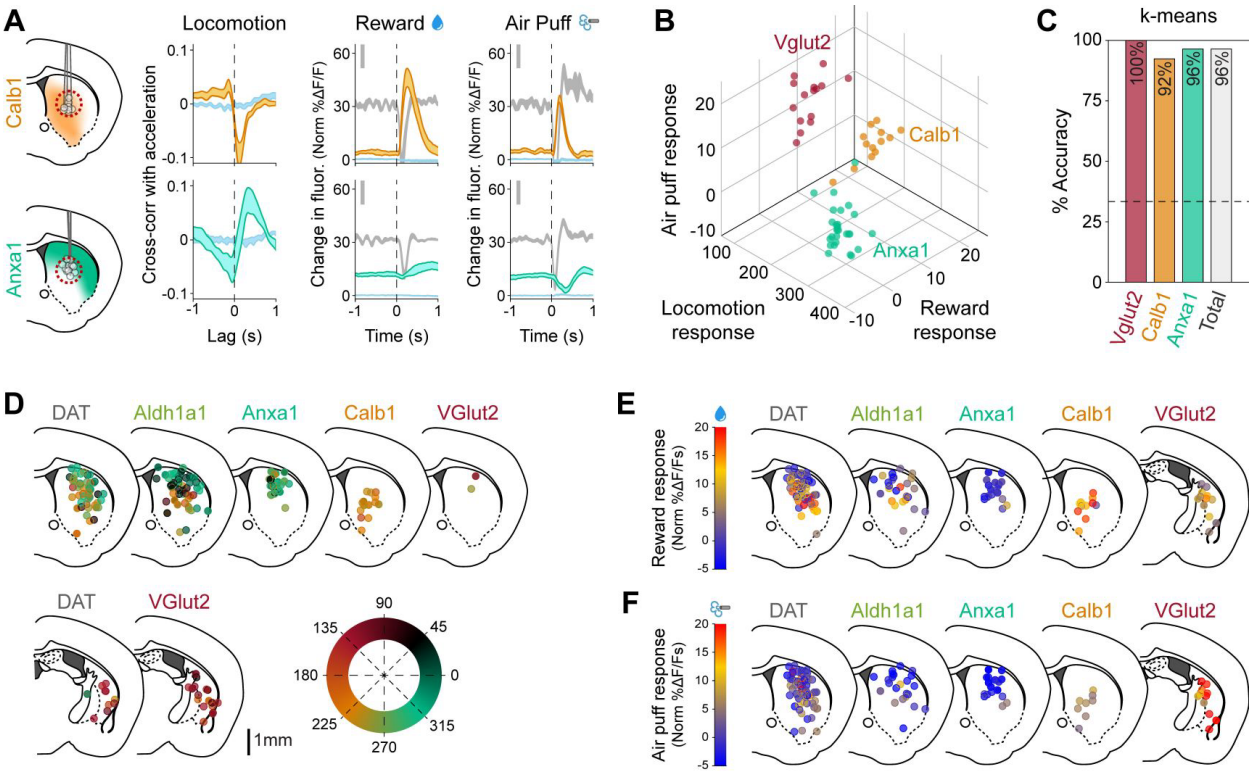

(**A**) Comparison of locomotion (cross-correlation between ΔF/F and acceleration), reward and air puff responses for Calb1 and Anxa1 recordings only from a region of striatum where their axons overlap (dashed red circle, left). Isosbestic controls in blue. Shaded regions denote mean ± s.e.m. Locomotion: Calb1 mice = 4, n = 12 recordings, Anxa1 mice = 4, n = 7. Reward and air puff: Calb1 mice = 3, n = 8 recordings, Anxa1 mice = 5, n = 15.

(**B**) 3D plot showing locomotion (PC1/PC2 angle, see Figure 16I), reward and air puff responses for each recording and each subtype.

(**C**) Unsupervised k-means classification distinguished subtypes based on locomotion (PC1 and PC2 scores), reward, and air puff responses, with total accuracy of 96%: 15/15 Vglut2, 12/13 Calb1 and 27/28 Anxa1 recordings correctly classified. Dashed line represents chance accuracy (33%).

(**D**) Locomotion response (PC1/PC2 angle, as shown in Figure 16E) mapped onto recording location for each subtype and DAT. Locations from the body (top) or the tail of the striatum (bottom) were collapsed into a single brain section. To reduce overlap, locations were shifted a random amount between ±0.4mm mediolaterally.

(**E**) Reward response mapped onto recording locations for each subtype and DAT. Locations from the body or the tail of the striatum were collapsed into a single brain section. To reduce overlap, locations were shifted a random amount between ±0.4mm mediolaterally.

(**F**) Same as E but for air puff response.

Furthermore, to explicitly demonstrate the connection between functional and genetic dopamine neuron subtypes, we plotted the locomotion response (PC1/PC2 angles from Figure 16I), response to rewards and response to air puffs for the subset of recordings where all 3 measurements were made (Figure 22B). Calb1+, Vglut2+ and Anxa1+ recordings resided in separable regions of this 3D functional space, with minimal overlap – despite recordings being made throughout striatum (see Figure 15D). We then asked whether an unsupervised classification method, k-means clustering, could distinguish the subtypes based on these functional dimensions. Indeed, when searching for 3 clusters within the functional space, k-means separated the recordings into clusters that matched the genetic subtypes with 96% accuracy (Figure 22C; of note, random chance = 33% accuracy; 100% accuracy for Vglut2+, 92% for Calb1+, and 96% for Anxa1+). Thus, our findings establish a clear connection between functional responses and genetic dopamine neuron subtypes and demonstrate that genetically defined subtypes of striatonigral dopamine axons have, on average within a small recording volume, markedly different signaling patterns during locomotion, reward, and aversive stimuli.

Finally, we plotted the recording locations for each subtype color-coded based on each one's response to locomotion (Figure 22D), reward (Figure 22E), and air puff (Figure 22F), showing that regardless of location Vglut2+, Calb1+, and Anxa1+ recordings show uniform signaling properties. On the other hand, recordings from heterogeneous DAT mice (where all subtypes were simultaneously labelled) and Aldh1a1+ displayed similar responses to certain subtypes in particular locations (e.g. dorsal striatum recordings were similar to Anxa1+, and posterior striatum recordings to Vglut2+ in DAT, Figure 22D-F), suggesting that a single subtype dominated signaling within the photometry recording volume in these striatal regions. However, DAT and Aldh1a1+ recordings that displayed a different mixture of PCs than any particular subtype (e.g.

middle depth striatum) suggest that a mixture of subtype axons were contained within the recording volume (Figure 22D-F).

3.7. Anxa1+ shows higher transient frequency than Calb1+ and Vglut2+

One of the hypotheses proposed to explain the vulnerability of DA neurons in Parkinson's disease suggests that their high firing rates and the resulting fluctuations in intracellular calcium could be responsible[224]. Given this, we sought to determine whether there were differences in transient frequency across subtypes that could explain the differential vulnerability of some subtypes vs others. We calculated the transient frequency for and found that indeed Anxa1+ has a higher frequency than Calb1+ and Vglut2+ (Figure 23A, B), which could contribute to its selective vulnerability in Parkinson's (see chapter 5.5.2). As for Aldh1a1+ and DAT, they show even higher transient frequencies than Anxa1+ and with greater variability (Figure 23B), consistent with the summation of transients from mixed subtypes.

However, there are several issues with this calculation. On one hand, the methodology used to detect transients is highly dependent on the signal-to-noise ratio of the recording, with higher noise levels potentially obscuring smaller transients and thus resulting in lower apparent transient frequencies. In fact, there is a clear relationship between these two measures in our experiments (Figure 23D). This is important because recordings from Anxa1+ neurons have much higher signal-to-noise ratios than Calb1+ and Vglut2+ (Figure 23C), which could explain their higher transient frequencies. However, if we only look at the subset of Anxa1+ recordings with comparable signal-to-noise ratios to the Vglut2+ and Calb1+ recordings (grey shaded area in Figure 23D), Anxa1+ recordings still have a statistically significant and much higher transient frequency (Figure 23E), with a mean of 0.68 vs 0.44 and 0.47 transients per second, a 50%

increase. Furthermore, Anxa1+ is the only subtype with higher transient frequency during run periods than during rest (Figure 23F) – though it is a tiny difference and not very consistent.

Figure 22: Transient frequency differences between subtypes

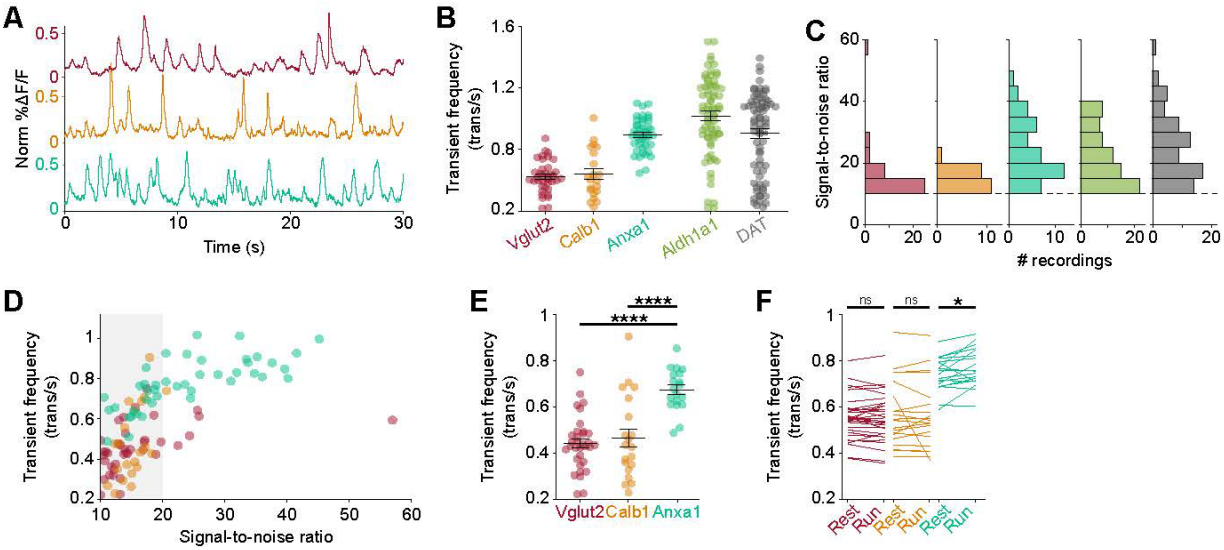

(**A**) Example recordings from Vglut2+, Calb1+, and Anxa1+ axons showing different transient frequencies at similar signal-to-noise ratios (18.9, 18.3, and 18.9 respectively).

(**B**) Calcium transient frequency for each recording of each subtype. Recordings from mixed subtypes (Aldh1a1+ and DAT) show higher frequency rates than isolated subtypes, as expected from the summation of transients from different subtypes.

(**C**) Signal-to-noise ratio for each recording of each subtype, showing higher values for Anxa1+ than Vglut2+ and Calb1+. In photometry recordings, the signal-to-noise ratio affects our ability to detect transients, and thus will affect measured transient frequencies. Recordings with signal-to-noise ratios below 10 (dashed line) were excluded from analysis (see Methods) and are thus not shown.

(**D**) Relationship between the measured transient frequency and signal-to-noise ratio for each recording of each homogeneous subtype. Grey region indicates the range of signal-to-noise ratios represented in all subtypes, used in E and F.

(**E**) Same as B but only for recordings with signal-to-noise ratios below 20 (represented in all subtypes), as show in grey in D, showing that at equivalent signal-to-noise ratios Anxa1+ still shows higher transient frequency. P-values: V-C = 1 (ns), V-Ax = 5×10^{-12}, C-Ax = 2×10^{-07} (Mann-Whitney U test with Bonferroni correction).

(**F**) Comparison between transient frequency during rest vs run periods for each homogeneous subtype (only signal-to-noise ratios below 10). P-Values: V = 1 (ns), C = 1 (ns), Ax = 0.03 (Paired Wilcoxon signed-rank test with Bonferroni correction).

On the other hand, these are population recordings and not single-cell recordings, so even in isolated subtypes transients represent the sum across multiple neurons. Thus, it is impossible to

conclude that neurons in one subtype have higher firing rates than others, as this could instead be a measure of synchrony within a subtype. Thus, even when accounting for signal-to-noise ratios, these results cannot be conclusive without single cell/axon experiments.

3.8. Discussion

Here, we first found functional heterogeneity within the well-known Aldh1a1+ subtype, which motivated our use of single-nucleus transcriptomics to refine the existing classification of dopamine subtypes and led to the discovery of a new subtype characterized by Anxa1 expression within the previously described SNc Aldh1a1+ subtype. We then isolated and recorded from this new Anxa1+ subtype, as well as the known Calb1+ and VGlut2+ subtypes, and found unique functional signaling patterns to rewards, aversive stimuli, accelerations and decelerations. We made two main findings. (i) While the Calb1+ and VGlut2+ subtypes robustly respond to unexpected rewards and aversive stimuli, such responses were not detected in the Anxa1+ subtype, even at striatal locations where its axons overlapped with the other subtypes. (ii) Acceleration- and deceleration-correlated responses were differentially observed in genetically distinct neurons. These findings establish a connection between functional responses and genetic subtypes of dopamine neurons across a range of functional dimensions, validating the behavioral relevance of molecular classification schemes.

Though we here found significant differences in functional responses between SNc dopamine subtypes across different midbrain and striatal regions, fiber photometry records the mean fluorescence signal from populations of axons or cell bodies in the ~300 micron recording volume. Thus, it is possible that some heterogeneity exists within the genetic subtypes at the single-cell/axon level. Nonetheless, similar signaling patterns to our reported averages have been

observed in single-cell[2,6–9,14,15,113] and single-axon[5] recordings. This suggests that the functional differences we observed between subtypes are due to the strong enrichment of particular functions at the single cell level for specific subtypes. Thus, genetic subtypes provide a tool to reproducibly access different dopamine neuron functions, which is particularly important given the literature's many conflicting observations/hypotheses on the role of dopaminergic neurons.

While the general assumption has been that all midbrain dopamine neurons respond to unexpected rewards, there has been scattered evidence against this dogma. A few single cell studies reported some SNc dopamine neurons that did not respond to rewards[6,139], and axonal imaging recordings in dorsal striatum found several single axons not encoding rewards[5]. However, other studies have found reward responses in similar regions[16,32,33]. Since we detected robust reward responses in Calb1+ and Vglut2+ neurons, but not in Anxa1+ neurons, and since these different subtypes have different midbrain distributions and striatal projection targets, our results may help explain the previous discrepancies; different subtype(s) may have been investigated based on the recording location in SNc or striatum. Further, our functional characterization of Vglut2+ neurons agrees with previous recordings from overlapping soma/axon regions that reported aversive stimuli and reward signaling [9,14,15], with insensitivity to reward-size[9,10]. Based on these properties, such neurons have been proposed to signal novelty or salience[14,15], or to reinforce avoidance of threatening stimuli[9]. Thus, of the three subtypes studied here that account for most SNc dopamine neurons, only Calb1+ neurons displayed robust reward size sensitivity, a hallmark of reward prediction error and involvement in positive reinforcement learning [3,133].

Previous research has reported that many SNc dopamine neurons signal at accelerations during a variety of motor tasks, but with differences in whether the neurons increase or decrease their firing at accelerations[2,5–8,113,115]. Since here we found that such signaling patterns were differentially

expressed by the different subtypes, and since their cell body and axon locations are anatomically biased, these previous discrepancies might also be explained by the unknowing recording of different subtype(s) across studies based on location. For example, recordings in more medial SNc/lateral VTA (Calb1+ location) found most neurons decrease their firing at accelerations and respond to rewards[7]; recordings from dorsal striatum axons (Anxa1+ axon location) found increases in signaling at accelerations and no detectable reward responses[5]; and recordings from a broader range of locations (and thus subtypes) in SNc found neurons with both increases and decreases of firing at accelerations[6]–all of which agree with our results when considering subtype anatomical distributions.

Numerous hypotheses have been proposed to explain the function of fast dopamine signaling during locomotion: some suggest they increase the probability of movement initiations or the vigor of movements[6,140], while others propose they function as a corollary discharge signal associated with particular reward-tied actions and involved in credit assignment[30] or motor learning[129,141]. Again however, these differences in results and interpretations may lie in which dopamine neuron subtypes were recorded or manipulated in previous studies–for example, the former idea is supported by the optogenetic activation of dorsal striatum axons[5] (likely Anxa1+ axons), while the latter is supported by studies of medial SNc and lateral VTA neurons[30] (likely Calb1+ somas). Future optogenetic perturbation studies focused on the specific subtypes described here should help to provide further understanding of their role in behavior. Such research will also need to consider that many dopaminergic neurons co-release other neurotransmitters–Vglut2+ neurons co-release glutamate[142] and Aldh1a1+ neurons may co-release GABA[143,144] (though see[143])–which likely play additional functional roles within striatum[142,145]. Importantly, however, previous research using fluorescent dopamine sensors indicate that, at least when such recordings are

targeted to regions dominated by a particular subtype such as the dorsal striatum[136], dopamine release is consistent with that expected based on the GCaMP transients reported here.

Finally, our results provide new potential research directions for different dopamine related diseases, such as Parkinson's disease, since there is emerging evidence that several of the subtypes studied here exist in humans[38]. The cell body locations and axonal projections of Aldh1a1+ match the pattern of dopamine loss in Parkinson's disease[23–26], and these neurons are especially vulnerable in Parkinson's disease[38,42], for which the Aldh1a1+ subtype has garnered considerable attention[38,42,141,146–148]. This highlights the importance of the functional heterogeneity found here, which led to our discovery of the new Anxa1+ subtype. Given the functional properties of these Anxa1+ neurons (acceleration-correlated signaling but no detectable reward response), this subtype may be particularly important in the context of Parkinson's disease.

3.9. Methods

To functionally characterize the different subtypes of DA subtypes, intersectional genetic strategies were used to isolate each SNc genetic subtype and label them with the calcium indicator GCaMP6f. We then used fiber photometry to record GCaMP calcium transients from groups of striatal axons of the isolated DA subtypes in head-fixed mice running on a treadmill while periodically receiving unexpected rewards or aversive stimuli.

3.9.1. Animals

All animals used in this study were maintained and cared following protocols approved by the Northwestern Animal Care and Use Committee. Cre mouse lines were maintained heterozygous by breeding to wild-type C57BL6 mice. The Th-Flpo line and the Ai93D reporter line were maintained homozygous. The DAT-tTA mouse line was maintained heterozygous by breeding

with the Ai93D reporter. The Aldh1a1-iCre and Anxa1-iCre lines was generated at Northwestern University by the Transgenic and Targeted Mutagenesis Laboratory. Mice were genotyped using primers detailed in the Key Resources Table.

Both males and females were used for all experiments. Adult mice were used for viral injections at 2 to 4 months old. For indiscriminate labelling of SNc dopamine neurons, DAT-IRES-Cre mice were injected with AAV1-CAG-Flex-GCaMP6f virus. For labelling of SNc Anxa1+ neurons, Anxa1-iCre mice were injected with AAV1-CAG-Flex-GCaMP6f virus. For labelling VGlut2+ or Aldh1a1+ dopamine neurons, we crossed VGlut2-IRES-Cre or Aldh1a1-iCre mice with Th-2A-Flpo mice[17], and offspring were injected with AAV8-EF1α-CreOn/FlpOn-GCaMP6f virus[117]. For labelling Calb1+ dopamine neurons, we crossed Calb1-IRES2-Cre mice with DAT-tTA, Ai93D[149] (CreOn/tTAOn GCAMP6f reporter) mice.

3.9.2. Generation and characterization of the Aldh1a1-iCre line

Because our previous Aldh1a1-CreER^{T2} strain displayed substantial mosaicism, resulting in only weak GcaMP6f signals, we opted to generate an Aldh1a1-iCre strain (Figure 24A). The Aldh1a1-iCre line was generated at Northwestern University by the Transgenic and Targeted Mutagenesis Laboratory. In brief, a P2A peptide directly followed by iCre and a BGH polyA sequence were inserted after the last encoded amino acid of Aldh1a1, using CRISPR mediated HDR (Guides 1-2, see Key Resources Table). First, PRXB6/N ES cells were electroporated and screened for insertion and correct locus with multiple primer pairs (Aldh1a1-iCre insertion primers Forward 1-3 and Reverse 1-3 , see Key Resources Table) followed by Sanger sequencing of iCre+ clones from outside the homology arms through the construct in order to confirm fidelity of the insertion. Clone C7 was expanded and injected into blastocysts to generate chimeras and used for all experiments herein. Aldh1a1-iCre mice were genotyped using primer set 3 described above. To

Figure 23: Validation of Aldh1a1-iCre and Anxa1-iCre mouse lines

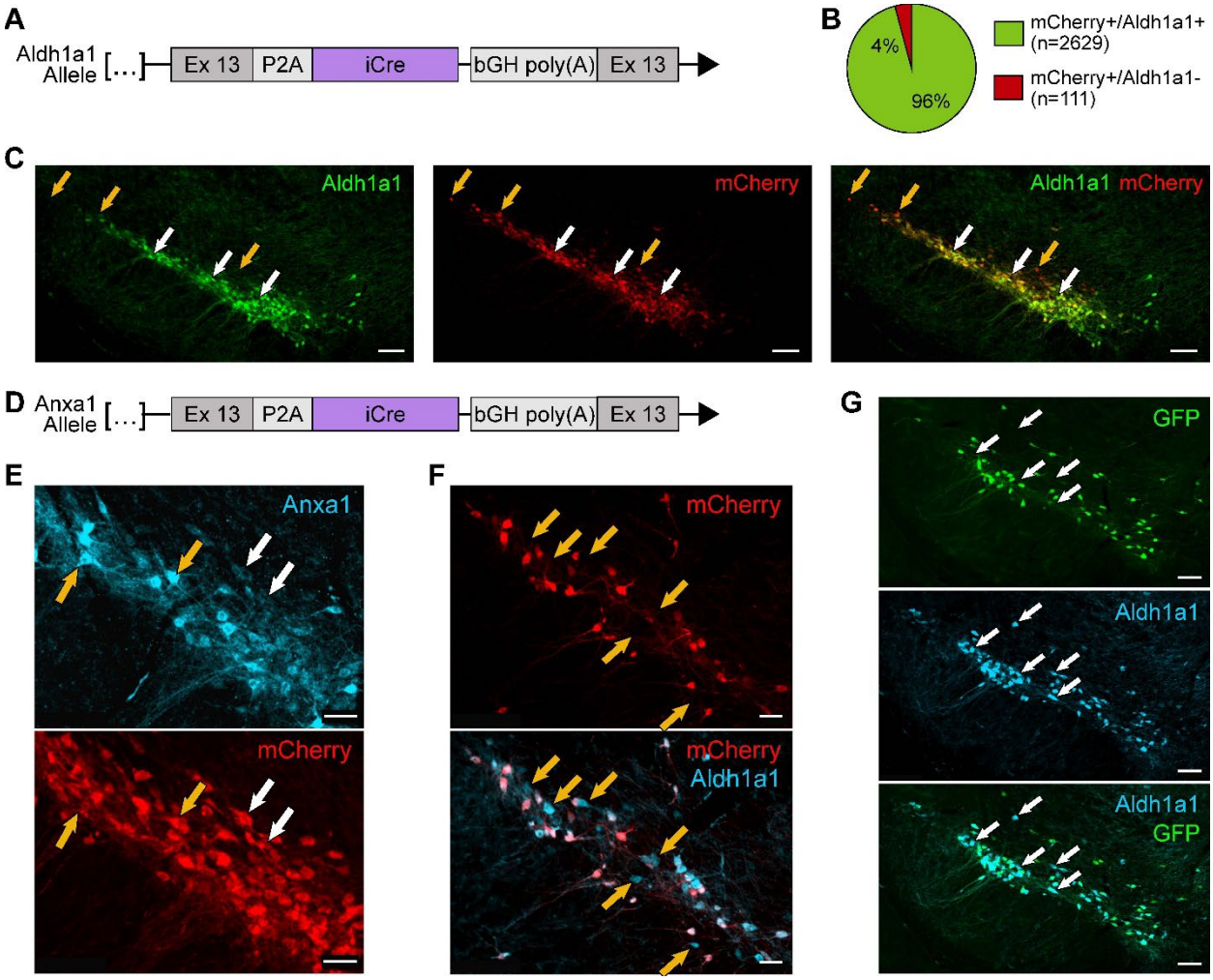

(**A**) Schematic representation of Aldh1a1-iCre transgenic line. Endogenous Aldh1a1 gene was targeted for insertion of a P2A peptide and iCre immediately following the peptide encoded by Exon 13.

(**B**) Ratio of mCherry virally labeled cells co-staining for Aldh1a1 (n=4 mice).

(**C**) Substantia nigra pars compacta immunofluorescence staining from Aldh1a1-iCre mice injected with an AAV5-DIO-mCherry virus. Co-staining shows excellent efficiency and fidelity of iCre recombination, which is notably limited to Th+ cells in this region. White arrows: examples of mCherry and Aldh1a1 co-stained cells. Orange arrows: mCherry-expressing cells with undetectable Aldh1a1 staining, which were primarily localized to the dorsal and lateral SNc. Scale bar = 100 µm.

(**D**) Schematic representation of Anxa1-iCre transgenic line.

(**E**) High magnification of immunofluorescence staining from Anxa1-iCre mice injected with an AAV5-DIO-mCherry virus shows that recombination occurs in cells with both high Anxa1 protein staining (orange arrows) as well as low Anxa1 protein (white arrows). Scale bar = 50 µm.

(**F**) IF staining for Aldh1a1 in the same virally labeled brains as previous panel shows that Anxa1-iCre mediated recombination occurs in only a subset of Aldh1a1-expressing neurons. Examples of Aldh1a1+/mCherry- cells are shown with yellow arrows. Scale bar = 50 µm.

(**G**) IF staining of GFP and Aldh1a1 in Anxa1-iCre, TH-Flpo, RC::FrePe mice. Recombination by iCre and

Flpo leads to GFP expression in Anxa1+ DA neurons. Co-staining with Aldh1a1 corroborates that Anxa1-iCre recombination is less broad than Aldh1a1 expression and confirms that viral labeling results were not due to insufficient viral delivery / diffusion (example of Aldh1a1+, GFP- cells shown with white arrows). Scale bar = 100 μm.
Experiment by Zachary Gaertner

---

determine the expression fidelity of this allele, 0.4 μl of AAV5-EF1α-DIO-mCherry was injected into SNc bilaterally (coordinates relative to bregma: x = ±1.45mm, y = -3.15mm, z = -3.1, -4.1, -4.4, -4.7mm, 0.1 μl at each depth) in n = 4 adult mice. Three weeks later, mice were perfused, and brains were sectioned at 25 μm for immunofluorescence staining. Floating sections were first blocked for 24 hours at 4°C in PBS containing 0.03% Triton-X and 5% normal donkey

serum. Sections were incubated with primary antibodies against Aldh1a1 (goat, R&D Systems), TH (mouse, Sigma-Aldrich; Pel-Freez Biologicals) and mCherry (rat, Thermo Fisher Scientific) in blocking buffer for 24 hours, followed by 4 washes in PBS-Tween20 and incubation with secondary antibodies (Donkey anti Goat Alexa Fluor 488, Donkey anti Mouse Alexa Fluor 647, Donkey anti Rabbit Alexa Fluor 647, Donkey anti Rat Cy3, and DAPI) for 2 hours at room temperature. Sections were then imaged at 20x on an Olympus BX61VS slide scanner. For each brain, 4-5 sections spaced at least 100 microns apart and centered about the area of maximal viral recombination were counted for mCherry+/DAPI+/Aldh1a1+ and mCherry+/DAPI+/Aldh1a1- cells (2740 cells total) (Figure 24B-C).

3.9.3. Generation and characterization of the Anxa1-iCre line

To access the Anxa1+ dopamine neurons, the Anxa1-iCre line (Figure 24D) was also generated by the Transgenic and Targeted Mutagenesis Laboratory, using similar methodologies as above. For CRISPR mediated HDR, Guides 3-4 (see Key Resources Table) were used. Clones were screened for insertion using iCre genotyping primers (Aldh1a1-iCre insertion Primers F3 and R3,

see Key Resources Table). To determine the expression fidelity of this allele, 0.4 µl of AAV5-EF1α-DIO-mCherry was also injected into SNc bilaterally at the same coordinates as above, and 25 µm sections were stained for immunofluorescence using the same protocol as above, but with Rabbit anti Anxa1 antibody (Thermo Fisher Scientific) in place of Aldh1a1. Sections were then imaged at 20x on an Olympus BX61VS slide scanner. Viral recombination occurred in cells with both high Anxa1 expression and faint Anxa1 expression (Figure 24E). To confirm that Anxa1-iCre recombination was limited to a subset within Aldh1a1-expression DA neurons, we also co-stained for Aldh1a1 and mCherry using the same antibodies as above, which showed many Aldh1a1+ cells that did not express the reporter (Figure 24F). To corroborate this further, we stained Anxa1-iCre, TH-Flpo, RC::FrePe mice for Aldh1a1 and GFP (the expression of which is dependent on both iCre and Flpo recombination) using the same protocol as above, which showed Aldh1a1 expression to be broader than Anxa1-iCre expression in development, thus confirming that our viral labeling results were not an artifact of insufficient viral delivery and/or diffusion (Figure 24G).

3.9.4. Integration of single-cell RNAseq datasets

Data from four prior single-cell studies (Tiklova et al. 2019[49], Saunders et al. 2018[48], Kramer et al. 2018[45], and La Manno et al. 2016[46], see Key Resources Table for data sources) was acquired for integration using Seurat version 3.2.0. For Saunders et al. data, specific clusters identified as TH+ substantia nigra neurons (SN clusters 4-1, 4-2, 4-3, 4-4, 4-5, 4-6, 4-7, 4-8, 4-9, & 3-7) were subsetted and used integration. Violin plots of number of reads and number of genes for each dataset were generated and used to determine cutoffs for pre-filtering of each dataset prior to integration to remove doublets or low-quality cells (Figure 25A).The following filters were ultimately applied: Saunders: nFeatures < 3500, mitochondrial read % <25, nCount < 10,000.

Tiklova: nFeatures > 6000, mitochondrial read % < 10, nCount < 3500000. Kramer: nFeatures > 5000, nCount > 400000. Datasets were normalized individually and integrated using the recently described SCTransform pipeline[150] with default settings and regression on percent mitochondrial reads. Principle component analysis was performed on the subsequent integrated dataset, and an elbow plot was used to determine the number of PCs used for clusters (18 PCs were ultimately used). Clustering was performed using the standard Seurat pipeline at default settings, resulting in 8 clusters (Figure 11A). Determination of marker genes for clusters was performed using the FindAllMarkers command in Seurat on the RNA assay with the following settings: min.diff.pct = 0.20, only.pos=TRUE, min.pct = 0.05). Of note, exploring differential expression of marker genes using a heatmap (not shown) revealed a unique signature distributed across multiple clusters that did not appear to fit any other subtypes. Examining the source of these cells revealed they came entirely from the Tiklova et al.[49] dataset. Therefore, to explore the potential inclusion of a unique group of cells stemming from that dataset, we re-clustered our dataset using the LIGER R package version 2.0.1, which differs from Seurat dataset integration in that it is designed to account for the potential inclusion of unique cell types stemming from only individual samples being integrated[151]. Clustering with LIGER revealed a cluster of distantly related cells which came entirely from Tiklova et al.[49] (Figure 25B). Due to the distinct signature of these cells which did not match the clusters they were placed in using the Seurat integration, these cells were subsequently filtered out of our dataset. After this, all clusters were represented by all source datasets (Figure 25C). Violin plots of the top 2 defining markers per cluster were generated using the Seurat VlnPlot command with default settings (Figure 25D).

Figure 24: Details of single-cell RNAseq dataset integration

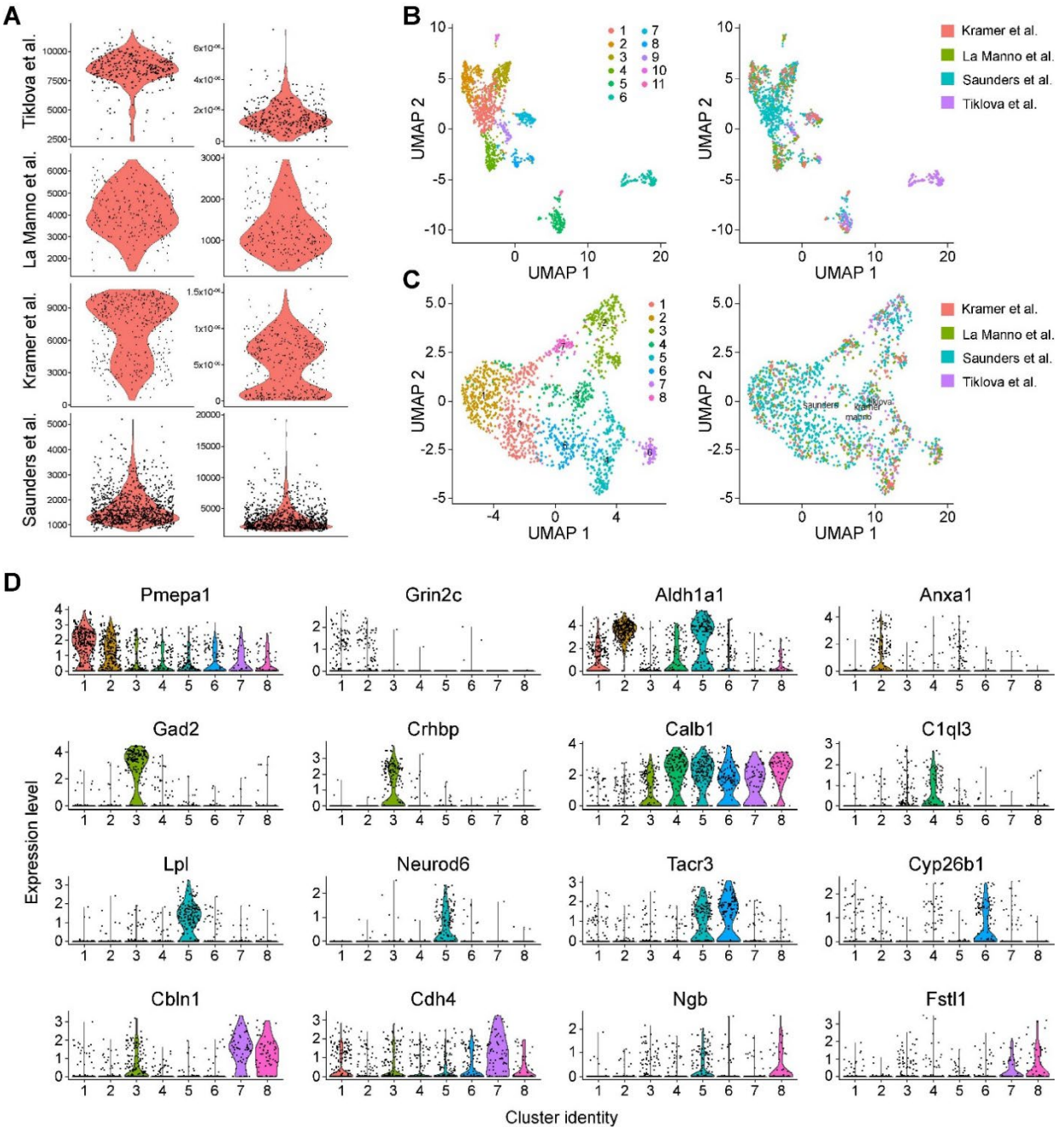

(**A**) Violin plots of number of genes and RNA counts from each source dataset, which were used to determine cutoffs for quality control filtering.

(**B**) LIGER clustering of the meta-dataset, revealing one cluster that was more distantly related to all other DA neurons and came solely from the Tiklova et al.[49] dataset. This cluster was subsequently removed.

(**C**) Cells colored by cluster (left) or source dataset (right), which reveals that all clusters were represented by each dataset.

(**D**) Violin plots of the top 2 defining marker genes for each cluster.

Analysis by Zachary Gaertner

3.9.5. Single nucleus RNA sequencing

To isolate nuclei for snRNA-seq library generation, n=5 DAT-CRE, CAG-Sun1/sfGFP mice (3 female, 2 male) were sacrificed and rapidly decapitated for extraction of brain tissue. A 2-3mm thick block of ventral midbrain tissue was dissected out and collected for subsequent isolation. Tissue was dounce homogenized in a nuclear extraction buffer (10mM Tris, 146mM NaCl, 1mM CaCl2, 21mM MgCl2, 0.1% NP-40, 40u/mL Protector RNAse inhibitor. Dounce homogenizer was washed with 4mL of a washing buffer (10mM Tris, 146mM NaCl, 1mM CaCl2, 21mM MgCl2, 0.01% BSA, 40U/mL Protector RNAse inhibitor) and filtered through a 30uM cell strainer. After three rounds of washing by centrifugation (500g for 5 minutes) and resuspension in a nuclei resuspension buffer (10mM Tris, 146mM NaCl, 1mM CaCl2, 21mM MgCl2, 2% BSA, 0.02% Tween-20), nuclei suspension was stained with DAPI and filtered through a 20uM strainer. This nuclei suspension was then sorted via FACS with a 100uM nozzle at a frequency of 30.0K and pressure of 20 PSI, with gates set for isolation of GFP+ singlet nuclei (Figure 26A). A total of 50,500 nuclei were sorted across all samples, which was subsequently used for preparation of two 10X Genomics Chromium libraries (one for pooled male mice, one for pooled female mice).

Library preparation was performed by the Northwestern University NUSeq Core Facility. Nuclei number and viability were first analyzed using Nexcelom Cellometer Auto2000 with AOPI fluorescent staining method. Sixteen thousand nuclei were loaded into the Chromium Controller (10X Genomics, PN-120223) on a Chromium Next GEM Chip G (10X Genomics, PN-1000120), and processed to generate single cell gel beads in the emulsion (GEM) according to the manufacturer's protocol. The cDNA and library were generated using the Chromium Next GEM Single Cell 3' Reagent Kits v3.1 (10X Genomics, PN-1000286) and Dual Index Kit TT Set A (10X Genomics, PN-1000215) according to the manufacturer's manual with following modification:

Figure 25: Details of single-nucleus RNA-seq analysis

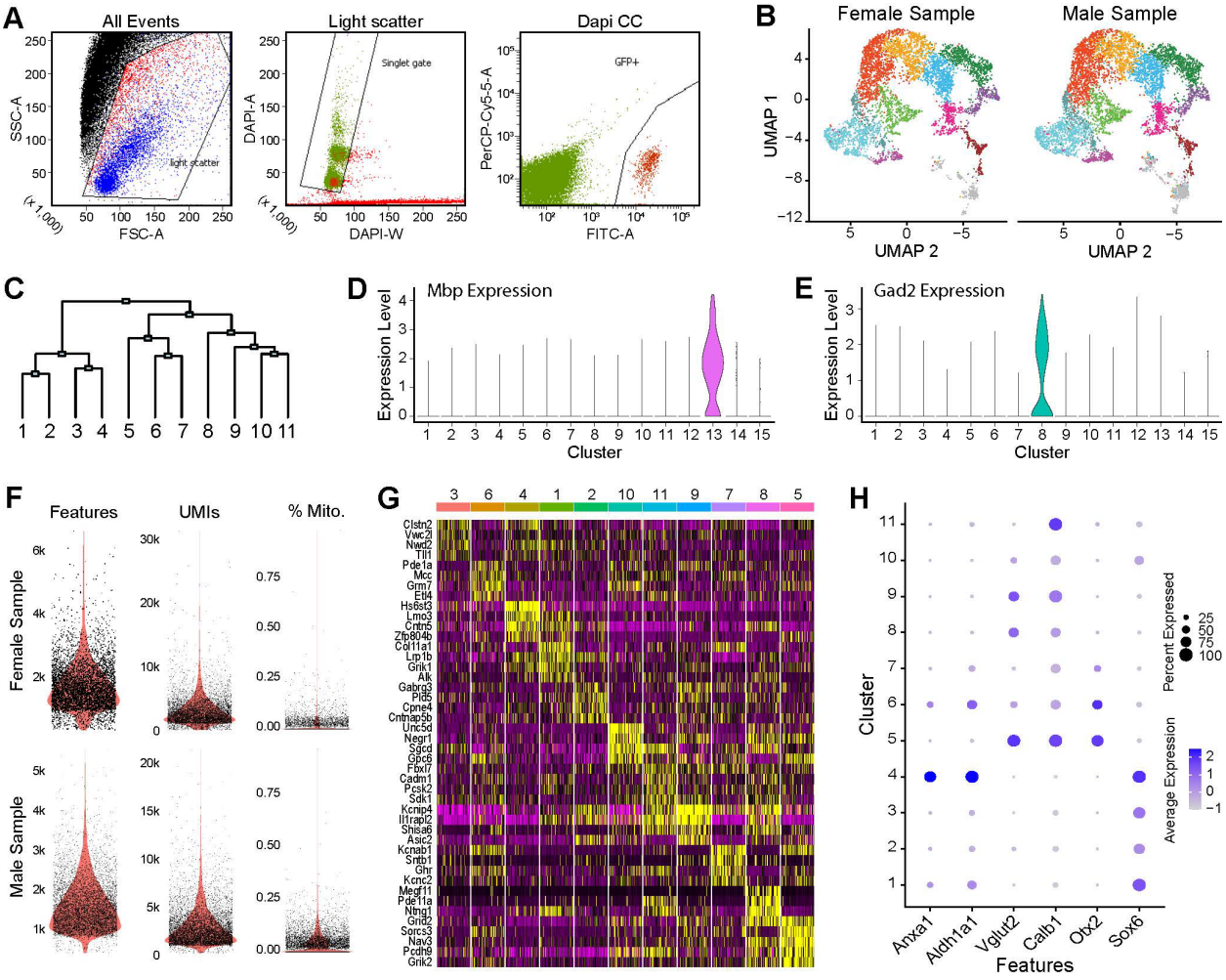

(**A**) Example plots from FACS sorting of GFP+ nuclei.

(**B**) Plots showing the distribution of cells from either the male or female samples, showing all clusters were represented by both samples.

(**C**) Diagram of hierarchical clustering estimation. Notably, clusters 1-4 appear to be Sox6+, 5-7 are Otx2+, and 8-11 are negative for both markers.

(**D**) Violin plots of Mbp, showing significant expression in cluster 13.

(**E**) Expression of Gad2, which is limited to cluster 8, suggesting this cluster represents a previously described population of dopamine neurons with some GABAergic characteristics.

(**F**) Quality control plots of number of genes (features), UMIs, and percent mitochondrial reads for each sample.

(**G**) Heatmap of top 4 differentially expressed genes for each cluster, excluding clusters 12, 13, 14 and 15, which do not appear to be classic midbrain dopamine neurons based on lower expression of pan-DA neuron markers (TH, DDC, DAT and Vmat2)

(**H**) Dotplot of expression (post zero-imputation) of several key marker genes of dopamine neuron subpopulations.

Experiment by Zachary Gaertner

PCR cycle used for cDNA generation was 16 and the resulting PCR products was size-selected using 0.8X SPRI beads instead of 0.6X SPRI beads as stated in protocol. Quality control for constructed library was performed by Agilent Bioanalyzer High Sensitivity DNA kit (Agilent Technologies, 5067-4626) and Qubit DNA HS assay kit for qualitative and quantitative analysis, respectively.

The multiplexed libraries were pooled and sequenced on Illumina Novaseq6000 sequencer with paired-end 50 kits using the following read length: 28 bp Read1 for cell barcode and UMI and 91 bp Read2 for transcript. Raw sequence reads were then demultiplexed and transcript reads were aligned to mm10 genome using CellRanger with --include-introns function.

3.9.6. Analysis of single nucleus RNA sequencing data

Outputs from CellRanger were read into Seurat version 4.0.2 using the Read10X command for each sample. Numbers of UMIs, features and mitochondrial reads were plotted for each dataset (Figure 26F) and used to determine cutoffs for quality control pre-filtering of each sample; nuclei with fewer than 500 unique features were removed from each dataset. The male and female datasets were then normalized and integrated using the SCTransform V2 pipeline[152] using all default settings and regression on percent mitochondrial reads. In total, the integration resulted in a final dataset of 12,065 nuclei, with a mean UMI count of 3435 and mean of 1683 features. Clustering was performed using the Seurat FindClusters command using 30 principle components and a resolution of 0.5. Differential expression tested was performed using the FindAllMarkers command on the SCT assay with default settings, with the exception of logfc.threshold = 0.15 in order to better detect differential expression of genes with low overall detection rates in the dataset. Determination of Sox6+ and Calb1+ significant clusters was made using a Wilcoxon Rank

Sum Test by running the FindAllMarkers Seurat command with the following settings: features = c("Sox6", "Calb1"), min.pct = 0, min.diff.pct = 0, logfc.threshold = 0, only.pos = TRUE.

In order to better visualize the expression of marker genes, we then performed zero-preserving zero-imputation using ALRA[153], which aims to increase the detection of low-expression genes while preserving true biological zeros. Zero-imputed data was used solely for visualizations of features as seen in Figure 12C,E,F and Figure 26H, but not for any statistical determination of differential expression. Heatmap of the top 4 marker genes for each cluster (Figure 26G) was generated using the top 4 differentially expressed genes (determined per average log fold change) for each cluster, filtering for only unique genes.

3.9.7. Stereotaxic viral injections and genetic strategies to isolate subtypes

The use of intersectional genetic strategies to isolate each SNc genetic subtype was necessary because the marker genes used to access each of these subtypes are not only expressed in DA neurons (for example Vglut2 is widely expressed in glutamatergic neurons throughout the brain). Cre mouse lines for each of these markers (Calb1-Cre, Vglut2-Cre, Aldh1a1-Cre and later Anxa1-Cre were crossed with a Th-Flpo line[17], where the recombinase Flpo is expressed under the control of Th, a marker of DA neurons. Th is also expressed in norepinephrine and epinephrine producing neurons, but these were avoided through anatomically targeting. A small volume (0.4 µl total) of an intersectional AAV virus[154] (AAV8-EF1α-CreOn/FlpOn-GCaMP6f, titer 6.10 $x10^{+13}$ diluted 1:1 in PBS) was pressure injected through a pulled glass micropipette into the SNc through a 0.5-1 mm diameter craniotomy (-3.25 mm caudal, +1.55 lateral from bregma) at 4 depths (-3.80, -4.10, -4.4, -4.7 mm from the dura surface, 0.1 µl per location) in adult mice (2-4 months old), labeling only DA neurons expressing a single subtype's marker (Figure 27B-C, F). This viral strategy anatomically restricts labelling to the SNc, which is essential to avoid norepinephrine/epinephrine

neurons, but also to avoid VTA subtypes – the marker genes that characterize SNc subtypes (Vglut2, Calb1, Aldh1a1, Anxa1) are also expressed in other distinct VTA subtypes[28,52]. This adult labelling strategy is also required because some markers (Sox6, Vglut2, Aldh1a1) are widely expressed in the brain during development, and thus transgenic reporters label a much wider set of neurons. This is not the case for Calb1, which is only expressed in the adult brain, and therefore the Calb1+ subtype can also be labelled with a transgenic reporter: Calb1-Cre/DAT-tTA/Ai93D[149] mice express GCaMP6f endogenously only in Calb1+ DA neurons – DAT is another marker of DA neurons) (Figure 27D). Furthermore, because Aldh1a1 and Anxa1 are not expressed in non-DA neurons in the region around the SNc, it is also possible to label these neurons using a single-recombinase genetic strategies (Aldh1a1-Cre or Anxa1-Cre + AAV1-CAG-FLEX-GCaMP6f virus, titer 2.00 $x10^{+13}$). For comparison with the standard practice of indiscriminately labelling DA neurons, experiments were also conducted in DAT-Cre mice injected with an AAV1-CAG-FLEX-GCaMP6f virus (Figure 27E). For experiments measuring DA release directly using $GRAB_{DA}$ (Figure 20), an AAV9-hSyn-GRAB_DA3m virus (BrainVTA #PT-4720, titer 5.51 $^{x10+13}$ diluted 1:1 in PBS) was injected into the striatum in 3 locations, X +1.8 Y +0.5 Z -1.9, X +1.8 Y +0.5 Z -2.9, and X +3.2 Y -1.25 Z -2.9 (0.2 µl per location) to express the DA sensor throughout the striatum. Fiber photometry was then conducted in these same 3 locations.

These strategies were used to label them each subtype with the calcium indicator GCaMP6f[116]. This is a genetically encoded fluorescent protein which increases its fluorescence as the intracellular levels of calcium increase. These changes in fluorescence are used as a proxy for neuronal firing (action potentials in the soma are accompanied by an increase in calcium concentration[155]), but also as a proxy for DA release from axons, as all known mechanisms for triggering axonal dopamine release involve increases in intracellular calcium concentration[119,120],

Figure 26: Methodology for functional characterization of DA subtypes

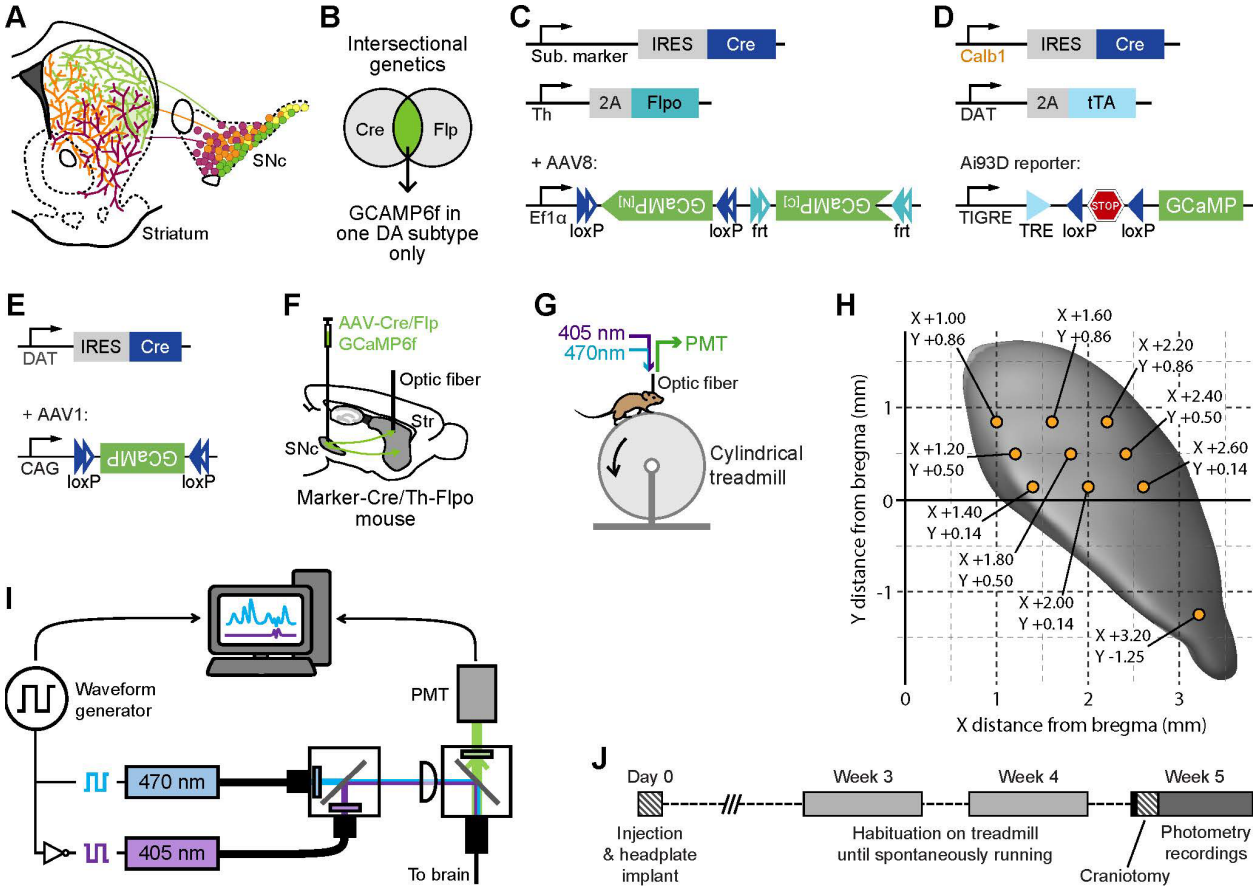

(**A**) Cell bodies and axons from different DA subtypes are anatomically biased but densely overlapping in SNc and striatum, respectively.

(**B**) Intersectional strategy used to isolate DA subtypes using two recombinases.

(**C**) Viral intersectional genetic strategy to isolate each subtype.

(**D**) Alternative transgenic strategy used to label Calb1+.

(**E**) Viral strategy used to indiscriminately label dopamine neurons.

(**F**) An intersectional virus is injected into the SNc to label each subtype with GCaMP6f, a calcium indicator. An optic fiber is then placed into the striatum, measuring changes in fluorescence that can be used as a proxy for DA release.

(**G**) Fiber photometry setup with mouse running head fixed on a cylindrical treadmill.

(**H**) Map of the striatum from above showing coordinates used to access different regions of striatum during fiber photometry.

(**I**) Fiber photometry setup. 470 and 405 nm (isosbestic) illumination are alternated at 100Hz using a waveform generator. Fluorescence is separated from the illumination light and detected using a PMT (photo multiplier tube). The output from the waveform generator is used to split fluorescence from 470 vs 405 nm illumination.

(**J**) Schematic of experimental timeline. 2 weeks after viral injection (on weeks 3 and 4) mice are head fixed on the treadmill and habituated until they run spontaneously. 4 weeks after injection, a craniotomy is made for access with the optic fiber, and fiber photometry recordings are obtained on week 5.

including anterogradely propagating action potentials[121–125] and local ACh modulation[37,126]. For our purpose, GCaMP has critical advantages over other strategies that directly measure extracellular calcium in striatum (i.e. dLight, GRAB-DA, microdialysis, voltammetry), as the detected calcium transients are generated only from the labeled genetic subtypes; non-labeled neurons do not contribute. Axons from different DA subtypes can densely overlap in many striatal regions[17] and these sensors detect DA released from all nearby axons, without subtype specificity. Microdialysis and voltammetry are particularly problematic in this regard due to their low temporal and spatial resolution[156], but the cellular resolution of fluorescent DA sensors (dLight, GRAB-DA) is still not sufficient to distinguish DA release from densely overlapping axons[120,135] of different subtypes.

Following the injections, the skull and craniotomy were sealed with Metabond (Parkell) and a custom metal headplate was installed for head fixation. The location of recording sites was marked on the surface of the Metabond for future access. For coordinates used, see Figure 27H – this map and set of coordinates were based on the Paxinos mouse brain atlas (the Allen atlas was found inaccurate in the mediolateral direction, with coordinates squished compared to the mouse brain, which was particularly problematic for targeting of the narrow posterior striatum) and adjusted experimentally for optimal access. For Calb1-IRES2-Cre/DAT-tTA/Ai93D mice, which express GCaMP6f endogenously, no injection was conducted and only the headplate was implanted at this time. 4 weeks were allowed for GCaMP6f expression to ramp up and fill dopaminergic somas in SNc and axons in striatum (Figure 27J).

3.9.8. Training and behavior

Starting 1-2 weeks after injection, mice were head-fixed with their limbs resting on a 1D cylindrical Styrofoam treadmill ~20 cm in diameter by 13 cm wide in the dark (Figure 27G). Mice

were habituated on the treadmill for 3-10 days until they ran freely and spontaneously transitioned between resting and running. Rotational velocity of the treadmill during locomotion was sampled at 1,000 Hz by a rotary encoder (E2-5000, US Digital) attached to the axel of the treadmill and a custom LabView program.

After mice ran freely, a subset of mice were water restricted for at least 3 days and received unexpected water rewards, aversive air puffs, and light stimuli while on the treadmill, using a custom LabView program. Large (16 µl) and small volume (4 µl) water rewards were delivered through a waterspout gated electronically through a solenoid valve, which was accompanied by a short 'click' noise. Air puffs were delivered by a small spout pointed at their left whiskers, which was connected to a ~20 psi compressed air source and triggered electronically through the opening of a solenoid valve for 0.2s. Triggering of this solenoid was also accompanied by a 'click' noise. For light stimuli, a blue LED placed ~30 cm in front of the head-fixed mouse was electronically triggered for 0.2s. Rewards, air puffs and light stimuli were alternated at random during recordings and delivered at pseudo-random time intervals (10-30s between any two stimuli).

3.9.9. Fiber photometry

Acute fiber photometry was then used to record GCaMP calcium transients from groups of striatal axons of the isolated dopaminergic subtypes in the head-fixed mice. 4 weeks after injection (and not more than 8 weeks, as overexpression of GCaMP can cause toxicity), mice were once again anesthetized, and a small craniotomy (1 mm in diameter) was drilled through the Metabond and skull, leaving the dura and cortex intact. Craniotomies were made at different locations depending on the experiment, which were pre-marked during the injection surgery – see Figure 27H. For more accurate targeting, a cross was drawn on the Metabond centered around the target location, so the center could be identified visually after the craniotomy. The craniotomies were then sealed

with Kwik-Sil (World Precision Instruments KWIK-SIL). After the mice recovered from this short (10-15 min) surgery for one day, they were head-fixed on the linear treadmill, and the Kwik-Sil covering the craniotomies was removed. One or two optical fibers (200 μm diameter, 0.57 NA, Doric MFP_200/230/900-0.57_1.5m_FC-FLT_LAF) were lowered slowly (5 μm/s) using a micromanipulator (Sutter MP285) into the brain to various depths measured from the dura surface. In the striatum, recording depths ranged from 1.6 to 4.1 mm; in SNc, depths ranged from 3.5 to 4.5 mm. Recordings started at 1.6 mm in striatum, and 3.5 mm in SNc, but if no ΔF/F transients were detected at those depths the fiber was moved down in increments of 0.25-0.5 mm in striatum or 0.15-0.2 mm in SNc, until transients were detected. From there, a 15 min recording was obtained, and the fiber was moved further down in the same increments. Subsequent recordings were obtained until a depth was reached where transients were no longer detected, at which point the fiber was pulled out of the brain slowly (5 μm/s). The diameter of the fiber (200 μm) is smaller than the 400 μm commonly used in fiber photometry, with the main advantage being the smaller damage caused by this fiber – which is particularly important in acute recordings, where the fiber can be inserted repeatedly. Nevertheless, the fiber still damages the tissue, and thus only 3-4 days of recordings can be made with the fiber in the same location before no transients are detected. To control for any movement artifacts, GCaMP fluorescence was also recorded at its isosbestic wavelength, 405 nm[118] (Figure 27G, I), at which fluorescence is not calcium dependent.

A custom-made photometry setup was used for recording (Figure 27I and Figure 28A for details). Blue excitation (470 nm LED, Thor Labs M70F3) and purple excitation light (for the isosbestic control) (405 nm LED, Thor Labs M405FP1) were coupled into the optic fiber such that a power of 0.75 mW emanated from the fiber tip. 470 and 405 nm excitation was alternated at 100 Hz using a waveform generator, each filtered with a corresponding filter (Semrock FF01-406/15-25 and

Semrock FF02-472/30-25) and combined with a dichroic mirror (Chroma Tech Corp T425lpxr). Green fluorescence was separated from the excitation light by a dichroic mirror (Chroma Tech Corp T505lpxr) and further filtered (Semrock FF01-540/50-25) before collection using a GaAsP PMT (H10770PA-40, Hamamatsu; signal amplified using Stanford Research Systems SR570 preamplifier). A Picoscope data acquisition system was used to record and synchronize fluorescence and treadmill velocity at a sampling rate of 4 kHz. Despite the use of low auto-fluorescence fibers, the setup does build up auto-fluorescence over time, which can saturate the PMTs after a few days of no use. To prevent this, the LEDs were turned on for 15-45 min before each recording day to bleach the setup, with the time depending on how recently the setup was used (45 min at least if it wasn't used for over 3 days).

3.9.10. Histology and fiber placement localization

To locate the recording location and confirm correct expression, mice were perfused transcardially with PBS (Fisher) then 4% paraformaldehyde (EMS) immediately after the last recording. It is critical to perfuse mice the day of or at most the day after the last fiber photometry session, as the fiber track will start to close and it complicates the identification of the recording location. Brains were stored in PFA at 4 °C overnight then transferred to 40% sucrose (Sigma) for at least 2 days before sectioning. Coronal slices (50 μm thick) were cut on a freezing microtome and stored at 4 °C in PBS. For immunostaining of dopaminergic neurons, sections were washed in PBS, blocked in PBS + 0.3% Triton-X (Sigma) + 5% normal donkey serum (Sigma), incubated overnight with primary antibodies Sheep anti-Tyrosine Hydroxylase (1:1000 dilution, RRID:AB_461070) and Rabbit anti-GFP, which recognizes GCaMP6f (1:1000 dilution, RRID:AB_221569), washed again in PBS + 0.3% Triton-X, then incubated with secondary antibodies tagging Tyrosine Hydroxylase with Alexa Fluor 555 (Donkey anti-Sheep Alexa Fluor 555, RRID:AB_2535857) and GCaMP6f

with Alexa Fluor 488 (Donkey anti-Rabbit Alexa Fluor 488, RRID:AB_2313584). Images of SNc and striatum were acquired on an Olympus or Keyence Slide Scanner (VS120 or BZ-X810, respectively) for verification of injection accuracy and fiber placement. Other brains were mounted and imaged without immunostaining for fiber placement only.

For the representation of recording locations in striatum shown in Figure 15D and Figure 22A,D-E, 20x magnification images of striatum were acquired on a Keyence slide scanner (BZ-X810) (see Method details, Histology). For the slice in each brain with the clearest fiber track, fiber tracks were marked onto the images. We then identified the closest reference slice for each imaged brain slice (reference slices from the Paxinos Mouse brain atlas), spaced 0.36 mm (bregma +0.86, +0.50, +0.14, -0.22, -0.58, -0.94, -1.34 mm; as shown in schematics in Figure 15D), and uniformly scaled this reference to approximately match the imaged slice. Recording locations for recordings included in each figure for each mouse were then marked on each slice, measuring depth from brain surface along the fiber track. The fiber tracks and recording locations mapped to these reference slides from all mice for each subtype were combined for Figure 15D and Figure 22A,D-E. Circles represent approximate light collection recording area for our 200 μm fibers (~300 μm in diameter). For compact representation in Figure 22A,D-E, all slices from the body of the striatum (bregma +0.85 to +0.14) or posterior striatum (bregma -0.58 to -1.34) were approximately aligned and combined.

3.9.11. Pre-processing of fiber photometry data

Fiber photometry data was analyzed using custom MATLAB code. Simultaneous traces (velocity from rotary encoder, trigger signals for reward, air puff, and light stimuli delivery, licking from a lick sensor, fluorescence detected by PMTs from one or two optic fibers, and output from waveform generator used to alternate 405 and 470 nm illumination every 10 ms) were collected at

4 kHz by a Picoscope6 data acquisition system. Fluorescence collected during 405 or 470 nm illumination (20 time-bins for each pulse of 405 or 470 nm excitation) was separated using the binary output from the waveform generator (Figure 28B). For each transition period between illumination sources, 5 time-bins were excluded to remove transition times (which contain artifacts due to imperfectly synchronized on/off times for the LEDs and warm up times). Traces were then re-binned to 100 Hz by averaging every 40 time-bins for velocity and every 40 time-bins for 405 and 470 fluorescents (but only including 15 of 40 bins for each source: excluding 20 bins when the alternate source was on and 5 transition bins).

Figure 27: Custom photometry setup and 405/470 separation

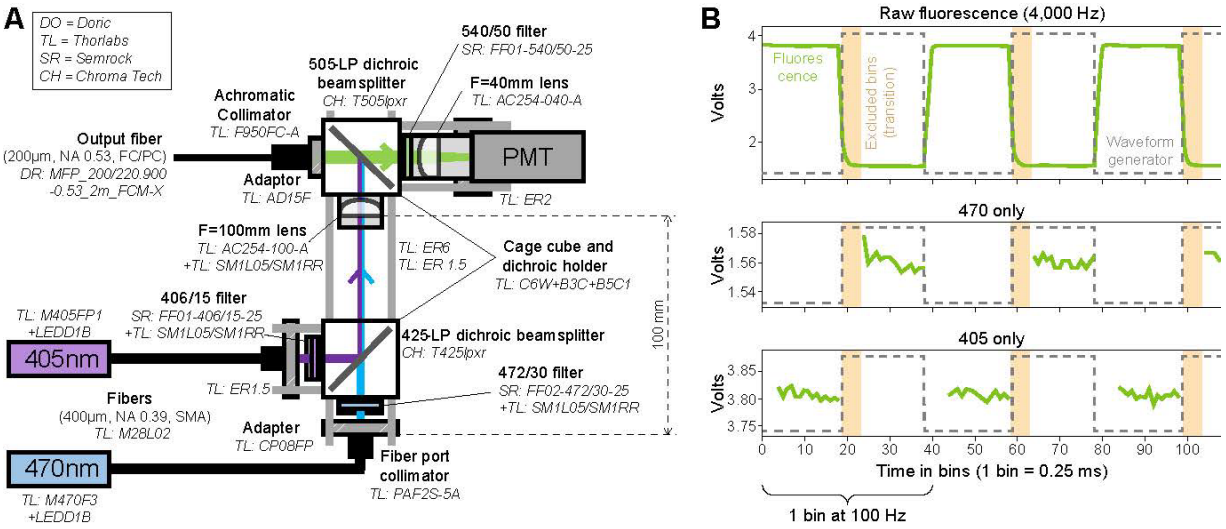

(**A**) Detailed schematic of the custom fiber photometry setup used, including all part numbers.

(**B**) Example of fluorescence data pre-processing to separate by illumination source (405 vs 470 nm). The output from the waveform generator (grey dotted line), which controls the alternation of the LEDs, is used to separate fluorescence occurring during 405 vs 470 nm illumination. 5 bins after the transition are excluded to eliminate transition artifacts. 40 bins (from raw 4,000 Hz data) are averaged together to get traces at 100 Hz, which are used for all further processing steps.

Fluorescence traces were first corrected for background signal (intrinsic fluorescence and any illumination bleed-through) by subtracting 85% of the baseline (baseline defined as 8th percentile

over a 20s window). This 85% was estimated from photometry recordings from cortex, which was unlabeled (no GCaMP expression), obtained from 10 recordings from 5 mice. 405 and 470 fluorescence traces were corrected independently. To calculate ΔF/F, traces were then normalized by baseline fluorescence division (8^{th} percentile over a 20s window) separately for 405 and 470. The subtraction and normalization steps together corrected for bleaching and removed any slow drifts in baseline. Next, traces were converted to ΔF/F units (baseline at 0) by subtracting the baseline (median of all non-transient bins for 470 nm traces, and median of all bins for 405 nm traces)

For comparison of traces between dopaminergic subtypes, ΔF/F traces were normalized so that the baseline remained at 0 and the largest transient peak for each trace was 100%. This is critical because different subtypes were found to show different ranges of ΔF/F values (with Aldh1a1+ and Anxa1+ showing higher ΔF/F than Calb1+ or Vglut2+), but also because of different densities of axons of each subtype (and thus GCaMP concentration) in different regions, which resulted in further variation in ΔF/F. Throughout all figures herein, Norm %ΔF/F units refer to this normalization (0-100 scale). 405 traces were normalized using the amplitude of the largest peak from the corresponding 470 traces. Example raw traces however show non-normalized traces.

3.9.12. Criteria for recording inclusion

Because a wide range of locations in striatum were unbiasedly sampled, including those with few or no axons from some subtypes, some recordings didn't show clear transients. For a fair comparison between recordings/subtypes, only recordings with high signal-to-noise ratios (greater than 10) were included in the analysis. To calculate signal-to-noise ratios for each recording, we selected well-isolated transients, as defined by having a large, fast rise (30 ΔF/F/s) immediately followed by a decay. We first removed all slow fluctuations except transients in (non-normalized)

ΔF/F traces by subtracting the 8th percentile over a window 2-3 times the width of observed ΔF/F transients (250 bins, 2.5s), and then smoothed the resulting trace over a 0.2s window (20 bins) to reduce noise. Transient rises and decays were identified by locating the zero-crossings on the derivative of the trace, also smoothed over 0.2s window. Only clearly isolated transients were included – those with a rise greater than 30 ΔF/F/s followed by a decay greater than -5 ΔF/F/s. Traces with less than 0.2 transients per second were excluded. Signal values for each recording were calculated as the 80th percentile of isolated transient peaks. Noise for each recording was calculated by smoothing each (non-normalized) ΔF/F trace over 10 bins (0.1s), then subtracting this smoothed trace from the original ΔF/F trace and using the standard deviation of the resulting trace as the noise value. The signal and noise values were divided to obtain signal-to-noise for each trace. These steps for determining signaling to noise for each trace were not used for any further analysis.

ΔF/F traces from 405 nm illumination (isosbestic control) were used to remove any movement artifacts. While GCaMP6f fluorescence intensity is dependent on calcium concentration when excited with 470 nm light, it is still fluorescent but in a calcium-independent way when excited with 405 nm light[118]. Therefore, calcium transients in neurons are detected with 470 nm illumination but are absent with 405 nm illumination, while movement artifacts are present in both traces. Movement artifacts were identified using the 405 nm traces from each recording as follows. (Non-normalized) 405 ΔF/F traces were smoothed over a 10-bin window (0.1s). This smoothed trace was subtracted from the original 405 ΔF/F trace, so that only the noise remained (same process as used above for 470 traces to separate noise and signal). A max noise value was calculated as the max absolute value of this noise trace. Any bins in the original 405 ΔF/F trace more than 3 times this max noise (or 3 times below -max noise) were excluded from further

analysis. Additionally, any sequential bins that were above max noise (or below -max noise) for longer than 0.2 s (20 bins, less than half the width of observed calcium transients) were also excluded, with an additional 0.1s (10 bins) on both sides also excluded. Any bins removed from the 405 ΔF/F trace were also removed in the corresponding 470 ΔF/F and other traces (velocity, reward delivery, licking…). If more than 5% of the bins in a recording met these movement artifact exclusion criteria, the entire recording was excluded.

3.9.13. Analysis of signaling during locomotion

Only locomotion time bins were included for locomotion analysis in Figure 10C-D,F-G, Figure 15 and Figure 30C-F. Locomotion vs rest bins were selected using a double threshold on the velocity trace in both positive and negative directions (thresh1 = ± 0.024 m/s, thresh2 = ± 0.010 m/s). Isolated 1 bin-long locomotion periods (no other movement within 2 bins on either side) were excluded, as well as rest periods shorter than 0.5 s. Time bins were considered as locomotion periods only if they lasted longer than 0.5 s and had an average velocity greater than 0.2 m/s. For a recording to be included in the locomotion analysis, the recording needed to include a total of at least 100 sec of locomotion.

Acceleration was calculated from the velocity traces as the difference between consecutive treadmill velocity time bins (first smoothed over 6 bins, 0.06s), then multiplied by the sampling frequency (100 Hz) for proper m/s^2 units.

Cross-correlations between ΔF/F and acceleration (Figure 10D, Figure 15C',E, Figure 22A and Figure 30C) were calculated for locomotion periods only (defined above) using MATLAB's *crosscorr* function over a 1s lag window (100 time bins). The same process was used to calculate the cross-correlation between corresponding 405 ΔF/F traces and acceleration, and any recording

with a peak cross-correlation (between 405 ΔF/F trace and acceleration) above 0.1 was excluded from all locomotion analysis.

For triggered averages of ΔF/F on accelerations and decelerations (Figure 15F and Figure 30E), isolated large accelerations and decelerations were selected by first locating the zero-crossings on the acceleration trace, considering individual accelerations/decelerations the interval between two zero-crossings of the trace. Accelerations/decelerations were included if they had a duration of at least 50 ms (0.05s) and a peak greater than 2 m/s^2 (accelerations) or lower than -2 m/s^2 (decelerations), but only if they were not surrounded by other large accelerations or decelerations (no acceleration > 2 m/s^2 or < -2ms^2 in a window of 0.25s on either side). Conversely, for triggered averages of acceleration on ΔF/F transient peaks (Figure 15G and Figure 30D), we selected well-isolated transients from non-normalized ΔF/F traces, as defined by having a large, fast rise (30 ΔF/F/s) immediately followed by a decay (as used in the calculation of signal-to-noise ratio above).

For plotting of cross-correlation and triggered averages above, traces were smoothed over 5 time-lag bins (0.05s). Shaded areas represent the mean ± standard error of the mean (s.e.m.), while accompanying heatmaps show cross-correlations/triggered averages for all individual recordings. Heatmaps in Figure 10D were sorted by the integral of the ΔF/F-acc cross-correlation at positive lags (see below), while heatmaps in Figure 15E-G and Figure 30C-E were sorted by PC1/PC2 angle (see PCA section below).

For analysis of timing differences between Calb1+ and VGlut2+ deceleration signaling shown in Figure 16A, the lag between ΔF/F transient peaks and deceleration peaks was quantified by locating in time either the minimum cross-corr value between 0-1s for the ΔF/F-acceleration cross-correlations for each recording (Figure 16A left), the maximum ΔF/F value between 0-1s for the

triggered average on deceleration (Figure 16A middle), or the minimum acceleration value between -1-0s for the triggered average on transient peaks (Figure 16A right).

For the initial functional characterization shown in Figure 10, differences in locomotion signaling were quantified by calculating the integral of the cross-correlation between ΔF/F and acceleration at positive lags (0-1s), where positive values indicate a peak in the cross-correlation and thus ΔF/F transients following accelerations, while negative values indicate a trough and thus ΔF/F transients following decelerations. For the quantification of acceleration/deceleration signaling across depths in striatum shown in Figure 10G (but also Figure 16B), depth from surface as shown in was defined as the depth at which the fiber tip was located from the brain surface, as measured by the micromanipulator used to move the fiber during photometry. To reduce overlap between data points at the same depth plotted, a random amount between +0.1 and -0.1 mm was added to each depth. This measure of locomotion signaling was also used to plot the relationship between locomotion signaling and reward responses in Figure 10F (for reward response calculation, see "Analysis of responses to rewards and air puffs" section below), and to sort the ΔF/F-acceleration correlation plots in Figure 10D.

3.9.14. Principal component analysis (PCA) of locomotion signaling

Principal component analysis (PCA) was applied to the matrix of all cross-correlation traces from striatal recordings (shown in Figure 15E), from all functionally homogeneous subtypes (VGlut2+, Calb1+ and Anxa1+), using MATLAB's *pca* function (without centering: *'Centered', 'off'*; however, equivalent results were obtained when we repeated the PCA analysis with centering, data not shown). This function outputs the principal components (loadings, eigenvectors), the scores for each recording's cross-correlation along each principal component (matrix of all SNc cross-correlation traces multiplied by the loadings matrix), and the variance explained by each principal

component across all recordings. For the representation of combinations of the first two principal components (PC1 and PC2) shown in Figure 16C, PC1 and PC2 were weighted by the standard deviation of their scores across recordings (~1 for PC1, ~0.7 for PC2), to accurately represent each quadrant in Figure 16D-F and Figure 30F. Figure 16D shows the PC1 and PC2 scores for each recording of each subtype. In Figure 16F, recordings were color-coded based on the depth from brain surface at which they were recorded, as measured by the micromanipulator used to move the fiber during photometry.

In the PC1/PC2 space shown in Figure 16D, the angle of each point from the origin represents the shape of the cross-correlation between acceleration and ΔF/F, and thus the different relationships between subtypes' signaling and acceleration, while the distance from the origin represents the amplitude of the cross-correlation. To quantify the shape of the cross-correlation across subtypes, we calculated the angle of each recording in the PC1/PC2 space (with each PC weighted by its standard deviation) and plotted it in a radial histogram (Figure 16E). P-values for reporting statistical significance of the difference between subtypes across this PC1/PC2 space were calculating by opening the angular space at 45° (the region where the least recordings from Calb1/VGlut2/Anxa1 fall) and using a Wilcoxon rank-sum test with Bonferroni correction (multiply p-values by 3) to compare subtypes. This angle was also used to sort cross-correlation and triggered average heatmaps in Figure 15E-G and Figure 30C-E, starting by the middle of the quadrant opposite to the center of mass for each subtype. Figure 22D shows the location of each recording color-coded based on the PC1/PC2 angle for that recording. The colormap was defined by assigning a different color to each the middle of each quadrant (45°, 135°, 225°, 315°), where the center of mass of each subtype approximately falls at.

3.9.15. Analysis of responses to rewards and air puffs

Reward delivery times were only included when the mice consumed the reward (detected by the lick sensor) within a 1s window from delivery. For analysis of rewards delivered at rest, rewards were excluded if there were any accelerations greater than 2.5 m/s^2 (or decelerations greater than -2.5 m/s^2) in a window of 0.75s before or after the reward delivery, or any accelerations greater than 1.5m/s^2 (or decelerations greater than -1.5m/s^2) within a 0.4s window after the reward (where responses to rewards are detected). Triggered averages on rewards (Figure 10E, Figure 19E-E, Figure 29C), air puffs (Figure 19F, Figure 29D), and rewards at rest (Figure 19J) were calculated by averaging normalized ΔF/F traces (or licking traces for Figure 19E) in a 1s window before and after included reward or air puff delivery times.

For plotting of triggered averages above, traces were smoothed over 5 time-lag bins (0.05s). Shaded areas represent the mean ± standard error of the mean (s.e.m.), while accompanying heatmaps show triggered averages for all individual recordings. Heatmaps in Figure 10E, Figure 19D-F,J and Figure 29C-D were sorted by reward response size (see below).

To calculate the size of the response to each stimulus (change in fluorescence) shown in Figure 10F, Figure 19G-I,K, Figure 22B,E and Figure 29E-G, we calculated the difference between the cumulative fluorescence in a 0.5s window after each reward or air puff delivery time (+0.05 to +0.55 s) and the cumulative fluorescence in a 0.5s window before each reward or air puff delivery time (-0.5 to 0 s). The response to reward or air puff is defined as the average of this value for all reward or air puff delivery times in a recording. The response to rewards calculated in this manner was used to sort all reward and air puff triggered average heatmaps in Figure 10E, Figure 19D-F,J and Figure 29C-D. Heatmaps for air puff responses (Figure 19F, Figure 29D) were sorted by the corresponding reward responses for each recording, with recordings with no rewards being shown

at the top (mice not licking for certain recordings result in a higher number of recordings included for air puff than reward analysis). Figure 22F show the location of each recording color-coded based on the reward or air puff response for that recording, calculated in this manner.

P-values for reporting statistical significance for each subtype's responses to rewards and air puffs (Figure 19G, Figure 29E) used a non-parametric statistical test (Wilcoxon signed-rank test), with p-values corrected for the number of comparisons conducted (Bonferroni correction). P-values for reporting sensitivity to reward size (Figure 19I, Figure 29F) were calculated using a non-parametric paired statistical test (Wilcoxon signed-rank test), with Bonferroni correction, between the responses to small and large rewards in the same recording.

3.9.16. K-means clustering

K-means clustering was run using the MATLAB *kmeans* function for 3 clusters on the values of reward and air puff responses (see previous section for calculation) and the scores along the first two principal components (PC1, PC2) from the PCA analysis on cross-correlations between ΔF/F and acceleration traces, for all axonal recordings from Calb1, VGlut2 and Anxa1 subtypes where all measures were obtained (mice were running above threshold and received rewards and aversive stimuli, following the same inclusion criteria as previously explained). From the 3 resulting clusters, each subtype was matched to the cluster with the greatest overlap (each cluster was matched to a different subtype), and accuracy (Figure 22C) was calculated as the percentage of recordings classified within that cluster. Because this k-means clustering was run on a 4-dimensional dataset (reward, air puff, locomotion PC1 score, locomotion PC2 score), Figure 22B instead shows the combination of PC1 and PC2 scores as an angle, as calculated above.

Table 2: Key Resources Table 2

REAGENT or RESOURCE	SOURCE	IDENTIFIER
Antibodies		
Sheep anti-Tyrosine Hydroxylase (TH)	Pel-Freez	Cat# P60101-0, RRID:AB_461070
Rabbit anti-GFP (for GCaMP6f)	Thermo Fisher Scientific (Invitrogen)	Cat# A-11122, RRID:AB_221569
Donkey anti-Sheep Alexa Fluor 555	Thermo Fisher Scientific (Invitrogen)	Cat# A-21436, RRID:AB_2535857
Donkey anti-Rabbit Alexa Fluor 488	Jackson ImmunoResearch Labs	Cat# 711-545-152, RRID:AB_2313584
Goat anti-Aldh1a1	R&D Systems	Cat# AF5869, RRID:AB_2044597
Mouse anti-Tyrosine Hydroxylase (TH)	Sigma-Aldrich	Cat# T2928, RRID:AB_477569
Rabbit anti-Tyrosine Hydroxylase (TH)	Pel-Freez	Cat# P40101-0, RRID:AB_461064
Rat anti-mCherry	Thermo Fisher Scientific (Invitrogen)	Cat# M11217, RRID:AB_2536611
Donkey anti-goat Alexa Fluor 488	Molecular Probes	Cat# A-11055, RRID:AB_2534102
Donkey anti-mouse Alexa Fluor 647	Thermo Fisher Scientific (Invitrogen)	Cat# A-31571, RRID:AB_162542
Donkey anti-rabbit Alexa Fluor 647	Thermo Fisher Scientific (Invitrogen)	Cat# A-31573, RRID:AB_2536183
Donkey anti-rat Cy3	Jackson ImmunoResearch Labs	Cat# 712-165-153, RRID:AB_2340667
Rabbit Anxa1 antibody	Thermo Fisher Scientific	Cat# 71-3400, RRID:AB_2533983
Virus strains		
AAV1-CAG-FLEX-GCAMP6f	Addgene	RRID:Addgene_100835
AAV8-EF1α-CreOn/FlpOn-GCaMP6f	Addgene	RRID:Addgene_137122
AAV5-EF1α-DIO-mCherry	Addgene	RRID:Addgene_37083
Experimental models: Mouse strains		
Aldh1a1-2A-iCre	New line	N/A
Anxa1-iCre	New line	N/A
Calb1-IRES2-Cre	The Jackson Laboratory	Strain #:028532, RRID:IMSR_JAX:028532

VGlut2-IRES-Cre	The Jackson Laboratory	Strain #:016963 RRID:IMSR_JAX:016963
DAT-CRE	The Jackson Laboratory	Strain #:020080, RRID:IMSR_JAX:020080
Th-2A-Flpo	Poulin et al., 2018[23]	N/A
DAT-PF-tTA	The Jackson Laboratory	Strain #:027178, RRID:IMSR_JAX:027178
Ai93D (TITL-GCaMP6f)	The Jackson Laboratory	Strain #:024107, RRID:IMSR_JAX:024107
CAG-Sun1/sfGFP	The Jackson Laboratory	Strain #:021039, RRID:IMSR_JAX:021039
Oligonucleotides		
Primers for Cre strains Cre-F: GCAGAACCTGAAGATGTTCGC	Pereira Luppi et al., 2020[38]	N/A
Primers for Cre strain Cre-R: ACACCAGAGACGGAAATCCATC	Pereira Luppi et al., 2020[38]	N/A
Primers for Dat-tTA strain tTA-F: GTTCTCCAGGGTCTCGTACTG	New	N/A
Primers for Dat-tTA strain tTA-R: GTACTGGCACGTGAAGAACAAG	New	N/A
Primers for Ai93D strain mutant-F: ACGAGATCAGCAGCCTCTGT	New	N/A
Primers for Ai93D strain mutant-R: CTGAACTTGTGGCCGTTTAC	New	N/A
Primers for Ai93D strain wt-F: TTCCCCAACGGTCACTTACT	New	N/A
Primers for Ai93D strain wt-R: CACACCTTTAATCCCGATGC	New	N/A
Primers for Th-2A-Flpo line Th-F: TAAGACCCTGCTGATGGTTGG	Pereira Luppi et al., 2020[38]	N/A
Primers for Th-2A-Flpo Th-R (wt): CATAGGGCATTCCTGTGGTTTG	Pereira Luppi et al., 2020[38]	N/A
Primers for Th-Flpo line Flpo-R: GCTTCACTGAGTCTCTGGCATC	Pereira Luppi et al., 2020[38]	N/A
Primers for Aldh1a1-iCre line iCre-F: AGATCCCTGATGGAGAACTCTG	New	N/A

Primers for Aldh1a1-iCre line iCre-R: CATCCTTGGCACCATAGATCAG	New	N/A
CRISPR mediated HDR guide 1: ACGACTATGCTGGTTAC	New	N/A
CRISPR mediated HDR guide 2: TCCCCCTTTAGGGGTGAGCA	New	N/A
CRISPR mediated HDR guide 3: AAGATTCTGGTGGCCCTCTG	New	N/A
CRISPR mediated HDR guide 4: ACTTAAGCCCATGCCAT	New	N/A
Aldh1a1-iCre insertion primers F1: CTATTCACTTGCAGTTGGCTTGG	New	N/A
Aldh1a1-iCre insertion primers R1: GTCCAGGGTTCTCCTCCACG	New	N/A
Aldh1a1-iCre insertion primers F2: GCTTGGAGGTTTCCTAAGTGTG	New	N/A
Aldh1a1-iCre insertion primers R2: GCATGATTTCAGGGATGGACAC	New	N/A
Aldh1a1-iCre insertion primers F3: AGATCCCTGATGGAGAACTCTG	New	N/A
Aldh1a1-iCre insertion primers R3: CATCCTTGGCACCATAGATCAG	New	N/A
Software and other resources		
MATLAB R2021a	MathWorks	https://www.mathworks.com/products/matlab.html
ImageJ	NIH	https://imagej.nih.gov/ij/
LabView	National Instruments	https://www.ni.com/en-us/shop/labview.html
Picoscope6	Pico Technology	https://www.picotech.com/oscilloscope/2000/picoscope-2000-overview
Paxinos and Franklin's the Mouse Brain in Stereotaxic Coordinates	Book	https://books.google.com/books/PaxinosMousBrainAtlas
R version 4.0.2	The R Project for Statistical Computing	https://www.r-project.org/
RStudio Version 1.2.5042	RStudio	https://www.rstudio.com/products/rstudio/download/
Saunders et al. RNAseq data	Saunders et al. 2018[48]	https://www.Dropviz.org

Tiklova et al. RNAseq data	Tiklová et al., 2019[49] PMID: 30718509	GEO: GSE116138
Kramer et al. RNAseq data	Kramer et al. 2018[45]	GEO: GSE115070
La Manno et al. RNAseq data	scRNAseq R Package	LaMannoBrainData() Command; https://bioconductor.org/packages/release/data/experiment/html/scRNAseq.html
Seurat R Package Versions 3.2.0, 4.0.2	CRAN	https://cran.r-project.org/web/packages/Seurat/index.html
LIGER R Package	Welch Lab Github	https://github.com/welch-lab/liger
scRNAseq R Package	Bioconductor	https://bioconductor.org/packages/release/data/experiment/html/scRNAseq.html
VS-ASW-S6	Olympus	https://www.olympus-lifescience.com/en/microscopes/virtual/vs120/
cellSens	Olympus	https://www.olympus-lifescience.com/en/software/cellsens/
ALRA R Package	Kluger Lab Github	https://github.com/KlugerLab/ALRA
Custom code		
MATLAB scripts for analysis	New	https://github.com/orgs/DombeckLab/repositories/Azcorra2022

4. Axons track somatic signaling within subtypes

4.1. Introduction

As we have discussed, midbrain DA neurons play a role in a wide range of behaviors[2,3,5–7,12,109,113,157], and a major target of these neurons is the striatum, where dopamine is released by their axons. However, it is currently unclear whether this dopamine release is driven mainly by somatic firing or by local striatal mechanisms. For decades, it was assumed that striatal dopamine release was controlled by anterogradely propagating action potentials originating in the midbrain somas; but this classical view has recently been called into question by research demonstrating the ability of local mechanisms to control striatal dopamine release independently of midbrain somatic firing[13,36,37,126,158].

Mechanistically, *in vitro* studies have shown that coordinated activation of striatal cholinergic interneurons can not only modulate, but also trigger dopamine release in the absence of somatic firing[36,37,126,158]. Pioneering *in vivo* studies have recently provided strong support for the idea that this local mechanism plays a significant role in dopamine release during behavior. One study recorded striatal dopamine and acetylcholine release dynamics (using fluorescent sensors and photometry recordings) during movement in freely behaving mice and found that dopamine and acetylcholine signaling co-varied with mouse movement direction, and that inhibition of nicotinic receptors in striatum decreased dopamine signaling[37]. Another study recorded VTA cell body firing (with single-unit recording) and striatal dopamine release (with photometry of a fluorescent dopamine sensor and microdialysis) during a reward-based choice task and found that dopamine release from striatal axons co-varied with reward expectation, while firing in the midbrain somas did not[13]. This study further observed fast striatal dopamine release during certain behavioral

epochs that did not correspond with somatic firing, suggesting these differences were due to local modulation. Thus, cholinergic mechanisms can drive dopamine release independently of somatic firing, and both *in vivo* covariations of dopamine-acetylcholine signaling and differences between midbrain somatic firing and striatal dopamine release dynamics support the idea that these mechanisms are relevant during behavior.

However, establishing that dopamine is released from axons independently of somatic firing *in vivo* requires that axonal and somatic recordings are made from the same neurons[29]. Thus, an alternative explanation for any observed soma-axon signaling differences is that the striatal dopamine detected was released by a different set of axons than those belonging to the recorded somas–an experimental recording problem that could be rectified by labeling and recording from only one genetic subtype at a time.

4.2. Somas of DA subtypes show similar functional responses as their axons

Isolating genetic subtypes allowed for the identification of clear differences in functional responses within axons (Chapter 3); however, it is still possible that local cholinergic modulation could explain these differences, since axonal arbors of different subtypes are densest in different regions, and these regions could be differently modulated by acetylcholine. Thus, we first asked whether the somas of these same subtypes show distinct functional responses, and whether these were similar to their corresponding axons.

We repeated the photometry recording experiments conducted in Chapter 3 but placing the optic fiber in SNc instead of striatum (in the somas, GCaMP transients are caused by somatic action potential firing[155]). We found that, just as in the axonal recordings, Calb1+ and Vglut2+ somas responded to rewards and air puffs, while no detectable reward response was found in Anxa1+

Figure 28: Somas of DA subtypes show different responses to rewards, and aversive stimuli

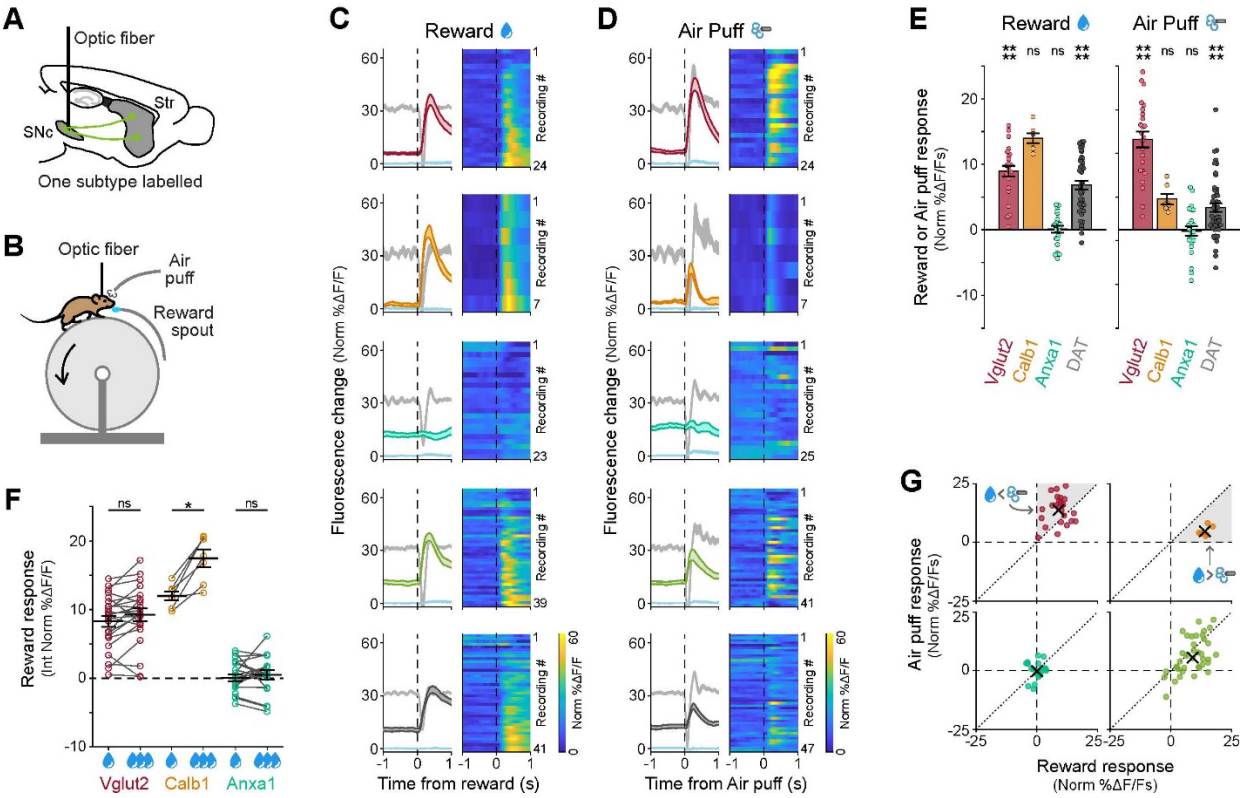

(**A**) Schematic of fiber photometry recording strategy, with optic fiber placed in SNc.

(**B**) Mouse running on treadmill during fiber photometry while receiving unexpected rewards and air puffs.

(**C-G**) Same as Figure 19D,F,G-I but for recordings made in SNc.

(**C**) ΔF/F averages triggered on reward delivery times for all recordings of each subtype and DAT. Isosbestic control shown in light blue, same scale as ΔF/F average. Acceleration shown in gray in the background (scale bar = 0.2 m/s^2). Shaded regions denote mean ± s.e.m. Heatmap shows triggered average for each recording, sorted by size of reward response. Vglut2 mice = 8, n = 24 recordings; Calb1 mice = 4, n = 7; Anxa1 mice = 6, n = 23; Aldh1a1 mice = 10, n = 39; DAT mice = 8, n = 41.

(**D**) ΔF/F averages triggered on air puff delivery times for all recordings of each subtype and DAT. Isosbestic control shown in light blue, same scale as ΔF/F average. Acceleration shown in gray in the background (scale bar = 0.2 m/s^2). Shaded regions denote mean ± s.e.m. Heatmap shows triggered average for each recording, sorted by reward size as in C. Vglut2 mice = 8, n = 24 recordings; Calb1 mice = 4, n = 7; Anxa1 mice = 6, n = 25; Aldh1a1 mice = 10, n = 41; DAT mice = 8, n = 41.

(**E**) Average reward and air puff responses for each subtype. Error bars denote ± s.e.m. p-values for reward: Vglut2 = 7 x10^{-05}, Calb1 = 0.06 (not significant), Anxa1 = 1 (not significant), DAT = 5 x10^{-07}. p-values for air puff: VGlut2 = 7 x10^{-05}, Calb1 = 0.06, Anxa1 = 1 (not significant), DAT = 3 x10^{-05}. Wilcoxon signed-rank test with Bonferroni correction.

(**F**) Comparison of responses to small vs large rewards for each subtype. Error bars denote mean ± s.e.m. p-values: Vglut2 = 0.1 (not significant), Calb1 = 0.047, Anxa1 = 1 (not significant). Paired Wilcoxon Signed Rank test with Bonferroni correction.

(**G**) Reward vs air puff responses for all recordings of each subtype and DAT. X shows mean for each subtype. Shaded regions are areas representing greater air puff than reward response (for Vglut2) or greater reward vs air puff response (for Calb1).

somas (Figure 29C-E). Calb1+ somas also showed greater responses to rewards and air puffs, and Vglut2+ somas on average had greater responses to air puffs than rewards (Figure 29G), as their axons did. Calb1+ somas also showed greater responses to larger rewards (Figure 29F). Furthermore, soma recordings from each of the subtypes showed highly similar signaling during locomotion compared to axons (Figure 30); though there were some slight differences (SNc recordings for each subtype fell slightly clockwise in the PC1/PC2 space compared to their axons), Calb1+, Vglut2+ and Anxa1+ recordings were well separated.

Finally, SNc recordings fell into the same, separable regions of the 3D functional space as axonal recordings of the same subtypes (Figure 31A) – though in SNc Calb1+ and Vglut2+ are functionally less well separated, unsurprisingly given that it is harder to anatomically avoid Calb1+/Vglut2+ neurons when recording the Calb1+ subtype in somas. Thus, axons and somas of the same dopamine neuron subtype displayed highly similar signaling during locomotion and responses to rewards and aversive stimuli. This is further evidence that functional responses map onto genetic subtypes, as somas of individual subtypes intermingled to a fair degree in SNc, particularly within the photometry recording volume.

4.3. Highly correlated signaling in somas and axons of isolated subtypes

However, it is still possible that somas and axons could have similar correlation to movements or stimuli, but low correlations to each other (for example, somas and axons could be active at different accelerations or stimuli). Therefore, we performed simultaneous striatal axon and SNc soma recordings. Before recording from dopamine neuron subtypes, we first asked whether we could reproduce the soma-axon signaling differences previously described in non-subtype specific recordings[13], but with GCaMP and in head-fixed mice running on a treadmill. We labelled non-

Figure 29: Somas of DA subtypes show different signaling during locomotion

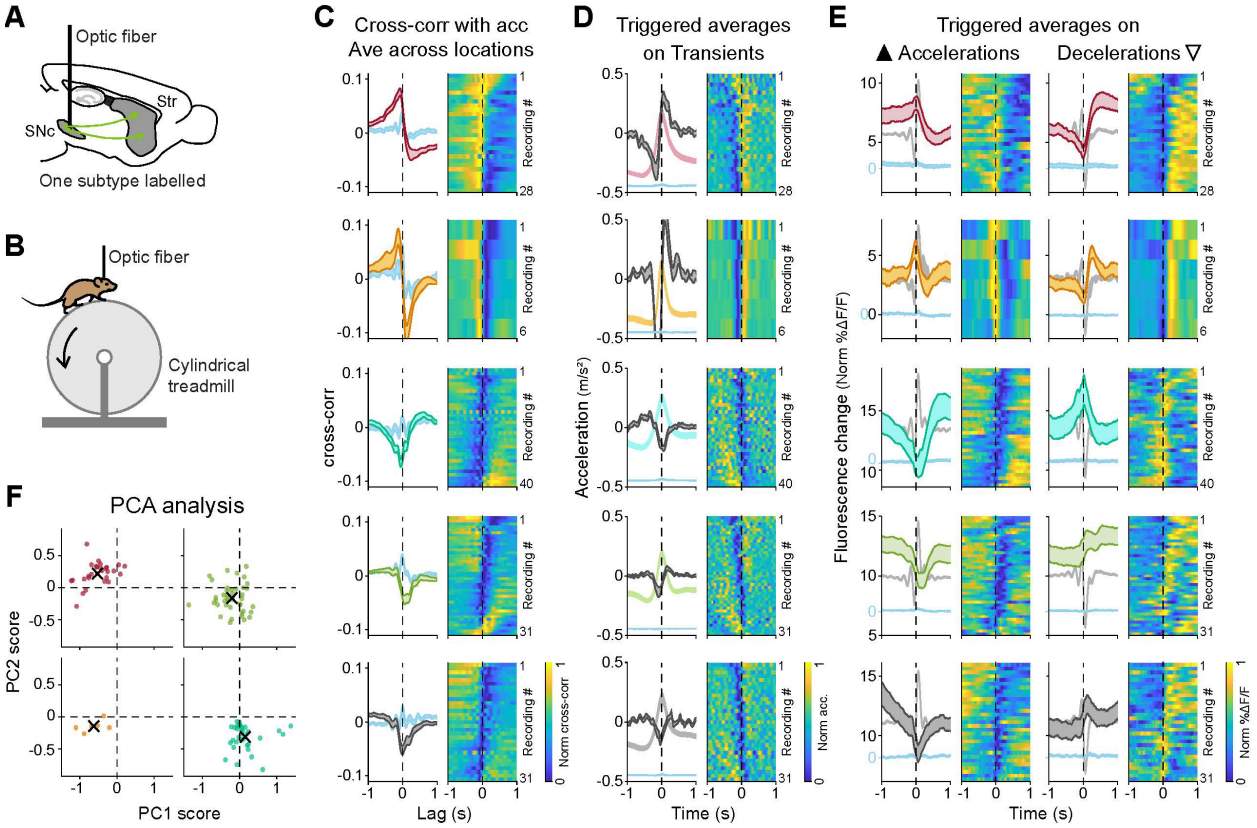

(**A**) Schematic of fiber photometry recording strategy, with optic fiber placed in SNc.

(**B**) Mouse running on treadmill during fiber photometry.

(**C-E**) Same as Figure 15E-G but for recordings made in SNc.

(**C**) Average cross-correlation between ΔF/F traces and acceleration for all recordings of each subtype. Isosbestic control shown in blue. Shaded regions denote mean ± s.e.m. Heatmap shows cross-correlation for each recording, sorted by PC1/PC2 angle (see Fig. 2L). Vglut2 mice = 11, n = 28 recordings; Calb1 mice = 3, n = 6; Anxa1 mice = 8, n = 34; Aldh1a1 mice = 12, n = 41; DAT mice = 8, n = 31.

(**D**) ΔF/F averages triggered on large accelerations (left, ▲) and large decelerations (right, ▽) for all recordings of each subtype. Isosbestic control shown in light blue, same scale as ΔF/F average but shifted. Acceleration shown in gray in the background (scale bar = 0.2 m/s2). Shaded regions denote mean ± s.e.m. Heatmap shows triggered average for each recording, sorted as in C.

(**E**) Acceleration averages triggered on large transients for all recordings of each subtype. ΔF/F average and isosbestic control shown in the background (scale bar = 5% Norm ΔF/F.) Shaded regions denote mean ± s.e.m. Heatmap shows triggered average for each recording, sorted as in C.

(**F**) Principal component scores for each recording of each subtype along PC1 and PC2 (same PCs obtained from the striatal recordings, as shown in Figure 16C-E). X shows mean for each subtype.

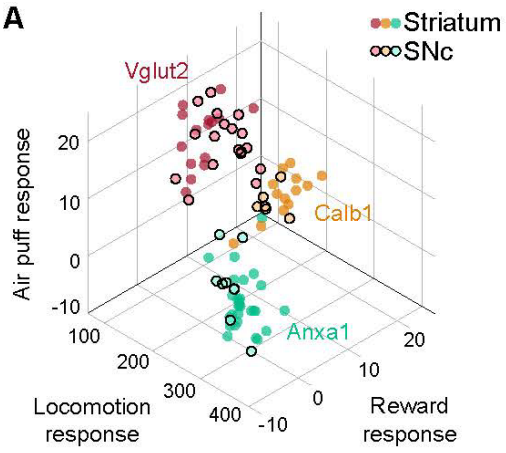

Figure 30: Functional responses of DA subtype somas are similar to their axons

(**A**) 3D functional plot showing locomotion (PC1/PC2 angle), reward and air puff responses for each recording and each subtype, comparing striatal recordings (same as Figure 22B) and SNc recordings.

subtype-specific dopamine neurons (DAT mice) and used fiber photometry to simultaneously record from populations of axons in the striatum with one fiber and SNc somas with another fiber (Figure 32A-B). We recorded from a range of random locations within striatum and SNc and often observed highly dissimilar signaling (ΔF/F) between striatal axons and SNc somas (Figure 32C top). Accordingly, the mean cross-correlation between axonal and somatic ΔF/F traces (Figure 32D-E top) was 0.37, which is a relatively low correlation for traces that have similar temporal dynamics (in contrast to cross correlations between ΔF/F and accelerations where the traces have dissimilar temporal dynamics, as in Figure 15). Therefore, similarly to previous reports[13], we found somatic and axonal dopamine neuron signaling that was often very different when dopamine neurons are indiscriminately labelled.

In contrast, when we repeated these soma-axon recordings from isolated subtypes (Vglut2+, Calb1+, and Anxa1+), we found highly similar signaling between striatal axons and SNc somas (Figure 32C middle), resulting in high cross-correlations (Figure 32C' middle), and this was consistent across recordings (Figure 32D-E middle). On average, the cross-correlation between soma and axon ΔF/F recordings was significantly higher compared to DAT+ recordings

Figure 31: Highly correlated signaling in axons and somas within genetic subtypes of dopamine neurons

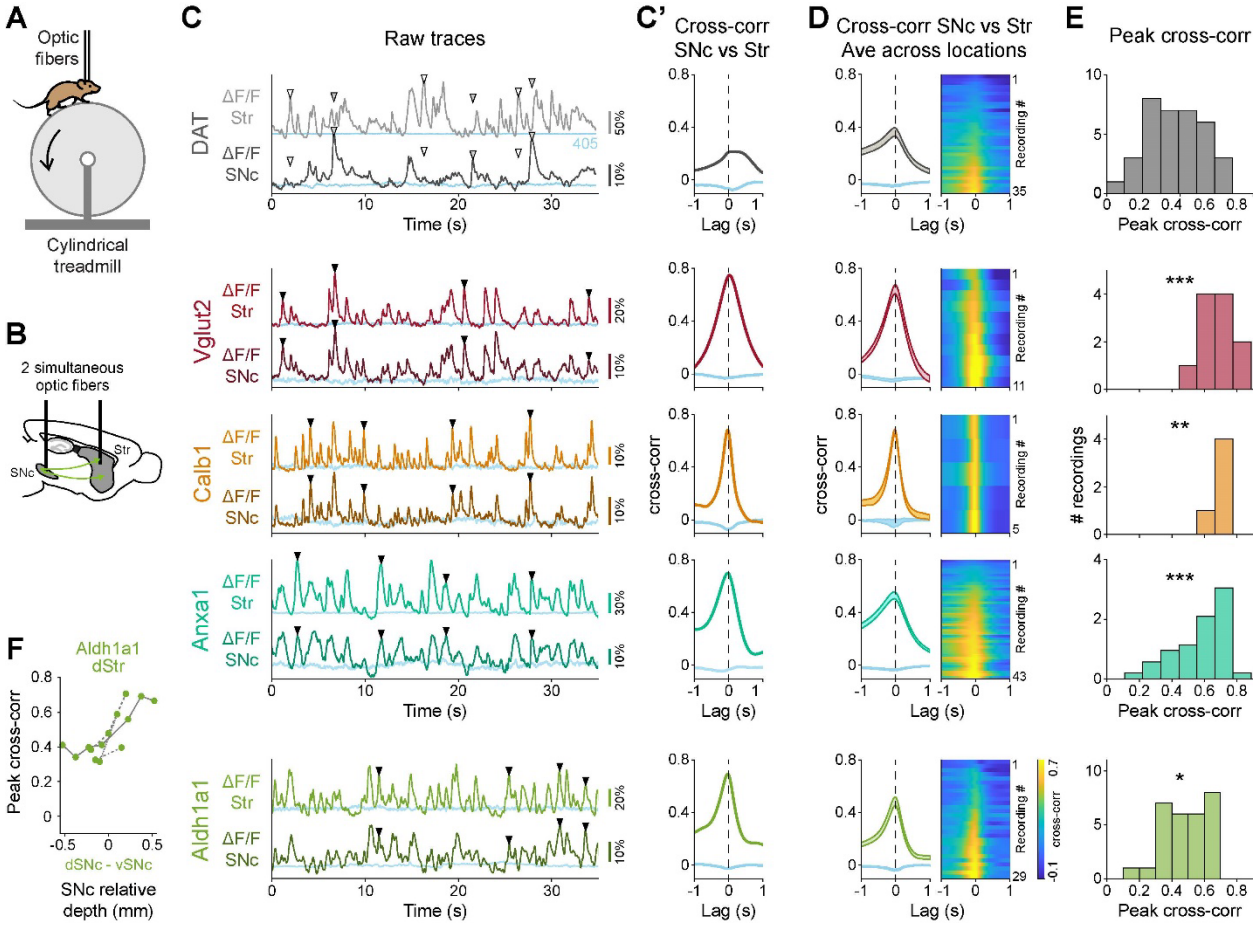

(**A**) Mouse running on treadmill during dual fiber photometry.

(**B**) Schematic of simultaneous photometry recordings from SNc and striatum.

(**C**) Example recordings for DAT and each subtype showing simultaneous fluorescence traces (ΔF/F) from SNc and striatum. Isosbestic controls in blue. ▼= Example transients present in SNc and in striatum, ▽= example transient present in striatum but not in SNc (white fill) or vice-versa (gray fill).

(**C'**) Cross-correlation between ΔF/F traces from striatum and SNc shown in C. Isosbestic controls in blue.

(**D**) Average cross-correlation between simultaneous ΔF/F traces from striatum and SNc for all recordings of each subtype and DAT. Isosbestic controls in blue. Shaded regions denote mean ± s.e.m. Heatmap shows cross correlations for each paired recording sorted by peak magnitude. DAT mice = 5, n = 35 recordings; Vglut2 mice = 4, n = 11; Calb1 mice = 2, n = 5; Anxa1 mice = 8, n=43; Aldh1a1 mice = 8, n = 29.

(**E**) Distribution of peak cross correlations between SNc and striatum for recordings of all subtypes and DAT shown in E. P-values for comparison to DAT: Vglut2 = 3 x10^{-04}, Calb1 = 3 x10^{-03}, Anxa1 = 3 x10^{-04}, Aldh1a1 = 0.03 (Mann-Whitney U test with Bonferroni correction).

(**F**) Peak cross correlations between dorsal striatum recordings from Aldh1a1 vs different relative depths in SNc, showing that for Aldh1a1 dorsal striatum signaling is best correlated to ventral SNc.

(Figure 32D-E; mean = 0.65 for Vglut2+, 0.67 for Calb1+, 0.58 for Anxa1+, compared to 0.37 for DAT; p-values for comparison with DAT+ = $3x10^{-04}$ for Vglut2+, 0.003 for Calb1+, $3x10^{-04}$ for Anxa1+, Mann-Whitney U test with Bonferroni correction). Overall, we conclude that recording from isolated dopaminergic functional subtypes leads to highly similar signaling patterns between somas and axons in behaving mice.

Results from Aldh1a1+ on the other hand were in agreement with it being a functionally heterogeneous population which includes Anxa1+ neurons and others which are functionally more similar to Calb1+ neurons. While some simultaneous SNc/striatum recordings showed high correlations between somatic and axonal transients (Figure 32C bottom), several other recordings had very low correlation peaks, probably due to somas and axons of different sub-populations being recorded. Further evidence in favor of this idea comes from utilizing the anatomical bias of Anxa1+ neurons and their axons within Aldh1a1+: when we plotted the cross-correlation peak between recordings from dorsal striatum axons and different depths within SNc (Figure 32F), we found that dorsal striatum Aldh1a1+ axons (where most are Anxa1+, Figure 13C) are best correlated with ventral SNc somas (where Anxa1+ neurons predominate, Figure 13A-B). This further supports the idea that differences in somatic and axonal signaling are due to recordings from different subtypes in each compartment, not necessarily cholinergic modulation.

4.4. Discussion

Here, we used fiber photometry to record calcium transients in SNc somas of isolated DA subtypes in head-fixed mice running on a treadmill and receiving unexpected rewards and aversive air puffs, replicating our axonal recordings in Chapter 3. We found that the somas of different subtypes show different signaling responses to locomotion, rewards and air puffs and, importantly, that these

responses match what we observed the corresponding subtypes' axons. This is further evidence that subtype identity determines function, as somas of subtypes in SNc densely overlap, especially within the ~300 μm volume of our photometry recordings. Furthermore, the close similarities between somatic and axonal functional responses shows that these responses are not exclusive to the axonal compartment, and thus it is unlikely that they would be generated there by local modulation.

Next, we simultaneously recorded from somas and axons to determine whether these compartments showed highly correlated transients. When we recorded in DAT-Cre mice, where all dopaminergic subtypes were indiscriminately labelled, we observed large discrepancies between axonal and somatic signaling, similar to previous observations from VTA dopaminergic neurons[13] and consistent with the idea that local cholinergic signaling plays a significant role in striatal dopamine release during behavior[37]. However, when the diversity of dopaminergic neurons was taken into account, we found high correlation between somatic and axonal signaling. This is consistent with the classical view that striatal dopamine release is controlled by anterogradely propagating action potentials originating in midbrain somas, rather than by local striatal modulation controlling dopamine release. This finding is also in agreement with previous reports demonstrating that cholinergic interneurons and dopamine axons in striatum are often desynchronized during behavior[159], making it difficult to explain the majority of dopamine release based on local cholinergic control.

However, this does not exclude the possibility that local cholinergic modulation may still play a role in controlling dopamine release at specific behavioral time points. For example, striatal dopamine and acetylcholine signaling have been found to synchronize at certain times during behavior, such as at locomotion initiation or during turning[37,159]. Regardless, our results here

provide evidence that axons track somatic signaling within dopaminergic subtypes, indicating that such subtypes should be considered in order to fully understand the mechanisms of dopamine release in striatum during behavior.

4.5. Methods

Experiments in this chapter were conducted and analyzed following the exact same methodology as those in Chapter 3, except when specified below.

4.5.1. Principal component analysis (PCA) of locomotion signaling in SNc

For SNc recordings, the cross-correlations between ΔF/F and acceleration for all recordings of all subtypes, as shown in Figure 30C, were decomposed using the same principal components calculated in Chapter 3 from the striatal cross correlations. Scores for SNc cross-correlations (Figure 30F) were calculated by multiplying the matrix of all SNc cross-correlation traces by the striatal loadings matrix (principal components). The % of SNc variance explained by each principal component (PC1 = 53.2% of variance, PC2 = 24.3%) was calculated as the variance without the mean subtracted (not centered).

4.5.2. Cross-correlation between SNc and striatum ΔF/F traces

All simultaneously recorded pairs of SNc/striatum recordings where both traces had a signal-to-noise ratio above 10 were included, regardless of behavior. Cross-correlations between SNc and striatum ΔF/F traces were calculated using MATLAB's *crosscorr* function over a 1s time-lag window (100 bins). For the isosbestic control cross-correlation shown in Figure 32C'-D, we calculated the cross-correlations between SNc-470 and striatum-405 ΔF/F traces and also between SNc-405 and striatum-470 ΔF/F traces, and averaged the resulting cross-correlation traces

together. Any pairs of recordings with a peak 405/470 average cross-correlation above 0.12 were excluded.

For plotting in Figure 32D, 405 and 470 cross-correlations were smoothed over 5 bins (0.05s). Shaded areas in represent the mean ± standard error of the mean (s.e.m.), while accompanying heatmaps show cross-correlations for all recordings. For comparison of peak cross correlations between each subtype and DAT (Figure 32E) we used a non-parametric statistical test for two independent populations (Mann-Whitney U test, also called Wilcoxon rank-sum test), with Bonferroni correction (p-values were multiplied by the number of comparisons performed).

4.5.3. Calculation of relative depth within SNc

For SNc recordings, due to the tilted nature of its main axis with respect to the brain surface and due to its small width (in depth), we used a measure of relative depth along the dorso-ventral axis (Figure 32F). To calculate this, for each session we considered dorsal-SNc the most dorsal depth at which significant transients were observed, and ventral-SNc the most ventral depth at which transients were observed. Relative depth was then measured with respect to the middle between the dorsal and ventral most depths, in mm.

5. Discussion

5.1. Summary of results

Given the functional diversity observed within DA neurons in the literature, and particularly how dopamine neurons projecting to different regions seem to show different functional responses, we hypothesized that different DA subtypes might each have a different function. Thus, we sought to test whether genetic subtypes of DA neurons, which have been previously described and can be accessed, show different functional responses even independently of their anatomy.

We first compared the functional responses of Sox6+ and Sox6- neurons, as this constitutes a main division of DA neurons. However, while we found differences in many aspects including their anatomical location in mice (both somas, Figure 1, and axons, Figure 2) and humans (Figure 4), their vulnerability in PD (Figure 4), their expression profiles (Figure 5), their developmental origin (Figure 6, Figure 7), and even their function (Figure 8), these were not functionally homogeneous populations. Despite technical challenges with recording from Sox6- axons, Sox6+ axons showed functional differences depending on their projection targets, and recordings from somas did not show clear differences between both subtypes.

Given this information, we moved to characterize a second level of division within SNc DA neurons but found that Aldh1a1+, a subset of Sox6+ neurons, was also functionally heterogenous (Figure 10). Thus, we reexamined the existing DA neuron classification schemes to search for new genetic subtype within the Aldh1a1+, and used a double approach (a meta-analysis of existing single-cell RNA-seq datasets, and a new single-nucleus RNA-seq dataset) to identify a new subtype characterized by the expression of Anxa1+.

Next, we functionally characterized the new Anxa1+ subtype together with two other SNc subtypes, Calb1+ and Vglut2+, which together make up the majority of SNc DA neurons, by analyzing calcium transients in axons of each subtype in striatum. We found that Anxa1+ neurons show acceleration-locked signaling (Figure 15) and do not respond to rewards or aversive stimuli (Figure 19), while Calb1+ and Vglut2+ neurons both show deceleration-locked signaling (Figure 15) and do respond to rewards and aversive stimuli (Figure 19), but with some differences. On one hand, their signaling during locomotion showed timing differences with respect to decelerations (Figure 16). On the other hand, Vglut2+ neurons had greater responses to air puffs than rewards, while Calb1+ neurons had greater responses to rewards, and these responses were sensitive to the size of the reward (which was not the case for Vglut2+ neurons) (Figure 19). Furthermore, all these differences were maintained even in regions of striatum where axons from different subtypes overlap (Figure 22), indicating that genetic subtype identity and not just the anatomical projection region determines their functional responses.

Finally, we confirmed that the somas of each of these subtypes showed the same signaling responses than their corresponding axons (Figure 31), and used simultaneous recordings from somas and axons to demonstrate that axonal signaling matches somatic signaling (Figure 32). This demonstrates that these signaling differences we observed between subtypes do not originate in the axons, for instance due to local modulation, but are similarly found in the somas, and must therefore be intrinsic to the genetic identity of each subtype.

5.2. Benefits and limitations of our approach

5.2.1. Accessing genetic subtypes of dopamine neurons

For decades, DA neurons in the midbrain were differentiated only anatomically, based on their location in the SNc, the VTA, or the Retrorubral area (RR)[84]. Some studies were able to identify genetic markers that were differentially expressed among these clusters[160,161], but technical limitations, which restricted the number of genes that could be studied per cell, prevented finer classifications. This is because a single marker is rarely sufficient to identify a genetic neuronal subtype[52,162,163]. Thus, it was not until the advent of single-cell transcriptomics, which allowed the study of the expression profiles of multiple genes within single cells, that genetic classification of DA neurons beyond anatomy have arisen[28]. These techniques allow the unbiased clustering of cells into subtypes by their full expression fingerprints, with each group later assigned an identifying marker gene *post hoc*[28].

However, identifying these marker genes is not trivial, particularly when subtypes are closely related. DA neurons share the expression of all typical neuron genes, plus those genes required for the synthesis, packaging, and release of DA[28]. Thus, only a small subset of genes are differentially expressed between DA subtypes and, even then, most differ only in their level of expression. This complicates the task of identifying unique marker genes for each subtype as, ideally, these are genes that are strongly expressed in one subtype, consistently in all cells of that subtype, and absent from all other subtypes. Due to these limitations (and other problems with single-cell sequencing techniques), the available marker genes for DA neurons are still not perfect. This explains, for example, while key markers of SNc DA subtypes are also expressed in VTA subtypes (like Vglut2), and why the marker for one of our subtypes (Calb1) labels the Vglut2+ subtype too. While we can use anatomical constraints to supplement the genetic strategy (by injecting in SNc and

avoiding VTA labelling, or by recording from striatal regions where Calb1+ but not Vglut2+ axons project to), the field would greatly benefit from the identification of unique markers for each subpopulation. Particularly important, given our results, would be the search for a unique marker of Calb1+/Vglut2- neurons, which are harder to separate anatomically than VTA vs SNc subtypes – though it is possible that such genes do not exist.

Another limitation of some of our marker genes is their expression beyond DA neurons (for example, Vglut2 is widely expressed in glutamatergic neurons throughout the brain). Here too we employ a secondary strategy, using intersectional genetics that limit labelling to cells that express not only the marker gene but also a DA neuron specific gene like Th or DAT (Figure 27B-D). However, this significantly increases the complexity of the reporters required –flex-reporters can be easily and rapidly modified from any existing reporter by just flipping the coding region and adding flanking loxP sequences[164], while intersectional reporters require splitting the coding region in two by an intron and setting each section under the control of a different recombinase, then checking that splicing is not impaired, that the final protein is correctly translated and functional, and that expression of half of the protein (in cells expressing one recombinase only) is not deleterious or partially functional[117]. Due to this, there is a limited catalog of intersectional reporters[117,149] compared to the wide range of Cre-dependent reporters, and the availability of novel reporters in their intersectional forms can be substantially delayed compared to their Cre-dependent versions (for example, AAV-Flex-GCaMP6f was available in 2013[116] while the intersectional version wasn't commercially available until 2020[117]).

Therefore, it is important to continue the efforts to refine the classification of DA neurons and the markers used to access each subtype. As we have discussed, the main limitation of previous single-cell RNA sequencing studies was the small number of DA neurons included in each study[28], which

complicates the identification of smaller or more closely related clusters. In particular, this strategy is dependent on the survival of intact neurons, which is not equally feasible in all brain regions and for all cell types[128] – it is thus possible that, given that not all DA subtypes are equally vulnerable to generation in humans (Figure 4E-H) or mice[47], the most vulnerable DA subtypes (Aldh1a1+ and thus Anxa1+) are underrepresented in these datasets. We attempted to address these limitations in a two-pronged approach: by integrating existing single-cell RNA-seq datasets from previous studies (Figure 11) and by using single-nucleus RNA-seq to generate a new, larger dataset (Figure 12). However, these strategies still have limitations. The meta-dataset analysis is still limited by biases introduced by individual source datasets and by cross-dataset integration methods, and by any differential survival of subtypes during the process of single-cell isolation. Furthermore, while our single-nucleus RNA-seq dataset includes an order of magnitude more cells than previous single-cell studies and does not require intact cell survival, it is only able to detect a smaller subset of RNAs which are actively being transcribed[128]. Thus, genes with low expression levels might not be detected in some cells, leading to their under-representation. This can be addressed, as we did, using ALTRA zero-preserving zero-imputation[153], which increases the detection of low-expression genes while preserving true biological zeros; but this technique introduces its own biases.

On top of the imperfections of genetic markers of DA subtypes, Cre lines and recombination-based reporters have their own limitations. Cre-mediated excision will never be 100% efficient (and Flp recombination even less)[164], so not all cells of a certain subtype will be labelled (for example, in our Calb-Cre/DAT-tTA/Ai93D genetic strategy only few VTA cells are labelled, when most of them express Calb1). This is less critical for the functional characterization of subtypes presented here, but it might be important for future experiments such as optogenetic inhibition of subtypes,

whose effectiveness would depend on the Cre-recombination efficiency. On the other hand, false positives (cells that do not express the marker gene but where Cre-recombination does take place) could be of concern. For instance, when recording from a subtype like Anxa1+ that does not show any response to rewards, a couple mis-labelled Calb1+ cells could cause a reward response to be detected above baseline. This could be the case with our Aldh1a1-iCre mouse line where, though only 4%, a few dorsal SNc Aldh1a1- cells are labelled (Figure 24B-C) – though it's unclear how much they contribute to the functional heterogeneity detected in Aldh1a1+ (Figure 10). Either way, recombinase strategies result in a binary expression pattern that does not parallel normal expression of genes and can result in unexpected labelling – for example, Anxa1+ expression in SNc cells can be either high, low or absent, and different genetic strategies can label only high-Anxa1 cells or both high and low-Anxa1 cells, resulting in different subsets of cells being studied.

However, with greater numbers of cells and genes measured comes the possibility of further and further subdividing neurons into more and more subtypes, and there is no clear criteria to determine where to stop: it is impossible to distinguish from gene expression alone what variability is relevant for the neuron identity and what isn't. For instance, our sn-RNA seq dataset identifies 11 DA clusters (Figure 12B), but the expression of the subtype marker genes studied in this work spans multiple of those clusters. It is thus possible that, either the subtypes here can be further subdivided into finer subtypes (as was done with the Aldh1a1+ and Anxa1+ subtypes), or that 11 clusters are too fine-grained and there are less subtypes. This is to say, classifications of DA neurons have little meaning until they have been validated by establishing their behavioral relevance.

Finally, it is important to highlight that the overlap between the subtypes we studied as well as the percentage of all SNc DA neurons that they account for are still unknown. While in Figure 14A we show an approximate scheme of the overlap between subtypes, it is inferred from gene

expression data and is yet to be validated and quantified. This is important to answer several questions: (i) are there additional subtypes within the SNc that we have not studied and might have their own unique role, or have we characterized the whole SNc? (ii) Are Aldh1a1+/Anxa1- neurons Calb1+, as their functional characterization suggests? Or are they a new subtype that we lack access to? What about Sox6+/Aldh1a1- cells? (iii) How many neurons are labelled in several subtypes? Are these negligible/artifacts? Which identity predominates?

5.2.2. Calcium indicators for recording neuronal signaling

As we have previously discussed, GCaMP is ideally suited for the functional characterization of DA subtypes because it allows functional recordings from axons and somas of genetically defined neurons. In the somas GCaMP transients are caused by somatic action potential firing[155], and in axons calcium transients can be used as a proxy for DA release[137], as all known mechanisms for triggering axonal DA release involve increases in intracellular calcium concentration[119,120,134], including anterogradely propagating action potentials[121–125] and cholinergic modulation[37,126]. Critically, the detected calcium transients are generated only from the labeled genetic subtype; non-labeled neurons do not contribute. This could be achieved in somas with electrophysiology and opto-tagging (linking spikes to genetically defined subtypes by expressing a light-gated ion channel like ChR2 in cells expressing a subtype marker, then activating those neurons with light pulses to identify those responding with action potentials)[6,13], but this is not feasible in the axons, as any recordings from striatum would be dominated by action potentials from medium spiny neuron and interneuron somas rather than dopaminergic axons. An alternative for recording from axons would be using extracellular dopamine sensors (i.e. dLight, GRAB-DA, microdialysis, voltammetry), but axons from different subtypes can densely overlap in the striatum[17] and these

sensors detect dopamine released from all nearby axons – thus, subtype specificity could not be achieved in areas of overlap, which can instead be done with GCaMP.

Another benefit of GCaMP recordings is that, for simultaneous recordings of somatic and axonal signaling (Figure 32), transients from both compartments have similar timescales and dynamics, which makes it much easier to compare. Previous studies recorded action potentials in somas and dopamine release in axons[13], which have drastically different timescales and thus their differences are hard to interpret.

GCaMP however also has its own limitations. For starters, it is prone to movement artifacts (through electrophysiological recordings and other optical reporters, such as dLight or GRAB-DA, are similarly affected). This is because movements of the brain relative to the recording optic fiber could cause a change in measured light due to local unevenness in GCaMP expression levels (changes in light because of changes in GCaMP concentration, not calcium-driven changes in the fluorescence of individual GCaMP molecules). Nonetheless, we control for these movement artifacts by simultaneously recording GCaMP fluorescence at its isosbestic wavelength, 405 nm[118]: this means that when illuminated at 405 nm, GCaMP is still fluorescent, but its intensity does not vary with calcium concentration. Thus, any calcium-independent changes in fluorescence will be detected at 405 nm illumination, which can then be used to correct[129,165,166] or exclude[167] traces from 470 nm illumination (calcium-dependent). Here we chose to exclude traces with movement artifacts rather than correcting them for two main reasons. On the one hand, correction procedures increase noise[167], and the relationship between GCaMP fluorescence at 405 and 470 nm isn't fully elucidated, so any corrections will also introduce additional biases. On the other hand, our head-fixed preparation resulted in very few movement artifacts, with most recording sessions being free

of them. Therefore, it was not advantageous to introduce additional noise and biases to all our recordings rather than excluding a subset of them.

However, the main limitation of GCaMP as a proxy for neuronal action potentials is its timescale. While a single action potential in DA neurons has a half-width of about 2 ms, the corresponding calcium transient has a half-width of ~300 ms[116] (0.3 s), over two orders of magnitude longer, thus providing a much lower time resolution. This is important for, as will be discussed in section 5.4, interpreting what the observed functional responses mean for the function of each subtype. However, this limitation is also a problem for DA sensors and other techniques to measure DA directly, which have an even slower time-resolution[137]. Nonetheless and critically for our conclusions, the differences we observe between subtypes stand regardless of the timescale of the reporter.

Furthermore, while there is a clear link between calcium transients and action potentials or neurotransmitter release[134,137,168], this relationship is not fully direct. For example, the relationship between axonal calcium and the amount of neurotransmitter released from axons can be modulated by available vesicle pool sizes[134]. This and other factors add minor variability to calcium traces[169], but the absence of accurate deconvolution techniques that can extract action potentials from calcium transients[134] indicates that we don't fully understand the relationship between the two or that there are too many parameters necessary to deconvolve that are not recorded. However, again this does not affect the conclusions reached here. Even if calcium transients could only partially predict dopamine release and/or somatic action potentials, it is very unlikely that the stark differences we observe would be compensated by additional factors and result in different subtypes showing similar signaling patterns; and even if this was the case, differences in the molecular mechanisms leading to similar signaling would be an important candidate to explain the

differential vulnerability of these subtypes[47] (Figure 4E-H). Furthermore, single-cell electrophysiology recordings have described firing patterns in individual DA neurons that mimic our results (discussed in detail in section 5.4), showing that these signaling patterns are not artifacts of calcium imaging.

5.2.3. Fiber photometry

Fiber photometry is a technique by which a small optic fiber is introduced into the brain, through which a fluorescent indicator (in our case GCaMP) is excited and its fluorescence collected. The main advantage of this technique, and why it was chosen for these experiments, is that it causes minimal damage in the tissue, compared to other imaging techniques like 2-photom imaging, which requires implanting a large cannula and removing all tissue above the region of interest[5]. This can be very useful for recordings with single-axon resolution but only in the dorsal striatum, removing a section of the cortex above it but leaving the corpus callosum and the striatum itself untouched[5]. However, to record from deeper regions of striatum, for example where Calb1+ neurons project to, this strategy would require great damage to the striatum, probably disturbing the animal's behavior and the striatal circuitry itself (particularly given the existence of feedback loops between regions of striatum and SNc[80,170]). The advent of GRIN-lenses provides access to ventral striatum with high spatial resolution[171]; but their 1 mm diameter still causes a lot more damage than our 200 μm optic fibers.

Another advantage of our approach is the acute placement of optic fibers, as it allows us to record from many locations in the same mouse. In particular, we can move the same optic fiber down through the brain, recording at successive steps and thus obtaining a comprehensive response-map across the dorso-ventral axis of the striatum. In contrast, classic fiber photometry methods involve chronically implanting an optic fiber into a single location[16,33]. However, acute fiber implants have

the limitation that it is harder to accurately identify the recording location within the brain in anatomical terms. While the dorso-ventral depth from the brain surface is provided accurately by the micro-manipulator used to move the fiber down (though in subsequent recording sessions it becomes slightly less accurate due to damage to the brain surface in previous days), the angle and the medio-lateral and antero-posterior location of the fiber are harder to determine. We estimate this location by perfusing the mice immediately after the last recording session and locating the fiber tract through histology. However, usually only the fiber track from the last session is visible, and while we assume that fibers in previous sessions were placed in close proximity to the last one, it does introduce additional variability. Furthermore, the glial scar that builds up around chronically implanted fibers[172], which marks the fiber track and facilitates its localization, is much less prominent in acute fiber experiments. And to complicate things further our thinner 200 µm fibers (compared to commonly used 400 µm fibers) result in a narrower fiber track, which is thus harder to identify.

The main drawback of fiber photometry however is that it lacks the spatial resolution to distinguish individual axons (and thus individual DA neurons). Instead, it collects the total fluorescence from all axons present in its collection field, approximately a sphere of ~300 µm in diameter for our 200 µm core fibers[173], which means it effectively averages out the signaling from tens to hundreds of labelled DA axons. This has several consequences. (i) We cannot be certain whether the average response we measure is representative of all the axons within the collection field, or whether there is additional heterogeneity. (ii) A single axons with a response (for example to rewards) that is absent in all other axons could not be distinguished from a small response present in all axons. (iii) Deconvolving the calcium trace to infer spiking, which is feasible for single-cell data[134], is much more challenging and inaccurate for photometry traces. (iv) When multiple cell compartments are

labelled (i.e., somas and neuropil), signals from each of them are impossible to distinguish, with the neuropil capable of dominating the fluorescence traces[171].

Nonetheless, the conclusions of this study are not affected. By recording from several locations across striatum we were able to assay different combinations of axons from the same subtype, so that, when the population was functionally heterogeneous as with DAT and Aldh1a1+, different recordings showed different functional responses (Figure 15 to Figure 19). On the contrary, recordings from Calb1+, Vglut2+, and Anxa1+ showed very similar functional responses regardless of recording location, and even in recordings from somas (Figure 31). Together, all this indicates that, while we cannot conclude that every neuron in each of these subtypes shows the same functional responses, Calb1+, Vglut2+, and Anxa1+ are highly enriched in a single functional type of neuron, to the point where the signaling from any other types is obscured by the majority. This is in contrast to Sox6+ and Aldh1a1+, which while enriched in Anxa1-like neurons compared to DAT, still have enough non-Anxa1-like neurons to be detected.

Furthermore, the absence of reward responses in photometry recordings from Anxa1+ axons (Figure 19) and somas (Figure 29) is very strong evidence that no (or very few) of the neurons labelled by this marker respond to rewards. It is true however that 3 out of 39 Anxa1+ recordings showed a significant response around rewards, though small. As we discussed previously, these were likely movement responses since no increases were observed when rewards were delivered at rest (Figure 19J-K). Nonetheless, it is possible that there are a few neurons labelled in these mice that either are not Anxa1+ (our genetic labelling strategies are not perfect, and some negative cells do get labelled) or are Anxa1+/Calb1+ (for example) with the Calb1+ identity dominating (our snRNA-seq analysis has shown some double-positive cells). Both possibilities are supported by the anatomical distribution of reward responsive recordings (Figure 22E), which show that

these small reward responses were found only in the most ventral Anxa1+ recordings – where any Calb1+ mislabeled neurons would project to.

The solution to this question of residual heterogeneity within subtypes will be answered by 2-photon imaging techniques with single axon or single cell resolution, or by opto-tagged electrophysiology recordings. As we have discussed, 2-photon imaging with cannula implantations can only be achieved from dorsal striatum, so this technique would be highly effective for analyzing heterogeneity among Anxa1+ axons. It would still be possible though, by imaging the most anterior dorso-medial striatum, to record from some Calb1+ axons, and placing the cannula over the posterior striatum should provide access to dorsal Vglut2+ axons (Figure 14). However, the question would remain of whether ventral axons of these same subtypes show different functional responses. In this case, GRIN-lenses could be employed to record from more ventral axons[171]; though any differences with photometry results could potentially be due to the damage caused. Alternatively, this question could be answered by recording from somas of genetically identified subtypes, either by opto-tagging and electrophysiological recordings[6,13], or by implanting a GRIN-lens over the SNc (this has already been achieved for VTA DA neurons[109,174], and while it would still cause significant damage it would be to the structures above the SNc and not the SNc itself).

Finally, concerns about the influence of other neuronal compartments to photometry recordings are also not critical to our conclusions. It has been observed that, when using fiber photometry to record from the striatum, measured changes in calcium are mostly driven by the neuropil, not somatic signaling[171]. This is a concern for recording from medium spiny neurons in striatum with a non-specific GCaMP labelling, so that not only somas express GCaMP. However, in our striatal recordings only DA axons (from one subtype) are labelled, and thus no other compartment can

contribute to the signal. On the other hand, this could be affecting our somatic recordings, as the dendrites of labelled DA neurons could contribute to or even dominate the measured calcium changes. Nonetheless, given that our somatic recordings match our axonal recordings (Figure 31), it is highly unlikely that the dendrites of these neurons show the same signaling patterns as the axons while the somas do something completely different. This could not be explained by local modulation in the axons, as this would not influence the dendrites in the remote SNc. If anything, contribution from the dendritic compartment could add noise to our somatic recordings, which could be the reason that axonal recording have higher signal-to-noise ratios. Either way, this question could be addressed using soma-restricted GCaMP labelling[175,176], which would exclude contributions from other compartments.

5.2.4. Behavioral paradigm

For the characterization of each DA subtype's signaling during locomotion, mice were head-fixed over a cylindrical treadmill and allowed to run freely. This method has been used before to study DA neuron[5] and cholinergic interneuron signaling[159] during locomotion, as well as cortical[177], cerebellar[178], or hippocampal[179] signaling amongst others, with similar results to those obtained in freely moving mice. Its main advantages are allowing acute fiber placement, reduced movement artifacts (the mice are head-fixed, so the brain does not move), and a simplification of the movement. For this last point, the treadmill limits the movements the mice can make, so that they can run forwards, move backwards (though this is rarely done in habituated mice), stay still, or groom. This is a much smaller set of behaviors compared to those performed by freely moving mice, which can turn, look up, rise on their back paws…[180] Furthermore, the redout of these behaviors, which is essential for analyzing their relationship with neuronal signaling, is much simpler in our treadmill setup – velocity is directly measured using a rotary encoder, and this single

measure in time is used as a descriptor of behavior. In contrast, analysis of freely-moving behavior is much more complicated[6,180], and thus prone to biases and variability. However, this same advantage means that behaviors are less naturalistic; though it ranks much higher in this measure than other behaviors used to study movement related brain signals (like mice constrained in a hanging basket[7]). Still, it is important to ensure that any results are not an artifact of the behavioral paradigm by testing the same hypothesis under other conditions. As will be discussed in section 5.4, similar functional responses have been observed in mice performing other movements, and thus it supports our results.

With mice on this treadmill, some also received unexpected water rewards and aversive air puffs to their face/whiskers, as well as a neutral light stimulus. Unexpected rewards and aversive stimuli constitute a classic paradigm to functionally probe DA neurons[5,14,15,34,139], though they are not comprehensive: many other tests have been used to functionally characterize dopamine neurons[35]. We here focuses on the most simple and straightforward tasks, as they have been used most widely and thus our results can be interpreted in relation to a wide range of previous works.

Nonetheless, there are some key functions of DA neurons that we could not probe, particularly reward expectation. While the reward prediction error (RPE) response that classically characterizes DA neurons[3] involves a positive response to unexpected rewards, a sensitivity to reward size, and a decrease to aversive stimuli, it importantly also involves (i) the transfer of the response to reward-predicting cues, (ii) the lack of response to expected rewards, and (iii) a decrease in response to an omission of an expected reward. None of these were tested in any of our genetic subtypes of DA neurons, and thus it is unclear whether Calb1+ neurons show characteristics of RPE beyond responding to unexpected rewards and reward size sensitivity. Furthermore, a recent discussion exists as to whether DA neurons encode RPE and/or intrinsic

value[13,35] (though, given our results, it is easy to hypothesize that different subsets of neurons might respond to each).

One limitation of our setup however comes from the system used to deliver these rewards and air puffs. In both cases, a solenoid valve is used to briefly allow the flow of water or pressure air respectively; and this opening and closing of the solenoid results in an audible "click" noise. This sound lets the mouse know the reward is available and induces them to lick; but it does mean that it is impossible to dissociate the response to the reward from the auditory stimulus. Thus, this might be an important confound. In fact, previous reports of DA neurons projecting to posterior the striatum (most probably Vglut2+ neurons) observed that these neurons respond to rewards and aversive stimuli[14] (as we observed for Vglut2+), but they argue that their response to rewards is due to the solenoid click and not the reward, suggesting these neurons only respond to aversive and salient stimuli[9]. Therefore, it will be important to test whether the response Vglut2+ neurons show to rewards is maintained when the click is muted.

Movement is an additional (and critical) confound for the interpretation of the responses to rewards and air puffs, as all of these stimuli are accompanied by movements. For instance, mice stop running when a reward is delivered and lick (which is a movement after all); and air puffs cause mice to rapidly stop running if they were, and causes them to move backwards in the treadmill in an attempt to get away from the air puff valve, positioned in their face, even if they were at rest. These confounds are important given that all SNc DA subtypes studied show some type of response to movement, and are often not or very loosely controlled for in the literature[9,34,165]. It is even possible that all responses to different stimuli can be explained by kinematics alone[115]; those this seems implausible given our results, which show the same responses to rewards when large body movements co-occur or not (at rest, Figure 19J-K). To determine whether the same is true

for air puffs is less straightforward, as all air puffs caused backwards movements. However, it would be possible to move the air puff valve to the rear of the mouse – if this was shown to be similarly aversive, we might expect that here the mice would accelerate forward to try to "run away" from the stimulus. If the response to this air puffs in the face and the rear shown caused similar responses in the neurons, despite different movements in response, it would be strong evidence that the response is due to the stimulus itself and not the accompanying behavior. This could be particularly interesting to analyze for Calb1+ neurons, as their small response to air puffs might be due to the large deceleration that occurs (as we already know Calb1+ neurons respond to decelerations). If this was the case and Calb1+ neurons don't increase firing to aversive stimuli, they would have a more similar response pattern to the classic RPE neuron.

Finally, it is interesting to consider that not all rewards and not all aversive stimuli might be equally relevant for all DA neurons. We here use water as a reward for water-restricted mice, but other works have used sugary water[115,181,182] or food pellets[34,183] instead. On the one side, consumption of water or sugary water only requires mice move their facial muscles to lick, which food pellets require complex limb movements to pick up the pellet and deliver it to the mouth, and this could involve different dopamine circuits. Furthermore, it has been observed that dopamine neurons projecting to different regions of striatum (and thus probably different subtypes) respond to either the nutritional or hedonic value of sugary water[181], which could cause differences in responses to water vs sugar/food rewards. As for aversive stimuli, there is a wide range of options that have been used, including air puffs[9,14,15,115], mild electric shocks[184,185], loud noise[34], and bitter water[9,110]. And again, DA neurons are not equally responsive to all – for instance, DA neurons projecting to the posterior striatum respond to air puffs but not bitter water[9], and showed a decrease in response to loud noise[34].

5.3. Subtypes as a novel framework of DA function

5.3.1. Multi-level validation of genetic classification schemes

As mentioned before, classifications of DA neurons have little meaning until they have been validated by establishing their behavioral relevance. This is because there are infinite successive divisions that can be made from detailed transcriptomics analysis, and there is no clear criteria to determine where to stop: it is impossible to distinguish from gene expression alone what variability is relevant for the neuron identity and what isn't.

Validating classification schemes can be done at many levels. First anatomically, by determining whether there is a difference in morphology between subtypes. These differences can be found in the size of their somas (there is no evidence of this in DA neurons, which has certainly contributed to the late identification of subtypes), the location of their somas[17] (Figure 14C), the target of their axonal projections[17] (Figure 14D, and Aldh1a1+ preferentially targets striatal striosomes[17]), the location of their dendrites (Aldh1a1+ has dendrites in the striosome-dendron bouquet structures in SNr[18]), and their inputs (DA neurons projecting to the tail of the striatum, most probably Vglut2+ neurons, have unique inputs compared to other DA neurons[27]). These anatomical differences are an important first evidence of the unique characteristics of genetic subtypes, but isn't enough on its own.

Secondly, we can validate subtypes by studying their electrophysiological properties. It is already known that SNc neurons differ by their T-type calcium channel-mediated rebound excitability[19], I_h current size[16], and burstiness[20]. In some cases, these differences have been mapped onto genetic subtypes of DA neurons: for instance, the sensitivity to excitatory inputs in the presence of DA autoinhibition differs between Calb1+ and Calb1- neurons[19] (which include Anxa1+ neurons). In

other cases, though DA subtypes were not considered, evidence hints that these differences might also map onto genetic subtypes. For example, DLS-projecting DA neurons show larger I_h currents[16] and higher burstiness than DMS-projecting neurons, probably Anxa1+ vs Calb1+ neurons respectively.

Third, we can study their vulnerability in Parkinson's Disease (PD) and PD models. It has long been known that not all DA neurons are equally vulnerable in PD, with the ventral tier of SNc[23–25] and axons in dorsal striatum[26] being particularly vulnerable and degenerating first – both regions where, in mice, Anxa1+ neurons predominate. We have now demonstrated that humans also present subsets of SNc DA neurons that express either Calb1 or Aldh1a1, with little overlap, and these subtypes are located in dorsal and ventral tier respectively and differentially degenerate in PD (Aldh1a1+ neurons are much more affected) (Figure 4). This differential expression of Calb1 and Aldh1a1 (as well as Sox6) in dorsal vs ventral tier in humans has also been recently shown by RNA-sequencing[72]. As for Anxa1+ however, evidence suggests that its distribution in mice might not match that in humans, as it has been shown to be enriched in human SNc dorsal tier compared to the ventral tier[72]. This does not mean that the Anxa1+ subtype does not exist in humans though, as it could just mean that Anxa1 is a marker of these subtypes in mice but not humans – we should thus explore other genetic markers of this population in mice to see which ones could also identify the same population in humans. Finally, the differential vulnerability of Aldh1a1+ neurons is also observed in a classic model of PD in mice[47], where degeneration is induced by the MPTP toxin[186], suggesting that while mice do not naturally suffer from PD the difference in vulnerability between subtypes might be maintained.

The ultimate test however is whether different subtypes have different functions, and whether all cells within that defined subtype have the same function. This task is a multi-step process, which

we here initiate by determining that different subtypes do indeed show different functional responses.

5.3.2. Interpreting the DA literature through the lens of subtypes

In recent years, many cases have been identified of SNc dopamine neurons with different responses to behaviors and stimuli[2,6–8,15,16,112,113], particularly for neurons projecting to different regions in striatum[5,9,14,16,114]. However, there are some inconsistencies in the results reported. Given our findings that different DA subtypes show different functional responses and knowing that subtypes have somas and axons in different (but overlapping) regions of SNc and striatum, we hypothesize this might explain previous these inconsistencies: different subtype(s) may have been inadvertently investigated.

For instance, while the general assumption has been that all midbrain dopamine neurons respond to unexpected rewards, there has been scattered evidence against this dogma. A few single cell studies reported some SNc dopamine neurons that did not respond to rewards[6,139], and axonal imaging recordings found several single axons not encoding rewards[5]. However, other studies have found reward responses in similar regions[16,32,33]. This controversy is particularly evident in the dorso-lateral striatum, where theoretically equivalent approaches (fiber photometry of GCaMP expressing axons or voltammetry) have shown different results, with some reporting no reward responses[5,114], others small responses[34], and other large responses[16,33,187] to unexpected rewards (reward response size was scaled in comparison with that of other regions of striatum, often the ventral striatum, showing strong responses to rewards). Since we detected robust reward responses in Calb1+ and Vglut2+ neurons but not in Anxa1+ neurons, and since these subtypes have different soma distributions and striatal projection targets, our results may help explain the previous discrepancies; different subtype(s) may have been investigated based on the recording location in

SNc or striatum. For instance, while recordings showing no reward responses were made in the dorsal-most[5] or very lateral[114] striatum, where Anxa1+ axons predominate, reports of reward responses were recorded in regions that were more ventral[16,187] (where Calb1+ axons or VTA axons would also be present) or more posterior[33] (where Vglut2+ axons would contribute).

Furthermore, our functional characterization of Vglut2+ neurons agrees with previous recordings from overlapping soma/axon regions that reported aversive stimuli and reward signaling[9,14,15], with insensitivity to reward-size[9,10]. Based on these properties, such neurons have been proposed to signal novelty or salience[14,15], or to reinforce avoidance of threatening stimuli[9]. However, the reward response of posterior striatum projecting neurons (i.e. Vglut2+ neurons) is disputed. Menegas et al.[9] showed that, when the salient 'click' noise linked to reward delivery (due to the opening of the solenoid valve) was muffled, the response of these neurons to the reward was similarly abolished, suggesting that they had responded to the sound and not the reward itself[14]. This was replicated in a later study where, with the click noise muffled, these neurons again showed no response to rewards[10]. Given that in our experimental design rewards were similarly accompanied by a click, it is possible that Vglut2+ neurons are responding to this salient sound, and not the reward itself; and this is further supported by the lack of sensitivity of these neurons to the size of the reward delivered. Thus, of the three subtypes studied here that account for most SNc dopamine neurons, only Calb1+ neurons displayed robust reward responses with size sensitivity, a hallmark of reward prediction error and involvement in positive reinforcement learning[3,133].

As for locomotion, previous research has reported that many SNc dopamine neurons signal at accelerations during a variety of motor tasks, but with differences in whether the neurons increase or decrease their firing at accelerations[2,5–8,113,115]. Since here we found that such signaling patterns

were differentially expressed by the different subtypes, and since their cell body and axon locations are anatomically biased, these previous discrepancies might again be explained by the unknowing recording of different subtype(s) across studies based on location. For example, recordings in more medial SNc/lateral VTA (Calb1+ location) found most neurons decrease their firing at accelerations (and respond to rewards)[7]; recordings from dorsal striatum axons (Anxa1+ axon location) found increases in signaling at accelerations (and no detectable reward responses)[5]; and recordings from a broader range of locations (and thus subtypes) in SNc found neurons with both increases and decreases of firing at accelerations[6] – all of which agree with our results when considering subtype anatomical distributions. Furthermore, these studies also confirm the validity of our GCaMP results, as they use single-cell recordings of action potentials and find similar responses to locomotion in individual DA neurons: some increase their firing at accelerations and others decrease it[6,7].

Finally, studies using optogenetics to manipulate DA neurons have also shown conflicting results: some have shown that excitation of SNc DA neurons drives locomotion[5,6], while others show no effects[7]. This could again be due to the subtypes involved: the study that did not find a causal link between DA activation and movement activated neurons in medial SNc and lateral VTA[7], where Calb1+ neurons predominate, while those that did activated either axons in dorsal striatum[5] or neurons in more central regions of SNc[6], where Anxa1+ neurons predominate. However, an alternative (or synergistic) explanation is that different "movements" were considered: the two studies that observed DA-driven movements looked at open field[6] or treadmill[5] locomotion, both much more naturalistic movement than what was studied on the third study: postural adjustments in mice restrained and suspended on a basket[7].

5.3.3. Medial and lateral SNc

There is however one set of studies that are harder to understand with our results. There is evidence that, beside the dorso-ventral division of SNc DA neurons (where ventral SNc neurons project to dorsal striatum and dorsal SNc neurons project to ventral SNc), there is also a medio-lateral division, where medial SNc (mSNc) neurons project to dorso-medial striatum (DMS) and lateral SNc (lSNc) neurons project to dorso-latera striatum (DLS)[16,188]. It is unclear what subtypes these populations match, thus making results hard to interpret.

One study labelled dopamine neurons projecting to DLS and DMS and recorded GCaMP transients using fiber photometry from somas in lSNc and mSNc, and observed that DMS projecting neurons showed a positive response to rewards but negative to an aversive stimulus, while DLS projecting neurons showed positive responses to both[16] – which seemingly conflicts with our results. Nonetheless, there are a couple confounds that could explain the differences. On the one hand, they use an electric shock instead of an air puff as an aversive stimulus and, as we know, dopamine neurons don't respond to all aversive stimuli in the same manner[9]. Furthermore, this study did not analyze how DMS and DLS projecting neurons signaled during locomotion, only checking that the two cohorts of mice did not show differences in movements. However, as we know, DA neurons respond differently to movements, and electric shocks certainly cause changes in movement in the mice, so the observed differences could be due to these movements rather than the stimulus itself. Finally, their experimental design introduces two levels of anatomical biases that could result in hard to interpret subsets of neurons labelled. By labelling neurons through their axons in striatum but recording from somas in SNc, they could be selectively recording from the subset of neurons that project to DLS but are located in lSNc – which would be enriched in DLS

projecting Vglut2+ neurons. Thus, while the results in Lerner et al.[16] seemingly conflict with what we have here found, there are too many confounds that make comparisons complicated.

Avvisati et al.[188] observed similar results, but took the remarkable step of testing these populations for the expression of markers of key genetic subtypes: Sox6, Aldh1a1 and Calb1. They thus showed that most lSNc-DLS neurons expressed Sox6 and Aldh1a1, while mSNc-DMS neurons were 60% Sox6+ and/or Aldh1a1+ and 20% were Calb1+. This illuminates the issues with anatomically guided recordings from DA neurons: multiple subtypes can be recorded from in a single area. Furthermore, while their DLS-projection neurons were mostly Aldh1a1+, they did not check for Anxa1+ expression (as we have just now uncovered this new subtype), and thus it remains possible, especially given how ventrally their DLS labelling is, that Aldh1a1+/Anxa1- neurons are labelled here too. This could explain the reward response found in some of these neurons.

Furthermore, again by recording from SNc they might be adding a second level of anatomical bias. They recorded from DA neurons in SNc by moving an electrode from the cortex down and identifying DA neurons of interest (by spiking properties or opto-tagging). Thus, neurons more dorsal in SNc (more probably Anxa1-) would be encountered first and thus have a higher chance of being recorded from. This issue, which would bias in vivo electrophysiological recordings of SNc DA neurons in favor of dorsal tier Calb1+ and/or Anxa2- neurons, can also explain the underrepresentation of reward-unresponsive, locomotion-locked DA neurons in the literature. Drawing a parallel to the VTA, this same bias could explain why value-coding DA neurons are rarely found in VTA recordings[13], as these neurons have been proposed to be located in medial-VTA[35], which is ventrally located compared to lateral VTA with respect to vertically moving electrodes.

Either way, evidence still shows that there is a bias for lSNc neurons projecting to DLS and mSNc projecting to DMS[16,188]; and this is not recapitulated by our subtypes. There are two possibilities to explain this. On the one hand, it is possible that there are further subdivisions within Anxa1+ neurons, which would match this medio-lateral distribution. However, another possibility is that this dichotomy is captured in the subdivision of Aldh1a1+ into Anxa1+ and Anxa1- neurons. While we have not characterized the medio-lateral distribution of Anxa1+ neurons compared to Aldh1a1+ in SNc, analysis of their projection arbors shows that Anxa1+ axons are less dense than Aldh1a1+ axons in dorso-medial striatum, not just in more ventral regions (Figure 13C). To conclusively answer this question, it will be essential to identify a marker or alternative strategy to access Aldh1a1+/Anxa1- neurons and compare them with Aldh1a1+/Anxa1+ neurons in DMS.

5.3.4. Subtypes as a novel framework

As has been shown, the DA literature is full of seeming contradictions and conflicting results, which makes it impossible to integrate all available data into a universal model of dopamine function. Thus, many such attempts, even in recent years, have dismissed subsets of results that did not support their models[29,31,115,189,190]. To address these issues, there is a recent push to consistently and accurately report and consider the anatomical location at which recordings were made from[35]. This would indeed be an important step to help solve this issue. However, as we have shown, anatomical boundaries are often arbitrary or blurry (for instance, different papers recorded from different regions of striatum while calling all of them "DLS"[16,33,114,187]), and in many regions axons from different subtypes overlap[17,188]. Instead, genetic subtypes of DA neurons provide a universal access point that can be reproducibly used across studies to access the same set of neurons, thus allowing easy comparisons across studies.

Furthermore, this work adds to the evidence that DA neurons in the SNc signal during movements, and that there is diversity in this signaling[5–8]. Thus, it is essential that all studies of DA function also record and control for movement, not just by checking that all animal groups responded with similar movements to the stimuli presented[16], but by trying to dissociate the responses of these neurons to the stimuli and the movements.

5.4. Functional roles of DA subtypes

5.4.1. Volume transmission vs targeted signaling

DA has been long be considered to act on its post-synaptic targets, such as medium spiny neurons in the striatum, through volume transmission. In this model, DA released from axons diffuses over large volumes, exerting its effects on many postsynaptic targets over extended periods of time[191,192]. If this is the case, it is hard to envision the role of the different signaling patterns here observed across dopamine subtypes, particularly given the overlap of their axons (and thus of their DA release sites). In these regions of overlap, DA released at different timepoints (for example at accelerations vs decelerations) would reach the same post-synaptic targets and be indistinguishable.

One hypothesis suggests that, while DA signal through volume transmission, it exerts selective signaling through the timing of DA release vs the activity of glutamatergic synapses[192]. In this model, post-synaptic neurons will only be affected by the DA signaling that coincides with their glutamatergic input. Another possibility is that the combination of DA signals produces a new mode of signaling. For instance, combined DA at accelerations and decelerations could signal "changes in velocity", irrespective of the direction, which could be potentially relevant to downstream targets (though no experiment has been conducted to prove or disprove this). As the

ratio of axons from one subtype or another changes across the striatum, the summation of their respective DA signaling could result in different timing of the DA peak in each region – which would result in apparent waves, as observed by Hamid et al.[32] However, these waves could be an artifact of the limited spatial resolution of imaging techniques, combining DA signals that are distinguished at the circuitry level.

In fact, there is growing evidence that DA signaling is much more spatially and temporally precise than previously thought[193–195]. DAT limits the extracellular concentration of DA beyond the release site, thus limiting the sphere of influence of DA to 20-100 DA synapses for high-affinity D2 receptors, but only one synapse for low-affinity D1 receptors[196], due to the decrease in concentration of DA with increasing distance from the release site. This asymmetry in the range of DA effect of D1 vs D2 receptors has interesting implications given the current hypothesis for the role of the direct (D1) and indirect (D2) striatal pathways. This model suggests that the activation of a select set of neurons of the direct pathway gates a wanted motor program, while global activation of the indirect pathway would suppresses competing programs[197]. In this context, DA signaling could have a precise effect on D1 neurons but a broader effect on D2 neurons, matching the selectivity of D1 and D2 neuron activation during behavior. This could mean that DA could exert both volume and targeted effects. Regardless, the mounting evidence for precise DA signaling in striatum supports the idea that different DA signals from axons of different subtypes in regions of overlap could be distinguished by the post-synaptic targets.

5.4.2. Movement control or learning?

We have shown that different DA subtypes show different signaling during locomotion – but its role is unclear. The first step to investigate this is to determine whether the DA signal lags behind the acceleration/deceleration, as this would exclude its role in direct control of movement.

From triggered averages of ΔF/F triggered on accelerations or decelerations (and vice versa) (Figure 15), we found that the rise of the calcium transient starts about the same time as the start of the acceleration (for Anxa1+) or deceleration (for Vglut2+ and Calb1+). However, the limitations of our experimental approach prevent us from conclusively determining which of the two precedes the other. The main problem, as mentioned above, is the slow timescale of GCaMP, which has much lower time-resolution than electrophysiological recordings: GCaMP6f has a rise time of 0.1-0.2 s[116]. Furthermore, GCaMP6f has a decay half-life ranging between 0.3 and 0.9 s[116], so that previous transients can bleed through in time into the next transient and complicate the identification of the start of the next transient. This is particularly problematic due to the cyclical nature of locomotion, by which mice continuously accelerate and decelerate at a frequency that is similar to GCaMP6f's timescale, so that there are often many transients close together (as exemplified by raw traces, Figure 15C). To add another layer of complexity, population recordings as obtained from fiber photometry show calcium transients that represent the combination of signals from many axons or somas, again complicating the identification of the start of the underlying action potentials. Thus, the start of the calcium transient and acceleration/deceleration are close enough in time that we cannot exclude the possibility that either precedes the other.

However, evidence from the literature suggests that the DA signaling precedes the acceleration/deceleration. In single-axon GCaMP imaging under the same behavioral paradigm, Howe & Dombeck[5] showed that calcium transients precede accelerations at the start of a movement bout (where no previous accelerations/decelerations are present to confound the results). Furthermore, single-cell recordings show that DA neurons in SNc increase their firing before accelerations associated with a range of movements[2,6,7,113,115]. Altogether this indicates that, at least for Anxa1+ neurons, DA signaling precedes acceleration. As for Calb1+ and Vglut2+,

single-cell studies have also identified DA neurons in SNc that decrease their firing at accelerations[2,6–8,113,115], but the timing for this relationship is less clear, with some arguing that in these neurons the decrease in firing lags behind the acceleration[6]. However, none of these studied analyzed the firing of DA neurons during decelerations, so it remains possible that Calb1+ and Vglut2+ neurons show increases in firing that precedes decelerations.

Nonetheless, DA signaling preceding acceleration or deceleration does not necessarily mean DA plays a causal role in controlling movement – it could instead carry a corollary discharge signal important for learning, for example by conveying an action prediction error[10,198,199] that could lead to learning of state-action associations. Distinguishing between these possibilities will require additional experiments – but it is important to keep in mind that different DA subtypes are probably involved in different functions, so all these hypotheses might be true.

One important way to test the causal role of DA subtypes in behavior and learning will involve optogenetically activating and inhibiting each subtype or ablating them. Optogenetic activation of indiscriminate SNc DA neurons have shown to drive locomotion and inhibition impairs it[6], and optogenetic activation of dorsal-striatum SNc axons (predominantly Anxa1+) also drives locomotion[5], together suggesting that Anxa1+ neurons might serve a role in driving or gating movement. On the other hand, some argue that these were due to unphysiological stimulation, and that optogenetic activation at physiological levels drives place-preference learning but not movement[7]. However, this study stimulated in dorso-medial SNc and calibrated its stimulation based on reward responses in less-dorsal striatal axons – it is highly probable that their stimulation affected predominantly Calb1+ neurons. Furthermore, their measure of movement involved detecting postural adjustments in mice suspended in a basket, an unphysiological behavior compared to open field[6] or treadmill[5] locomotion as used in previous studies. A third line of

evidence on the other hand suggests that SNc DA neurons might be involved in state-action associations: pairing unilateral optogenetic activation of SNc DA neurons with a cue causes rats to initiate contralateral movements in response to that cue[129]. Finally, the ablation of Aldh1a1+ neurons (which contain Anxa1+), the only subtype-specific manipulation to date, had a small but significant effect on locomotion, and caused a strong impairment on motor learning[141]. It is important to keep in mind however that the tamoxifen dependent Aldh1a1 Cre line used in this study is inefficient and results in 20% of Aldh1a1+ neurons surviving, an incomplete ablation that could explain the small motor impairments. Regardless, all together the evidence suggests that Anxa1+ neurons probably play a role in both motor control and motor learning, possibly by gating and facilitating wanted motor plans and reinforcing them in a context-dependent manner for future repetition. This is further supported by comparing the projection arbor of Anxa1+ neurons with cortico-striatal input maps[200,201], as this region receives input from cortical areas that process trunk and limb sensorimotor information[201].

What about Vglut2+ and Calb1+ neurons? Both subtypes show the opposite signaling pattern during locomotion compared to Anxa1+ neurons, namely calcium transients at decelerations, so one possibility is that might gate/facilitate stopping behaviors or act in opposition to Anxa1+ neurons to inhibit movements. It is also important to consider the differences between Calb1+ and Vglut2+ signaling during locomotion, which suggests that these two populations would have different roles. These differences were not observed in single cell studies; but it is possible that SNc recordings missed the lateral Vglut2+ population.

Another possibility is that the different locomotion responses we have detected are not locked to whole body accelerations and decelerations, as measured by our treadmill, but rather are each locked to the movement of different body parts or groups of body parts. This is particularly

interesting given the cortico-striatal input map[201], by which different regions of striatum receive different sensory-motor cortical inputs. For example, Calb1+ neurons could be related to oculo-motor movements, while Anxa1+ might be related to limb movements.

5.4.3. Vglut2: salience, aversion, or action prediction error?

Thanks to its anatomical segregation from other SNc subtypes, particularly its projections to posterior striatum, several studies provide insights into the role of the Vglut2+ subtype (while none checked for the identity of the neurons they studied, most DA projections to posterior striatum are from Vglut2+ neurons, and thus it is fair to link these studies to Vglut2+ neurons).

Initial observations showed that, as we have here seen, DA neurons projecting to posterior striatum respond to rewarding, aversive, and neutral stimuli, suggesting that these neurons signal novelty or salience[14]. The same hypothesis was suggested from single-cell recordings in macaques, which observed that DA neurons in lateral SNc (where Vglut2+ neurons are found in mice) responded to rewarding and aversive stimuli[15]. However, this idea was soon challenged by showing that the response to reward was abolished when the click sound that accompanied the reward was silenced, that mice avoided optogenetic stimulation of these neurons, and that their ablation impaired normal avoidance of novel objects[9]. Instead, they suggested that posterior-striatum projecting neurons are involved in the reinforcement of avoidance of threatening stimuli.

In contrast, a recent paper has proposed that posterior-striatum projecting DA neurons signal an action prediction error[10]. This idea comes from the observation that these neurons respond to contralateral movements during exploration and in an auditory discrimination task (but not to rewards), and that the amplitude of this response was modulated by whether the action was predicted in the current state. This hypothesis is particularly interesting given that the posterior

striatum receives inputs from motor as well as sensory cortical regions[201], which matches its putative role in forming state-action associations.

We here find data to support both hypotheses: Vglut2+ neurons respond to movements but also to aversive air puffs. However, in this study we cannot dissociate the air puff response from the ensuing movement, so it is possible that, as suggested as in Greenstreet et al.[10], these are movement related signals (though future analysis and experiments could help dissocate the two). One possibility to unite the two could be that, while the action-prediction error of Vglut2+ neurons might be value-free, it could be modulated by salience, so that actions associated with more salient stimuli/state (for example aversive stimuli) would be more strongly reinforced.

5.4.4. Goal directed actions vs habit formation

Classically, the dorso-medial (DMS) and dorso-lateral (DLS) striatum has been proposed to be involved in goal directed actions and habit formation, respectively[202–204]. Goal directed actions are performed if they produce an outcome that an organism wants or values, while habits are actions that occur automatically in a certain context or state regardless of the action's outcome. Given that Anxa1+ neurons project to this habit-forming DLS and show movement-locked signaling, they are well positioned to serve as an action reinforcer driving habit formation. This idea matches the model of striatal function described in Miller et al.[205], in which habits can be formed in a value-independent manner by reinforcing actions that occur in certain states without consideration for the outcome of that action: just like Anxa1+ neurons encode movements but not rewards. Furthermore, striatal patches, which are required for habit formation[206,207], receive selective innervation from Aldh1a1+/Anxa1+ neurons[17] and form specialized striosome-dendron formations onto SNc DA neurons[208], probably Aldh1+/Anxa1+ neurons given their dendritic projections (Figure 14), providing further evidence of the role of these neurons in habit formation.

Nevertheless, this hypothesis is not necessarily in opposition with Anxa1+ neurons gating and invigorating movements: they could serve a dual purpose of facilitating habitual (or common) movements while additionally reinforcing them for future occurrence.

On the other hand, Calb1+ neurons innervate the dorso-medial striatum, which is involved in goal-directed actions[202]. Computational models suggest that this requires reward prediction errors (RPE) for learning[205,209], which is interesting given that, out of all the DA subtypes surveyed Calb1+ neurons are the most similar to classic RPE characteristics, particularly given its sensitivity to reward-size[210]. However, it is unclear how the locomotion-response shown by these neurons could be involved in learning of goal-directed actions, and their positive response to air puffs seems to contradict it – though, as discussed, it is possible that the air puff response observed is due to the movement it causes and not the aversive stimulus itself. These variables would be important to dissociate in order to fully understand the role of Calb1+ neurons in DMS.

5.4.5. Inputs to and feedback loops between DA subtypes

It is also important to consider that DA subtypes and the striatal circuitry they are involved in are not isolated from the others. The Ascending Spiral model[80] suggests that SNc and striatum can be divided into several parallel closed-loop circuits, in which a striatal region that receives input from a certain subset of DA neurons project back to these same DA neurons. On top of this, each circuit also inhibits the next closed-loop circuit, in an ascending spiral from limbic to motor circuits. In mice, this has been suggested to apply to the DMS and DLS sub-circuits, with the ascending spiral predicting DMS disinhibition of DLS projecting DA neurons and involved in the formation of habits[211]. However, recent evidence suggests that, while both this ascending spiral (but also the opposite descending spiral, DLS to DMS-projecting DA neurons) exist and have functional

synapses[16,170], they are unable to modulate DA neuron firing, thus questioning the prominence of this cross-talk.

This question is particularly important given that the striatum is one of the main inputs to SNc DA neurons[16,27], and thus could be critical to understand their functions. Attempts to determine differential inputs between subsets of DA neurons have not found striking differences[16,27] except when comparing DA neurons projecting to posterior striatum[27]. This is most probably because they used anatomical divisions rather than genetic tools to access different neuron subsets, mainly by their projection targets, and thus there will be a mixture of subtypes labelled in each case. Regardless, the differences in inputs observed suggest that genetic subtypes of DA neurons probably have different inputs, which would explain the different functional responses they show. An important next step thus will be to use intersectional rabies tracing strategies to determine the inputs to different genetically defined DA subtypes, which will be particularly interesting when comparing Anxa1+ neurons and other DA neurons.

5.4.6. Co-release of glutamate and GABA by DA neurons

Another interesting property of DA neurons is that some of them co-release other neurotransmitters in addition to DA[21,22]. For example, Vglut2+ neurons have been shown to co-release glutamate, an excitatory neurotransmitter (Vglut2 encodes a vesicular glutamate transporter)[212]. In VTA Vglut2+ neurons (a distinct subtype than the SNc Vglut2+ subtype studied here), this glutamate co-release has been shown to drive positive reinforcement even in the absence of dopamine release from these neurons[142], though the opposite is also true (DA release alone can also drive reinforcement[213]), suggesting these could be parallel or synergistic mechanisms. However, the role of glutamate co-release from SNc Vglut2+ neurons is yet to be elucidated. If these neurons are involved in reinforcing the avoidance of threatening stimuli[9], it is possible that both DA and glutamate co-

release from SNc DA neurons reinforce threat avoidance in parallel, mirroring the reward reinforcement of glutamate and DA in VTA Vglut2+ neurons. However it is also possible that DA and glutamate release are both involved in action prediction error[10], or that each neurotransmitter exerts its own function. In fact, this last hypothesis could explain the differences observed by Greenstreet et al.[10] and Menegas et al.[9] – interestingly, the former used dLight to detect DA release from posterior striatum neurons, while the latter used GCaMP to detect calcium transients, which could be representative of DA and/or glutamate release. However, it is unclear whether different neurotransmitters can be independently released from the same neuron[214–217].

On the other hand, DA neurons in VTA and SNc have been also shown to co-release the inhibitory neurotransmitter GABA[145]. Early evidence suggested that this GABA might be synthesized through a non-canonical pathway mediated by the Aldh1a1 enzime[144], which would suggests that the Aldh1a1+ subtype would be the one co-releasing GABA. Given the very different functional responses of Aldh1a1+ neurons vs Vglut2+ neurons, their co-release of an inhibitory vs an excitatory neurotransmitter could be very interesting, particularly in the dorso-lateral striatum, which receives motor-cortex inputs and to which both subtypes project to. However, this idea has been recently challenged, instead showing that expression of Aldh1a1 is not necessary for GABA co-release, instead showing that neurons import GABA from the extracellular matrix through the GABA transporter Gat1 (Slc6a1 gene)[143]. If this case, there is no indication of what subtype might be involved in GABA co-release. Either way, while GABA co-released from DA axons has been shown to inhibit downstream medium spiny neurons[143,145], it is still unclear what role it might play in the striatal circuitry.

While the co-release of other neurotransmitters by DA neurons is important to understand the different functions of DA subtypes, it does not affect our results. Calcium transients in different

subtypes, which should be indicative of release of any neurotransmitter, show clear differences in their functional responses, and it is highly unlikely that these differences are compensated for by the release of opposing neurotransmitters. This co-release of DA neurons instead adds another layer of complexity to the identity and function of different DA subtypes.

5.5. Implications for Parkinson's disease

5.5.1. Genetic subtypes in human SNc

Here we studied genetic subtypes of SNc DA neurons in mice, so it is important to show that these subtypes are conserved in humans before making any inferences on what these results mean for human disorders.

There is strong evidence that DA neurons in the human SNc can be divided into different subtypes that are analogous to mice and can even be characterized by the expression of the same genetic markers. For instance, Calb1 is expressed in DA neurons in the human SNc, and these neurons are biased to the dorsal tier[24,25], while Vglut2 expression is found laterally in the human SNc[76,218]. On the other hand, both Sox6 and Aldh1a1+ are also expressed in human DA neurons, and these are biased to the ventral tier[42] (Figure 4A), all of which matches the distribution of these subtypes in mice (Figure 14). In the case of Anxa1 on the other hand, it is possible that it is not as useful a marker in human SNc neurons as it is in mice, as RNA-seq analysis comparing ventral and dorsal tiers of human SNc showed that Anxa1+ was enriched in the dorsal tier[72] – unlike in mice where it is located in ventral SNc.

This however does not exclude the significance of the Anxa1+ subtype in humans and in PD. For instance, it is possible that in humans there is no equivalent to the Aldh1a1+/Anxa1+ population in mice, so that the human Aldh1a1+ subtype matches the mouse Anxa1+ subtype, or that in

humans the VTA Anxa1+ subtype is harder to separate from the SNc Anxa1+ subtype. However, another possibility is that Anxa1+ is not the ideal translational marker to identify this population. It is important to remember that the genetic markers used to access and refer to these subtypes alone do not define the identity of the neurons – this is determined by a whole set of differentially expressed genes. Because immunohistochemistry experiments preceded single-cell profiling studies, subtype markers gene selection has often been guided by previous literature linking these genes to PD pathophysiology[17]. Instead, we here selected Anxa1 as a subtype marker based only on our analysis on mice SNc neurons. Thus it is possible that another genetic marker might similarly provide access to the Anxa1+ subtype but also to the equivalent subtype in humans. Further exploration of the expression profile of these neurons and comparison with human RNA-seq studies[72] will hopefully yield such a marker.

5.5.2. Differential vulnerability of subtypes in PD

The degeneration of DA neurons in Parkinson's disease (PD) has been long known, but not all DA neurons are equally vulnerable. SNc DA neurons are more vulnerable than nearby VTA neurons[1], and even with the SNc degeneration is not uniform, with neurons in the ventral SNc being much more vulnerable than those in dorsal SNc or the pars lateralis[23,219]. Furthermore, DA axons projecting to the dorsal striatum are also particularly vulnerable in PD[26]. These anatomical biases point to the hypothesis that the Aldh1a1+/Anxa1+ SNc subtype (which has somas in ventral SNc and in mice projects to dorsal striatum) degenerates most prominently in PD, compared to the Calb1+ and Vglut2+ subtypes. Supporting this idea, expression of Calb1 and Vglut2 has been associated with resistant neurons in human PD patients[24,25], which we here confirm for Calb1 (Figure 4H), and these genes themselves have been implicated in reducing the vulnerability of DA neurons in PD using animal models[25,74,75,218,220–222]. On the other hand, Sox6+/Aldh1a1+ neurons,

which in mice include the Anxa1+ subtype here uncovered, are more vulnerable in PD[42,223] (Figure 4G) and PD mouse models[47].

Furthermore, transcriptomic analysis of Sox6+ neurons (which include the Anxa1+ subtype) vs Sox6- neurons (which include the Calb1+ and Vglut2+ subtypes) shows that the former is enriched in expression of PD genes (discovered via GWAS studies) and several pathways often associated with PD pathogenesis (Figure 5). This further supports the link between the Anxa1+ subtype and PD.

There are many hypotheses to explain the selective vulnerability of some DA neurons, including mitochondrial dysfunction and metabolic stress. While this is not the focus of this work, and though we have no conclusive evidence, the work presented here does suggest that Anxa1+ neurons might have properties that would make them more vulnerable to degeneration. Neuronal firing *per se* requires high energy demand and metabolic stress, particularly in DA neurons due to the resulting fluctuations in intracellular levels of calcium (for a detailed review see Duda et al. 2016[224]). We have found that Anxa1+ neurons show more frequent calcium transients than Calb1+ or Vglut2+ neurons (see raw traces in Figure 15 and Figure 23), which could contribute to their increased vulnerability to degeneration. However, it is important to remember that they are population recordings that sum the calcium transients of many neurons, and thus it is possible that these higher calcium transient rates are due to asynchrony among Anxa1+ neurons compared to Vglut2+ and Calb2+ neurons – single-cell recordings will be necessary to confirm or refute this result. Furthermore, the enormous axonal terminal fields of DA neurons[81] results in additional metabolic burden[225], and have also been proposed to create a mitochondrial "sink" that reduces the ability of the soma to cope with its metabolic demands[226]. In this regard, two lines of evidence suggest that Anxa1+ neurons might have larger axonal arbors than other DA neurons. On the one

hand, delving into the paper that first described the large arborizations of DA neurons[81] shows that DA neurons projecting to dorsal striatum (precisely where Anxa1+ axons predominate) have much larger arbors than those projecting to ventral striatum (on average 55.8 vs 31.4 mm respectively, almost double). On the other hand, our data suggests that, within Aldh1a1+ neurons, those with responses matching the Anxa1+ subtype have larger axonal arbors than those not matching Anxa1+. This is because axonal recordings in striatum show a majority of axons are Anxa1+like (about ¾, Figure 19), while in somas the opposite is true: only about ¼ of recordings show Anxa1+like responses (Figure 29), suggesting that a smaller proportion of the somas match a greater proportion of the axons. However, this is not conclusive evidence, as other factors could be affecting this – for instance, there could be a medio-lateral bias in Anxa1+ vs Anxa1- somas that results in our somatic recordings including more Anxa1- somas and more Anxa1+ axons.

5.5.3. A Seesaw Model for movement control by DA neurons

The opposite signaling of Anxa1+ neurons vs Calb1+ and Vglut2+ neurons during locomotion (where Anxa1+ neurons are active during accelerations while Calb1+ and Vglut2+ are active during decelerations), together with the fact that optogenetically activating dorsal striatum (probably Anxa1+ axons) drives movement[5], suggests an interesting hypothesis. It is possible that Anxa1+ neurons positively gate or invigorate movements while Vglut2+ and/or Calb1+ neurons gate competing movements, weaken movements, or drive decelerations/stopping movements, acting in opposition but balancing each other out in baseline, healthy conditions (decelerations and accelerations would occur as a result of rises in signaling in one or another subtype, which would tilt the balance transiently) (Figure 33 top). In Parkinson's Disease, this balance is abolished by the selective degeneration of Anxa1+ neurons, by which Calb1+ and Vglut2+ neurons

predominate, resulting in movement impairments (Figure 33 bottom). However, much work remains to test this hypothesis.

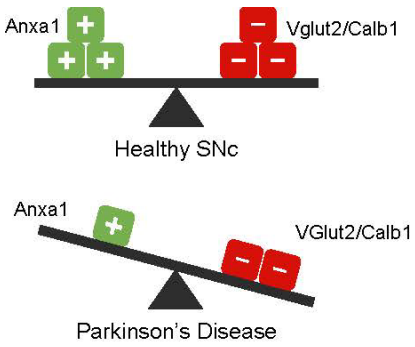

Figure 32: A seesaw model for DA movement control

Schematic for a potential model on how different DA subtypes might collaborate to maintain proper movement control .

Top – in a healthy SNc, the pro-motor Anxa1+ neurons are in balance with anti-motor Vglut2+ and/or Calb1+ neurons, with accelerations and decelerations occurring as a result of transient rises of signaling in one or another subtype.

Bottom – in PD, Anxa1+ neurons unequally degenerate so that anti-motor neurons predominate, resulting in movement impairments.

5.5.4. Relationship with the Subthalamic nucleus

While in classic models of basal ganglia function the subthalamic nucleus (STN) is part of the indirect pathway, recent evidence suggests a more complicated story, where the STN also inputs onto DA neurons in the SNc. Furthermore, there is evidence that this STN-SNc connection might not be equivalent for all DA subtypes. For instance, SNc DA neurons projecting to posterior striatum (mostly Vglut2+ neurons) receive significantly more inputs from STN than other subsets of neurons[27], and consequently stimulation of the STN evoked DA release from these same neurons[227]. This is interesting given that deep brain stimulation (DBS) of the STN in humans can alleviate motor symptoms in PD patients[228]. If, as we propose in the seesaw model above, the imbalance between remaining Anxa1+ neurons and spared Calb1+/Vglut2+ neurons in PD patients is responsible for their motor symptoms, and deep brain stimulation of the STN inhibits the output of this nucleus[229] (though this is still unclear) and thus de-excites the Vglut2+ neurons in SNc, this might re-instate the balance and thus improve the motor symptoms.

5.6. Local cholinergic modulation

While it has been classically assumed that somatic action potentials travel along axons and drive neurotransmitter from axonal terminals, this view is now being questioned for DA neurons. *In vitro* studies show that striatal cholinergic interneurons can not only modulate, but also trigger DA release from axons in the absence of somatic firing[36,37,126,158], and some recent evidence suggests that this might be the case *in vivo*[13,37]. The strongest evidence comes from the observation that measured DA release in the Nucleus Accumbens does not always match firing of somas in the VTA[13], which can be explained by local cholinergic modulation driving this additional DA release. However, we here consider an alternative explanation to these differences[29,35]: that the DA measured was released from a different subset of neurons than those recorded from. Indeed, we show that, if we record from mice where DA subtypes are indiscriminately labelled, we can recapitulate these results, but these differences are abolished when single subtypes are studied, in which case signaling in axons and somas matches. This proves that the results shown in Mohebi at al.[13] are not necessarily the result of local modulation, but could be instead due to a set of intermingling axons in the striatal area studied that come from somas not studied in the single cell recordings.

While our results show that somatic control and not local modulation is the main driver of DA release from axons, they cannot exclude that local modulation might play a role in particular behaviors. For instance, while striatal DA and cholinergic signaling are often desynchronized during behavior[159], they do synchronize at certain times such as at locomotion initiation or during turning[37,159] (though further work is needed to determine whether DA is triggered by acetylcholine or vice versa[230], or whether they are driven by independent inputs). Thus, completely rejecting the role of local modulation on the other side would require an exhaustive interrogation of

naturalistically relevant behaviors. However, our results do increase the requirements for any further work to conclusively prove that *in vivo* DA release is triggered by local modulation: either by developing a methodology to record from the soma and axon of a single neuron in vivo or, until this is feasible, by controlling for different subtypes and checking that the "mismatching" responses are not present in other neurons overlooked for their anatomical distribution (intermingling axons from a single neuron might be enough to detect a response missing from all other axons in an area).

Furthermore, even if cholinergic interneurons do not trigger DA release *in vivo*, they could still play an important modulatory role by modifying the amount of DA release, its timing, the ratio of DA to other co-released neurotransmitters, etc. For example, there is evidence that cholinergic receptors on DA axons can modulate the amount of DA released in response to action potentials[231]. This subtler effect could have significant consequences and thus should not be dismissed, and it could explain the remaining differences observed in our simultaneous soma-axon calcium recordings. However, because we use a calcium indicator, this would require cholinergic modulation to influence DA release in a calcium independent, which is improbable given that all known mechanisms for axonal DA release involve increases in intracellular calcium concentration, including local modulation[37,126]. Instead, it is more likely that the remaining differences we observe are due to different soma and axon calcium dynamics, or due to recording noise – in fact, modeling shows that the addition of noise levels comparable to that of our recordings reduces the correlation between identical traces to about a maximum peak of 0.8-0.85.

One source of contamination in our somatic recordings could be the contribution of non-somatic compartments. In fiber photometry recordings from GCaMP labelled medium spiny neurons in striatum, it has been shown that the photometry signal correlates better with the calcium signals

originating from the neuropil, mainly dendrites of these neurons, rather than their somas[171]. This cannot affect our striatal recordings (only DA axons are labelled in our case, no other cells or cellular compartments); but it could certainly affect our somatic recordings in SNc, adding a source of noise, and potentially explaining the lower signal-to-noise ratio observed in our somatic vs axonal recordings. Regardless, this possible dendritic contribution to the photometry signal does not affect our conclusions. Even if the dendritic signal completely obscured the somatic signal, the similarities we observed between these recordings and the axonal recordings would mean that the dendritic signaling matches axonal signaling, making it highly almost absurd to imagine that the intermediate compartment, the soma, would be doing something different.

Instead, the only explanation for our results that is compatible with local cholinergic modulation as the main driver of DA release would require that action potentials generated at the axonal terminals backpropagate all the way back to the somas. While there is evidence that locally generated action potentials can travel across the dendritic arbor within striatum (at least in slice[37]), there is no evidence of this reaching the soma past the axonal initial segment, particularly *in vivo*. However, even if this was the case, it would require subtype-specific cholinergic modulation, beyond just anatomical precision (as we have shown, axons of different subtypes in the same region show different functional responses, and these are matched by their axons). Thus, this work's main conclusion that different genetic dopamine neurons subtypes show different functions still stands.

References

1. Hirsch, E., Graybiel, A. M. & Agid, Y. A. Melanized dopaminergic neurons are differentially susceptible to degeneration in Parkinson's disease. *Nat. 1988 3346180* **334**, 345–348 (1988).
2. Schultz, W., Ruffieux, A. & Aebischer, P. The activity of pars compacta neurons of the monkey substantia nigra in relation to motor activation. *Exp. Brain Res.* **51**, 377–387 (1983).
3. Schultz, W., Dayan, P. & Montague, P. R. A neural substrate of prediction and reward. *Science (80-.).* **275**, 1593–1599 (1997).
4. Schultz, W. Multiple dopamine functions at different time courses. *Annual Review of Neuroscience* vol. 30 259–288 (2007).
5. Howe, M. W. & Dombeck, D. A. Rapid signalling in distinct dopaminergic axons during locomotion and reward. *Nature* **535**, 505–510 (2016).
6. Da Silva, J. A. *et al.* Dopamine neuron activity before action initiation gates and invigorates future movements. *Nature* **554**, 244–248 (2018).
7. Coddington, L. T. & Dudman, J. T. The timing of action determines reward prediction signals in identified midbrain dopamine neurons. *Nat. Neurosci.* **21**, 1563–1573 (2018).
8. Dodson, P. D. *et al.* Representation of spontaneous movement by dopaminergic neurons is cell-type selective and disrupted in parkinsonism. *PNAS* **113**, E2180–E2188 (2016).
9. Menegas, W., Akiti, K., Amo, R., Uchida, N. & Watabe-Uchida, M. Dopamine neurons projecting to the posterior striatum reinforce avoidance of threatening stimuli. *Nat. Neurosci.* (2018).
10. Greenstreet, F. *et al.* Action prediction error: a value-free dopaminergic teaching signal that drives stable learning. *bioRxiv* 2022.09.12.507572 (2022).
11. Berke, J. D. What does dopamine mean? *Nat. Neurosci.* 1 (2018).
12. Howe, M. W., Tierney, P. L., Sandberg, S. G., Phillips, P. E. M. & Graybiel, A. M. Prolonged dopamine signalling in striatum signals proximity and value of distant rewards. *Nature* **500**, (2013).
13. Mohebi, A. *et al.* Dissociable dopamine dynamics for learning and motivation. *Nature* **570**, 65–70 (2019).
14. Menegas, W., Babayan, B. M., Uchida, N. & Watabe-uchida, M. Opposite initialization to novel cues in dopamine signaling in ventral and posterior striatum. *Elife* 1–26 (2017).
15. Matsumoto, M. & Hikosaka, O. Two types of dopamine neuron distinctly convey positive and negative motivational signals. *Nature* **459**, 837–841 (2009).
16. Lerner, T. N. *et al.* Intact-Brain Analyses Reveal Distinct Information Carried by SNc Dopamine Subcircuits. *Cell* **162**, 635–647 (2015).
17. Poulin, J.-F. F. *et al.* Mapping projections of molecularly defined dopamine neuron subtypes using intersectional genetic approaches. *Nat. Neurosci.* **21**, 1260–1271 (2018).
18. Evans, R. C. *et al.* Functional Dissection of Basal Ganglia Inhibitory Inputs onto Substantia Nigra Dopaminergic Neurons. *Cell Rep.* **32**, (2020).
19. Evans, R. C., Zhu, M. & Khaliq, Z. M. Dopamine inhibition differentially controls excitability of SNc dopamine neuron subpopulations through recruitment of T-type calcium channels. *J. Neurosci.* **37**, 0117–17 (2017).

20. Farassat, N. *et al.* In vivo functional diversity of midbrain dopamine neurons within identified axonal projections. *Elife* **8**, 1–27 (2019).

21. Trudeau, L. E. *et al.* The multilingual nature of dopamine neurons. *Prog. Brain Res.* **211**, 141–164 (2014).

22. Tritsch, N. X., Granger, A. J. & Sabatini, B. L. Mechanisms and functions of GABA co-release. *Nat. Rev. Neurosci.* **17**, 139–145 (2016).

23. Fu, Y., Paxinos, G., Watson, C. & Halliday, G. M. The substantia nigra and ventral tegmental dopaminergic neurons from development to degeneration. *J. Chem. Neuroanat.* **76**, 98–107 (2016).

24. Yamada, T., McGeer, P. L., Baimbridge, K. G. & McGeer, E. G. Relative sparing in Parkinson's disease of substantia nigra dopamine neurons containing calbindin-D28K. **526**, 303–307 (1990).

25. German, D. C., Manaye, K. F., Sonsalla, P. K. & Brooks, B. A. Midbrain Dopaminergic Cell Loss in Parkinson's Disease and MPTP-Induced Parkinsonism: Sparing of Calbindin-D25k—Containing Cells. *Ann. N. Y. Acad. Sci.* **648**, 42–62 (1992).

26. Kish, S. J., Shannak, K. & Hornykiewicz, O. Uneven Pattern of Dopamine Loss in the Striatum of Patients with Idiopathic Parkinson's Disease. *N. Engl. J. Med.* **318**, 876–880 (1988).

27. Menegas, W. *et al.* Dopamine neurons projecting to the posterior striatum form an anatomically distinct subclass. *Elife* **4**, 1–30 (2015).

28. Poulin, J. F., Gaertner, Z., Moreno-Ramos, O. A. & Awatramani, R. Classification of Midbrain Dopamine Neurons Using Single-Cell Gene Expression Profiling Approaches. *Trends in Neurosciences* vol. 43 155–169 (2020).

29. Kim, H. G. R. *et al.* A Unified Framework for Dopamine Signals across Timescales. *Cell* **183**, 1600-1616.e25 (2020).

30. Coddington, L. T. & Dudman, J. T. Learning from Action: Reconsidering Movement Signaling in Midbrain Dopamine Neuron Activity. *Neuron* **104**, 63–77 (2019).

31. Schultz, W., Stauffer, W. R. & Lak, A. The phasic dopamine signal maturing: from reward via behavioural activation to formal economic utility. *Current Opinion in Neurobiology* vol. 43 139–148 (2017).

32. Hamid, A. A., Frank, M. J. & Moore, C. I. Wave-like dopamine dynamics as a mechanism for spatiotemporal credit assignment. *Cell* **184**, 2733-2749.e16 (2021).

33. Tsutsui-Kimura, I. *et al.* Distinct temporal difference error signals in dopamine axons in three regions of the striatum in a decision-making task. *Elife* **9**, 1–39 (2020).

34. van Elzelingen, W. *et al.* A unidirectional but not uniform striatal landscape of dopamine signaling for motivational stimuli. *Proc. Natl. Acad. Sci.* **119**, (2022).

35. De Jong, J. W., Fraser, K. M. & Lammel, S. Mesoaccumbal Dopamine Heterogeneity: What Do Dopamine Firing and Release Have to Do with It? *Annu. Rev. Neurosci.* **45**, 109–129 (2022).

36. Threlfell, S. *et al.* Striatal dopamine release is triggered by synchronized activity in cholinergic interneurons. *Neuron* **75**, 58–64 (2012).

37. Liu, C. *et al.* An action potential initiation mechanism in distal axons for the control of dopamine release. *Science (80-.).* **375**, 1378–1385 (2022).

38. Pereira Luppi, M. *et al.* Sox6 expression distinguishes dorsally and ventrally biased dopamine neurons in the substantia nigra with distinctive properties and embryonic origins. *Cell Rep.* **37**, 109975 (2021).

39. Damier, P., Hirsch, E. C., Agid, Y. & Graybiel, A. M. The substantia nigra of the human brain. I. Nigrosomes and the nigral matrix, a compartmental organization based on calbindin D(28K) immunohistochemistry. *Brain* **122 (Pt 8**, 1421–1436 (1999).

40. Giguère, N., Nanni, S. B. & Trudeau, L. E. On Cell Loss and Selective Vulnerability of Neuronal Populations in Parkinson's Disease. *Front. Neurol.* **9**, (2018).

41. Kordower, J. H. *et al.* Disease duration and the integrity of the nigrostriatal system in Parkinson's disease. *Brain* **136**, 2419–2431 (2013).

42. Liu, G. *et al.* Aldehyde dehydrogenase 1 defines and protects a nigrostriatal dopaminergic neuron subpopulation. *J. Clin. Invest.* **124**, 3032–3046 (2014).

43. Nalls, M. A. *et al.* Identification of novel risk loci, causal insights, and heritable risk for Parkinson's disease: a meta-analysis of genome-wide association studies. *Lancet Neurol.* **18**, 1091–1102 (2019).

44. Mendez, I. *et al.* Cell type analysis of functional fetal dopamine cell suspension transplants in the striatum and substantia nigra of patients with Parkinson's disease. *Brain* **128**, 1498–1510 (2005).

45. Kramer, D. J., Risso, D., Kosillo, P., Ngai, J. & Bateup, H. S. Combinatorial Expression of Grp and Neurod6 Defines Dopamine Neuron Populations with Distinct Projection Patterns and Disease Vulnerability. *eNeuro* **5**, 152–170 (2018).

46. La Manno, G. *et al.* Molecular Diversity of Midbrain Development in Mouse, Human, and Stem Cells. *Cell* **167**, 566-580.e19 (2016).

47. Poulin, J. F. *et al.* Defining midbrain dopaminergic neuron diversity by single-cell gene expression profiling. *Cell Rep.* **9**, 930–943 (2014).

48. Saunders, A. *et al.* Molecular Diversity and Specializations among the Cells of the Adult Mouse Brain. *Cell* **174**, 1015-1030.e16 (2018).

49. Tiklová, K. *et al.* Single-cell RNA sequencing reveals midbrain dopamine neuron diversity emerging during mouse brain development. *Nat. Commun.* **10**, 581 (2019).

50. Hook, P. W. *et al.* Single-Cell RNA-Seq of Mouse Dopaminergic Neurons Informs Candidate Gene Selection for Sporadic Parkinson Disease. *Am. J. Hum. Genet.* **102**, 427–446 (2018).

51. Panman, L. *et al.* Sox6 and Otx2 Control the Specification of Substantia Nigra and Ventral Tegmental Area Dopamine Neurons. *Cell Rep.* **8**, 1018–1025 (2014).

52. Poulin, J. F., Tasic, B., Hjerling-Leffler, J., Trimarchi, J. M. & Awatramani, R. Disentangling neural cell diversity using single-cell transcriptomics. *Nat. Neurosci.* **19**, 1131–41 (2016).

53. Andersson, E. *et al.* Identification of Intrinsic Determinants of Midbrain Dopamine Neurons. *Cell* **124**, 393–405 (2006).

54. Bodea, G. O. *et al.* Reelin and CXCL12 regulate distinct migratory behaviors during the development of the dopaminergic system. *Dev.* **141**, 661–673 (2014).

55. Blaess, S. *et al.* Temporal-spatial changes in Sonic Hedgehog expression and signaling reveal different potentials of ventral mesencephalic progenitors to populate distinct ventral midbrain nuclei. *Neural Dev.* **6**, 1–20 (2011).

56. Joksimovic, M. *et al.* Spatiotemporally separable Shh domains in the midbrain define distinct dopaminergic progenitor pools. *Proc. Natl. Acad. Sci. U. S. A.* **106**, 19185–19190 (2009).

57. Metzakopian, E. *et al.* Genome-wide characterization of Foxa2 targets reveals upregulation of floor plate genes and repression of ventrolateral genes in midbrain dopaminergic progenitors. *Dev.* **139**, 2625–2634 (2012).

58. Yan, C. H., Levesque, M., Claxton, S., Johnson, R. L. & Ang, S. L. Lmx1a and Lmx1b Function Cooperatively to Regulate Proliferation, Specification, and Differentiation of Midbrain Dopaminergic Progenitors. *J. Neurosci.* **31**, 12413–12425 (2011).

59. Prakash, N. *et al.* A Wnt1-regulated genetic network controls the identity and fate of midbrain-dopaminergic progenitors in vivo. *Development* **133**, 89–98 (2006).

60. Brown, A., Machan, J., … L. H.-J. of C. & 2011, undefined. Molecular organization and timing of Wnt1 expression define cohorts of midbrain dopamine neuron progenitors in vivo. *Wiley Online Libr.* **519**, 2978–3000 (2011).

61. Arendt, D., Bertucci, P. Y., Achim, K. & Musser, J. M. Evolution of neuronal types and families. *Curr. Opin. Neurobiol.* **56**, 144–152 (2019).

62. Fiorenzano, A., Sozzi, E., Parmar, M., Storm, P. & Fico, A. Dopamine neuron diversity: recent advances and current challenges in human stem cell models and single cell sequencing. *mdpi.com* **10**, (2021).

63. Yamaguchi, T., Ehara, A., Nakadate, K. & Ueda, S. Tyrosine hydroxylase afferents to the interstitial nucleus of the posterior limb of the anterior commissure are neurochemically distinct from those projecting to neighboring nuclei. *J. Chem. Neuroanat.* **90**, 98–107 (2018).

64. Surmeier, D. J. & Surmeier, D. J. Determinants of dopaminergic neuron loss in Parkinson's disease. *FEBS J.* **285**, 3657–3668 (2018).

65. Cebrián, C. *et al.* MHC-I expression renders catecholaminergic neurons susceptible to T-cell-mediated degeneration. *Nat. Commun.* **5**, (2014).

66. Dzamko, N. *et al.* Toll-like receptor 2 is increased in neurons in Parkinson's disease brain and may contribute to alpha-synuclein pathology. *Acta Neuropathol.* **133**, 303–319 (2017).

67. Vaswani, A. R. *et al.* Correct setup of the substantia nigra requires reelin-mediated fast, laterally-directed migration of dopaminergic neurons. *Elife* **8**, (2019).

68. Kouwenhoven, W. M. *et al.* VGluT2 Expression in Dopamine Neurons Contributes to Postlesional Striatal Reinnervation. *J. Neurosci.* **40**, 8262–8275 (2020).

69. Poulin, J. F. *et al.* PRISM: A Progenitor-Restricted Intersectional Fate Mapping Approach Redefines Forebrain Lineages. *Dev. Cell* **53**, 740-753.e3 (2020).

70. Lendahl, U., Zimmerman, L. B. & McKay, R. D. G. CNS stem cells express a new class of intermediate filament protein. *Cell* **60**, 585–595 (1990).

71. Joyner, A. L. & Zervas, M. Genetic inducible fate mapping in mouse: Establishing genetic lineages and defining genetic neuroanatomy in the nervous system. *Dev. Dyn.* **235**, 2376–2385 (2006).

72. Monzón-Sandoval, J. *et al.* Human-specific transcriptome of ventral and dorsal midbrain dopamine neurons. *Wiley Online Libr.* **87**, 853–868 (2020).

73. Surmeier, D. J., Obeso, J. A. & Halliday, G. M. Selective neuronal vulnerability in Parkinson disease. *Nature Reviews Neuroscience* vol. 18 101–113 (2017).

74. Shen, H. *et al.* Genetic deletion of vesicular glutamate transporter in dopamine neurons increases vulnerability to MPTP-induced neurotoxicity in mice. *Proc. Natl. Acad. Sci. U. S. A.* **115**, E11532–E11541 (2018).

75. Steinkellner, T. *et al.* Role for VGLUT2 in selective vulnerability of midbrain dopamine neurons. *J. Clin. Invest.* **128**, 774–788 (2018).

76. Root, D. H. *et al.* Glutamate neurons are intermixed with midbrain dopamine neurons in nonhuman

primates and humans. *Sci. Rep.* **6**, 30615 (2016).

77. Inoue, K. ichi *et al.* Recruitment of calbindin into nigral dopamine neurons protects against MPTP-Induced parkinsonism. *Mov. Disord.* **34**, 200–209 (2019).

78. Fallon, J. H. & Moore, R. Y. Catecholamine innervation of the basal forebrain IV. Topography of the dopamine projection to the basal forebrain and neostriatum. *J. Comp. Neurol.* **180**, 545–579 (1978).

79. Gerfen, C. R. The neostriatal mosaic. I. Compartmental organization of projections from the striatum to the substantia nigra in the rat. *J. Comp. Neurol.* **236**, 454–476 (1985).

80. Haber, S. N., Fudge, J. L. & McFarland, N. R. Striatonigrostriatal pathways in primates form an ascending spiral from the shell to the dorsolateral striatum. *J. Neurosci.* **20**, 2369–2382 (2000).

81. Matsuda, W. *et al.* Single Nigrostriatal Dopaminergic Neurons Form Widely Spread and Highly Dense Axonal Arborizations in the Neostriatum. *J. Neurosci.* **29**, 444–453 (2009).

82. Prensa, L., Neuroscience, A. P.-J. of & 2001, undefined. The nigrostriatal pathway in the rat: a single-axon study of the relationship between dorsal and ventral tier nigral neurons and the striosome/matrix striatal. *Soc Neurosci.* (2001).

83. Vogt Weisenhorn, D. M., Giesert, F. & Wurst, W. Diversity matters – heterogeneity of dopaminergic neurons in the ventral mesencephalon and its relation to Parkinson's Disease. *Journal of Neurochemistry* 8–26 (2016).

84. Björklund, A. & Dunnett, S. B. Dopamine neuron systems in the brain: an update. *Trends Neurosci.* **30**, 194–202 (2007).

85. Simmons, S. C., Wheeler, K. & Mazei-Robison, M. S. Determination of circuit-specific morphological adaptations in ventral tegmental area dopamine neurons by chronic morphine. *Mol. Brain* **12**, (2019).

86. Kim, H. F., Ghazizadeh, A. & Hikosaka, O. Separate groups of dopamine neurons innervate caudate head and tail encoding flexible and stable value memories. *Front. Neuroanat.* **8**, 120 (2014).

87. Watabe-Uchida, M. & Uchida, N. Multiple dopamine systems: Weal and woe of dopamine. *Cold Spring Harb. Symp. Quant. Biol.* **83**, 83–95 (2018).

88. Bye, C., Thompson, L., neurology, C. P.-E. & 2012, undefined. Birth dating of midbrain dopamine neurons identifies A9 enriched tissue for transplantation into parkinsonian mice. *Elsevier*.

89. Brignani, S. *et al.* Remotely Produced and Axon-Derived Netrin-1 Instructs GABAergic Neuron Migration and Dopaminergic Substantia Nigra Development. *Neuron* **107**, 684-702.e9 (2020).

90. Chabrat, A. *et al.* Transcriptional repression of Plxnc1 by Lmx1a and Lmx1b directs topographic dopaminergic circuit formation. *Nat. Commun. 2017 81* **8**, 1–15 (2017).

91. Prasad, A. A. & Pasterkamp, R. J. Axon guidance in the dopamine system. *Adv. Exp. Med. Biol.* **651**, 91–100 (2009).

92. Mayer, C. *et al.* Developmental diversification of cortical inhibitory interneurons. *Nature* **555**, 457–462 (2018).

93. Kamath, T. *et al.* A molecular census of midbrain dopaminergic neurons in Parkinson's disease. *bioRxiv* (2021).

94. Mai, J. K. & Paxinos, G. The Human Nervous System. *Hum. Nerv. Syst.* (2012).

95. Olszewski, J. & Baxter, D. Cytoarchitecture of the human brainstem. By Jerzy Olszewski and

Donald Baxter. Published and distributed in North America for S. Karger by J. B. Lippincott Company, Philadelphia and Montreal. 1954. 199 pages. Price $16.00 (Reviewed by Gerhardt von Bonin). *J. Comp. Neurol.* **101**, 825–825 (1954).

96. Jensen, P. *et al.* Redefining the serotonergic system by genetic lineage. *Nat. Neurosci.* **11**, 417–419 (2008).

97. Martin, M. Cutadapt removes adapter sequences from high-throughput sequencing reads. *EMBnet.journal* **17**, 10–12 (2011).

98. Dobin, A. *et al.* STAR: ultrafast universal RNA-seq aligner. *Bioinformatics* **29**, 15–21 (2013).

99. Anders, S., Pyl, P. T. & Huber, W. HTSeq—a Python framework to work with high-throughput sequencing data. *Bioinformatics* **31**, 166 (2015).

100. Love, M. I., Huber, W. & Anders, S. Moderated estimation of fold change and dispersion for RNA-seq data with DESeq2. *Genome Biol.* **15**, (2014).

101. Mootha, V. K. *et al.* PGC-1α-responsive genes involved in oxidative phosphorylation are coordinately downregulated in human diabetes. *Nat. Genet.* **34**, 267–273 (2003).

102. Subramanian, A. *et al.* Gene set enrichment analysis: a knowledge-based approach for interpreting genome-wide expression profiles. *Proc. Natl. Acad. Sci. U. S. A.* **102**, 15545–15550 (2005).

103. Liberzon, A. *et al.* Molecular signatures database (MSigDB) 3.0. *Bioinformatics* **27**, 1739–1740 (2011).

104. Schultz, W. & Dickinson, A. Neuronal coding of prediction errors. *Annu. Rev. Neurosci* **23**, 473–500 (2000).

105. Schultz, W. The reward signal of midbrain dopamine neurons. *News Physiol. Sci.* **14**, 249–254 (1999).

106. Eshel, N., Tian, J., Bukwich, M. & Uchida, N. Dopamine neurons share common response function for reward prediction error. **19**, 479–486 (2016).

107. Dabney, W. *et al.* A distributional code for value in dopamine-based reinforcement learning. **577**, 671–675 (2020).

108. Berridge, K. C. The debate over dopamine's role in reward: The case for incentive salience. *Psychopharmacology (Berl).* **191**, 391–431 (2007).

109. Engelhard, B. *et al. Specialized coding of sensory, motor and cognitive variables in VTA dopamine neurons*. *Nature* vol. 570 509–513 (Nature Publishing Group, 2019).

110. Lutas, A. *et al.* State-specific gating of salient cues by midbrain dopaminergic input to basal amygdala. *bioRxiv* **22**, 687707 (2019).

111. de Jong, J. W. *et al.* A Neural Circuit Mechanism for Encoding Aversive Stimuli in the Mesolimbic Dopamine System. *Neuron* **101**, 133-151.e7 (2019).

112. Bromberg-Martin, E. S., Matsumoto, M. & Hikosaka, O. Dopamine in Motivational Control: Rewarding, Aversive, and Alerting. *Neuron* **68**, 815–834 (2010).

113. Fan, D., Rossi, M. A. & Yin, H. H. Mechanisms of action selection and timing in substantia nigra neurons. *J. Neurosci.* **32**, 5534–5548 (2012).

114. Brown, H. D., Mccutcheon, J. E., Cone, J. J., Ragozzino, M. E. & Roitman, M. F. Primary food reward and reward-predictive stimuli evoke different patterns of phasic dopamine signaling throughout the striatum. *Eur. J. Neurosci.* **34**, 1997–2006 (2011).

115. Barter, J. W. *et al.* Beyond reward prediction errors: The role of dopamine in movement kinematics. *Front. Integr. Neurosci.* **9**, 39 (2015).

116. Chen, T. W. *et al.* Ultrasensitive fluorescent proteins for imaging neuronal activity. *Nature* **499**, 295–300 (2013).

117. Fenno, L. E. *et al.* Comprehensive Dual- and Triple-Feature Intersectional Single-Vector Delivery of Diverse Functional Payloads to Cells of Behaving Mammals. *Neuron* **107**, 836-853.e11 (2020).

118. Tian, L. *et al.* Imaging neural activity in worms, flies and mice with improved GCaMP calcium indicators. *Nat. Methods* **6**, 875–881 (2009).

119. Lee, S. J. *et al.* Cell-type-specific asynchronous modulation of PKA by dopamine in learning. *Nat.* | **590**, 451 (2021).

120. Patriarchi, T. *et al.* An expanded palette of dopamine sensors for multiplex imaging in vivo. **17**, (2020).

121. Petreanu, L. *et al.* Activity in motor–sensory projections reveals distributed coding in somatosensation. *Nat. 2012 4897415* **489**, 299–303 (2012).

122. Cox, C. L., Denk, W., Tank, D. W. & Svoboda, K. Action potentials reliably invade axonal arbors of rat neocortical neurons. *Proc. Natl. Acad. Sci. U. S. A.* **97**, 9724–9728 (2000).

123. Turner, T. J. Nicotine Enhancement of Dopamine Release by a Calcium-Dependent Increase in the Size of the Readily Releasable Pool of Synaptic Vesicles. *J. Neurosci.* **24**, 11328–11336 (2004).

124. Woodward, J. J., Judson Chandler, L. & Leslie, S. W. Calcium-dependent and -independent release of endogenous dopamine from rat striatal synaptosomes. *Brain Res.* **473**, 91–98 (1988).

125. Tritsch, N. X. & Sabatini, B. L. Dopaminergic Modulation of Synaptic Transmission in Cortex and Striatum. *Neuron* (2012).

126. Cachope, R. *et al.* Selective Activation of Cholinergic Interneurons Enhances Accumbal Phasic Dopamine Release: Setting the Tone for Reward Processing. *Cell Rep.* **2**, 33–41 (2012).

127. Chen, K., Vincis, R. & Fontanini, A. Disruption of Cortical Dopaminergic Modulation Impairs Preparatory Activity and Delays Licking Initiation. *Cereb. Cortex* **29**, 1–14 (2019).

128. Grindberg, R. V. *et al.* RNA-sequencing from single nuclei. *Proc. Natl. Acad. Sci. U. S. A.* **110**, 19802–19807 (2013).

129. Saunders, B. T., Richard, J. M., Margolis, E. B. & Janak, P. H. Dopamine neurons create Pavlovian conditioned stimuli with circuit-defined motivational properties. *Nat. Neurosci.* **21**, 1072–1083 (2018).

130. Võikar, V., Kõks, S., Vasar, E. & Rauvala, H. Strain and gender differences in the behavior of mouse lines commonly used in transgenic studies. *Physiol. Behav.* **72**, 271–281 (2001).

131. Crabbe, J. C. Genetic differences in locomotor activation in mice. *Pharmacol. Biochem. Behav.* **25**, 289–292 (1986).

132. Schultz, W. Multiple dopamine functions at different time courses. *Annu Rev Neurosci* **30**, 259–288 (2007).

133. Tobler, P. N., Fiorillo, C. D. & Schultz, W. Adaptive coding of reward value by dopamine neurons. *Science (80-.).* **307**, 1642–1645 (2005).

134. Neher, E. & Sakaba, T. Multiple Roles of Calcium Ions in the Regulation of Neurotransmitter Release. *Neuron* **59**, 861–872 (2008).

135. Sun, F. *et al.* A Genetically Encoded Fluorescent Sensor Enables Rapid and Specific Detection of Dopamine in Flies, Fish, and Mice. *Cell* (2018).

136. Patriarchi, T. *et al.* Ultrafast neuronal imaging of dopamine dynamics with designed genetically encoded sensors. *Science (80-.).* **360**, (2018).

137. Parker, N. F. *et al.* Reward and choice encoding in terminals of midbrain dopamine neurons depends on striatal target. *Nat. Neurosci.* **19**, 845–854 (2016).

138. Moss, M. M., Zatka-Haas, P., Harris, K. D., Carandini, M. & Lak1, A. Dopamine Axons in Dorsal Striatum Encode Contralateral Visual Stimuli and Choices. *J. Neurosci.* **41**, 7197–7205 (2021).

139. Schultz, W. Predictive reward signal of dopamine neurons. *Journal of Neurophysiology* vol. 80 1–27 (1998).

140. Lahiri, A. A. K. & Bevan, M. D. Dopaminergic transmission rapidly and persistently enhances excitability of D1 receptor-expressing striatal projection neurons. *Neuron* 1–65 (2020).

141. Wu, J. *et al.* Distinct Connectivity and Functionality of Aldehyde Dehydrogenase 1a1-Positive Nigrostriatal Dopaminergic Neurons in Motor Learning. *Cell Rep.* **28**, 1167-1181.e7 (2019).

142. Zell, V. *et al.* VTA Glutamate Neuron Activity Drives Positive Reinforcement Absent Dopamine Co-release. *Neuron* **107**, 864-873.e4 (2020).

143. Melani, R. & Tritsch, N. X. Inhibitory co-transmission from midbrain dopamine neurons relies on presynaptic GABA uptake. *Cell Rep.* **39**, 110716 (2022).

144. Kim, J. I. *et al.* Aldehyde dehydrogenase 1a1 mediates a GABA synthesis pathway in midbrain dopaminergic neurons. *Science (80-.).* (2015).

145. Tritsch, N. X., Ding, J. B. & Sabatini, B. L. Dopaminergic neurons inhibit striatal output through non-canonical release of GABA. *Nature* **490**, (2012).

146. Anderson, D. W., Schray, R. C., Duester, G. & Schneider, J. S. Functional significance of aldehyde dehydrogenase ALDH1A1 to the nigrostriatal dopamine system. *Brain Res.* **1408**, 81–87 (2011).

147. Carmichael, K. *et al.* Function and Regulation of ALDH1A1-Positive Nigrostriatal Dopaminergic Neurons in Motor Control and Parkinson's Disease. *Frontiers in Neural Circuits* vol. 15 42 (2021).

148. Sgobio, C. *et al.* Aldehyde dehydrogenase 1-positive nigrostriatal dopaminergic fibers exhibit distinct projection pattern and dopamine release dynamics at mouse dorsal striatum. *Sci. Rep.* **7**, 1–13 (2017).

149. Madisen, L. *et al.* Transgenic mice for intersectional targeting of neural sensors and effectors with high specificity and performance. *Neuron* **85**, 942–958 (2015).

150. Hafemeister, C. & Satija, R. Normalization and variance stabilization of single-cell RNA-seq data using regularized negative binomial regression. *Genome Biol.* **20**, 1–15 (2019).

151. Welch, J. D. *et al.* Single-Cell Multi-omic Integration Compares and Contrasts Features of Brain Cell Identity. *Cell* **177**, 1873-1887.e17 (2019).

152. Choudhary, S. & Satija, R. Comparison and evaluation of statistical error models for scRNA-seq. *Genome Biol.* **23**, (2022).

153. Linderman, G. C. *et al.* Zero-preserving imputation of single-cell RNA-seq data. *Nat. Commun.* **13**, (2022).

154. Fenno, L. E. *et al.* Targeting cells with single vectors using multiple-feature Boolean logic. *Nat. Methods* **11**, 763–772 (2014).

155. Badura, A., Sun, X. R., Giovannucci, A., Lynch, L. A. & Wang, S. S.-H. Fast calcium sensor proteins for monitoring neural activity. *Neurophotonics* **1**, 025008 (2014).

156. Jaquins-Gerstl, A. & Michael, A. C. A review of the effects of FSCV and microdialysis measurements on dopamine release in the surrounding tissue. *Analyst* **140**, 3696–3708 (2015).

157. Cataldi, S., Lacefield, C., Shashaank, N., Kumar, G. & Sulzer, D. A dopamine-dependent decrease in dorsomedial striatum direct pathway neuronal activity is required for learned motor coordination. *bioRxiv* 2021.06.07.447452 (2022).

158. Ding, J. B., Guzman, J. N., Peterson, J. D., Goldberg, J. A. & Surmeier, D. J. Thalamic gating of corticostriatal signaling by cholinergic interneurons. *Neuron* **67**, 294–307 (2010).

159. Howe, M. *et al.* Coordination of rapid cholinergic and dopaminergic signaling in striatum during spontaneous movement. *Elife* **8**, (2019).

160. Brichta, L. & Greengard, P. Molecular determinants of selective dopaminergic vulnerability in Parkinson's disease: An update. *Front. Neuroanat.* **8**, (2014).

161. Anderegg, A., Poulin, J. F. & Awatramani, R. Molecular heterogeneity of midbrain dopaminergic neurons - Moving toward single cell resolution. *FEBS Lett.* **589**, 3714–3726 (2015).

162. Zeng, H. & Sanes, J. R. Neuronal cell-type classification: challenges, opportunities and the path forward. *Nat. Rev. Neurosci. 2017 189* **18**, 530–546 (2017).

163. Tasic, B. Single cell transcriptomics in neuroscience: cell classification and beyond. *Curr. Opin. Neurobiol.* **50**, 242–249 (2018).

164. Nagy, A. Cre recombinase: The universal reagent for genome tailoring. *Genesis* vol. 26 99–109 (2000).

165. Wei, W., Mohebi, A. & Berke, J. Striatal dopamine pulses follow a temporal discounting spectrum. *bioRxiv* 2021.10.31.466705 (2021).

166. Kim, C. K. *et al.* Simultaneous fast measurement of circuit dynamics at multiple sites across the mammalian brain. *Nat. Methods* **13**, 325–328 (2016).

167. Owen, S. F., Berke, J. D. & Kreitzer, A. C. Fast-Spiking Interneurons Supply Feedforward Control of Bursting, Calcium, and Plasticity for Efficient Learning. *Cell* **172**, 683-695.e15 (2018).

168. Grienberger, C. & Konnerth, A. Imaging Calcium in Neurons. *Neuron* **73**, 862–885 (2012).

169. Cossart, R., Ikegaya, Y. & Yuste, R. Calcium imaging of cortical networks dynamics. *Cell Calcium* **37**, 451–457 (2005).

170. Ambrosi, P. & Lerner, T. N. Striatonigrostriatal Circuit Architecture for Disinhibition of Dopamine Signaling. *bioRxiv* **40**, 111228 (2021).

171. Legaria, A. A. *et al.* Fiber photometry in striatum reflects primarily nonsomatic changes in calcium. *Nat. Neurosci. 2022 259* **25**, 1124–1128 (2022).

172. Sych, Y., Chernysheva, M., Sumanovski, L. T. & Helmchen, F. High-density multi-fiber photometry for studying large-scale brain circuit dynamics. *Nat. Methods* **16**, 553–560 (2019).

173. Pisanello, M. *et al.* The three-dimensional signal collection field for fiber photometry in brain tissue. *Front. Neurosci.* **13**, 82 (2019).

174. Farrell, K., Lak, A. & Saleem, A. B. Midbrain dopamine neurons signal phasic and ramping reward prediction error during goal-directed navigation. *Cell Rep.* **41**, 111470 (2022).

175. Chen, Y. *et al.* Soma-Targeted Imaging of Neural Circuits by Ribosome Tethering. *Neuron* **107**,

454-469.e6 (2020).

176. Shemesh, O. A. *et al.* Precision Calcium Imaging of Dense Neural Populations via a Cell-Body-Targeted Calcium Indicator. *Neuron* **107**, 470-486.e11 (2020).

177. Rasmussen, R. *et al.* Cortex-wide Changes in Extracellular Potassium Ions Parallel Brain State Transitions in Awake Behaving Mice. *Cell Rep.* **28**, 1182-1194.e4 (2019).

178. Albergaria, C., Silva, N. T., Pritchett, D. L. & Carey, M. R. Locomotor activity modulates associative learning in mouse cerebellum. *Nat. Neurosci.* **21**, 725–735 (2018).

179. Dombeck, D. A., Harvey, C. D., Tian, L., Looger, L. L. & Tank, D. W. Functional imaging of hippocampal place cells at cellular resolution during virtual navigation. *Nat. Neurosci.* **13**, 1433–1440 (2010).

180. Markowitz, J. E. *et al.* The Striatum Organizes 3D Behavior via Moment-to- Moment Action Selection Normal syllable sequence Lesion Syllable A. *Cell* **174**, 1–15 (2018).

181. Tellez, L. A. *et al.* Separate circuitries encode the hedonic and nutritional values of sugar. *Nat. Neurosci.* **19**, 465–470 (2016).

182. Jin, X. & Costa, R. M. Start/stop signals emerge in nigrostriatal circuits during sequence learning. *Nature* **466**, (2010).

183. Chang, C. Y., Gardner, M., Di Tillio, M. G. & Schoenbaum, G. Optogenetic Blockade of Dopamine Transients Prevents Learning Induced by Changes in Reward Features. *Curr. Biol.* **27**, 3480-3486.e3 (2017).

184. Berry, J. A., Phan, A. & Davis, R. L. Dopamine Neurons Mediate Learning and Forgetting through Bidirectional Modulation of a Memory Trace. *Cell Rep.* **25**, 651–662 (2018).

185. Oleson, E. B. & Cheer, J. F. On the role of subsecond dopamine release in conditioned avoidance. *Frontiers in Neuroscience* (2013).

186. Mustapha, M. & Taib, C. N. M. MPTP-induced mouse model of Parkinson's disease: A promising direction for therapeutic strategies. *Bosn. J. Basic Med. Sci.* **21**, 422–433 (2021).

187. Eshel, N. *et al.* Striatal dopamine integrates cost, benefit and motivation. *bioRxiv* 2022.09.20.508777 (2022).

188. Avvisati, R. *et al.* Distributional coding of associative learning within projection-defined populations of midbrain dopamine neurons. *bioRxiv* (2022).

189. Schultz, W. Dopamine reward prediction-error signalling: a two-component response. *Nat. Rev. Neurosci. 2016 173* **17**, 183–195 (2016).

190. Schmidt, R. & Berke, J. D. A Pause-then-Cancel model of stopping: evidence from basal ganglia neurophysiology. *R. Soc. Publ.* (2017).

191. Agnati, L. F., Zoli, M., Strömberg, I. & Fuxe, K. Intercellular communication in the brain: Wiring versus volume transmission. *Neuroscience* vol. 69 711–726 (1995).

192. Arbuthnott, G. W. & Wickens, J. Space, time and dopamine. *Trends in Neurosciences* vol. 30 62–69 (2007).

193. Paget-Blanc, V. *et al.* A synaptomic analysis reveals dopamine hub synapses in the mouse striatum. *Nat. Commun.* **13**, 1–19 (2022).

194. Liu, C., Goel, P. & Kaeser, P. S. *Spatial and temporal scales of dopamine transmission*. *Nature Reviews Neuroscience* vol. 22 345–358 (Nature Publishing Group, 2021).

195. Rice, M. E. & Cragg, S. J. Dopamine spillover after quantal release: Rethinking dopamine transmission in the nigrostriatal pathway. *Brain Res. Rev.* **58**, 303–313 (2008).

196. Cragg, S. J. & Rice, M. E. DAncing past the DAT at a DA synapse. *Trends in Neurosciences* vol. 27 270–277 (2004).

197. Cui, G. *et al.* Concurrent activation of striatal direct and indirect pathways during action initiation. *Nature* **494**, 238–242 (2013).

198. Gadagkar, V. *et al.* Dopamine neurons encode performance error in singing birds. *Science (80-.).* **354**, 1278–1282 (2016).

199. Bogacz, R. Dopamine role in learning and action inference. *bioRxiv* (2019.

200. Hunnicutt, B. J. *et al.* A comprehensive excitatory input map of the striatum reveals novel functional organization. *Elife* **5**, (2016).

201. Hintiryan, H. *et al.* The mouse cortico-striatal projectome. *Nat. Neurosci.* 1–19 (2016).

202. Thorn, C. A., Atallah, H., Howe, M. & Graybiel, A. M. Differential Dynamics of Activity Changes in Dorsolateral and Dorsomedial Striatal Loops during Learning. *Neuron* **66**, 781–795 (2010).

203. Kupferschmidt, D. A., Juczewski, K., Cui, G., Johnson, K. A. & Lovinger, D. M. Parallel, but Dissociable, Processing in Discrete Corticostriatal Inputs Encodes Skill Learning. *Neuron* **96**, 476-489.e5 (2017).

204. Graybiel, A., Harbor, S. G.-C. S. & 2015, undefined. The striatum: where skills and habits meet. *cshperspectives.cshlp.org* **7**, (2015).

205. Miller, K. J., Shenhav, A. & Ludvig, E. A. Habits without values. *Psychological Review* vol. 126 292–311 (2019).

206. Jenrette, T. A., Logue, J. B. & Horner, K. A. Lesions of the Patch Compartment of Dorsolateral Striatum Disrupt Stimulus-Response Learning. *Neuroscience* **415**, 161–172 (2019).

207. Nadel, J. A., Pawelko, S. S., Copes-Finke, D., Neidhart, M. & Howard, C. D. Lesion of striatal patches disrupts habitual behaviors and increases behavioral variability. *PLoS One* **15**, (2020).

208. Crittenden, J. R. *et al.* Striosome-dendron bouquets highlight a unique striatonigral circuit targeting dopamine-containing neurons. *PNAS* **113**, 11318–11323 (2016).

209. Barnett, W. H., Kuznetsov, A. & Lapish, C. C. Distinct corticostriatal compartments drive competition between adaptive and automatized behavior. *bioRxiv* (2022).

210. Schultz, W. Dopamine reward prediction error coding. *Dialogues Clin. Neurosci.* **18**, 23–32 (2016).

211. Lerner, T. N. & Kreitzer, A. C. Neuromodulatory control of striatal plasticity and behavior. *Current Opinion in Neurobiology* vol. 21 322–327 (2011).

212. Hnasko, T. S. *et al.* Vesicular Glutamate Transport Promotes Dopamine Storage and Glutamate Corelease In Vivo. *Neuron* **65**, 643–656 (2010).

213. Wang, D. V. *et al.* Disrupting Glutamate Co-transmission Does Not Affect Acquisition of Conditioned Behavior Reinforced by Dopamine Neuron Activation. *Cell Rep.* (2017).

214. Adrover, M. F., Shin, J. H. & Alvarez, V. A. Glutamate and Dopamine Transmission from Midbrain Dopamine Neurons Share Similar Release Properties But Are Differentially Affected by Cocaine. *J. Neurosci.* (2014).

215. Vaaga, C. E., Brown, S. T. & Raman, I. M. Cerebellar modulation of synaptic input to freezing-related neurons in the periaqueductal gray. *Elife* **9**, 1–28 (2020).

216. Kawano, M. *et al.* Particular subpopulations of midbrain and hypothalamic dopamine neurons express vesicular glutamate transporter 2 in the rat brain. *J. Comp. Neurol.* **498**, 581–592 (2006).

217. Fortin, G. M. *et al.* Segregation of dopamine and glutamate release sites in dopamine neuron axons: regulation by striatal target cells. *FASEB J.* **33**, 400–417 (2019).

218. Steinkellner, T. *et al.* Dopamine neurons exhibit emergent glutamatergic identity in Parkinson's disease. *Brain* **145**, 879–886 (2022).

219. Damier, P., Hirsch, E. C., Agid, Y. & Graybiel, A. M. The substantia nigra of the human brainII. Patterns of loss of dopamine-containing neurons in Parkinson's disease. *Brain* **122**, 1437–1448 (1999).

220. Buck, S. A. *et al.* VGLUT2 Is a Determinant of Dopamine Neuron Resilience in a Rotenone Model of Dopamine Neurodegeneration. *J. Neurosci.* **41**, 4937–4947 (2021).

221. Buck, S. A. *et al.* Roles of VGLUT2 and Dopamine/Glutamate Co-Transmission in Selective Vulnerability to Dopamine Neurodegeneration. *ACS Chem. Neurosci.* **13**, 187–193 (2022).

222. Yuan, H. H., Chen, R. J., Zhu, Y. H., Peng, C. L. & Zhu, X. R. The neuroprotective effect of overexpression of calbindin-D28k in an animal model of Parkinson's disease. *Mol. Neurobiol.* **47**, 117–122 (2013).

223. Cai, H., Liu, G., Sun, L. & Ding, J. Aldehyde Dehydrogenase 1 making molecular inroads into the differential vulnerability of nigrostriatal dopaminergic neuron subtypes in Parkinson's disease. *Translational Neurodegeneration* vol. 3 (2014).

224. Duda, J., Pötschke, C. & Liss, B. Converging roles of ion channels, calcium, metabolic stress, and activity pattern of Substantia nigra dopaminergic neurons in health and Parkinson's disease. *J. Neurochem.* **139**, 156–178 (2016).

225. Chan, C. S., Gertler, T. S. & Surmeier, D. J. A molecular basis for the increased vulnerability of substantia nigra dopamine neurons in aging and Parkinson's disease. *Mov. Disord.* **25**, S63–S70 (2010).

226. Liang, C. L., Wang, T. T., Luby-Phelps, K. & German, D. C. Mitochondria mass is low in mouse substantia nigra dopamine neurons: Implications for Parkinson's disease. *Exp. Neurol.* **203**, 370–380 (2007).

227. Todd, K. L., Lipski, J. & Freestone, P. S. Subthalamic nucleus exclusively evokes dopamine release in the tail of the striatum. *J. Neurochem.* **162**, 417–429 (2022).

228. Gill, C. E. *et al.* Deep Brain Stimulation for Early-Stage Parkinson's Disease: An Illustrative Case. *Neuromodulation Technol. Neural Interface* **14**, 515–522 (2011).

229. Vitek, J. L. Mechanisms of deep brain stimulation: Excitation or inhibition. *Mov. Disord.* **17**, S69–S72 (2002).

230. Chuhma, N., Mingote, S., Moore, H. & Rayport, S. Dopamine neurons control striatal cholinergic neurons via regionally heterogeneous dopamine and glutamate signaling. *Neuron* **81**, 901–912 (2014).

231. Rice, M. E. & Cragg, S. J. Nicotine amplifies reward-related dopamine signals in striatum. *Nat. Neurosci. 2004 76* **7**, 583–584 (2004).

Vita

2012-2016 BSc in Molecular Biology & Biochemistry, Universidad Autónoma de Madrid, Madrid (Spain).

2015-2016 Neuroscience specialization as an international exchange student at the Ohio State University, Columbus, Ohio (USA). Undergraduate research thesis in the lab of Dr. Anthony Brown.

2016-2022 Ph.D. in Neuroscience, Northwestern University, Evanston, Illinois (USA). Ph.D. Advisors Dr. Daniel Dombeck and Dr. Rajeshwar Awatramani.

Publications

Azcorra*, M., Gaertner*, Z., Davidson, C., Ramakrishnan, C., Fenno, L., Kim, Y. S., Deisseroth, K., Awatramani, R. & Dombeck, D. A. (2022). Dopaminergic axons track somatic signaling in behaving mice. *BioRxiv.* https://www.biorxiv.org/content/10.1101/2022.06.20.496872v1

Gaertner, Z. **Azcorra, M.**, Awatramani, R., & Dombeck, D. A. (2022). Molecular heterogeneity in the substantia nigra: a roadmap for understanding PD. *Neurobiology of Disease.* https://doi.org/10.1016/j.nbd.2022.105925

Luppi*, M. P., **Azcorra*, M.**, Caronia-Brown, G.*, Poulin, J. F., Gaertner, Z., Gatica, S., Moreno-Ramos, O. A., Nouri, N., Dubois, M., Ma, Y. C., Ramakrishnan, C., Fenno, L., Kim, Y. S., Deisseroth, K., Cicchetti, F., Dombeck, D. A. & Awatramani, R. (2021). Sox6 expression distinguishes dorsally and ventrally biased dopamine neurons in the substantia nigra with distinctive properties and embryonic origins. *Cell reports*. https://doi.org/10.1016/j.celrep.2021.109975

Boyer, N. P., **Azcorra, M.**, Jung, P., & Brown, A. (2020). Imaging and Analysis of Neurofilament Transport in Excised Mouse Tibial Nerve. *JoVE*. https://dx.doi.org/10.3791/61264

Howe, M., Ridouh, I., Mascaro, A. L. A., Larios, A., **Azcorra, M.**, & Dombeck, D. A. (2019). Coordination of rapid cholinergic and dopaminergic signaling in striatum during spontaneous movement. *Elife*. https://doi.org/10.7554/eLife.44903.001

*Co-first authors